SERIES ON HYDRAULIC MACHINERY – VOL. 2

Abrasive Erosion & Corrosion of Hydraulic Machinery

Editors
C. G. Duan | V. Y. Karelin

Imperial College Press

Abrasive Erosion & Corrosion of Hydraulic Machinery

HYDRAULIC MACHINERY BOOK SERIES

- **Hydraulic Design of Hydraulic Machinery**
  Editor: Prof. H Radha Krishna
- **Mechanical Design and Manufacturing of Hydraulic Machinery**
  Editor: Prof. Mei Z Y
- **Transient Phenomena of Hydraulic Machinery**
  Editors: Prof. S Pejovic, Dr. A P Boldy
- **Cavitation of Hydraulic Machinery**
  Editors: Prof. S C Li
- **Erosion and Corrosion of Hydraulic Machinery**
  Editors: Prof. Duan C G, Prof. V Karelin
- **Vibration and Oscillation of Hydraulic Machinery**
  Editor: Prof. H Ohashi
- **Control of Hydraulic Machinery**
  Editor: Prof. H Brekke

The International Editorial Committee (IECBSHM):

Chairman: *Prof. Duan C G*
Secretary: *Prof. Li S C*
Dr. A P Boldy
Treasurer: *Dr R K Turton*

Committee Members:

Prof. H Brekke (Norway)
Prof. E Egusquiza (Spain)
Dr. H R Graze (Australia)
Prof. P Henry (Switzerland)
Prof. V Karelin (Russia)
Prof. Li S C (China)
Prof. M T de Almeida (Brazil)
Prof. M Matsumura (Japan)
Prof. A Mobarak (Egypt)
Prof. H Netsch (Canada)
Prof. S Pejovic (Yugoslavia)
Prof. H Petermann (Germany)
Prof. C S Song (USA)
Prof. H I Weber (Brazil)
Prof. V P Chebaevski (Russia)
Prof. M Fanelli (Italy)
Prof. R Guarga (Uruguay)
Dr. H B Horlacher (Germany)
Prof. G Krivchenko (Russia)
Prof. D K Liu (China)
Prof. C S Martin (USA)
Prof. Mei Z Y (China)
Prof. H Murai (Japan)
Prof. H Ohashi (Japan)
Prof. D Perez-Franco (Cuba)
Prof. H C Radha Krishna (India)
Prof. C Thirriot (France)
Prof. G Ziegler (Austria)

Honorary Members:

Prof. B Chaiz (Switzerland)
Prof. J Raabe (Germany)

SERIES ON HYDRAULIC MACHINERY – VOL. 2

Committee Chairman: C. G. Duan Series Editor: S. C. Li

Abrasive Erosion & Corrosion of Hydraulic Machinery

Editors

C. G. Duan
International Research Center on Hydraulic Machinery, Beijing, China

V. Y. Karelin
Moscow State University of Civil Engineering, Russia

ICP

Imperial College Press

Published by

Imperial College Press
57 Shelton Street
Covent Garden
London WC2H 9HE

Distributed by

World Scientific Publishing Co. Pte. Ltd.
P O Box 128, Farrer Road, Singapore 912805
USA office: Suite 202, 1060 Main Street, River Edge, NJ 07661
UK office: 57 Shelton Street, Covent Garden, London WC2H 9HE

British Library Cataloguing-in-Publication Data
A catalogue record for this book is available from the British Library.

ABRASIVE EROSION AND CORROSION OF HYDRAULIC MACHINERY

Copyright © 2002 by Imperial College Press

All rights reserved. This book, or parts thereof, may not be reproduced in any form or by any means, electronic or mechanical, including photocopying, recording or any information storage and retrieval system now known or to be invented, without written permission from the Publisher.

For photocopying of material in this volume, please pay a copying fee through the Copyright Clearance Center, Inc., 222 Rosewood Drive, Danvers, MA 01923, USA. In this case permission to photocopy is not required from the publisher.

ISBN 1-86094-335-7

Printed in Singapore by Mainland Press

CONTENTS

Foreword of the Editor xi

Contributing Authors xiii

1 Fundamentals of Hydroabrasive Erosion Theory 1
V. Ya Karelin, A.I. Denisov and Y.L. Wu

1.1 Introduction 1
1.2 Mechanism of Hydroabrasive Effect Produced by Particles 4
1.3 Abrasive Erosion of Hydraulic Turbine 21
1.3.1 Illustrative Examples of Hydraulic Abrasive in Hydraulic Turbines 21
1.3.2 Silt Erosion of Hydro-turbines 25
1.4 Abrasive Erosion of Pump 34
1.4.1 Examples of Hydraulic Abrasion Taking Place in Pumps 34
1.4.2 Silt Erosion in Pumps 36
1.5 Technical and Economic Effect Caused by The Erosion Arising in Hydraulic Turbines and Pumps 42
1.6 Approach to Anti Abrasive from Hydraulic Machinery 48
1.6.1 Approach Avenues on Anti-silt Erosion of Hydraulic Machinery 48
1.6.2 Anti-abrasion Hydraulic Design of Pumps 49
1.6.3 Prediction of Silt-Erosion Damage in Pump Design by Test 49
References 51

2 Calculation of Hydraulic Abrasion 53
V. Ya Karelin, A.I. Denisov and Y.L. Wu

2.1 Calculation of Hydraulic Abrasion Proposed by V. Ya Karelin, and A.I. Denisov 53
2.2 Prediction Model of Hydraulic Abrasion 74
2.2.1 Prediction Erosion Model Proposed by Finnie and Bitter 74

2.2.2 Mechanistic Model Developed by The Erosion/Corrosion Research Center 84
2.2.3 Prediction Erosion Model Proposed by McLaury et al. 88
References 93

3 Analysis and Numerical Simulation of Liquid-Solid Two-Phase Flow 95
Y.L. Wu

3.1 Basic Equations of Liquid-Solid Two-Phase Flow through Hydraulic Machinery 95
3.1.1 Introduction 95
3.1.2 General Concepts of Multiphase Flow 97
3.1.3 Basic Equations of Multiphase Flow 101
3.2 Closed Turbulent Equations for Liquid-Solid Two-Phase Flow through Hydraulic Machinery 110
3.2.1 Closed Turbulence Model Using the Modeled Second Correlation 110
3.2.2 The Algebraic Turbulence Stresses Model of Two-Phase Flow 117
3.2.3 The k-ε-k_p Turbulence Model of Two-Phase Flow 120
3.2.4 Lagrangian-Eulerian Model for Liquid-Particle Two-Phase Flow 125
3.3 Numerical Simulation of Liquid-Particle Two-Phase Flow through Hydraulic Machinery by Two-Fluid Model 132
3.3.1 Numerical Method for Simulating Liquid-Particle Two-Phase Flow 132
3.3.2 Calculated Examples of Two-Turbulent Flow by Using Two-Fluid Model 141
References 152

4 Design of Hydraulic Machinery Working in Sand Laden Water 155
H. Brekke, Y.L. Wu and B.Y. Cai

4.1 Hydraulic Design of Turbines 155
4.1.1 Introduction 155
4.1.2 Impulse Turbines 156
4.1.3 Reaction Turbines 172

4.2 Effects of Silt-Laden Flow on Cavitation Performances and Geometric Parameters of Hydraulic Turbines 181
4.2.1 Effects of Silt-Laden Flow on Cavitation Performances of Hydrauliv Turbines 181
4.2.2 Model Experiments on Cavitation of Turbines in Silt-Laden Flow 186
4.2.3 Selection of Geometric Parameters of Turbines Operating in Silt-Laden Flow 187
4.3 Hydraulic Design of Slurry Pump 196
4.3.1 Internal Flow Characters through Slurry Pumps 196
4.3.2 Effects of Impeller Geometry on Performances of Slurry Pumps and Its Determination 202
4.3.3 Vane Pattern 208
4.3.4 Hydraulic Design of Centrifugal Slurry Pumps 212
4.3.5 Hydraulic Design of Slurry Pump Casing 216
4.3.6 Hydraulic Design for Large-Scale Centrifugal Pumps in Silt-Laden Rivers 219
4.4 Hydraulic Design of Solid-Liquid Flow Pumps 220
4.4.1 Working Condition of Solid-Liquid Flow Pumps 220
4.4.2 Hydraulic Design of Solid-Liquid Flow Pumps 223
4.4.3 Examples of the Design 230
References 232

5 Erosion-Resistant Materials 235
M. Matsumura and B.E. Chen

5.1 Selection of Erosion-Resistant Materials 235
5.1.1 Multiposion Test in a Real Water Turbine 235
5.1.2 Laboratory Erosion Tests 241
5.1.3 Selection of Materials for Hydraulic Machines 246
5.2 Metallic Materials 250
5.2.1 Testing Apparatus and Procedure 251
5.2.2 Test Results 255
5.2.3 Damage on Pump Components 257
5.2.4 Requisites for Laboratory Tests 258
5.3 Organic Polymer Linings 262
5.3.1 Conventional Polyurethane Lined Pipe 263

5.3.2 Room-Temperature Curing Polyurethane (RTV) 265
5.3.3 Durability of RTV Lined Pipe 269
5.3.4 Cost Estimation 272
5.4 Ceramics 273
5.4.1 Bulk Ceramics 275
5.4.2 Cemented Carbides 279
5.4.3 Coatings 282
5.5 Metal Protective Coating 285
5.5.1 Bead Welding 285
5.5.2 Paving Welding 291
5.5.3 Alloy Powder Spray Coating 292
5.6 Non-Metallic Protection Coating 298
5.6.1 Epoxy Emery Coating 299
5.6.2 Composite Nylon Coating 303
5.6.3 Rubber Coating of polyurethane 305
5.6.4 Composite Enamel Coating 307
5.7 Surface Treatment against Erosion Damage 308
5.7.1 Quenching and Tempering 309
5.7.2 Diffusion Permeating Plating 309
References 312

6 Interaction between Cavitation and Abrasive Erosion Processes 315
V. Ya Karelin, A.I. Denisov and Y.L. Wu

6.1 Effect of Suspended Particles on Incipient and Developed of Cavitation 315
6.2 Effect of Cavitation on Hydroabrasive Erosion 330
6.3 Relationship between Hydroabrasive Erosion and Cavitational Erosion 338
References 348

7 Corrosion on Hydraulic Machinery 349
M. Matsumura
7.1 Fundamentals of Corrosion 349
7.1.1 Corrosion Cell 349
7.1.2 Electrode Potentials 351
7.1.3 Polarization 356
7.1.4 Polarization Diagram 359

7.2 Application of Corrosion Theories 361
7.2.1 Pourbaix Diagram 361
7.2.2 Influences of pH and Fluid Velocity upon Corrosion Rate 363
7.2.3 Cathodic Protection 366
7.2.4 Passivity 368
7.2.5 Stainless Steel 369
7.2.6 Polarization-Resistance Method 371
7.3 Corrosion of Pump Parts 373
7.3.1 Corrosion Caused by Velocity Difference 373
7.3.2 Corrosion Promoted by Mixed Use of Different Materials (Galvanic Corrosion) 377
7.3.3 Crevice Corrosion and Other Localized Corrosion 381
7.4 Interaction of Corrosion with Erosion 387
7.4.1 Experiment on Slurry Erosion-Corrosion 387
7.4.2 Basic Equations Describing the Combined Effect of Erosion and Corrosion 394
7.4.3 Analysis on a Single Crater 397
7.4.4 Parameters Affecting the Mutual Interaction Mechanism 404
References 406

This page is intentionally left blank

Foreword of the Editor

This book entitled *Abrasive Erosion and Corrosion of Hydraulic Machinery* is one of the many volumes of the Book Series on Hydraulic Machinery organised and edited by its International Editorial Committee. This volume deals with the abrasive erosion and corrosion of hydraulic machinery, the theory and practical subjects being arisen from the engineering reality.

The abrasive erosion damage is one of the most important technical problem for hydro-electric power stations working in silt laden water, and the pumping plants to be employed in diversion of solid particle-liquid two phase flow in many industrial and agricultural sectors. In countries with rivers of high silt content the exploitation of those rivers are inevitably faced with the silt erosion problem.

From the point of view of the requirements from industry and the achievements attained from research on the abrasive erosion and corrosion, a volume on generalization and summarization of this subject should be worth much. The works of this volume try to expound the fundamental theory, research situation, and achievements from laboratory and practice engineering of the abrasive erosion and corrosion of hydraulic machinery.

This volume consists of seven chapters. Chapter 1 describes the fundamentals, the abrasive erosion theory, and the abrasive erosion of hydraulic turbines and pumps. Chapter 2 analyses the influence factors on silt erosion. Chapter 3 describes the particles laden flow analyses. Chapter 4 deals with the design of hydraulic machinery working in silt laden water. In Chapter 5, the anti-abrasive erosion materials used for manufacturing and site repair of hydro-electric plants and pumping stations are described. Chapter 6, discusses the inter-relation between abrasive erosion and cavitation erosion. The corrosion of hydraulic machinery is discussed in Chapter 7.

This Volume is written by 7 authors from 4 countries who are long time experts in the field of abrasive erosion and corrosion. Most chapters of this volume were written by two or three authors and composed of their contributions. The editor's work was to draw up the frame outline of the chapters and sections, invite authors, and composting the contents of the whole book including making some necessary readjusting among the works contributed by different authors.

In the case of different authors approaching the same subject, they may offer different point of view and materials collected from different sources, which really are useful for a better understanding on the subject.

When this Volume is completed, we are deeply obliged to Prof. S. C. Li and Dr. A. P. Boldy of University of Warwick, Prof. Y.L. Wu and Prof. Z.Y. Mei of Tsing Hua University, for their valuable works not only in this volume, but also in their devotion to the work for our International Editorial Committee of Book Series on Hydraulic Machinery.

For this Volume, our colleagues in the International Research Centre on Hydraulic Machinery especially Prof. Y.L. Wu and Miss Q. Lei who rendered great assistance in the editing of camera ready manuscript of this volume. Here, we wish to extent our sincere thanks to them.

Duan C G and V Y Karelin, Editors

Contributing Authors

Duan Chang Guo, Professor,

International Research Centre on Hydraulic Machinery.
Postgraduate School, North China Institute of Water Power.
Beijing Univeristy of Polytechnic, Beijing, China.

Born in Beijing, male, Chinese. Graduated from Tsinghua University in 1962. Appointed Associate Professor and Professor at Postgraduate School, North China Institute of Water Power and Beijing Univeristy of Polytechnic in 1972 and 1978 respectively. Involved in teaching, research and engineering project in the field of hydraulic machinery and hydropower for 39 years. President of Executive Committee of the International Research Centre on Hydraulic Machinery (Beijing). Former Executive Member of IAHR Section on Hydraulic Machinery and Cavition. Chairman of the IECBSHM.

Vladimir Yakovlevich Karelin, Doctor, Professor,

Moscow State University of Civil Engineering,
Moscow, Russia.

Born in 1931 in Ekaterinbug, male, Russian. Graduated from Moscow V.V.Kuibyshev Engineering Bulding Institute (Moscow State University of Civil Engineering at present) in 1958. Appointed Professer and Rector of Moscow State University of Civil Engineering. Full member of Rusian Academy of Architecture and Building Sciences, several branch academies. Academician of the Russian Engineering Academy. Honored Doctor of some Russian and Foreign Universities. Author of more than 270 scientific works, including eight textbooks and eight monographs, several of which were published abroad.

Hermod Brekke, Professor,
Division of Thermal Energy and Hydropower, Section Hydro Machinery, Norwegian University of Science and Technology, Trondheim, Norway.

Awarded M.Sc. Mechanical Engineering in 1957 and conferred Doctor Technical in 1984 at NTNU, respectively. After graduation involved in development and design of all kinds of hydraulic turbines and governors at Kvaerner Brug, Oslo, Norway. Head of division for turbine development 1973-83. Appointed Professor in hydraulic turbomachinery at NTNU in 1987. Elected member of Norwegian Academy of Technical Science (1977), Member of IAHR Board, Section on Hydraulic Machinery, Equipment and Cavitation. IAHR Section Chairman 1989. Chief delegate for IEC EC4 for Norway from 1986. Vice president in executive committee of the International Research Centre on Hydraulic Machinery, Beijing.

Wu Yu Lin, Professor,
Department of Hydraulic Engineering,
Tsinghua University, Beijing China.

Born 1944 in Beijing China. Educated at Tsinghua University. Master Degree 1981. Advanced studies in Department of Fluid Engineering, Cranfield Institute of Technology, UK, 1984. Doctor of engineering degree from Tohoku University, 1996. Professional experience includes design and installation of hydropower equipment. Research interests include internal flow and turbulent flow computation; multiphase flow; design of slurry pumps and various new types of pumps. Invited researcher in Institute of Fluid Science, Tohoku University, Japan. Member of Fluid Machinery Com-mittee, Chinese society for Thermophysics Engineering Council member of Division of Fluid Engineering, Chinese Society of Mechanical Engineering.

Masanobu Matsumura, Professor,
Faculty of Engineering, Hiroshima University, Japan.

Born in 1939 in Tokyo, male, Japanese. Graduated in 1962 with B.S. from Hiroshima University. Awarded Master and Doctor degree from Tokyo Institute of Technology, Japan in 1964 and 1967 respectively. Appointed lecturer in 1967, Associate Professor in 1962, and Professor in 1982 at Hiroshima University respectively. Dean of Faculty of Engineering, Hiroshima University. Member of Dean's Council, Hiroshima University.

Chen Bing-Er, Professor,
Gan Su Industry Technology University
Lan Zhou, Gan Su, China

Born in 1928. Appointed professor in Hydraulic Machinery of Gan Su Industry Technology University. Member of International Research Centre on Hydraulic Machinery (Beijing), now retired. Involved teaching and research on hydraulic machinery for 40 years.

Alexej Ivanovich Denisov, Doctor
Moscow State Building University, Moscow, Russia.

Born in Moscow 1935, male, Russian. Graduated from Moscow V. V. Kuibyshew Engineering Building Institute in 1958. Senior Researcher of Moscow State Buliding University (MSBU). Belongs to a group of the specialists in mechanical equipment of large water – economical systems including protection against cavi-tation – abrasive wear with use of metallopolymers and emergency repair products. Author of more the 75 scientific works several of which were published abroad.

Cai Bao Yuan, Professor,

China Mechanical Industry Technology Company, Beijing, China

Born in 1937, Chinese, Graduated from Tsinghua University Beijing in 1964. Chief Engineer of China Mechanical Industry Technology Company. Professor of Shanghai Science and Engineering University from 1994. Member of International Research Centre on Hydraulic Machinery (Beijing).

Chapter 1

Fundamentals of Hydroabrasive Erosion Theory

V. Ya. Karelin, A. I. Denisov and Y.L. Wu

1.1 Introduction

Hydraulic abrasion of the flow-passage components of hydraulic machines (hydro-turbines, pumps) should be interpreted as a process of gradual alteration in state and shape taking place on their surfaces. The process develops in response to the action of incoherent solid abrasive particles suspended in the water or in another working fluid and also under the influence of the fluid flow. Whilst the abrasive particles present in the flow act upon the circumvented surfaces mechanically, the effect of pure water on the surfaces is both mechanical and chemical (corrosive action). Therefore, Hydraulic abrasion can be considered as a compound mechanical-abrasive process.

Under the action of abrasive particles on the metal surface in contact with the fluid, wear in hydraulic machinery is primarily a result of particle erosion, the mechanisms of which typically fall into one of two main categories: impact and sliding abrasion.

Impact erosion is characterized by individual particles contacting the surface with a velocity (V) and angle of impact (α) as shown in Figure 1.1a. Removal of material over time occurs through small scale deformation, cutting, fatigue cracking or a combination of the above depending upon the properties of both the wear surface and the eroding particle.

Sliding abrasion is characterized by a bed of particles bearing against the wear surface with a bed load (s) and moving tangent to it at a velocity (Vs) as shown in Figure 1.1 b. The formation of the concentration gradients causing the bed and the resultant bed load are both due to the centrifugal forces acting on the flow with the curved surface. Removal of material over time occurs through small scale scratching similar to the free cutting mode of impact erosion [1.1, 1.13].

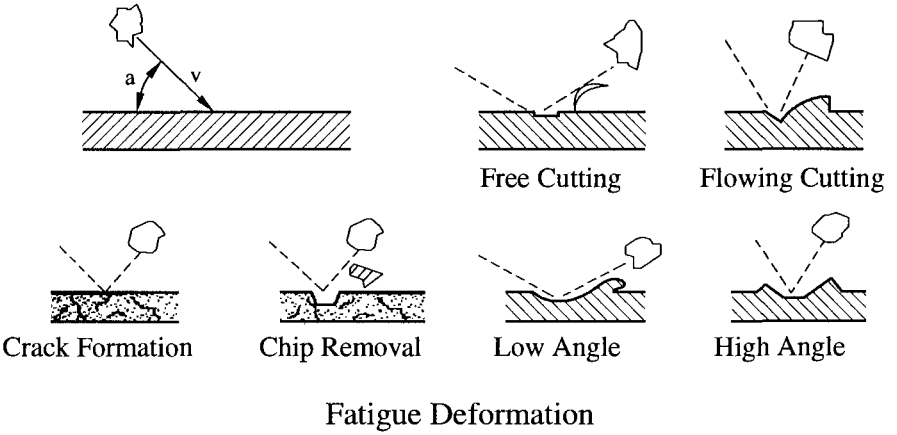

Figure 1.1 a Impact erosion

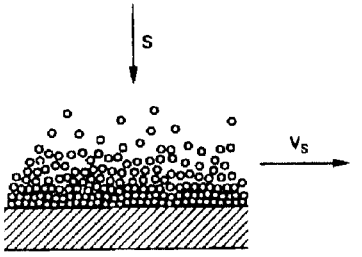

Figure 1.1 b Sliding abrasion

Mechanism of hydraulic abrasion of particles has been reviewed recently by Visintainer, et al. (1992) [1.1], Addie et al. (1996) [1.2] and J. Tuzson and H. McI. Clark [1.3]. A relatively recent studies of the status of two-phase, solid-liquid flow were presented by Pagalthivarthi et al. (1990) [1.4] and Wu Y.L. et al (1998) [1.5]. Most studies assume dilute suspensions or single particle, and do not take into account that the maximum packing density limits solid concentration. Virtually solid (closely packed) particle layers can accumulate in certain boundary regions as pointed out by Tuzson (1984) [1.6]. Ore beneficiation slurries are concentrated to 30 to 50% by volume, the maximum packing corresponding to about 75%. Particle impact dynamics have been studied in detail, (Brach, 1991) [1.7]. Energy loss and restitution theories are supported by tests with steel balls. The specific case of a two-dimensional cylinder in a uniform flow was analyzed by Wong and Clark (1995) [1.8] and was used to model conditions in a slurry pot erosion tester.

The study of Wong and Clark also includes comparisons with slurry erosion rate data from slurry pots and therefore addresses the material removal issue. Satisfactory correlation of an energy dissipation model with erosion rates was found especially for particles larger than 100 mm. Pagalthivarthi and Hemly (1992) [1.9] presented a general review of wear testing approaches applied to slurry pump service. They distinguished between impact erosion and sliding bed erosion. Tuzson (1999) investigated the specific case of sliding erosion using experimental results from the Corolis erosion-testing fixture, which produces pure sliding erosion [1.3]. These studies have been also supplemented (Clark et al, 1997) [1.10]. Knowledge of the relationship between the fluid and particle flow conditions near the wall and the material removal rate is essential for erosion estimates. It appears that the specific energy - the work expended in removing unit volume of material - provides a satisfactory first measure of the erosion resistance of the material. However, its general use must be qualified since values are known to vary with, for example, erodent particle size.

Abrasive erosion of hydraulic machinery has been reviewed extensively by Duan C.G. in 1983 [1.11] and in 1998 [1.12].

1.2 Mechanism of Hydraulic Abrasive Effect of Particles

1.2.1 Mechanism of Hydro-abrasion

According to the observation described in [1.12] and [1.13]. The surface failure under the action of water (exclusive of cavitation phenomena) may arise as a result of friction taking place between the continuous water stream and the surface of the immersed elements, as well as due to the impact effect exerted by the water flow acting on the surface.

The most predominant factor causing deterioration of the surface is the impact produced by abrasive particles suspended in the water, therefore this erosion process turns out to be purely mechanical.

The disruption is a result of the continuous collisions between the solid particles and the surface. At the moment of collision the kinetic energy of a moving particle is converted into the work done by deformation of the material of hydraulic machinery. During residual deformations, a certain volumetric part of the surface layer will be separated from the bulk mass of a component, leaving a trace which is characterized by significant roughness caused by action pattern, crystalline structure and heterogeneity of the metal. Countless collisions of these flow convey particles with the component surface, even if they give rise to elastic strains only, ultimately result in the surface failure due to emergence of fatigue processes. Formation of micro cuts on the metal surface can be regarded as a result of multiple recoils and encounters taking place between the abrasive particles and this surface. With the hydraulic abrasion mechanism presented, it is obviously that deterioration intensity of the material forming hydraulic machine elements will mainly depend on the kinetic energy of the particles conveyed by the flow, i.e. on their mass and velocity of travel, as related to the surface, and also on concentration value of abrasive particles contained in the flow.

In the analysis given below the mechanism of hydraulic abrasive action performed by particles is presented with due respect of their impact effect, illustrated as a predominant factor causing the surface erosion.

A number of factors influence the development of abrasion process of a hydraulic machine. These factors include: mean velocity of particles; mass of a particle; concentration of abrasive particles in a liquid flow, i.e. number of particles per unit of liquid volume; size distribution of the particles or their

average grain size; angle of attack at which the particles collide with the surface; duration of the effect produced by the particles (of given size and concentration) on the surface.

When considering a stationary plate as a unit of area, flown normally to its face surface by a uniform steady liquid stream, it becomes possible to derive the mathematical relationship representing the main laws of hydro-abrasive erosion.

Without regard to the deterioration pattern, the plate erosion developed under the action on its surface of a single solid particle I' is proportional to the kinetic energy possessed by this moving particle, i.e.

$$I' = \alpha \frac{mc^2}{2} \tag{1.1}$$

where m is mass of the particle, c is average particle velocity of translation, α is coefficient defined by the flow conditions, the material of the particle and the plate, as well as other factors.

The number N of abrasive particles contacting with the plate surface for time interval t can be defined by the expression

$$N = \beta \varepsilon v t \tag{1.2}$$

where β is coefficient dependent on the flow conditions around the plate and conveying capabilities of the flow, v is mean velocity of the flow, ε is the particle concentration.

The plate erosion for time interval t is as follows:

$$I = I'N = \alpha\beta \frac{m \cdot c^2 \varepsilon v t}{2} \tag{1.3}$$

It can be assumed that velocity c of the solid particles suspended in the flow is proportional to flow speed v, i.e.

$$c = \gamma v$$

therefore, equation (1.3) will be

$$I = \alpha\beta\gamma^2 \frac{m\varepsilon v^3 t}{2}$$

or

$$I = km\varepsilon v^3 t \tag{1.4}$$

Equation (1.4) shows that the abrasive erosion of a stationary component, by-passed by a liquid flow with solid particles suspended, varies in direct proportion to the mass of particles, their volumetric concentration, the 3rd power of the flow velocity and duration of the effect exerted by the flow.

Assuming that deterioration of a unit of mass caused by solid particles requires, some work to be done, it is possible to deduce, on the basis of energy theory laws, general equations governing abrasion taking place, for instance, at the front edge and surface of a blade used as a part of a pump impeller.

Based on that assumption that the flow pattern around this blade is similar to the flow around a cylinder (Figure 1.2 a), one can discover that the N number of particles crossing, for a unit of time, section 1 ~ 1' restricted by streams 1 ~ 2 and 1' ~ 2', is equal to

$$N = wS_e / q \tag{1.5}$$

where w is relative motion speed of the flow, s is effective cross-section area 1 ~ 1' and q is volume of a solid particle.

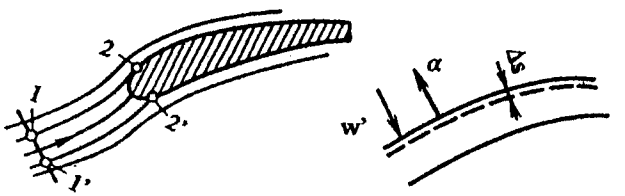

a. leading edge b. pressure face

Figure 1.2 Diagram of the blade components circumvented by a particle suspended flow

The kinetic energy of solid particles expended to deteriorate the blade surface 2 ~ 2' and based on equation (1.1) and (1.2) is equal to

$$\alpha\beta\gamma^2 \frac{mw^2}{2} N = \alpha\beta\gamma^2 \rho_T q \frac{wS_e}{q} \frac{w^2}{2} = \alpha\beta\gamma^2 \varepsilon\rho_T \frac{w^2}{2} S \qquad (1.6)$$

Let us assume that the volumetric erosion of the blade main lip, produced by a suspension-conveying flow for time t, amounts to $F\Delta S$, where F is midsection of the blade and ΔS is average thickness of the deteriorated material layer. Then the work consumed to perform this erosion is equivalent to $AF\Delta S\rho_m$, where ρ_m is density of the blade material. Therefore,

$$\alpha\beta\gamma^2 \varepsilon\rho_T \frac{w^3}{2} St = AF\Delta S\rho_m \qquad (1.7)$$

form whence the linear erosion effected on cylindrical surface by this suspension-conveying flow will by

$$\Delta S = \frac{\alpha\beta\gamma^2}{A} \frac{S}{F} \varepsilon \frac{\rho_T}{\rho_m} \frac{w^3}{2} t \qquad (1.8)$$

Presenting the flow effective area versus midsection of the body relationship as $\eta = S / F$, as done for the cases stated earlier, we shall obtain the final expression for linear erosion of the surface flown around by the suspension-conveying stream

$$\Delta S = k\eta \frac{\varepsilon}{A} \frac{\rho_T}{\rho_m} w^3 t \qquad (1.9)$$

When the working surface of a blade is flown around by the hydraulic mixture (Figure 1.2 b), the layer being formed nearby the surface has concentration amounted to N_0 particles in a unit of volume. The number of particles contacting a unit of surface area for a unit of time is equal to

$N_0 w' \omega \beta$, where w' is pulsation momentum developed closely to blade wall. The kinetic energy, expended at pulsation and in deterioration of the surface, is equal to

$$N_0 \omega' \beta \gamma^2 \frac{w^2}{2} \rho_T q$$

The material layer disrupted on the blade surface for time t equals ΔS. In this case the worn material volume per unit of blade surface is ΔS 1. The work to be done in order to disrupt the material mass corresponding to the indicated volume is A P_m ΔS. In the case under consideration the linear erosion will be

$$\Delta S = \frac{\alpha \beta \gamma^2}{2} \frac{N_0 w'}{A} \frac{\rho_T}{\rho_m} w^2 q t \tag{1.10}$$

The volume of particles $N_0 q$ contained in the hydraulic mixture layer adjacent to the blade surface is a function of volumetric concentration of solid particles ε, normal flow acceleration a nearby the surface, mean relative velocity in the inter-blade channel ω, characteristic channel linear dimension D and drag coefficient of a particle C:

$$N_0 q = f(\varepsilon, a, w, D, C) = \varepsilon' \tag{1.11}$$

It may be assumed with feasible approximation that the pulsation standard of the flow speed nearby the blade is proportional to the local relative flow velocity, w, i.e. $w' = \lambda w$, where λ is proportionality coefficient. Consequently, the linear erosion of the blade surface will become

$$\Delta S = \frac{\alpha \beta \gamma^2 \lambda}{2} \frac{\varepsilon'}{A} \frac{\rho_T}{\rho_m} w^3 t \tag{1.12}$$

or finally

$$\Delta S = K' \frac{\varepsilon'}{A} \frac{\rho_T}{\rho_m} w^3 t \qquad (1.13)$$

This is the theoretical evaluation of abrasion intensity. In practice, the erosion of hydraulic machines is complicated by a large number of additional factors. And there is no exact mathematical dependence, for the time being, to define them. Variable concentration and structural in homogeneity of suspected particles, continuous alteration and pulsation of both velocities and pressures during the motion of the flow, by-passing the elements of the machine, division of the flow into several individual streams, availability of sharp turns and non-uniformity in distribution of speed values within their cross-sectional areas, variance in operation and design features of hydraulic machinesall these factors complicate the actual pattern of the abrasion. Nevertheless, the results obtained by the comparison of equation (1.4), (1.9) and (1.13) with the experimental analysis data show that they reveal the basic mechanisms of hydraulic abrasion with fairly good accuracy.

Specifically, the experimental research analyses aimed at studying abrasion behavior, as applied to operation of impeller pumps, were carried out at the V.V. Kuibyshev Moscow Civil Engineering Institute (USSR). An experimental stand with closed-loop water circulation (Figure 1.3) was designed to include a regulation tank, a modified centrifugal pump and pipes. The components subjected to abrasion were special blades of an open-type impeller. The impeller outlet diameter under consideration was 125 mm with four cylindrical-type blades, and with the height of 21 mm at the output.

The inlet pipe diameter was 117 mm and that of the discharge branch was equal to 75 mm. The head in this pump was equal to 9.5 m with pump capacity being 13 l/s. The relative speed of the suspension-conveying flow reached in the impeller channels up to 16 m/s.

The erosion of the specimens tested was evaluated by using the expression $\Delta G/G \times 100\%$, where ΔG was loss in mass of a blade (g) after the installation had operated for t time interval (*hour*) and G was initial mass of this blade (g).

The erosion rate per hour was defined using the expression

$$I_h = \Delta G/G_t \times 100\% \qquad (1.14)$$

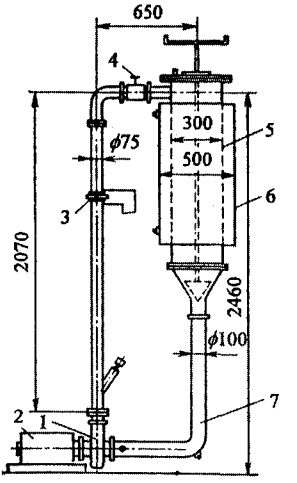

1-pump; 2-electric motor; 3-membrane; 4-latch;
5-tank; 6-cooling casing; 7-suction pipeline

Figure 1.3 Diagram of an experimental rig

The blades were made from two different materials (aluminum, steel CT3) and installed on the shroud of an impeller in pairs. The test was carried out utilizing of river sand containing 45% of minerals with Moh's scratch hardness number reaching 5. The experimental results obtained on erosion-to-concentration ratio, indicate that the erosion rate, within the concentration ranges studied, is directly proportional to the concentration level (Figure 1.4 a) and can be evaluated by equation (1.4), (1.9) and (1.13). The results of the experiments are in good agreement with the data on other similar studies. As an example, Figure 1.4 b shows test results obtained on a water-jet impact stand, which also confirmed that losses in specimen mass ΔG increase linearly with rise of the solid particle content in the flow.

At the same time these experiments demonstrated that the erosion intensity, at a fairly high content of abrasive matter, grows slower, as compared with a rapid growth of abrasive matter concentration. It is attributed to the fact that not all the particles, present in an effective hydro-mixture flow, come into contact with the surface to be worn. Some of them,

being repelled from the surface flown around by the stream, collide with the particles contained in the flow running over surface. According to the results obtained this effect starts to manifest itself appreciably at concentrations reaching $\varepsilon = 15 \div 20\%$, i.e. the level exceeding substantially the sediment matter content present in natural waterways.

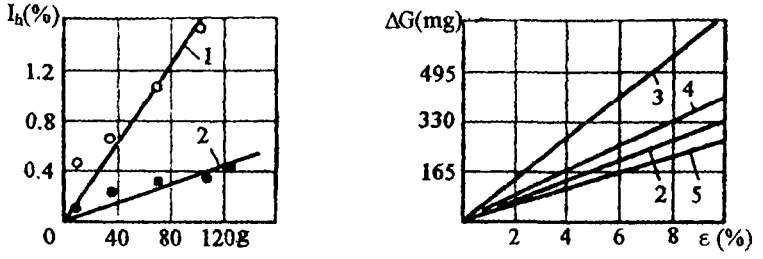

(a) (b)

1-aluminum; 2-steel CT3; 3-brass; 4-armco-iron; 5-steel 12X18H9T

(a) tests carried out on a stand designed at the V.V. Kuibyshev MIEI
(b) tests carried out on a water-jet impact rig

Figure 1.4 Dependence of erosion rate and loss in mass of the specimens on volumetric concentration of the hydro-abrasive mixture

The hardness of sediment matter conveyed by a flow is of great significance. In a number of papers, it is stated that, of all the solid matter suspended in the water, only those particles may be actually hazardous for the device which possess hardness higher than that of the material used for fabrication of the components to be accommodated in the flow-passage portion of hydraulic machines (i.e. particles with Moh's scratch hardness equaling 5 to 5.5 and higher). Taking into account the part played, in fatigue erosion of materials, by abrasive particles of lower hardness, one can agree with the opinion expressed in certain papers according to which the transition from one erosion pattern to another is defined by the following rule.

$$K = \frac{H_{vm}}{H_{va}} \tag{1.15}$$

where K is the ratio of hardness, H_{va} and H_{vm} are respectively hardness of abrasive particles and that of the material of the machine.

When $K_T < 0.6$, the disruption taking place is direct, while at $K_T \geq 0.6$ there is evident transition to multicyclic fatigue erosion.

Hence, in order to evaluate erosion intensity in hydraulic machines operating on a silt-laden river, it is quite obligatory to know the mineralogical composition of its sediment matter that is defined by the geological structure of the river-bed. Table 1.1 can be used for comparative evaluations of hydraulic abrasion intensities.

Table 1.1

Abra-sivity class	Rock's specification according to their abrasivity	Abra-sive measure (mg)	Typical rocks forming classes
1	Super-low abrasive	Below 5	Limestones, marbles, soft sulphides, apatite, halite, shales
2	Low abrasive	5 to 10	Sulphide and baryte-sulphide ores, argillites, soft slates
3	Below medium abrasive	10 to 18	Jaspilites, hornstones, magnetic thin lamella rocks, iron ores
4	Medium abrasive	18 to 30	Quartz and arkose fine grain sandstones, diabases, coarse grain pyrites, vein quartz, quartz limestones
5	Above-medium abrasive	30 to 45	Quartz and arkose middle grain and coarse grain sandstones, fine grain graintes, porphyrites, gabbro, gneisses
6	Higher-medium abrasive	45 to 65	Granites, diorites, porphyrites, nepheline syenites, pyroxenites, quartz slates
7	High abrasive	65 to 90	Porphyrites, diorites, granites
8	Most abrasive	above 90	corundum containing rocks

Let us consider, as an example, sediment conditions in the Vakhsh irrigating canal originating in the Vakhsh River (Tajik SSR, USSR). Table 1.2 illustrates the content percentage of minerals with different hardness values, as related to the total amount of sediment matter, as well as values in fractures taken separately; the results were estimated on the basis of the probes taken and analyzed.

Table 1.2

Minerals	Moh's scratch hardness	Content in general flow %	Content in fractures, % and fracture sizes, mm				
			0.01 ~ 0.05	0.05 ~ 0.10	0.10 ~ 0.25	0.25 ~ 0.50	>0.50
Quartz, zircon	≥ 7	37.7	51.4	49.4	70.0	71.5	71.5
Feldspars of ore type	7 ~ 5	6.0	8.7	9.1	10.6	10.5	10.7
Calcium, biotite	<5	16.4	39.9	41.5	19.4	18.0	17.8
Silty particles	-	39.9	-	-	-	-	-
Total		100.0	100.0	100.0	100.0	100.0	100.0
All the minerals with hardness number 5		43.7	60.1	58.5	80.6	82.0	82.2

Influence of factors, which determine the mass of a single particle, on the abrasive erosion intensity can be qualitatively evaluated. These factors include volume of a particle, q, and sediment density, ρ_T. With the water density ρ_0 equaling unity, the mass of a suspended solid particle will be

$$m = q(\rho_T - 1) = \frac{1}{6}\pi d_h^3(\rho_T - 1) \qquad (1.16)$$

where d_h is diameter of a particle in the sediment.

Substituting m value into equation (1.4) we shall have, after integration of the numerical multipliers,

$$I = k' d_h^3 (\rho_T - 1) \varepsilon v^3 t \qquad (1.17)$$

i.e with the specified sediment matter densities, and all other things being equal, the intensity of hydraulic abrasion is proportional to the 3rd power of the diameter of solid particles.

However, the dependence stated in equation (1.17) is in poor agreement with the data obtained in number of experiments. The erosion curve, for instance, plotted in relative values shows, according to, that with the particle grain size exceeding 0.2 mm, the sand grain dimensions have no effect on erosion rate (see Figure 1.5 a).

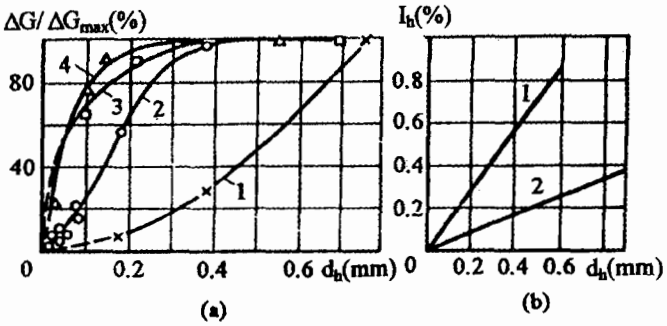

(a) alteration of relative erosion
(b) erosion rate alteration (1. aluminum; 2. steel CT3)

Figure 1.5 Influence of the particle grain size on the hydraulic abrasion

On the other hand, when making use of sharp-sided particles, we shall have different dependence (see Figure 1.5 a).

The experiment, carried out with utilization with utilization of sand having grain size values 0.15, 0.3, 0.6 and 1.2 mm, has indicated (Figure 1.5 b) that with sediment concentrations and suspension-conveying mixture velocities being permanent, the erosion rate is directly proportional to the grain size and can be expressed as

$$I_h = I_h' \times d_h \qquad (1.18)$$

where I'_h is erosion rate per hour, as related to the sand grain size $d_h = 1$ mm and depending on concentration and mineral composition of sediments.

These data fit well with the results obtained for specimens fabricated form different metals and tested in a rotary-type stand. The test results indicate that when these specimens are affected by abrasive particles with average diameters varying 0.1 to 0.5 mm, while they move with a constant speed in a hydro-mixture having unchangeable concentration, the erosion increases in direct proportion.

Such significant quantitative and qualitative differences in experimental data and their discrepancy from the theoretical estimation can be explained by decrease in actual motion velocity of solid particles c (see equation 1.1) at rise in their size, in addition to the divergence in the methods used for carrying out the experiments and difficulties encountered in defining of said divergences.

Assuming that the square of a particle velocity, as related to the liquid, is proportional to the particle mass and also evaluating the deteriorating capability of such a particle by its kinetic energy affecting the surface to be disrupted, it is possible to fine that this energy will be utmost at $c = 0.5\ v$, i.e. as the particle mass increases, its energy rises at the beginning and then it starts to decline.

In the actual motion conditions, existing in the inter-blade channels of pump impellers and created by a suspension-conveying flow, such factors as separation of solid particles and divergence between their paths and the flow direction line are of great significance as well.

Within the limits of concentration change and that of grain sizes of solid matter present and typical of natural waterways, see, for instance, the granulometric composition described for the Vakhsh irrigation canal:

♦ Sediment particle sizes (mm) :	< 0.01	0.01~0.05	0.05~0.1	0.1~0.25	0.25~0.5	>0.5
♦ Fracture contents (%) :	39.6	27.6	14.1	18.4	0.2	0.1

The relationship between the abrasion intensity, taking place in the components of general application pumps, and grain size of sediment matter particles should be assumed as linear [1.14].

With reference to the density of solid particles it should be emphasized that the experience, gained in the operation of these pumps, confirms the

validity of equation (1.17). Therefore, with the heavier particles contained in the water, it is assumed that the expected erosion should increase.

In addition to mass, governed by such parameters as size and density, and hardness, another factor of great significance is the shape of moving abrasive particles. It is known that solid particles with sharp sides are especially hazardous in the sense of their ability to deteriorate the surface circumvented by the flow. But to evaluate this factor quantitatively, with respect to its effect on erosion intensity, is extremely difficult, since the particle shapes. As a rule, vary continuously as a result of mutual collisions and their friction against the surfaces restraining the flow.

As seen from equation (1.4), (1.9) and (1.13) the main factor governing hydraulic abrasion intensity, at the given parameters of hydroabrasive mixture, is the local velocity. However, the views, which many researchers have on the velocity index of power n, are inconsistent with each other. Although the theoretical analysis suggests that it is equal to the 3rd power, the results obtained on experimental rotary-type stands correspond to $n = 2.5 \sim 3.0$, those obtained on disk stands measure $n = 1.8 \sim 2.7$, and those obtained in jet-water impact stands are equals to $n = 2.0 \sim 2.2$.

All the stands of the indicated types are unfit, in our view, for experiments to be carried out with the aim of defining the effect of a hydro-mixture velocity on the erosion of pumps, since to determine this velocity actual value is an extremely difficult task. Besides, the influence pattern itself, evolved in the effect performed by hydro-mixture on the surface to be worn, predetermines emergence of vortexes and various secondary streams, which distort the whole pattern of interaction taking place between the flow and the surface. Therefore, in the experiments carried out in the V.V. Kuibyshev Moscow Civil Engineering Institute (MIEI) we used a Venturi nozzle with divergence angle $\theta = 5°$, Figure 1.6 illustrates loss in mass of aluminum specimens at different velocities of a suspension-conveying flow containing solid fracture $\rho = 5$ g/l at $d_h = 0.1 \sim 0.25$ mm. It is found that the index of the power n is not constant but varies from 2.5 to 3.0 with increase of flow rate absolute values. It should be noted that in carrying out the quantitative evaluation of index n the results of our study are in good agreement with experimental data obtained on hydraulic abrasion of cylindrical specimens placed in straight pipelines.

Discrepancy of the results obtained can be explained by complexity in determining the actual flow velocity nearby the surface being disrupted and

the velocity of the solid particles contained in the flow, as well as due to the presence of turbulence and boundary layer of variable thickness. The flow velocity alteration affects the particle concentration nearby the surface (see equation 1.11), and the velocity rise, in this case, results in decrease of this concentration and vice versa.

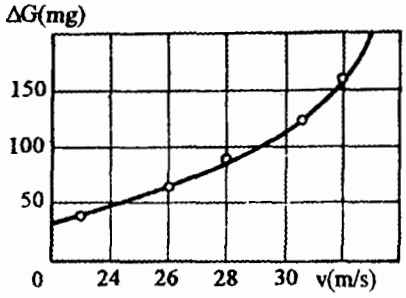

Figure 1.6 Dependence of the hydraulic abrasion on the flow rate

During the erosion of planar surfaces by a suspension-conveying flow with small content of solid particles the erosion intensity, in our view, is proportional to flow velocity v in power n, where $3 > n > 2$.

The derivation of equation (1.4) is based on the assumption that an abrasive particle collides with the surface of a streamlined component with a normal impact. Alteration in angle corresponding to inclination of the velocity vector with respect to the component surface, which is often named as an angle of attack, is accompanied by respective alteration of the external effect pattern produced and acting on the surface layer and by corresponding quantitative and qualitative alterations in the surface deterioration process.

At the angle of incidence $\alpha = 90°$ the particles exert normal impacts against the component surface. Due to differences existing in velocity, form, mass and mechanical properties of particles, there appear, at the moment of an impact, stresses of different orders in the surface layer of the material. As this takes place, a certain part of the kinetic energy possessed by a solid particle is consumed to produce elastic strain of the material, and the remaining energy portion is expended for plastic deformation and material deterioration, as well as for crushing of the solid particle under review.

Normal impacts of abrasive particles are capable of producing brittle and endurance failures material micro-volumes in the surface layer; failure of soft materials can also take place and produced by shearing.

As the angle of attack reduces, the strength of particle impact decreases as well, and its normal component becomes proportional to $sin\alpha$. A number of authors assume that the tangential component in the impact impulse causes the material failure only at those values of $ctg\alpha$, which exceed the coefficient of friction produced by a particle against the surface of a specimen being worn.

When these angles of incidence are small, the material failure is effected in such cases by shearing or peeling.

As an example demonstration the process alteration, taking place during deterioration of the surface layer material caused by alteration in the direction of a stream flowing around a component. Figure 1.7 illustrates gas abrasive erosion intensity versus angle of incidence relationship, where the specimens tested were fabricated from hardened and non-hardened steel and from rubber. These materials were tested on a laboratory stand. The airflow velocity was set at 100 m/s and the quartz sand particles used had sizes 0.2 to 1.5 mm. It should be noted here that the material erosion intensity dependence of the angle of attack are qualitatively similar both in hydro-abrasive and gas-abrasive processes.

At the incidence angles approaching normal ones, the hardened steel (curve 1, Figure 1.7) erosions faster than it does at smaller angle, and with a greater rate than the non-hardened steel and rubber do. This result from brittleness of hardened steel; the surface layer in such steel cannot at certain areas withstand, at set conditions of external influence pattern, the impacts produced by a certain number of abrasive particles.

The soft steel specimens (curve 2) are likely to undergo, at the prescribed conditions, a sort of poly-deformation failure process. The surface layer in rubber specimens (curve 3) absorbs, at the present flow velocity of particles moving with $\alpha = 90°$, the greater part of the kinetic energy possessed by abrasive particles, and the rubber in this case erosions out slower, as compared with the other material,

While the erosion rate in hardened steel specimens reduces with decrease of the attack angles, which is caused by gradual reduction of the normal impact strength component, the deterioration process, which develops with

reference to the steel and rubber, is accompanied at certain values of an angle of incidence, with qualitative changes.

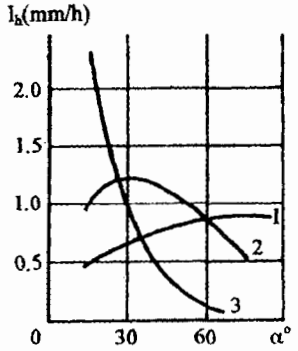

1. hardened steel, with hardness 840 kgf/mm^2
2. non-hardened steel, with hardness 128 kgf/mm^2
3. rubber, with Shore hardness 70 ~ 74

Figure 1.7 Dependence of the erosion rate in specimens of steel and rubber on the solid particle angles of incidence

At $\alpha < 73°$ the erosion rate of soft steel rises due to increase of the tangential component in the impact impulse, which results in the material failure effected by shearing. At $\alpha < 30°$ the soft steel erosion rate falls down again, which results from a continuous decrease, taking place in the normal component of the impact strength. The rubber erosion rate rises drastically at $\alpha < 64°$, and at $\alpha = 28°$, it already exceeds the erosion rate in the other materials tested (curve 3 is placed above curves 1 and 2). At small angles of incidence the rubber ability to absorb kinetic energy of solid particles reduces, which results in the material failure.

The experimental results obtained have illustrated that during alterations of incidence angles in the range 15° to 90°, the phenomena observed may allegedly be classified as an inversion of erosion resistance resulted from alterations in the external influence pattern affecting the surface layer. It can be assumed that such erosion resistance inversion will also occur during alterations in the abrasive action activity (specifically, at the appropriate

alterations in mass, particle shapes and velocity of their motion). At a normal impact, for instance, a certain combination of particle motion speed and particle mass may arise, at which the rubber will practically remain unworn, since the whole particle kinetic energy will be balanced with the elastic strain of the rubber.

With reference to the effect on the erosion rate caused by duration of the influence exerted by the hydro-abrasive mixture, there is linear dependence between the deterioration volume and influence time observed practically in all the experimental studies. The experiments carried out at the V.V. Kuibyshev MIEI have proved that the linear nature of function $I = f(t)$ is preserved with various mixture concentrations (Figure 1.8 a) and solid particle sizes (Figure 1.8 a) and solid particle sizes (Figure 1.8 b).

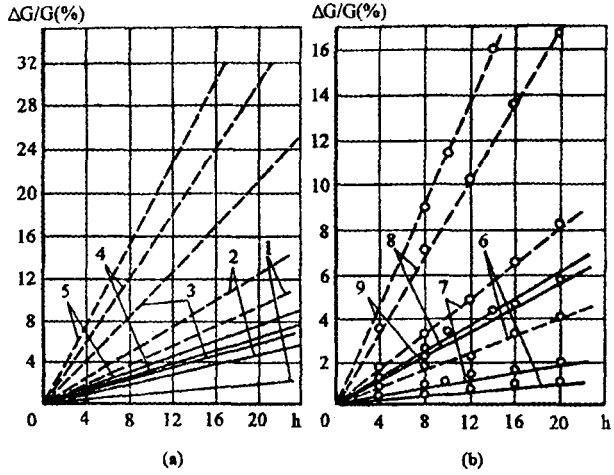

1.$\rho = 9$ g/l; **2**.$\rho = 36$ g/l; **3**.$\rho = 72$ g/l; **4**.$\rho = 108$ g/l; **5**.$\rho = 126$ g/l; **6**.$d_h = 0.15$~0.3 mm; **7**.$d_h = 0.3$~0.6 mm; **8**.$d_h = 0.6$~1.2 mm; **9**.$d_h = 1.2$ mm; (dash lines-aluminum, solid lines-steel)

Figure 1.8 Relative erosion versus hydro-abrasive mixture action duration relationship at different concentration contents (a) and particle grain sizes (b)

It should be noticed in conclusion that hydraulic abrasion intensity also depends, undoubtedly, on the material type used to fabricate components being worn out by a suspended matter conveying flow.

1.3 Abrasive Erosion of Hydraulic Turbine

1.3.1 Illustrative Examples of Hydraulic Abrasion in Hydraulic Turbines

Let us consider, as examples typifying the hydraulic abrasion occurring in flow passages of hydro-turbines, the results of regular full-scale study carried out on hydroelectric units used in derivation water-power station No.1 and No.2 situated on one of the waterways in the Uzbek SSR (Central Asian region of the USSR).

The following classification was used to evaluate the hydraulic abrasion patterns:

1. Metallic luster - A shining surface with no traces of paint, scale or rust
2. Fine-scaly erosion - A surface with rare, separately located and skin-deep minute scales
3. Scaly erosion - A surface entirely covered with skin-deep fine scales
4. Large-sized scaly erosion - A surface entirely covered with deep and enlarged scales
5. In-depth erosion - A surface covered with deep and long channels
6. Through holes or entire erosion-out of the metal.

An average annual sediment concentration for No.1 and No.2 accounts for 1.27 kg/m^3 and this parameter range varies from 0.23 kg/m^3 (in December) to 3.69 kg/m^3 (in June). The mineralogical composition analyses have shown that exceeding 5, in accordance with Moh's scratch hardness number scale, amounts to 41% of the average annual hard matter content.

The hydroelectric station No.1 includes two sets accommodated with radial-axial turbines having 1.8-m diameter, with the rated head being 34 to 37 m and maximum capacity of 22 kg/m^3. The specified power values of these two units are 6.5 and 5 MW, respectively. The hydro-turbine runners are fabricated from stainless steel, the other elements in the flow-passage portion of the device are made of carbon steel. The hydroelectric station No.2 has two similar units accommodated with radial-axial turbines with 2-m diameter, the rated head being 21.5 m and maximum capacity equaling 23 kg/m^3; the set power in there units is equivalent to 4.2 MW each. The runner and other elements of the turbine are made of cast carbon steel.

The periodic full-scale surveys carried out during the scheduled maintenance overhauls of the components of the hydraulic sets have revealed that these elements have acquired, in the course of about 10 months of operation, abrasion of the kind described below.

The spiral case in one of the hydroelectric units, made by welding from sheet steel, has fine-scaly erosion throughout the entire surface, which is increased at the approach to the turbine stator. It was found that this fine-scaly erosion tends to increase over the entire surface in the spiral case. At the joints of the spiral members, i.e on the weld seams (closer to the stator) large-sized scaly erosion was revealed. Maximum sizes of scales reached up to150 $\times$ 15 mm with 10 mm in depth.

The guide case is designed to include 20 case steel blades having 560 mm in height. The blades had the greatest erosion on pressure sides neat the leading edge. Arc-weld building restored the most damaged places. On the blades of the runner 4 holes were found in the lower parts of the leading edges, the largest of which was up to 300$\times$70 mm. On the inner surface of the impeller the erosion revealed was not so large and was located on its lower by-pass. During the survey carried out 3 months later it was found that eleven blades out of thirteen had through holes nearby the lower rim, the largest being up to 290$\times$90 mm.

The upper parts in the blades were covered on both sides with metallic luster, in the middle parts the erosion was scaly and in the lower areas there were all signs of deep erosion.

The inner face in the runner lower rim was worn out extensively as well. In the lower portion of the runner upper rim surface, being by-passed by the flow, there took place large-sized scaly erosion occurred. During the further visual inspection of a new runner, which had operated in the turbine for about

12 months, it was discovered that on three blades out of thirteen, through holes which were placed nearly the runner lower rim; the largest hole was up to 100 × 70 mm.

The upper portions in these blades had metallic luster, whereas the face sides in lower parts of all the blades had scaly erosion, which was located closer to the rim.

A pronounced erosion-out was noticed as well on the inner surface of the runner lower rim which had scaly erosion turning, in some places, into a deep one.

In the time interval between two overhauls the upper and lower seal rings in the runner were subjected to the greatest erosion-out.

The inner surface in the spiral case of the other hydroelectric unit had fine scaly erosion. The stator columns in their upper and lower parts had worn-out journals, whereas the middle portions in these columns were smooth and shiny. Ring-shaped erosion grooves of different depths were revealed at the points where the column border on the bosses accommodated in the spiral case.

The erosion pattern in the blades of the guide case was scaly and characterized by different intensity levels. The palaces nearby trailing edges of blades, ad well as those located at the journal parts of lower necks, had the greatest erosion.

The inner face in the lower rim of the turbine impeller was subjected to an enormously pronounced erosion-out. In the external surface of the lower rim, in addition to the mechanical erosion traces, there were remarkable signs of cavitational erosion.

The streamlined surface in the runner upper rim has fine-scaly erosion in its top potion and large-sized scaly erosion in the lower part of the rim. All the blades in the runner and the inner face in the lower rim have in-depth erosion. The trailing edges in the blades have been worn out to take a sharpened "knife"- like shape incorporation jags.

The results obtained on the erosion of other units in the above-mentioned water-power stations are of the same nature.

Another example deals with description of the erosion taking place in turbines installed in one of the hydroelectric stations in the Tadjik SSR (USSR), which was based on the results of surveys carried out during the full-scale tests in the first stage (the spiral case, the guide case) and in the second stage (the turbine runner). The average annual sediment matter

concentration here amounts to 3.2 kg/m^3. The runner diameter in the radial axial turbine is 2.2 m. The rated head is 38.5 m, maximum capacity is equal to 25 m^3/s and the specified power of the unit is for 8.3 MW.

The spiral case of circular shape in its cross section is fabricated from cast iron and designed to include bosses for the accommodation of the stator columns. The inner surface in the spiral case is covered with insignificant fine-scaly erosion, with the exception of the spiral lower area at the approach to the stator columns, where this erosion turns to become large-sized scaly and deepened. The bosses fabricated in the spiral for accommodation of the stator columns are subjected to significant erosion.

The guide case is designed to include 24 case metal blades each 450-mm height. The water flow rate reaches 18 m/s at the rated power level. The blades are subjected to scaly erosion of various intensity levels. The lower parts of the face surface in the blades, near the trailing edges and journal portions of the lower necks, are the areas which are most subjected to erosion.

The turbine runner fabricated from conventional carbon steel (CT3) acquired significant erosion even after 1710 hours of operation and at the end of approximately two years of operation its erosion-out was so great that the runner in question turned out to become unfit for renewal.

The runner blades turned out to be the most greatly worn-out components. 12 blades out of 14 had approximately the same erosion level. Four regions can be degree on the face sides of the blades differing from each other by degree and nature of the erosion:

1) The vertical portion immediately adjacent to the leading edgeit has medium- and large-sized scaly erosion;
2) The horizontal area in the leading edgeit has deep comb-shaped erosion with grooves of approximately 20 to 25 mm in depth;
3) The strip-shaped area adjacent to regions 1 and 2, which has groove-like erosion and width of nearly 200 to 250 mm, with indicated grooves being inclined, at a certain angle with respect to the blade vertical part, and dispersed in a fan-shaped manner in its lower portion;
4) The trailing edges become notched and worn out in a "knife"shape manner, being drastically damaged at their curved portions. The deep "pull-ups" of metal reach to the depth 160 to 200 mm within the blade width; the area of these pull-ups reaches 300 cm^2 and more.

Two blades had erosion pattern that differed in some way from the erosion described earlier and being typical of the greater number of runners. The main difference resides in the fact that the mentioned deep "pull-ups" of metal, located at the trailing edge, are revealed in these blades in the vertical area, i.e. not in the region adjacent to the lower rim. This deference, may be basically attributed to inhomogeneity of the material used for fabrication of runners and brought about during the case.

Relatively insignificant erosion was found on the upper rim surface washed by the flow. The whole surface may be divided, in accordance with the erosion level, into three concentric regions:

1) The upper portion (up to the leading edges in the blades) is covered with large-sized and medium-sized scaly erosion;
2) The medium portion (from the leading edges to the middle part of the blades) is covered with medium-sized and fine-scaly erosion.
3) The remaining portion (the central part) is subjected to deep scaly erosion.

The lower rim of the runner has erosion of different nature; the inner part of the rim is subjected to the greatest erosion, especially in the regions adjacent to the blades. On the inner surface of the lower rim, near the leading edges, cavities which measure 50 × 20 mm and are 10 to 15 mm deep are found. The outer surface in the lower rim is practically intact.

1.3.2 Silt Erosion of Hydro-turbines

The section deals with some special features in the erosion of certain components comprising the flow-passage portion in hydro-turbines that define the energy quality of these turbines. Specific factors will be considered determining the behavior of the abrasive erosion process in hydro-turbines.

In a number of hydroelectric stations operating with water which contains a great amount of sediment matter (for instance, in such regions of the Soviet Union as Trans-Caucasus and Middle Asia) the components associated with the flow-passage portions in these hydro-turbines were affected with a considerable erosion. This results, first, in a decline of the efficiency in these units and, secondly, reduces the inter-repair time operation, i.e. the operation interruptions, needed to provide maintenance service, become more frequent. Finally, the amount of a rebuilding overhaul is greatly increased.

The erosion intensity can be characterized by an efficiency fall in turbines, which, for example, amounted to nearly 10% in the course of one year operation, at one of the water-power stations in Trans-Caucasus. Such a significant drop in the efficiency can be mainly accounted for a failure in the runner and labyrinth packing of the device. Let us consider the case in a more detailed way.

The attrition of a runner, effected by sediment matter, develops within its entire surface flown around by the stream, yet the area being most damaged is distributed at the trailing edges of the blades. The erosion action produced by the sediment matter is amplified by cavitation erosion; while the working surfaces in the blades are subjected to the erosion produced by sediment matter, their rear sides are mainly influenced by cavitation attack.

The combined effect produced by sediment matter and cavitation results in disappearance of entire trailing edge of the blade. The fast deterioration of the blade trailing edge is additionally results from their small thickness that is about 2 mm. After a year of operation a turbine with the runner diameter D_1 = 1200 mm had the blade edges entirely failed with a region measuring 80 x 200 mm. Blades and lower rim are the places where the damage occurs most seriously. The face (concave) side of a blade is subjected to abrasive erosion increasing in the direction of the trailing edge. The rear side is affected by cavitation action with the maximum distracted zone being located in the regions of the trailing edge and the lower rim.

The combined action of the abrasive erosion and cavitation results in failure (disappearance) of entire areas amounting to 50 mm presently, with the build-up provided at the sides of runners fabricated from a cavitational-resistant alloy and the thickness of trailing edges reaching 2 to 8 mm, the entire disappearance of certain blade area does not arise, yet the thickness of trailing edges diminishes up 2 ~ 3 mm.

The erosion in the lower rim of a runner starts to develop from the inner side, with an acute rise towards the lower part of the rim up to the depth of 10 mm, which equals approximately 1/3 of the rim thickness.

The attrition of trailing edge decreases the turbine efficiency without any reduction of the device capacity (the latter can even grow at the cost of an increase in clear gap size between the blades), since the flow leaves the blades in a shape which can be named as not entirely uncoiled. Taking this into account, it was offered to thicken the trailing edges in the runner blades driven by the water containing sediment matter. In order to validate the suggested

thickness to be used for such blades, the laboratory tests were carried out on a small low pressure jig having a 250-mm diameter; the model PO82 runner tested had 1.8 ~ 1.9 mm thick trailing edges, instead of the conventional thickness of 0.3 mm. These tests have shown that a six-fold increase of the blade edge thickness reduces the efficiency by 0.5% at $n_1' = 65$ rev/min. Then the turbine runner blade edge was thickened up to 6 ~ 8 mm, i.e. four times, which resulted, at the beginning, in reduction of the efficiency, this time by no more 0.3%. However, this decline is temporary, since in the course of the erosion development the mentioned edge becomes thickener, and the device efficiency is recovered.

The destruction of the blade area within trailing edges can be regarded as their undercutting, and its effect was studies in detail with the use of the aforementioned jig with 250-mm diameter. According to the data presented in Figure 1.9, it follows that this undercutting, while increasing the carrying capacity of the turbine, affects its efficiency insignificantly, in the sense of decreasing it. When such undercut facing is, for instance, within 0 ~ 11 mm, the efficiency of the 250 mm diameter runner is lowered by 0.5%, whereas its capacity is increased by 8%.

In operational conditions a pure radial undercutting does not occur; the trailing edges rather become distortedly curved due to an increased erosion taking place within the lower rims of the blades.

With reference to the thickened trailing edges, it is observed that their configuration is preserved yet their thickened reduces 3 to 4 times due to the abrasive erosion action.

The results obtained in the testing of the PO82 runner, with 250-mm diameter (Figure 1.9 b), performed with different trailing edge thicknesses, show the relationship between the thickness reduction of trailing edges and the device efficiency. The thickness reduction in these edges, within the 1.6 to 0.3-mm range, favours a rise in turbine efficiency by 1%. Therefore, when the trailing edges in a turbine runner reduce from 8 to 2 mm, the turbine efficiency should presumably increase by 0.75%.

The lower rim erosion versus the efficiency results are presented by the data obtained during laboratory tests of the PO82 runner carried out with different angles of taper (Figure 1.9 c).

The erosion value in the runner lower rim (being 10 mm near its lower periphery) will correspond to the alteration in the rim angle of taper by 2°22', which should not affect the turbine efficiency (Figure 1.9 c).

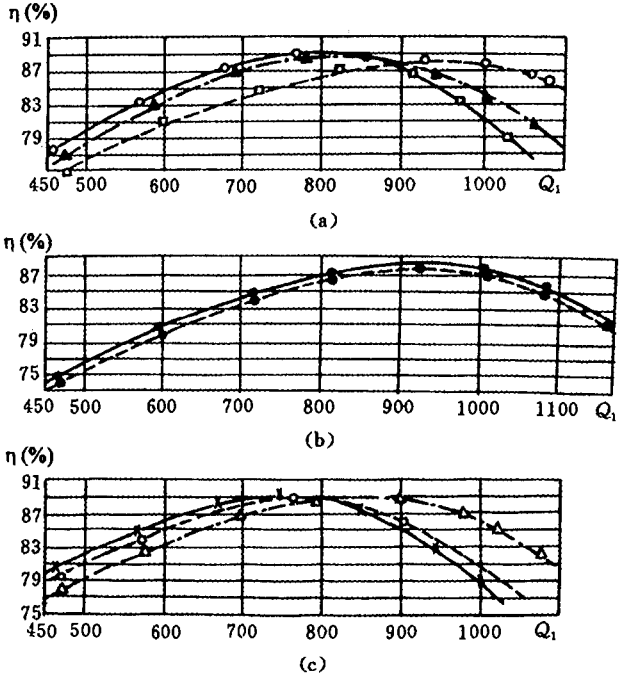

o-without facing; ▲-with the facing of 0 ~ 11 mm;
□-the same with 0 ~ 16 mm; ●-thickness of trailing edges, 0.3 mm;
o-the same with 1.6 mm; x-2°54'; d-5°48'; Δ-13°.

(a) different thickness
(b) of the blade trailing edges and different angles of taper in the lower rim
(c) with $n_1' = 65$ rev/min

Figure 1.9 Testing of the PO 82 runner used with different facings

The illustrated analysis, of how the runner geometry is changed due to the erosion process, shows that any substantial decline in the turbine efficiency is hardly probable.

It remains unclear how the erosion of the runner surface, being washed by the water flow, affects the turbine efficiency. Under the influence of this

erosion the runner surface acquires a scaly appearance and, as the erosion deepens, this surface resembles a furrow-eroded view.

Owing to the fact that the direction of these furrows coincides with that of the water flow, it should be assumed that the surface erosion, under the operational conditions involved, cannot affect substantially the turbine efficiency value.

According to the measurements performed, this efficiency level is somewhat increased at the initial stage of the turbine operation, observed soon after its repair service. As the operation mode alters, due to non-coincidence between the direction of the furrows and that of the water flow, the turbine efficiency may slightly drop, being affected by the surface roughness.

This fall of the efficiency, however, will be insignificant, since the depth of the surface scales is not yet great (up to 0.2 ~ 0.3 mm), and the mentioned furrows appear only within the trailing edge of a blade.

The thickening of the blade edges mentioned here was also carried out on runners of some other hydroelectric stations, also operating in the conditions of intensive erosion produced by sediment matter.

The operation of an runner, with thickened edges and cavitational-resistant build-up applied at the rear sides of blades, have shown that after a year of operation the trailing edges are practically preserved, but become thinner (as related to the device efficiency, its fall was about 4%).

The second factor causing a decline in the turbine efficiency is the erosion of labyrinth seals, and in this respect, the lower labyrinth packing is the component being worn out most greatly. This accounts, most probably, for the fact that the lower part of the flow conveys the greatest amount of the sediment matter, with the particle sizes being the largest.

The erosion of labyrinths brings about a sharp rise in the volumetric loss. The estimates carried out have shown that the efficiency reduction, in a turbine of a power station, arising due to this cause may be as high as 5%, i.e. a half of the greatest efficiency fall.

The capacity losses through seals include the volumetric loss and the loss by the friction of the turbine components against the water (Figure 1.10). The friction losses resulted from the erosion of the labyrinth maintain their meaning, of course, with a small deviation of the friction coefficient C_f from the number R_e being neglected. Hence, the turbine efficiency fall will be mainly affected by the volumetric loss, which increases as the erosion of the labyrinths develops.

The leakage through unworn labyrinth seals (Figure 1.10 a and c) are defined on the basis of the friction losses in the passage gap and those arising to overcome the resistance at the inflow and outflow of the water stream. The calculated value of the volumetric loss, arising while the flow passes through the upper and lower labyrinths, is equal to 0.087 m^3/s. Consequently, the volumetric efficiency of the turbine is about 99.13%, whereas the capacity loss in it due to leakage in seals, is 0.87%.

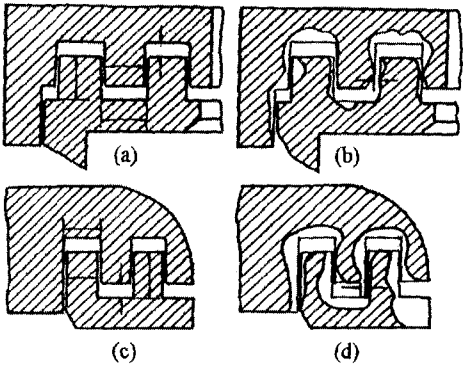

a, c - at the start of operation; b, d - after one year of operation

Figure 1.10 Erosion of the turbine upper (a, b) and lower (c, d) labyrinth seals

When the labyrinth packing become worn (Figure 1.10 b and d), the gaps in the labyrinths grow to reach 3 ~ 6 mm, the edges in these slot gaps get rounded and the resistance coefficient value, at a sudden constriction or widening, becomes close to zero. In this case the resistance in a labyrinth is formed by the friction resistance arising along the labyrinth length and by the resistance to overcome the flow turns. Using the friction coefficients available, one can calculate the leakage through the worn labyrinths, which will be equal to 0.674 m^3/s. The turbine volumetric efficiency in this case is 93.26% and the capacity loss is 6.74%. When comparing leakage values obtained with the worn and unworn labyrinth seals, it becomes evident that due to the erosion of these labyrinths the turbine volumetric efficiency decreases by 5.87%. The increased leakage value brings about a decline in

both the volumetric and hydraulic efficiencies of a turbine. Besides, such leakage causes the reduction of the turbine head and creates fluctuations in its operation. Consequently, the total efficiency falls in the turbine become higher. The effect caused by the erosion of the guide device components as applied to the turbine efficiency, should be considered as most insignificant. As the guide device is being worn, the tailpieces in the blades become thinner and furrows appear on the working faces of the blades in the direction of the water flow line. This erosion pattern does not influence the formation of the flow in the front of a runner and will only contribute to an increase of leakage when the guide device is closed. Thus, the analysis of the erosion taking place in the individual components and assemblies, such as an runner, a guide device, in respect of this erosion influence on the efficiency of the device, have shown that a decline in the device efficiency is determined mainly by the erosion of the labyrinths, which should be of increased strength. The erosion resistance of these labyrinth can be increased by either fabricating them from a material harder than a conventional carbon steel or by constructing the labyrinths with a more sophisticated configuration that can ensure lower leakage. Labyrinths rings made of austenitic-ferrite steels may prove to possess a sufficient level of erosion resistance.

As stated earlier (see Chapter 1.2), the erosion resistance of components in hydraulic machines and, specifically, in hydro-turbines, to the abrasive effect exerted by sediment matter, i.e the capability of these components to withstand, for a sufficient time period, the action of a flow containing the sediment particles suspended therein, depends on a number of factors. These factors can be divided into two groups. The first group is distinguished by the external forces acting on a component. It includes:

1) mineralogical and granulametric composition of the sediment matter;
2) traveling velocity of the suspended particles;
3) shape of particles;
4) concentration of the particles;
5) duration of the effect produced by the particles.

all these factors define the abrasive quality of the water flow.

The second group unites the abrasive quality features of the material used to fabricate the components of a hydro-turbine.

In accordance with their mineralogical composition the sediment matter ingredients passing the turbines of water-power stations can be divided into hard fraction (quarts, tourmaline, feldspar etc.), with Moh's hardness number

exceeding or equaling 4, as well limaceous particles with the hardness being less than 4.

The content of solid minerals, in accordance with the results obtained in a research study performed on a number of hydroelectric stations, amounts to 20 ~ 50% of the total sediment matter content. The granulametric composition or grain size structure is of great importance as well.

Assuming that the particles traveling through hydro-turbines have the size not exceeding 0.2 mm in diameter, it is believed that there is a direct proportional relationship between the erosion rate and the particle grain size. In the course of comparison made between the granulometric composition of the sediment matter traveling through one station and the composition of the same for another station, the indicated relationship allows to adjust their granularity to the same level.

In evaluation of the effect produced by the velocity of suspended sediment particles on the abrasive erosion, it should be noted that this factor is the decisive in determining the erosion degree. As it was mentioned earlier, the erosion of any component in the flow-passage portion of a hydro-turbine is proportional to the flow velocity raised to 3rd power, which was confirmed by the laboratory tests carried out on an abrasive erosion stand including an experimental runner. The erosion-velocity relationship was defined for velocities in the range of 10 to 20 m/s. The flow rate alterations were established by changes in the amount of revolutions performed by the runner. The sand used for these tests included grain sizes of 0.1 ~ 0.25 mm in diameter. The results illustrating the dependence of the erosion rate in the specimens on the flow velocity are obtained. The chart presents a theoretical curve stating the cubed relationship between the erosion and velocity (for steel IXI8H9T). According to the graph, when the velocity increase, the actual curve proceeds somewhat higher, i.e. the erosion is proportional to the velocity, which is powered higher than the 3rd power. Therefore, with an increase of the velocity the exponent of the power slightly rises. This accounts, probable, for the fact that the length of a particle free travel become shorter, and a particle collides with the specimens more frequently.

The effect of the grain shape on the abrasive erosion, by way of illustration shown with use of sand particles, was considered earlier, in Section 1.2.

Let us now consider briefly the second group of factors, which are defined by properties of a material used to fabricate components.

During the abrasive erosion, individual sand particles, when producing impacts with their sharp sides upon a component surface, chip-off minute metal particle from this surface. The sand grains will leave scratch marks on the metal surface in case the hardness of the latter is lower than that of the sand grains. Consequently, the first factor affecting the abrasive erosion of a component is considered to be its surface hardness. The analyses performed have conformed that the erosion rate for pure metals is directly proportional to their hardness. The corrosive resistance of a materiel does not play a significant part during the abrasive erosion process.

The effect of the microstructure on the erosion resistance of materials during the abrasive erosion process can be illustrated on some non-ferrous metal alloys. It was noticed that the cast and plasticized copper alloys examined in the course of a study (copper, tin bronze, alloy brass, aluminum bronze) turned out to be less resistant than a conventional carbon steel, and their resistance to attrition, in this respect, does not depend on their hardness. The pure copper, for instance, is equal, in terms of erosion resistance, to the most hard aluminum bronze.

The intensive erosion of conventional gray cast iron also can be taken as an example illustrating the effect produced by their inhomogeneous structure. It is the graphite constituent that fails first in these metals, followed by the steel base that breaks off afterwards. At the same time the white cast iron, having one steel base, i.e. cementite, exceeds the conventional carbon steel, in its erosion resistance, by a factor of 3.6. Thus, the main factor for homogeneous materials is their hardness, whereas for metals with non-uniform structure it is their microstructure.

All the materials, from the standpoint of their durability against the erosion, can be compared among themselves by using an appropriate coefficient illustrating how much one material is higher or lower, in its erosion resistance, than the other, as related to a reference. The conventional carbon steel 25 can be taken, for instance, as such a reference. The mentioned erosion resistance factors can be obtained in the course of laboratory tests.

1.4 Abrasive Erosion of Pump

1.4.1 Examples of Hydraulic Abrasion Taking Place in Pumps

Let us consider, as illustrative examples of hydraulic abrasion taking place in pumps, certain results obtained during the study carried out on some pump-houses in Azerbaijan (USSR), operation with water which contained a great amount of sediment matter (above 2.5 kg/m^3).

When analyzing operational conditions of pumping plants in the Azerbeijan SSR, it can be ascertained that deterioration of the flow-passage portion components in a pump (in impellers, walls of cases etc.) takes place not only due to cavitation but also owing to hydroabrasive effect produced by suspended matter and abrasive-cavitation phenomena, remarkably enhanced when the pumps operate in those points of the curve "Q-H" which differ from the optimum.

Visual inspection of the centrifugal pump impellers with 1.5-m diameter has shown that peripheral regions in these impellers were mainly the regions subjected to the greatest erosion. Here one can reveal areas of uniform hydraulic abrasion as well as regions with deep channels and grooves. Certain blades and impeller rims include through holes. The erosion is increased in the direction faced towards the periphery, reaching its maximum level on the working surfaces of blades, at points of separation of the stream from the surface being flown around.

In axial pumps cavitational-abrasive erosion takes place on the rear faces of the blades included in impellers with 0.8-m diameter The worn-out surfaces in these regions are of sponge-shaped structure and such erosion sometimes occurs at the leading and trailing edges of the working blades.

These components, being made of carbon steel, were significantly worn out after 1 to 1.5 year of operation. Visual inspection of these blades has revealed that their surfaces are covered with multiple cavities measuring 10×20 mm in area and up to 6 mm in depth, formed as a result of the effect exerted by cavitation and sediment matter. In addition to the damage of impellers the motionless components in the hydraulic machines were deteriorated as well. An illustrative example of this is found in the surface failure, which took place in the impeller case of a large propeller-type pump. The case under review, fabricated from case iron, is designed to include two

compartments (the lower and upper ones). The metal deterioration pattern formed a strip of 29 ~ 25 mm in size and 2 ~ 3 mm in depth. The case surface of the impeller has a complete porous structure in the failure region.

An example of erosion taking place in centrifugal pumps under the influence of suspended sediment matter is available from the results obtained during the survey carried out on the units of a large irrigation system pump-house situated on the Kure river. The pumping plant is equipped with eight pumps of the 24 Z4 NDN model. This pumping station operates 6 months a year. The pump impellers having 0.6-m diameter were subjected to the erosion.

A conventional factory-made pump impeller is worn-out for a period of one to one and a half season of operation, and its blades are the components subjected to the greatest erosion.

Visual inspection of the damages emerged on the impeller blade surfaces in the 24 Z4 NDN pump has revealed the following. Traces of deterioration caused by abrasive erosion have shapes resembling large-size grooves with smooth surface. The inner and outer surfaces in the blades are covered with deep scaly erosion with the trailing edges of the impeller blades being notched.

The erosion is characterized by availability of distinctive separation edges and peculiar-shaped grooves and cuts stretched in the direction of the flow stream. Individual grooves are 30 ~ 50 mm long, 5 ~ 6 mm wide and 1 ~ 3 mm deep. The entire working surface areas in these blades are covered with grooves and cuts of the indicated shape. This results, probably, from mutual action of cavitation being formed by the surface unevenness and suspended matter present in the area of the pulsation cavity.

The joint effort exerted by both the sediment matter and cavitation resulted in deterioration of entire blade areas. At the completion of one year of operation, in the water including suspended sediment particles, there are cases of complete absence of edges in the pump blades within the area reaching up to 5 cm in width.

The pump is provided with protective seal rings: two of them are stationary and the other two rings are mounted on the external rim of the impeller. The stationary seal rings, being fabricated from case iron, are replaced generally twice a season. The seal rings of the impeller are usually fabricated from cast iron as well. These rings get worn out during one month. Therefore they are replaced with rings fabricated from a steel strip 3 mm

thick and 15 mm wide; the rings are mounted in hot state and then machined to shape. These rings prove operable in the course of three months.

To prevent the pumps from hydraulic abrasion, the trailing edges of the impeller blades, specifically, are built up in thickness. The operation of impellers with thickened edges has demonstrated that such edges maintain serviceability in the course of one to one and half year of operation.

1.4.2 Silt Erosion in Pumps

The results obtained during the methodical observations over different types of pumps subjected to intensive hydroabrasive erosion and to cavitational-abrasive action, along with numerous data given in some publications, allow to define, in a fairly precise manner, those components within the flow-passage portion of pumps, which are most susceptible to erosion. In this respect, when considering the erosion elements, associated with the flow-passage portion of a pump, it is hardly possible to avoid mentioning the cavitation phenomena, which accompany often the hydraulic abrasion process in question.

It should be noted with reference to the cavitation that the general pressure drop at the inlet to a pump results in an upset of the pump operation, or bring about such a significant distortion of its performance which creates the operational conditions considered to be unacceptable; moreover, they are not characteristic of the situation enabling to evaluate the cavitation erosion taking place within the working components of a pump. The greatest interest, in this regard, refers to the local pressure fall, which causes emergence of local cavitation zones. Although the influence level of these zones on the energy quality and vibration state of a pump assembly is insignificant, they may become, nevertheless, a source of intensive erosion.

The impellers in the impeller pumps of all types are the elements subjected to the cavitational erosion most greatly, due to the hydrodynamic processes which develop in them. It is estimated that for the optimum behavior, with due regard for the meridian and circumferential constituents, the relative flow velocity, at the inlet to the interblade channels of the impeller, is equal to 20 ~ 45 m/s, depending on the standard size of a device. As the flow travels around the blade leading edges with velocity so high and, in accordance with the leading edge shape and the shape of the front region in the blade, the local pressure drop can reach the level of 0.2 ~ 0.3 MPa. Consequently, the

emergence of cavitation in these areas is possible even at a significant excessive pressure. Steady cavitational zones within the areas adjacent to the leading edge can be found practically in all the modes differing from the optimum operation. It was established also that in operations with a partial delivery ($Q < Q_{opt}$) the cavitational zones are formed at the rear face of a blade (zone 1 in Figure 1.11 a, b); in speed-up operations ($Q > Q_{opt}$) they are generated at the working surface side (zone 2). As a result of the flow separation from the rear surface, the cavitational erosion also affects those regions of the blades, which are immediately adjacent to the trailing edges (zone 3). The erosion intensity in these regions in dependent on the edge shape, and it increases, as a rule, with a rise in the flow delivery.

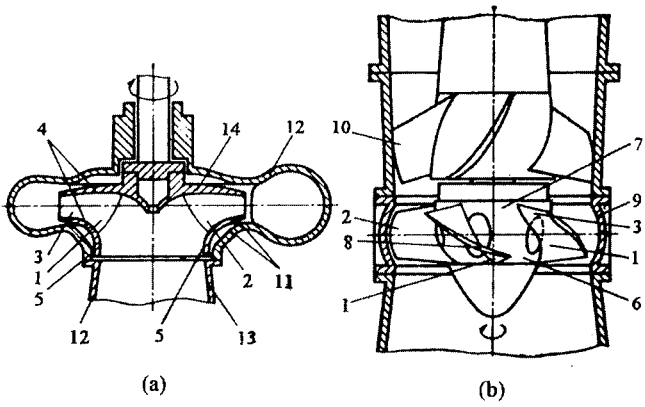

(a) centrifugal pump (b) axial-flow pump

Figure 1.11 Map of the erosion arising incentrifugal (a) and axial-flow pumps (b)

As a result of the dynamic interaction between the in-flowing steam with the components forming the inter-blade channels of the impellers in centrifugal pumps, cavitational zones can emerge in the regions adjacent to the adjoin line of the impeller blades with the disk surfaces (Figure 1.11 a, zone 4) and on the inner surfaces of the impeller outer disks within the one-way entrance (Figure 1.11 a, zone 5); they can also arise on both disks of impellers in the two-way entrance, due to deviation of the stream flow line at

the bend. In a similar way erosive destruction took place within the surface of the impeller hubs in axial-flow pumps, at the places where the blade inner faces adjoined (Figure 1.11 b, zone 6), as well as within the cylindrical regions of the hub, under the blade journals (zone 7).

In axial-flow and mixed-flow pumps the end faces in impellers (Figure 1.11 b, zone 8) and the impeller case walls (zone 9) are the places which are damaged most frequently, as a result of the slit-shaped cavitation so characteristic of the hydraulic machine type under review. The presence of a gap (a slit) between the impeller end faces and the case walls, which provide free rotation of the impeller, allows the water to flow from the area positioned above the impeller to the region located beneath the impeller; the great pressure differential at the both sides of a blade creates extremely high flow velocities of this secondary stream. As a result a local pressure drop occurs, thus forming on the blade suction surface a cavitational zone traveling within the case inner surface with the velocity equal to the circumferential rotational speed of the impeller. In addition to the hard operational conditions affecting the material of the impeller case, its surface is subjected to high fluctuation loads. The case surface is affected by alternating loads generating in its material fatigue stresses which contribute to accelerate its failure.

In axial-flow and mixed-flow pumps with a spiral casing, the latter's walls are subjected to cavitation in the places adjacent to impeller case. In a number of instances the cavitational failure affects the blades of the leveling device (Figure 1.11 b, zone 10) which, probably, results from discrepancy between the angle of the flow in leakage and that of the blade positioning.

A high velocity of the flow relative motion, in the pockets formed by the impeller disks and the case in centrifugal pumps, can bring about formation of cavitational zones on the outer surfaces of the disks and inner sides of the case (Figure 1.11 a, zone 11). Among the other components forming the flow-passage portion in pumps, where the emergence of local cavitaional zones is possible, it is necessary to distinguish the gaps and slits foreseen by the design and located between the rotational and stationary components of the device: inner surface of the inlet immediately adjacent to the impeller; guide fins mounted in the inlet pipes of certain designs, in order to reduce the spinning of the flow prior to its entrance into the impeller; tug of the spiral casing.

The hydraulic abrasion in pumps, as compared with the cavitational erosion, is of more general nature, since the presence of sediment solid particles, suspended in the water being transferred, contribute to the failure of

practically all the surfaces in contact with the water stream. The pump components subjected to the abrasive erosion, as related to the effect produced by them on the energy quality of the unit, can be divided into five basic groups.

The first group of components subjected to hydraulic abrasion includes impellers of the impeller pumps which are intensively destructed when the water contains suspended abrasive particles.

In centrifugal and mixed-flow pumps incorporating closed-type impellers the erosion process occurs within the following components:

* blade of an impellerthe process develops most intensively at the working side and, especially, heavy damage is distributed at the leading edges, on the both sides, and at the trilling edges on the working face side (see Figure 1.11 a, zone 2). In this respect, the areas adjacent to the rear disk are subjected to the greatest erosion;
* inner faces of the rear disk (see Figure 1.11 a, zone 14), most intensively at the area of the impeller hub, i.e. in the region of the flow turn;
* inner face of the front disk (it is worn more uniformly and significantly less than the front disk).

The components being worn in axial-flow and mixed-flow pumps, with closed-type impellers, are as follows:

* working surfaces of blades, in which the erosion intensity increases in the direction towards the trailing edges;
* end face edges of bladesas a result of the erosion caused by a slit-shape cavitation, with the sharply increased intensity when the water contains abrasive particles;
* rear surfaces of blades in the areas adjacent to the leading edges, due to vortex-type streams flowing around the blade in non-specified operations.

The second group of components subjected to an intensive hydraulic abrasion is compiled from components included in guide and leveling devices used in some types of pumps.

To the third group of components being worn, it is necessary to ascribe those which constrict the rotating impeller, i.e. the impeller case walls in axial-flow and mixed-flow pumps and the walls in casings of centrifugal pumps.

The fourth group comprises sealing components and bearings included in a pump shaft. The solid particles getting into these seals contribute to a rapid erosion of their elements. The destruction of seals, in addition to volumetric losses, can be caused, in a number of cases, by solid particles getting into the bearings, which is quite intolerable.

The fifth group includes inlet and outlet devices of pumps. According to the data obtained in a number of analyses, it is possible to conclude that the hydraulic abrasion rate developed in the pump outlets, particularly in the centrifugal pumps, which is presented by losses in mass per unit of time, exceeds considerably the erosion intensity in the impellers. However, the component which is decisive in determining the inter-repair time duration, under the conditions of hydroabrasive effect, is an impeller, since the outlets and casings in a pump are greater in their size and mass. Moreover, the partial erosion in the latter affects the performance of a pump in a lesser degree.

With reference to the combined effect produced on the pump components by both the cavitation process and the solid particles contained in the liquid transferred, it should be noted that to ascertain the exact boundaries of the areas subjected to the cavitational-abrasive erosion is rather difficult in practice, since in operational conditions one of the two erosion patterns is predominate, as a rule, over the other, therefore, the erosion subjected surface possesses distinctive features characteristic of one of them.

However, as to the intensity of the cavitational-abrasive erosion, it cannot, by any means, be evaluated by an ordinary summation of individual patterns of failure and is defined, in accordance with the specific operational conditions, by a set of various factors.

In order to solve practical problems in connection with, specifically, the operational reliability of the pump units, it is necessary to use quantitative parameters capable of providing the evaluation of the erosion process under review. They are, first of all, as follows:

Area S and depth b for a certain period of the pump operation T, S and b values can be presented both in absolute units (cm^2, m^2, mm or cm) and in shares (%) of the total area or initial thickness of the component being worn.

The loss in volume V of the material used to fabricate a component being worn for time T. To determine the meanings of V (mm^3, cm^3) in practice, the dependencies used are as follows:

$$V = \sum (k_1 \cdot S_1 \cdot b_1 + k_2 \cdot S_2 \cdot b_2 + \cdots + k_i \cdot S_i \cdot b_i) \tag{1.19}$$

or

$$V = k \sum (S_1 \cdot b_1 + S_2 \cdot b_2 + \cdots + S_i \cdot b_i) \tag{1.20}$$

where S_i and b_i are correspondingly area and depth of individual regions of erosion, k_i or k are coefficients with allowances made for the erosion taking place within the surface and depth of a component.

The loss in mass ΔG for a certain time period T can be expressed in absolute value (mg, g and kg)

$$\Delta G = V \cdot \rho \tag{1.21}$$

where ρ is material density of a component being worn, or

$$\Delta G = G_{in} - G_{fin} \tag{1.22}$$

where G_{in} and G_{fin} are respectively the initial and final masses of the component being worn.

The relative values of G' corresponding to loss in mass are also used in practice, which looks like

$$G' = \frac{\Delta G}{G_{in}} = \frac{G_{in} - G_{fin}}{G_{in}} \tag{1.23}$$

In the field conditions of operation, when dealing with hydraulic machines which have great geometric size and weight, it is essential that, for approximate evaluation of the erosion, and in accordance with the regulations laid down in the I.E.C. standard [1.15], the mass of electrodes M_{el} be used, required to rebuild the surface destructed. The M_{el} value is defined by actual consumption or approximately by the expression

$$M_{el} = (1 + \frac{0.6}{b_{max}}) \cdot \rho_{el} \cdot V \tag{1.24}$$

where ρ_{el} is material density of the electrodes, b_{max} is maximum depth of the destruction. Equation (1.24) takes into account the treatment of the surface being rebuilt in a component, after the building up.

In number of cases the erosion is estimated by the operational time of a machine which was used period to a certain level of failure in a check component, or by alteration arising in the energy quality of a device, for instance, by a drop in its efficiency by a certain value. The erosion indicator to be chosen is selected due to operational conditions and the problems that should be solved by making use of field measurements.

The erosion rate is generally defined by estimation of the erosion per unit of time. In accordance with the erosion index chosen, the expressions used in practice are as follows:

$$I_S = \frac{S}{T} \quad ; \quad I_V = \frac{V}{T} \quad ; \quad I_G = \frac{\Delta G}{T} \tag{1.25}$$

The limits of failure to be developed within the flow-passage portion of, for instance, pumps and caused by cavitation, sediment matter or cavitational-abrasive effect are functions of:

1) the standard size of pumps (parameters n_s, Q);
2) the materials used to fabricate the components composing the flow-passage portion of a device;
3) the specification of water-power stations and a water flow (chart of water delivery, availability and composition of pumps);
4) the duration of the interrepair period of operation.

1.5 Technical and Economic Effect Caused by the Erosion Arising in Hydraulic Turbines and Pumps

Technical and economic results of the erosion, being developed in hydro-turbines due to attrition process caused by suspended sediment matter and cavitation, manifest themselves in two ways. First, the development of the process leads to a decline in energy properties of turbines (a decrease in efficiency and, in certain cases, in power capacity), with the associated fall of the electric energy output. Secondly, the process necessitates repair jobs

aimed at removal of erosion aftereffect in components composing in hydroturbines the flow-passage portion; such maintenance service requires a considerable amount of labour and material expenses. As this takes place, the total extra costs rise so high as to acquire an independent technical and economic value.

The impairment of energy properties in turbines due to cavitational-abrasive erosion taking place in the components, associated with the flow-passage portion of the devices, has been ascertained during the full-scale testing performed. A drop in the efficiency of a heavily worn-out turbine, as compared with a repaired turbine with a newly installed impeller, amounts to 12 ~ 14% within the entire operational range of the power variation limits. The decrease of efficiency and reduction of electric power output in turnaround time, brought about by this, can be amounted, with a sufficient level of accuracy, to 6 ~ 7% value of the total output. Assuming that the total electric energy generated by the hydroelectric unit in the inter-repair time (above 12,000 h) is equal to about 75 ~ 80 million kwh, it can be estimated that the energy underproduction, through deterioration of the turbine quality, amounts to about 5 million kwh.

In assessing this aspect of the problem, special attention should be given to the fact that the greatest drop of the turbine efficiency, caused by the cavitational-abrasive erosion, appears, approximately by the end of high waters taking place in mountain rivers, therefore the worsening of hydroelectric station performances are particularly susceptible to changes arising in this winter period being most scarce both in energy and water discharge volume. Besides, while a turbine efficiency drop, in the time of a summer flash flood, may fail to be attended, in certain occasions, with a fall in its capacity and output (due to a speed-up flow rate formed by a redundant run-off volume), in winter and spring times, however, the mentioned efficiency drop results in decreasing both the guaranteed power and the amount of the electric energy generated, owing to a deficiency in the water flow. The real cost of this under-produced energy is, of course, much higher than in the other seasons of the year.

Rebuilding of heavily worn-out turbine impellers entails certain difficulties associated with configuration intricacies in the surface shape of impeller blades, as well as with difficulties preventing a fee access to them.

At the same time the reclamation of relatively small damages presents no special problems and helps to practically restore the energy properties of the

device almost completely. It should be noted, however, that according to the data obtained during the operation of hydroelectric stations built on mountain rivers, with a great amount of suspended sediment matter in their water, after near 5 to 6 years of operation it was found necessary to replace, in a number of cases, the impellers used in the hydro-turbines involved.

The results obtained during the full-scale tests of certain hydro-turbines have shown that a drop in efficiency, caused by deterioration of blade subjected to attacks of sediment matter, is not obligatorily accompanied by a decrease in the power being developed. Moreover, after replacement of one of the heavily worn-out impellers with a new one, the turbine power capacity in one of the hydroelectric units has reduced. Such events have taken place in a number of other water power stations. This result from reduction of the flow area in an impeller (in its outlet portion) caused by the metal built-up on its surface. As the impeller blades and rim surfaces proceed to erosion out, their flow sections increase as well, which gives a rise to the water flow rate, increasing thereby the output of the device. The impeller efficiency in this case alters insignificantly and, in certain cases, it may be somewhat large at the initial stage of the erosion process.

An important factor, for evaluation of the erosion control effectiveness, in the hydro-turbines with increased erosion-out, refers to the idle time provided for examination of hydroelectric units and maintenance service to be carried out. An analysis of the downtime and a study on the technical and economic results, incurred by the hydroelectric units during their inactive state, have shown that in the course of 2 years almost 90% of the entire dwell time is attributable to the reasons related to the cavitational-abrasive erosion of the equipment. The total loss associated with the costs of extra repair jobs and underproduced electric energy, in the downtime of the turbines during their maintenance, amounts to 80%, on average, of all the loss.

Similar estimates performed for other water-power stations provided figures which are no lower than those that have just been stated; there are cases in which the total loss, sustained in response to obtained action of both the cavitation and sediment matter, exceeds 90% of all the loss.

The basic energy measure governing the operational effectiveness of a pump is its efficiency:

$$\eta = \eta_h \cdot \eta_v \cdot \eta_m \tag{1.26}$$

where the suffices "*h*", "*v*" and "*m*" are correspondingly related to the values of hydraulic, volumetric and mechanical efficiency meanings.

The efficiency components never remain permanent but alter their values with operational variations arising within the performance of a pump. The deliveries, which are at variance with the rated conditions and maximum efficiency, bring about a rise in the relative level of a friction independent loss. The hydraulic loss grows, first of all, due to the flow pattern deviation from the conditions ensuring the radial inflow and rated outflow of the water from the impeller. The volumetric loss varies as well, according to the position being occupied by the machine control elements and the pressure distribution within the flow-passage portion of the device. The mechanical loss remains practically constant in its absolute value, whereas at small loads its relative value grows.

It is the full efficiency meaning that characterizes, with all the variations mentioned, a pump operation at different modes. Besides, the full efficiency values and, hence, the energy quality of a pump, vary in the course of time. Due to the erosion process, deteriorating the working components of the device and arising as a result of the cavitation and the effect of the sediment matter, a rise in all the aspects of a general loss occurs and, consequently, a decrease in all constituents of the efficiency.

The surface roughness increase, caused, specifically, by cavitational erosion, leads to enlargement of the friction dependent hydraulic loss, whereas the failure of leading and trailing edges in the impeller blades serves to deviate the flow line from its design parameters. All this adds up to an acute fall in the hydraulic constituent of pump efficiency.

The erosion in the case walls and in the end face edges of the impeller caused by a slit shaped cavitation in axial-flow pumps, as well as the failure of the packing components brought about by sediment matter in centrifugal pumps, create an increased leakage; the latter, with the volumetric loss being increased, also contributes to a fall in the device efficiency.

With the machine erosion being developed, the mechanical loss manifests itself as well. Owing to enlargement of gaps, the flow pattern between the impeller and the case starts to vary, which may result in a considerable loss consumed on the disk friction. Moreover, the unavoidable non-uniformity in the erosion of impellers can create an upset of balance, which leads to a destruction of bearings, a unilateral erosion of the shaft and severe vibrations, all contributing to lower the mechanical efficiency of the pump.

As an example illustrating the worsening of a pump performance, due to the cavitational-abrasive erosion of its components, Figure 1.12 gives the data obtained during the tests carried out at the V.V. Kuibyshev Moscow Civil Engineering Institute (MIEI); the tests were performed to determine the energy quality of the pump operating with water streams which contain a large amount of sediment matter. The decrease in the efficiency of heavily worn-out pump, as compared with the efficiency of a repaired pump, amounts to 10 ~ 12% for an axial-flow pump and 12 ~ 15% for centrifugal pump, within the entire range of the delivery variation.

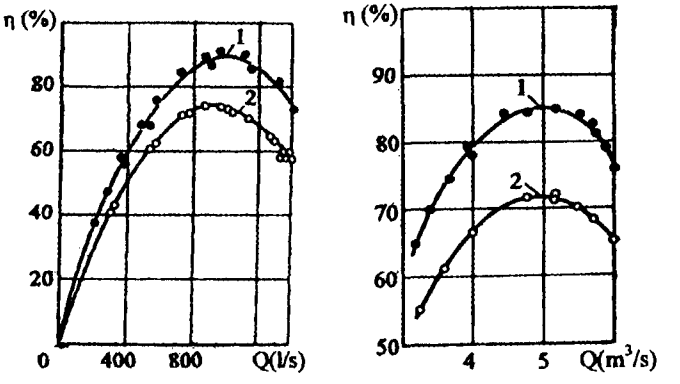

a. centrifugal pump b. axial-flow pump

Figure 1.12 Impairment of the performance caused by the cavitational-abrasive erosion of pump

It is interesting to note that the decline in performance of pumps, due to erosion process, does not arise straight away, with the intensity varying in the course of time. In many cases it is noticed that the efficiency grows by 1 ~ 2% in the initial stage of a pump operation, after the overhaul. The performance of the device began to decline on the expire of some time.

To explain this, a certain number of successively performed tests are of interest, in which one and the same device was examined to determine its energy properties; the tests involved allow to trace all the performance variations of the device caused by the intensive cavitational-abrasive erosion.

The analysis of the test result obtained has shown that the operation of pumps in the inter-repair time can be divided into four periods.

1) The operational period, which follows immediately after the overhaul, is characterized by a gradual improvement of a pump performance. The rough surfaces of the components, forming the flow-passage portions in the pumps, being subjected to the action of the sediment matter, get grinned and smoothed. As a result, the friction dependent losses decrease to improve the performance of the device. Moreover, the sediment matter acting on the impeller blades make their shapes more sloping. The blade shape section obtained by design can only be partly appropriate to given hydraulic conditions. The liquid flow with the sediment matter contained therein makes the inter-blade channel acquire a shape which reduces the resistance to the flow motion.

2) The period distinguished by the performance stability. Worsening of the performance does not arise. It accounts for the fact that the hydraulic abrasion manifests itself in the region adjacent to the trailing edges of the blade, where the flow velocities are the highest. The sediment matter particles smooth the trailing edges, thus providing only a gradual undercutting of the latter. This cannot affect significantly the loss variations in the impeller. The blade shape section is not deteriorated yet, therefore the blade fulfills its purpose entirely, providing withdrawal of the flow from under the impeller at a definite angle and with a specified speed.

The invariability of the device performance in this stage also proves that the impeller seals are kept in a satisfactory stage, since, in case of their failure, the volumetric loss increases, thus affecting negatively the efficiency value.

3) The period of a sharp decline of the performance. Quantitative changes in an impeller result, in the final analysis, in an acute decline of the pump performance. The trailing edges of the impeller blade are undermined to the level which cannot bear the pressure differential from both sides, which result in damage of these edges. The conditions at which the water stream outflow under the impeller, are greatly worsened. The efficiency of the device drops in this period by 8 ~ 10%.

4) The period of further decline of the performance. The value of the required cavitational margin, after breakage of the blades, increases, thus making the suction height too great, which predetermines development of cavitational phenomena. Intense crackling, noise and vibration accompany the

pump operation in this period as well. The combined action of both the cavitation and sediment matter brings about a further deterioration of the leading edges in blades.

The technical and economic outcome of cavitational-abrasive effect exerted by the sediment matter manifests itself in a rather complex manner. First, the energy quality of a pump declines, thereby increasing the resultant electric energy expenditure, and secondly, maintenance service is needed to eliminate the after effect of the erosion process involved. Finally, it is necessary to increase the number of reserve units, i.e. the cost of a hydroelectric station rises.

According to the data presented in Figure 1.12, it follows that the electric energy over expenditure brought about by the decrease of efficiency in the pumps can be estimated with an accepted level of accuracy; this decrease amounted to about 6 ~ 7% of the total electric energy value consumed by the pumps in the inter-repair time. The problem of maintaining the pump equipment efficiency at a high level is extremely important and topical.

An analysis of the costs, involved with repair service of the worn-out components in pumps, reveals that the greater part of this expenditure, when dealing with small size pumps includes the cost of spare part replacements and the labor costs related to dismantling and mounting processes.

Rebuilding of heavily worn-out impellers and other components, associated with the flow-passage portion of large pumps, entails great difficulties and expenses. The repair service in such pumps, concerning their surfaces mainly, is arranged to include building-up of the worn-out areas or their facing with high-alloy steels.

1.6 Approach to Anti Abrasive from Hydraulic Machinery

1.6.1 Approach Avenues on Anti-silt Erosion of Hydraulic Machinery

A lot of rivers are with much silt. The hydraulic machinery installed on those rivers will suffer from silt-erosion damage leading to very low efficiency and

short service life with frequent overhaul. There are following approach avenues could be considered to lighten silt erosion of hydraulic machinery [1.11, 1.12]:

(1) Anti-erosion design (hydraulic and construction).
(2) Selection of type and parameters of machines.
(3) Anti-erosion material.
(4) Manufacturing technology.
(5) Operation control.
(6) Prediction of silt-erosion damage.

1.6.2 Anti-abrasion Hydraulic Design of Pumps

For hydraulic machinery working in silt-laden water, the hydraulic design of impeller should be based on sand water two-phase flow analysis [1.16, 1.17], which can not only obtain high efficiency and cavitation property for working condition of both clean and silt water, but also improve the anti-abrasion ability. Based on the two-phase flow analysis, a series of IRC anti-erosion pump impeller models with different specific speed n_s has been developed by International Research Center on Hydraulic Machinery in Beijing (IRC). The important parameters of the pump impellers have been optimized. The inlet angle of blade of the IRC pump impellers is larger than that of clear water pumps, the outlet angle of blade is smaller. The relative outlet width of the impellers is between 0.1 ~ 0.16, the wrap angle of their blade is about 90°110°, their blade number is 6 or 7.

The efficiency of the series pumps come up to 90% or more, and the efficiency curve is flat, and the high efficiency region is from 0.8 Q_d (design discharge) to 1.2 Q_d with the cavitation factor's meeting the requirements of the project, which they were designed for. In silt-laden water of the design silt density (10 kg/m^3), the efficiency of the pumps is as high as 88.75% to 91.82%.

While the silt density is smaller than 10 kg/ m^3 and the diameter of silt particle is smaller than 270μm, silt density has no clear effect on the hydraulic performances of the pumps [1.17].

1.6.3 Prediction of Silt-Erosion Damage in Pump Design by Test

Prediction of the damage intensity by silt erosion is an essential subject for the pumps working in silt-laden water. A high-speed abrasion test in a testing-

computing mode for the damage prediction of impeller has been developed by IRC. This prediction method has the following functions:

(1) To predict the location of the impellers suffered from silt erosion and eroded level in order to make an appropriate anti-silt-erosion treatment in manufacture.

(2) To predict the eroded volume in order to judge the anti-erosion ability of the test impellers.

Test impellers are coated with special coating mixture that can be eroded in an accepted speed of damage by sand. Then a fast abrasion damage test of the impeller was carried out at the muddy water experiment rig in IRC.

Set up some meshes on the pump impellers and measure the pre-experiment coat thickness and the post-experiment coat thickness. The coat can be measured and mapped in the three-dimensional passage formed by two adjacent blades and the front and rear covers of the impellers. In order to express directly the relative abrasion resistance of different pump models, an evaluation method based on the total abrasion volume using the abundant data of the above abrasion test has been suggested [1.16].

References

1. 1 Visintainer, R.J., Addie, G.R., Pagalthivarthi, K.V. and Schiele, O.H. (1992). 'Prediction of Centrifugal Slurry Pump Wear', *Internat. Conf. On Pumps and Systems*, Beijing, China, May 19 ~ 21, pp. 203 ~ 221.

1. 2 Addie, G.R., Pagalthivarthi, K.V. and Visintainer, R.J., (1996). 'Centrifugal Slurry Pump Wear Technology and Field Experience', 1996 *ASME, FED*, 236, *Fluids Eng. Div. Conf.*, Volume 1, pp. 703 ~ 715.

1. 3 Tuzson, J. and Clark, H. McI., (1998). 'The Slurry Erosion Process in the Coriolis erosion tests', Proceedings of 1998 Fluids Engineering Division Summer Meeting, June 21 ~ 25, Washington, DC, FEDSM98-5144.

1. 4 Pagalthivarthi, K.V., Desai, P.V. and Addie, G.R., (1990). 'Particle Motion and Concentration Field in Centrifugal Slurry Pumps', *Particulate Science and Technology*, Hemisphere Publishing, pp. 77 ~ 96.

1. 5 Wu Y.L. et al, (1998). 'Silt-laden Flow through Hydraulic Turbine Runner by Turbulence Simulation', *Hydraulic Machinery and cavitation, Proceedings of XIX IAHR Symposium, World Science,* 1998, Singapore, pp.111 ~ 120.

1. 6 Tuzson, J. (1984). 'Laboratory Slurry Erosion Tests and Pump Wear Rate Calculations', *ASME Journal of Fluids Engineering*, 106, June, pp. 135 ~ 140.

1. 7 Brach, R.M., (1991). Editor, *Mechanical Impact Dynamics*, Chapter 6.3 Particle-Surface Collisions: Erosion and Wear, John Wiley, New York, 116, March, pp. 147 ~ 153.

1. 8 Clark, H. McI. and Wong, K.K., 1995, 'Impact Angle, Particle Energy and Mass Loss in Erosion by Dilute Slurries', *Wear,* 186 ~ 187, pp. 454 ~ 464.

1. 9 Pagalthivarthi, K.V. and Helmly, F.W., (1992). 'Applications of Materials Wear Testing to Solids Transport via Centrifugal Slurry Pumps', *Wear Testing of Advanced Materials, ASTM STP 1167,* Eds., Divakar, R. and Blau, P.J., American Society for Testing and Materials, pp. 114 ~ 126, Philadelphia,

1. 10 Clark, H. McI., Tuzson, J. and Wong, K. K., (1997). 'Measurements of Specific Energies for Erosive Wear Using a Coriolis Erosion

Tester', Oral presentation to the *International Tribology Congress*, London, Sept. 1997, submitted to *Wear*.

1. 11 Duan, C.G., (1983). 'Sand Erosion of Hydraulic Turbine', Press of Tsinghua University, Beijing (in Chinese).

1. 12 Duan, C.G., (1998). 'Approach to the Demand on Anti Abrasive Erosion from Hydraulic Machinery Project', *Hydraulic Machinery and cavitation, Proceedings of XIX IAHR Symposium, World Science,* Singapore, pp.59 ~ 69.

1. 13 Karelin, V.Ya., (1983). 'Silt Abrasion of Turbo-pumps' , Machinery Engineering Press, Moscow (in Russian).

1. 14 Raabe, T., (1976). 'Calculation of the meridional velocity distribution in a mixed flow impeller with respect to spatial special shape and losses'. Paper 1 ~ 3, *International Conference on Pump and Turbine Design and Development,* Glasgow.

1. 15 Cavitation Pitting Evaluation in Hydraulic Turbines, (1978). Storage Pumps and Pump-Turbines. IEC Standard, Publication 609, IEC, Geneva.

1. 16 Zhao, J.T., Ma, C.M. and Jiang, D.Z., (1998). 'Solid-Liquid Two-Phase Flow in Pump Impeller', *Hydraulic Machinery and cavitation, Proceedings of XIX IAHR Symposium, World Science,* Singapore, pp. 762 ~ 773.

1. 17 Duan, C.G. et al, (1996). 'Development of Pump Models Working in Sand-Laden Water', *Proceedings of 18th IAHR Symposium of Hydraulic Machinery and Cavitation*, Beijing.

Chapter 2

Calculation of Hydraulic Abrasion

V. Ya. Karelin, A. I. Denisov and Yulin. Wu

2.1 Calculation of Hydraulic Abrasion Proposed by V. Ya. Karelin and A. I. Denisov

As noted previously (see Sections 1.1 and 1.2 in chapter 1), hydraulic abrasion of the components forming the flow-passage portion of hydraulic installations (turbines, pumps) is described by the process of gradual alteration taking place in the physical state and shape of the surface being streamlined by the flow; this process develops as a result of the action effected by incoherent solid abrasive particles suspended in water or in any other working fluid. Whereas the abrasive particles contained in the water perform a mechanical effect on the surface mentioned, the effect of the pure water upon it is both mechanical and corrosive.

Under the attack of these abrasive particles, acting on the metal surface in contact with the fluid a gradual erosion of this surface taken place due to both continuous impingements exerted by the particles and thus causing elastic deformation, and separation of metal microchips and particles being knocked out.

The process of hydraulic abrasion, within the components forming the flow-passage portion of hydraulic machines and affected by attack of solid particles suspended in the flow, is influenced by a number of factors, namely: an average motion velocity of the particles; the mass of particles; the concentration of abrasive particles in the fluid or the number of particles in

the flow volume unit; size distribution of particles and their average grain size; the incidence angle of impingement as related to the surface; the time interval of the attack effected by the particles (of specified size and concentration) on the surface flown about by the fluid; the erosion resistance of the structural materials used.

There is no comprehensive formula presently capable of evaluating hydraulic abrasion quantitatively with due consideration of the particular values characterizing the afore mentioned parameters. There is, however, a number of theoretical and experimental data enabling to reveal the relationship mechanism of abrasive erosion or the erosion caused by separate and interconnected factors.

Specifically, there can be suggested, as applied to hydro-turbines, the following generalized expression for evaluation of abrasive erosion [2.1]:

$$J = \frac{A \cdot p \cdot t \cdot W^3}{\varepsilon} \tag{2.1}$$

where J is the erosion extent, mm; ρ is the average annual concentration of abrasive particles, kg/m^3; t is the time interval comprising the period within a year which the abrasive particles attack the surface, they collide with; W is the flow velocity, m/s; ε is the erosion resistance of the material used (equaling the unity for carbon steels); A is the index of the slurry abrasively depending on shapes of the particles and to be determined experimentally, mm s^3/year.

In equation (2.1) the numerator defines the abrasive power of the stream flow, whereas the denominator characterizes the ability of the material used to withstand the abrasive attack exerted by the slurry. However this relationship, when applied in practice, has certain difficulty, because, as the fluid flow about curved surfaces, for instance, over the concave and convex sides of a blade, the erosion level developed will be variable even with the flow velocities are equal, since the abrasive particles, due to inertial forces arising, will be pressed to the blade concave side and rejected from the convex one. Therefore the erosion extent can be evaluated, for instance, by the time interval required for maintenance-free operation of turbines or by necessity for repair service to be provided when surveying the impeller and nozzle used

as a whole. In this case the flow velocities are calculated, for example, at the exit from the impeller or nozzle.

The criteria specifying the necessity for performing repair service of an impeller are mainly as follows: erosion out of trailing edges within a blade, up to entire disappearance of their thickness, or erosion-and-tear of the lower rim to the extent of up to one third of its thickness. In this case the time specifying the attack period effected by the slurry, t, corresponds to the maintenance interval.

To determine the erosion extent, or the necessity for performing the maintenance service of a newly designed turbine, let us consider it together with one of turbines chosen within an operating hydroelectric plant. The hydroelectric station is to be selected from among those having a known slurry mechanism and erosion level; besides, it is better to choose the one with an annual repair interval $t = 1$, provided that its components are fabricated from carbon steel ($\varepsilon = 1$). It is essential, in this respect, that the turbines being compared should be identical or closely similar in their design type.

Consequently, the erosion extent J_r for the turbines of an operating hydroelectric plant introduced as

$$J_r = A_r \cdot p \cdot w_r^3 \tag{2.2}$$

is a known value.

The erosion level J_p for the turbines of a newly designed hydroelectric station will be calculated from

$$J_p = A_p \cdot p \cdot w_p^3. \tag{2.3}$$

When the standard sizes, of both the operating station and the one being designed are identical, the necessity for maintenance servicing of the latter arises when $J_p = J_r$; in this case

$$J_r = \frac{A_p \cdot p \cdot w_p^3}{\varepsilon_p}. \tag{2.4}$$

Hence, the servicing time interval expressed in years or the turbine maintenance-free time, t_p, is obtained from

$$t_p = \frac{J_p \cdot \varepsilon_p}{A_p \cdot p \cdot w_p^3} \tag{2.5}$$

When comparing the erosion of the turbine being designed with that of the operating one, their sizes are not taken into account, i.e. the scale factor is ignored, and this effect manifests itself in the following.

The relative erosion of any component, for instance, that of an impeller can be evaluated as the ratio of its weight loss to the total component weight. The weight losses developed are proportional to the surface area being flown over, that is to the diameter raised to the power two, whereas the weight is proportional to the impeller diameter cubed. Thus, the erosion of turbines to be used in the hydroelectric station being worked out, can be obtained from

$$J_p = \frac{D_p^2}{D_p^3} \tag{2.6}$$

whereas the erosion in the operating hydroelectric plant is calculated from

$$J_r = \frac{D_r^2}{D_r^3} \tag{2.7}$$

When comparing the erosion of identical components, used in both the operating hydroelectric plant and the one being developed, we shall obtain

$$\frac{J_r}{J_p} = \frac{D_p}{D_r} \tag{2.8}$$

i.e. the erosion of the components being compared is inversely proportional to the diameters of the impellers.

With regard to the scale factor, the maintenance-free interval of or a newly designed hydroelectric plant will be equal to

$$t_p = \frac{J_r \cdot \varepsilon_p \cdot D_p}{A_p \cdot p \cdot w_p^3 \cdot D_r} \tag{2.9}$$

or, if presented as a generalized expression, it will look like

$$t_p = \frac{A_r \cdot P_r \cdot w_r^3 \cdot \varepsilon_p \cdot D_p}{A_p \cdot P_p \cdot w_p^3 \cdot \varepsilon_r \cdot D_r} \tag{2.10}$$

The maintenance intervals calculated from this formula coincide adequately with the actual maintenance intervals.

For the calculation of hydraulic abrasion rate one can use the formula offered by Prof. Bovet (Switzerland):

$$J = \mu w \left(\frac{\rho - \rho_w}{R} \right) V^3 \tag{2.11}$$

where J is the erosion; μ is the friction coefficient between surfaces of a hydro-turbine impeller blade and slurry abrasive particles; w is the volume of particles; ρ is the specific gravity of particles; ρ_w is the specific gravity of water; R is the radius of an impeller; V is the particle motion velocity. This formula demonstrates the necessity for taking into account the particle motion velocity (in the third power).

To evaluate the hydraulic abrasion-out extent within the impellers, utilized, for instance, as a part of hydraulic turbines, it is possible to make use of statistical data obtained in the process of their operation. The erosion index, in this case, will correspond to the weight loss amount of an impeller blade, as related to the number of working hours consumed during the maintenance-free operation of the installation.

While selecting the hydro-turbines, in order to restrict the erosion extent to be developed, the relative water motion velocity within an impeller should not exceed 15 m/s, which is governed by choosing the hydro-turbine rotational speed required. In accordance with the admissible limiting rotational speed range, in this respect, should be within 250 to 350 rev/min. The relationship between the rotational speed, Q and H, within the relative water motion velocity equaling 15 m/s, was calculated as well. The maximum rotational

speed is not influenced by H, while it is varied in accordance with Q, m^3/s. The minimum rotational speed grows with a rise of H. when the concentration of slurry particles suspended in the water is considerable; it is advisable that an average rotational speed be chosen. For H exceeding 250 m; it is recommended that active hydro-turbines be employed.

To reduce the erosion extent developed in impellers used in centrifugal pumps, the relative water velocity in an impeller should not exceed 35 m/s. For the devices used to pump over the water containing a large amount of slurry particles the rotational speed to be selected should not exceed 1000 rev/min.

In [2.2] a series of tests were undertaken on different pump materials to study the effect of slurry properties and pump material on abrasion erosion, using a test facility, which incorporates most of these parameters. An analytical model, for hard and brittle materials under different running conditions was obtained. Experimental and calculated results for cast iron, as an example of a hard and brittle material, are comparable on a specimen weight loss basis.

The jet abrasion test facility was designed to evaluate erosion resistance of different materials that are being subjected to abrasive particles. The main asset of the test facility is its simple design although each erosion parameter can be measured.

With a variable speed motor slurry velocities ranging from 5 to 30 m/s at the nozzle exit can be obtained. Measurement of the slurry velocity is readily carried out by instantaneously redirecting the flow with a Jaco air-operated pinch valve through the same nozzle size into a graduated pail. By recording the time of sampling together with the volume of sample collected by reading the level from a sight tube on the side of the pail, the nozzle exit velocity is obtained.

The particle size of the sand sample is determined by selecting one of four different mesh sizes ranging from 37 to 3.5 or equivalent openings of 0.41 ~ 0.50 mm. A particle size range of 0.41 ~ 0.50 mm was used for experimental verification in this study. The impingement angle can be varied from approximately 15° to 90° by adjusting the specimen holder.

The erosion index is calculated from the following equation:

$$W = \frac{Q_r C_w T_w}{T_S W_{loss}} \times 10^3 \tag{2.12}$$

where Q is the volume of sample; γ (g.cm^{-3}) is the density of the mixture; C_w is the concentration; T_w (min) is the time (given by time of testing-sample time, T_S) of erosion and W_{loss} is the specimen removed per gram of sand. Erosion can be expressed as an absolute value of mass loss or as an erosion index.

By combining all the parameters from the investigations an equation of the following form is produced:

$$\Delta W = \frac{1}{2} K C_V^{0.682} \left(\frac{H_1}{H_2}\right)^n d^{0.616} V^{2.39} \{1 + \sin(\frac{\alpha - \alpha_1}{90 - \alpha_1} 180 - 90)\} f(t) g \tag{2.13}$$

where C_V is the volumetric concentration; H_1 is the eroded material hardness; H_2 is the solid particle hardness; n is a function of H_1/H_2 according to $n = 3.817$ if $H_1/H_2 < 1.9$, and $n = 0.268$ if $H_1/H_2 > 1.9$; d is the solid particle size, mm; V is the velocity of particles at the nozzle exit and $f(t)$ is an assumed linear function as suggested by Brauer and Krieger. Here d is the impingement angle.

The constant K in equation (2.13) was obtained from all the previous results for velocity, hardness, particle size and concentration and with the help of the least-squares method. The final equation expressing erosion for cast iron is

$$\Delta W_{CI} = 1.342 \times 10^{-5} C_V^{0.682} \left(\frac{H_1}{H_2}\right)^n d^{0.616} V^{2.39} \{1 + \sin(\frac{\alpha - \alpha_1}{90 - \alpha_1} 180 - 90)\} T \tag{2.14}$$

where n is again a function of H_1/H_2.

From the analytical model, the prediction of erosion resistance for any sample of cast iron under any running condition can be obtained.

Erosion intensity, as indicated previously, depends on a number of different factors. With the frictional force involved the erosion rate of an impeller blade, for instance, when calculated in a slurry pump with reference

to the impingement exerted by a single abrasive particle, can be calculated from

$$J = K_1 \gamma_a \, dA/d\Delta \tag{2.15}$$

where K_1 is the proportionality coefficient; dA is the work done by an abrasive particle during its travel over an infinitesimal surface $d\Delta$; γ_a is the density of this abrasive particle.

The elementary work performed by the frictional force during an infinitesimal time period dt will equal to

$$dA = fN(V_p - V_o)$$

where f is the friction coefficient; N is the normal component of reaction acting in a blade; V_p and V_o are correspondingly the radial and circumferential velocities of a particle.

The normal component of reaction is calculated from

$$N = 2m\omega V_p \tag{2.16}$$

where m is the abrasive particle mass; ω is the angular frequency of the impeller rotation.

Based on equation (2.16) the elementary work done can be expressed as

$$dA = 2m\omega f(V_p - V_o)V_p dt \tag{2.17}$$

Substituting here $V_p \, dt$ by $d\Delta$ and replacing the value dA in equation (2.15) we shall obtain

$$J = K_2 m\omega f \gamma_a (V_p - V_o) \tag{2.18}$$

where K_2 is the proportionality coefficient.

The abrasive particles, with respect to the surface of an impeller blade, can travel with both slip and rolling motion. The blade erosion can take place

as the particle travels with slip motion and the particle-to-surface impingement angle being 45° (intensive erosion).

Using the quantities for values V_p and V_o, the equation (2.18) can be presented as:

$$J = K_2 m\omega^2 fR\gamma_a[\sqrt{0.7}\sqrt{b^2/R^2 - 1} - 0.5(b/R - 1)] \qquad (2.19)$$

where R is the radius used when the abrasive particle makes contact with the blade surface; b is the blade width.

Having differentiated equation (2.16) we shall obtain the maximum erosion intensity:

$$\partial I/\partial b = K_2 m\omega^2 fR\gamma_a[\sqrt{0.7}b/[R^2(b/R)^{0.5} - 1] - 0.5/R] = 0$$

According to the curves obtained the variations in the impeller blade erosion intensity, observed within the divergence length corresponding to the experimental and theoretical data calculated, do not exceed 3 percent. The erosion intensity of blades increases at small values of ratio b/R. It is therefore directly proportional to the radius employed.

The erosion of blades depends as well on the amount of particles colliding with the surface during their travel within the hydro-mixture flow. With regard to equation (2.16) the erosion to be defined can be expressed in the following generalized form:

$$J = Kn\omega^2 m\gamma_a Rf[\sqrt{0.7}\sqrt{b/r - 1} - 0.5 - (b/R - 1)]$$

Hence, to decrease the erosion rate to be generated in blades it is necessary to reduce the rotational speed of the impeller, to decrease the amount of solid particles in the fluid, which can be accomplished through a more intensive de-slurring process and, additionally, to make the friction coefficient higher, specifically, by vulcanizing the working surfaces of impellers.

The erosion level in slurry pumps depends, among other things, on the grain size used in pulps.

The abrasive particles contained in the pulp have different shapes and the pump components are worn out under the action effected by faces of these

particles. It is assumed that each of these particles possesses similar faces and penetrates into the surface with one of its protrusions. Therefore the penetration force value will depend on diameter d, number n of particles $P = 1/n$ of $n = 1/d^2$, and consequently, this penetration force of a particle per area unit can be expressed as

$$P = kd^2 \tag{2.20}$$

where k is the proportionality coefficient.

Assuming that this abrasive particle penetrates into the surface of an elastic component and possesses the shape of a tough triangle, we shall obtain

$$P = 2ta[\pi + 1 + 24 - 2a + \cos(24 - a)/\cos\alpha] \tag{2.21}$$

where t is the tangential stress exerted by the particle towards the surface; $2a$ is the indentation area; α is the angle at the top of a particle's protrusion; f' is the value defining the friction developed between the particle being forced into the surface and the metal, $f' = 0.5\ arcsine\ \tau^{-1}$; f is the maximum value of frictional force.

If the particle travels along the surface of metal having specific gravity γ, the erosion level per distance unit can be expressed as

$$\Delta G = \gamma a^2 tga \tag{2.22}$$

Solving equation (2.22) for a, while substituting its values into equation (2.21) we can obtain

$$P = 2t[\Delta G(\gamma tga)^{-1}]^{0.5}[\pi + 1 + 24 + \cos(f' - a)/\cos\alpha] \tag{2.23}$$

Taking into account that f' and a are constant quantities, the relationship given by equation (2.23) can be presented as

$$P = 2\tau[T\Delta q(\gamma + tg\alpha)^{-1}]^{0.5}$$

Having substituted P in equation (2.20) by its values, we shall obtain the erosion level developed:

$$\Delta G = Kd^4 qtg\alpha(4\tau^2 T^2)^{-1} \tag{2.24}$$

The total erosion depends on the amount of particles coming in contact with the surface, i.e.

$$G = \sum_{i=1}^{i=t} AN$$

where N is the number of all particles.

When expressing the particle size through effective diameter d_{ef}, thus classifying the pulp graininess, the ratio of the number of particles contained in the fraction used, to their total number can be expressed as $d_i = d_{ef}\beta_i$, where β_i is the ratio of the particle average diameter size, in the given fraction, to the effective diameter.

In this case the erosion is calculated from

$$G_\Sigma = Ad_{ef}^4 N \sum_{i=1}^{i=t} a_i\beta_i \tag{2.25}$$

Taking into account the relationship between the effective diameter and the total area of the abrasive medium we can calculate the amount of particles contained in the specified fraction:

$$n = 6\Delta Q / \pi d^3 \gamma_a$$

where ΔQ is the total weight of a separate fraction; d is the mean diameter of a particle present in a separate fraction; γ_a is the specific gravity of an abrasive particle.

The total surface of particles contained in a separate fraction will be presented as $\Delta F = 6\Delta Q / d\gamma a$, whereas that of the abrasive medium will correspond to:

$$F = 6/\gamma a \sum_{i=1}^{i=t} \Delta Q/d^1$$

Having expressed ΔQ and d^1 in terms of total weight Q and effective diameter d_{ef}, we shall obtain

$$F = \frac{6Q}{\gamma d_{ef}} \sum_{i=1}^{i=t} \frac{a_i}{\beta_i} \tag{2.26}$$

Substituting d_{ef} into equation (2.25) we can define the total erosion of the surface:

$$G_{\Sigma} = AN\sigma^4 Q\gamma a^{-4} F^{-4} BC \tag{2.27}$$

here

$$B = \sum_{i=1}^{i=t} d_1 B_1 \qquad \text{and} \qquad C = \sum_{i=1}^{i=t} \frac{a_i}{\beta_i}$$

Analyzing the relationship specified in equation (2.27), it is safe to note that the erosion level in the surface of a component is inversely proportional to the total area of the abrasive medium raised to the 4th power, as well as to the specific gravity, amount of moving particles and extent of their smoothness.

As seen from the results obtained from slurry pumps tested, the illustrated formula can be used to make calculations referred to conveying the materials with grain sizes of up to 1 mm.With increase of abrasive particle grain sizes the surface erosion is reduced to a certain extent.

According to the erosion taking place in components of slurry pumps is directly proportional to the duration of attack effected on pump components by the abrasive and by concentration of abrasive particles present in the hydro-mixture used; it increases with increasing particle size, with a rise in density and hardness of these particles and depends, as well, on the shape and erosion resistance of the material being used for fabrication of these components.

When particles travel along the passage channel within a slurry pump, there arises a slip motion of the particles in relation to the component surface,

with the appearance of a frictional force being developed in the contact area. This friction is caused by two reasons: the adhesion taking place in the area of real contact, with emergence of frictional bonds between the participating bodies, and these bonds are to be sheared by the adhesive force during mutual slipping being developed; penetration of the harder surface into the softer one, which result in generation of external force, spent to effect cubic strain within the metal.

As a result, the total frictional force developed, while an abrasive particle makes contact with the surface of a component, will correspond to

$$S_{fr} = P_a + P_m \tag{2.28}$$

where P_a is the adhesive force; P_m is the strain (displacement) force developed within the metal.

Taking into account that the friction of traveling abrasive particles is associated with kinetic energy, the energy of a particle, while the latter separates from the component surface, can be presented, with certain assumptions, as the energy of friction:

$$E_{fr} = E_a + E_{s1} + E_{bp} \tag{2.29}$$

According to Coulomb-Amonton's law $S_{fr} = f_{fr} \cdot N_n$, where f_{fr} is the friction coefficient; N_n is the normal force.

Let us present equation (2.29) in the form of energy. In doing so we can assume that at the first moment, while a particle comes in contact with the component surface, there is created contact contiguity within certain separate points only; therefore the area of points making contact grows from zero to the area region comprising the erosion region of the material $F = \pi D\lambda$, whereas the area of frictional bonds is concentrated at the circumference of a particle $F_a = \pi Dx(\lambda - \lambda_n)\eta$.

The energy effecting the surface erosion during impingement of particles within the region of elastic deformation is $E_a = f_{a \cdot fr} E \sin\alpha_1$; where $f_{a \cdot fr}$ is the friction coefficient obtained from adhesion; α_1 is the impingement angle formed by the particle and surface.

The energy enabling separation of a particle corresponds to $E_{bp} = f_{bp}E_b$, where f_{bp} is the friction coefficient developed, as the particle separates from the surface.

The energy of elastic deformation (slipping) is equal to $E_{s1} = f_{p1} \sin \alpha_2$, where f_{p1} is the friction coefficient developed within the actual area of contact; α_2 is the angle of particle separation.

If the actual particle-to-surface contact area corresponds to

$$F_{p1} = \pi D \lambda_{p1} \eta_2$$

then the total area of contacting will be presented as

$$F_c = F_a + F_{p1} = m^1 F \{\eta_2 + [(m^1)^{-1} - 1]\eta_1\}$$

where m^1 is the coefficient specifying physical-mechanical properties of the component, the particle and of the latter's impingement velocity, $m^1 = \lambda_{p1}/\lambda$; η_1 is the relative area where the particle makes contact with the surface; η_2 is the relative area comprising penetration of irregularities region where the particle penetrates the surface involved.

Replacing in equation (2.28) the values of its components and dividing them by quantity E, we shall obtain the equation enabling the determination of the friction coefficient to be formed when the particle-to surface impingement takes place:

$$f_{fr}^1 = f_a(1 + K_y^2) \sin \alpha_1 + f_{s1} \qquad (2.30)$$

As noted previously, one of the factors defining the erosion developed is the movement velocity of a particle.

Let us consider the interaction between a solid particle of spherical shape with a steel surface (for instance, with the interaction velocity of 100 m/s). As a result an imprint is formed which has the radius and diameter similar to those of the particle. If the interaction velocity is increased to the level of 200 m/s, the impingement is accompanied with development of thermal effect

resulting in formation of a hollow, with its diameter and depth exceeding several times the diameter of the particle proper.

It is evident that the motion velocity of particles traveling within pumps does not correspond to the indicated value meaning. However, the energy of particles being pumped over is rather high, if we assume that the impeller circumferential velocity is 35 m/s. Some experts point out that the weight loss in specimens is nearly equal, no matter what steel is used to fabricate them, i.e. soft or hard, alloyed or plain, provided that they are subjected to erosion being developed by particles of quartz sand acting perpendicular to the surface affected. This indicates how significant is the factor related to the incidence angle size. Microscopic study of eroded surfaces reveals the presence of severely distorted surface layers when the latter are attacked at an angle closely similar to the normal one, whereas the same layers are less distorted by particles brought about at sharp impingement angles.

Consequently, the erosion develops as a result of deformations formed at angles similar to the normal angle and appears in the form of shearing when the incidence angle is small [2.3].

These two processes take place simultaneously and the deformation, in this respect, depends on both the incidence angle and quality of the material subjected to abrasive erosion.

Erosion caused by elastic deformation

The equation derived, when considering the impingement effect exerted by an elastic particle colliding with an elastic surface, enables to determine the maximum velocity, V_{max}, at which the interaction involved is maintained within the existing elastic limits.

When the particle velocity exceeds this maximum velocity, the energy excess ensures formation of plastic deformation.

The particles n with the total mass M, when interacting with the surface, at an angle α, transmit the energy to the surface, and the amount of this energy is calculated from:

$$E = 1/2M(V_{\sin\alpha} - V_{\max}) \tag{2.31}$$

With the energy e designated as the energy equaling the amount required to remove a volume unit of the material involved, the formula of erosion can be presented by the following equation:

$$J = \frac{1/2(V_{\sin a} - V_{\max})}{e} \tag{2.32}$$

Erosion caused by shearing

This type of erosion occurs at sharp incidence angles when the material possesses a certain degree of viscosity. The main parameters in this case are the velocity and the impingement angle.

The normal component of the particle velocity $VN = V_{sin\alpha}$ is beneficial for penetration of the particle into the material surface, whereas its tangential component, as related to the surface, i.e. $VT = V_{cos\alpha}$, contributes to formation of "chip" effect. If VN less than V_{max}, the solid body are subjected to deformation and the damage risk, in this respect, is by far reduced. When, however, VN exceeds V_{max}, plastic deformation is being formed, and the tangential component mentioned previously results in development of shifting distortion, which causes shearing-off. The energy needed for deformation and removal of the material is obtained at the cost of the kinetic energy possessed by particles.

With development of deformation the energy of the particle is reduced which results in decrease of the particle normal velocity and of the tangential component referred to the surface. If the energy is absorbed entirely, with the absence of the noted tangential component VT, this energy can be calculated from

$$E = \frac{1}{2}\frac{M}{n}VT^2 \tag{2.33}$$

The amount of the material sheared, with the interaction of particles n having the total mass M, and provided that σ is the energy required to remove a volume unit of the material, is calculated from the following equation:

$$W = \frac{1/2\, MVT^2}{\sigma} \tag{2.34}$$

The latest expression specifies the erosion phenomenon take place in pumps designed to pump over fluids containing abrasive particles.

When creating an analytical model referring to hydraulic abrasion process and methods aimed at improving erosion resistance of structural materials, as well as at substantial reduction of the erosion developed in hydro-mechanical installations, great importance is attached to an experimental study of models specifying the failure patterns observed within the material surface involved and to determination of the quantitative parameters required for proper selection of the desired design configurations.

In this respect, an analysis of the results obtained in a certain number of studies reveal that the erosion of plastic materials (carbon steels) varies considerably, depending on *the angle of the flow direction as related to the surface*, namely, it increases when angle α grows from 10 to 40 ~50°, with the subsequent drop when $\alpha > 60°$.

For material differing from carbon steels by their strain strength properties the relationship between the surface erosion and incidence angle has a different nature. For brittle materials (of solid alloys) the highest erosion rate is observed at incidence angles approaching the normal one. The erosion variation pattern observed with an aluminum alloy and depending on angle α is identical with that of carbon steel. The erosion of an elastic material (rubber) decreases promptly with increase of the incidence angle.

The analysis results obtained from a study of steel specimens demonstrate that the surface damage at $\alpha = 10°$ mainly occurs through shearing, being accompanied with formation of grooves, marks and scratches. It is quite possible, however, that micro volumes of material worn may be attributed to the erosion caused by plastic or repeated elastic deformations, which are specified by presence of distorted formations, on the surface under study, being of nearly symmetrical form. Emergence of this sort of erosion is associated with the impingement effect taking place between the abrasive particles involved, with bending of their motion paths and variation of other parameters prior to the impingement, as compared with motion parameter of a slurry-conveying flow.

Due to the action of normal component taking place at $\alpha = 25°$, the penetration force of a particle and, correspondingly, the width of grooves are somewhat increased, but the impingement-slip contacting, together with the erosion caused by shearing, basically prevail. The micro traces of penetrated particles are presented by grooves of prolonged shape oriented along the flow direction and exceeding by an order of magnitude the width and depth of traces formed by penetrated particles. There are traced on the surface, at $\alpha =$

25° as previously but with somewhat increased frequency, distorted formations of symmetrical shape.

As the angle between the abrasive particles and the surface being worn out increases up to 45°, the effect of impingement contacts, in combination with slipping, is observed more distinctly. At the time of an impingement-slipping contact there simultaneously arise both compressive strain and shearing tension in the surface layer, which are evidenced by a considerable number of hollows and banks of material displaced, per unit surface area; these hollows and banks of material are extended along the action of forces applied, as a result of the action effected by abrasive particles. The surface failure effected by shearing continues to proceed, however, the penetration of particles, at the initial stage of contacts made, develops more effectively due to a considerable increase of the interactive force component, i.e. the depth and width of grooves being developed exceed significantly, by their sizes, the corresponding sizes of micro erosions observed at $\alpha = 10°$, whereas the respective sizes of longitudinal orientation are preserved (or insufficiently altered). The strip area size being removed at singular impingements ensures a considerable rise in the amount of the material removed as a whole, when compared with the erosion amount observed at $\alpha = 10°$.

When the angle of interaction between the abrasive particles and the surface being worn is increased up to 65°, the surface of metal is basically subjected to direct erosion, with the traces of plastic deformation appearing more frequently. Within the elasticity distorted micro areas, when the surface is subjected to failure caused by low-concentration streams of hydro-mixtures, with the latter affecting this surface at high angles, the different stages in formation of erosion products and the adequate discreteness of the process developed are traced more distinctly.

When the hydro-mixture stream is oriented vertically ($\alpha = 90°$) the abrasive particles effect a direct impingement thus causing the deformation of adequate nature. The main cause of erosion in this case refers to plastic deformation. There arise here main sites of erosion presented on the surface in the form of hollows, dints and scaly metal surface layer.

The results obtained by experimental studies reveal that the main cause of the erosion, being developed under conditions of contacts made between the surface and fine-grain particles ($d \leq 0.25$ mm), attributes evidently to fatigue failure and shearing of the surface (at $\alpha = 10°$).

When the contacts are made with participation of larger particles (d = 0.7 ~ 1.0 mm), the signs of plastic deformation and failure are observed even at α = 45°.

With further increase of solid particle sizes there comes a moment when deformative aspects of failure start to develop intensively alongside with surface shearing. These erosion patterns develop more effectively at large angles of the stream direction, i.e. when the normal force component of the impingement attains its maximum value. On a low-carbon steel surface, for instance, worn out by a hydro-mixture flow containing large particles of quartz sand, it is traced rather distinctly.

Thus, the hydraulic abrasion of a steel surface, depending on the angle of the stream direction, develops exclusively due to impingement effect of particles, in accordance with a low-cycle polydeformative or brittle failure pattern, alongside with microshearing; it can also be caused by predominant or simultaneous development of corrosive and multi-cycle failure process, especially in those cases where the solid material used is specified by relatively low abrasive properties (for instance, when the abrasive action is caused by finest particles of a smoothed abrasive). The total erosion in this case is formed, as a rule, due to various simultaneously developed failure processes.

An analytical study of experimental data enables the definition of the quantitative parameters specifying percentage ratio of the erosion intensity observed at different impingement angles at which the hydro-mixture comes in contact with the surface of low-carbon steel.

Revealing of the formation nature and removal of the erosion micro volumes, as well as the latter's shapes and sizes for different structural materials, in relation with physical-mechanical properties and provided that the hydrodynamic flow parameters and contact conditions are preserved as equal, are of great interest.

The results of experimental studies demonstrate that an increase in material hardness, depending on the pattern and mechanism of failure, can influence the process development rate in a varied way, i.e. it can decelerate the process during the slip erosion, when emergence of local failure zones and separation of surface micro volumes are mainly associated with distortions cause by displacement and shear, or accelerate the same process during brittle flaking, when elasticity of the material is considerably reduced.

The studies carried out with various materials having different erosion mechanisms of steels and alloys, reveal one common and very important property, i.e. the zones of initial contacts made by abrasive particles with the surface, and the corresponding sizes of erosion traces are sufficiently small (ranging 0.5 to 40 μm). The erosion resistance of structural materials is governed by capability of separate micro structural components of the surface to resist the destructive deformations being developed. Therefore, in order to ensure high erosion resistance under the conditions of hydraulic abrasion process, it is advisable that the materials to be chosen should possess the polycrystalline structure specified by sufficiently thin microstructure of 1 μm.

Smoothness and variety of forms, as well as shape and orientation of protrusions in solid particles govern the terms of contact making and the level of kinetic energy loss during the impingement process; the difference in sizes and parameters of traces referred to the surface erosion has, in the final analysis, a considerable effect on the development intensity of hydraulic abrasion.

The accomplished analyses demonstrate as well the effect on erosion of materials caused by chemical and rheological properties of the conveying medium. An increase of density and viscosity in the conveying medium, due to a rise in concentration of fine particles above a certain level, results in a decrease of hydraulic abrasion rate as a whole. In this case, the corrosion of metal developed in the presence of abrasive hydro-mixture may be responsible for intensive local failure of certain areas within the equipment components.

It should be noted that the contact conditions formed when the solid particles interact with surfaces of the equipment components employed, are extremely diverse, i.e. there takes place a casual nature of changes observed within the hydrodynamic parameters of a hydro-mixture flow, the chemical and rheological properties of its conveying medium, as well as within the grain size, smoothness and orientation of micro protrusions specifying the abrasive used. This leads to variations observed within the strain energy amount consumed, to spread in the range of size limits referred to erosion formations being developed on the surface concerned and, as a result, the parameters of hydraulic abrasion process are varied as well.

The analytical studies, aimed at evaluation of the effect caused by the abrasive flow velocity and particle grain size on the process development nature, with the conditions and parameters of contact making maintained invariable, enable come to the conclusion that the hydraulic abrasion of

materials is characterized by certain energy barrier levels, and when these levels are exceeded by abrasive particles contained in a hydro-mixture, it results in qualitative changes within the process concerned.

Therefore, in working out the design models of hydraulic abrasion it is required to take into consideration the fact that the energy of contacting, made between the abrasive particles and surface, has a decisive effect on the mechanism and rate of the process being developed.

In accordance with the failure patterns observed, within different structural materials and with the specific energy of contacts being varied, there exists a number of critical energy levels, W_{cr}, and their quantities can be varied as well, within two or more orders of magnitude, due to the loading conditions used. In view of randomness specifying the parameters and conditions of interaction between the abrasive particles and surface, the analytical estimation of values W_{cr}, together with other parameters characterizing abrasive and erosion resistance properties of the materials engaged in contacting, creates certain obstacles, and this deprives of possibility to construct a comprehensive design methodology for describing a erosion process by using a theoretical analysis alone.

Based on the study results obtained, the relationship to be used for calculation of erosion, to be developed with the materials making contact with a hydroabrasive mixture, can be given, in a generalized form, by the following expression corresponding to the known energy conception associated with surface erosion:

$$\Delta m = \rho_m g \sum_{i=1}^{n} f_i N_i W_i / W k_i \tag{2.35}$$

To calculate value W_i there can be employed such parameters as traces of contacts made by abrasive particles on the surface being worn out, because the energy required for separation of erosion microvolumes is proportional, in accordance with the known assumptions, to the surface area of the erosion formations evolved, whereas the erosion process rate is proportional to the quantity of the material removed at every interaction of solid particles with surface.

An analysis of the experimental data obtained makes it possible to assert that the probability distribution of an unknown random variable ω is governed

by the normal distribution law and, consequently, the mathematical expectation of energy W_i imparted by the particles, with the loading conditions being varied, can be described by using the Gaussian distribution.

2.2 Prediction Model of Hydraulic Abrasion

2.2.1 Prediction Erosion Model Proposed by Finnie and Bitter

Bitter (1963) classified the mechanisms of erosion wear into two categories, i.e. those of cutting and deformation [2.4, 2.5]. When a particle hits the target surface with relatively small angle, i.e. when the collision is more tangential, the particle tends to scratch the surface and to remove a small amount of its material. This process is called "cutting wear". On the other hand, when the surface is exposed to repeated collisions with relatively large incident angle, it undergoes the fatigue rupture through so-called cold work and a small amount of the surface material is removed in the form of small fragments during a subsequent impact. This process is known as "deformation wear". Several proposals are found in the literature to express each of these processes. Of these, the following equations by Finnie (1972) [2.6] and Bitter (1963) [2.4, 2.5] are adopted to calculate the cutting and the deformation wear, respectively:

$$W_c = \begin{cases} \dfrac{\rho_m C_1 V_p^2}{K_2 \psi}\left[\sin 2\alpha - \dfrac{K_1}{C_2}\sin^2\alpha\right] & for\ \tan\alpha < \dfrac{C_2}{K_1} \\ \dfrac{\rho_m C_2 V_p^2}{K_2 \psi}\left[\dfrac{C_2}{K_1}\cos^2\alpha\right] & for\ \tan\alpha > \dfrac{C_2}{K_1} \end{cases} \tag{2.36}$$

$$W_D = \frac{\dfrac{1}{2}\rho_m (V_p \sin\alpha - K_3)}{C_3} \tag{2.37}$$

where

$$K_1 = 2\left(1+\frac{m_p d_p^2}{4I_p}\right)$$

$$K_2 = \left[\frac{40}{\pi^4}\rho_p\left(\frac{1-q_p^2}{E_p}+\frac{1-q_m^2}{E_m}\right)^{-4}\right]^{1/5}\left(V_p \sin\alpha\right)^{2/5}$$

$$K_3 = \frac{\pi^2}{2\sqrt{10}}(1.59Y)^{3/2}\left(\frac{1}{\rho_p}\right)^{1/2}\left[\frac{1-q_p^2}{E_p}+\frac{1-q_m^2}{E_m}\right]^2$$

$$E = \frac{4}{3}\left[\frac{1-q_p^2}{E_p}+\frac{1-q_m^2}{E_m}\right]$$

where W_C and W_D are the removed mass of target material due to cutting abrasion per single particle collision and that due to deformation abrasion per single particle collision, respectively. The cutting and the deformation wear generally occur simultaneous and they are often supposed to be independent of each other so that the total ambient of the eroded mass of target. W_T can be written as the simple sum of those two contributions. W_C, W_D and W_T have the dimension of [kg/kg]. Three empirical constants, C_1, C_2 and C_3 in which all subtle factors that affect the erosion process, such as the grain structures of both particle and target material or the shape of particles should be absorbed. The values of these constants obtained by the preliminary experiments were 0.15, 4 and 1.035×10^{11}. And E, E_p and E_m are the Young's module, in which the subscript m is refereed to the target material, p is to the particle. I_p is the moment of inertia of particle. m_p is the mass of particle. q is the Poisson's ratio. And V_p and α is the incident velocity and the angle of particle.

Takehiko Yokomine et al made the numerical simulation of erosion of gas-solid suspension flow in a pipe with a twisted-tape insert by using the prediction method recently [2.7]. The generated swirling motion of particles, however, will have the possibility of crucial erosion damage on the pipe wall and tape surface. In order to clarify the effect of gap width on the erosion and quantify the erosion damage in the gas-solid suspension swirling pipe flow with twisted-tape insert, numerical simulation of erosion was performed by

using Eulerian/Lagrangian approach and two-way coupling method. When the gap is small, the belt-shaped highly concentrated region of particles is formed near the pipe wall and causes the crucial erosion damage like ditch on the pipe wall. If the gap is large, the erosion damage can be decreased and the uniform distribution of particles near the pipe wall is realized. The latter effect is advantageous to the use of increased heat capacity by adding particles.

P. Drtina and M. Krause (1994) [2.8] also applied the method developed by Finnie (1972) for ductile materials to predict the abrasion of the guide vanes of a hydraulic turbine. The abrasion rate, ER, is defined as the mass of material removed to the mass of particle in the carrier fluid, that is,

$$ER = p_n \rho_m / S_w \tag{2.38}$$

where S_w is the weight of sands in a unit volume, ρ_m is the material density of metal, and p_n is the penetration rate to be estimated. Basically the abrasion rate, ER, depends on the kinetic energy of impinging particle and its incidence angle α:

$$ER = KV_p^n f(\alpha) \tag{2.39}$$

with

$$f(\alpha) = \frac{1}{3}\sin^2 \alpha \qquad 0 < \alpha < 0.4\pi$$

$$f(\alpha) = \sin 2\alpha - 3\cos^2 \alpha \qquad 0.4\pi < \alpha < 0.5\pi$$

where n has been set to 2. It has to be kept in mind that for a given mass of abrasion particles impinging on a surface the totally removed material calculated via the foregoing equation will be independent of the particle size. Finnie pointed out that this is true only for particles with diameters exceeding 100 μm. Below this value abrasion becomes less effective with decreasing particle size.

In order to verify the model and the computation method of silt abrasion in hydraulic turbines, the test results of the hydraulic abrasion through guide vanes in a model hydraulic turbine by P. Dritina and M. Krause (1994) [2.8]

are selected to be compared with the present prediction by Yulin Wu. And the silt condition and the flow condition through the vane are as follows:

Particle size	$d_p = 0.060$ mm
Vane orientation	$\beta = 59^\circ$
Inlet angle	$\gamma = 29^\circ$
Turbulence intensity	5%
Inflow velocity	16.3 m/s

The three dimensional computation of silt-laden two-phase flow through the guide vanes was carried out by using two-fluid model proposed in Chapter 3. Figure 2.1 to Figure 2.3 show the flow calculation results and the silt abrasion prediction results. Among them, Figure 2.1 (a) and (b) show the pressure distribution through the vane passage at the three-dimensional domain. Figure 2.2 (a) and (b) show the velocity distributions bother for the liquid flow (Figure 2.2 (a)) and for the particle phase flow (Figure 2.2 (b)) on the middle plane through the vane passage. Figure 2.3 is the silt abrasion rate on the vane surfaces as the three-dimensional predicted results in the present work. And Figure 2.4 (a) and (b) are the predicted silt abrasion depth on the pressure and suction surfaces of the vane. The same depth and the field-tested results by P. Dritina and M. Krause (1994) are shown in reference [2.8]. The same depth as those in Figure 2.4, as the field tested results by P. Dritina and M. Krause (1994) are shown in Figure 2.5 (a) and (b). From the comparison between the results, it is clear that the present computation for prediction of silt abrasion is reasonable.

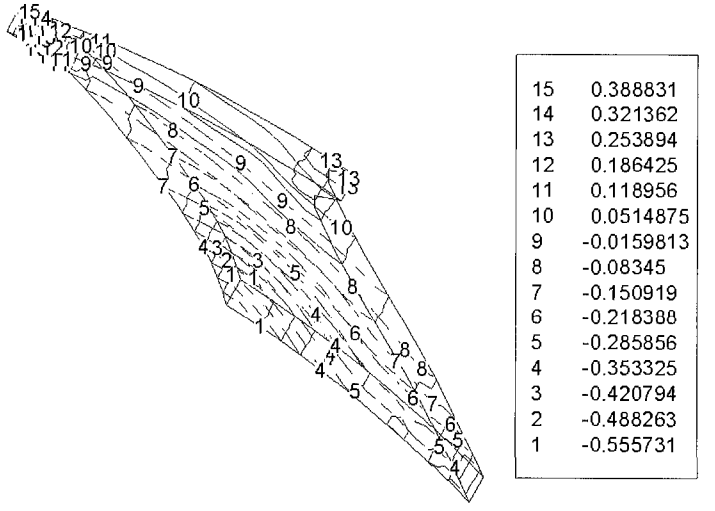

(a) At the three-dimensional domain

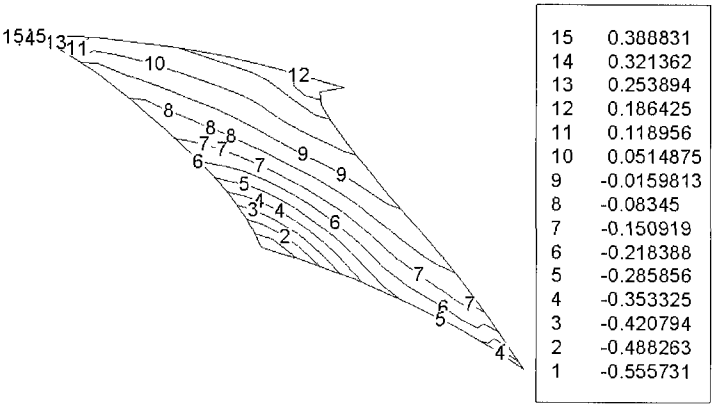

(b) On the middle plane of the domain

Figure 2.1 Pressure distribution through the vane passage

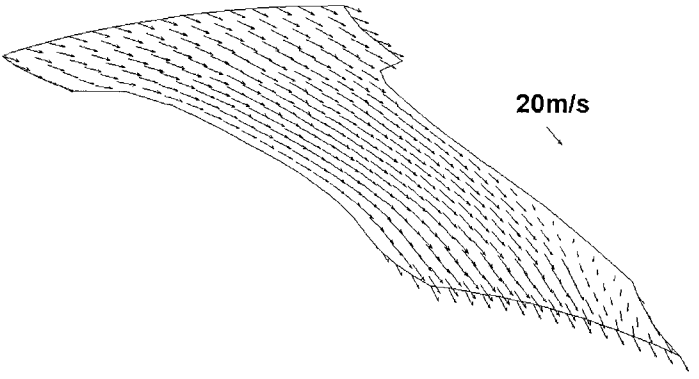

(a1) Liquid phase on the middle plane

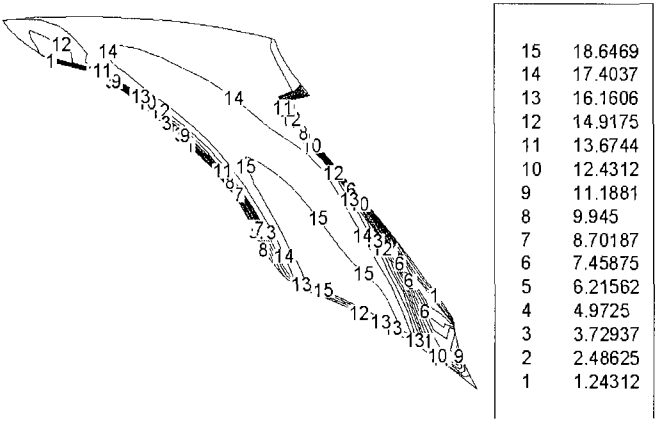

(a2) Liquid phase (isoline) on the middle plane

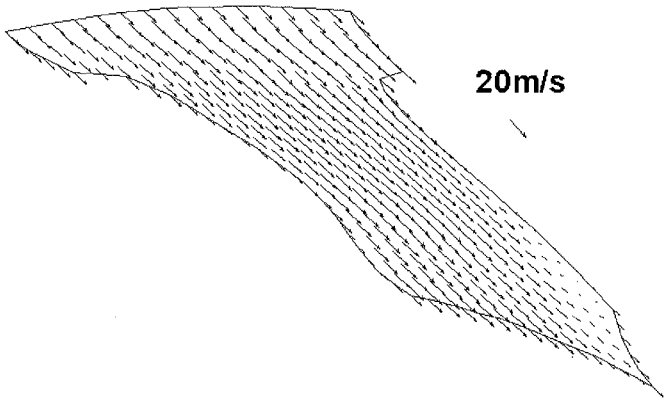

(b1) Particle phase on the middle plane

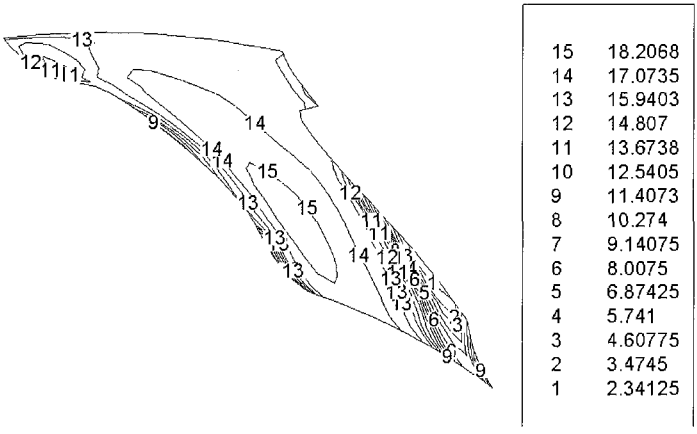

(b2) Particle phase (isoline) on the middle plane

Figure 2.2 Velocity distributions through the vane passage

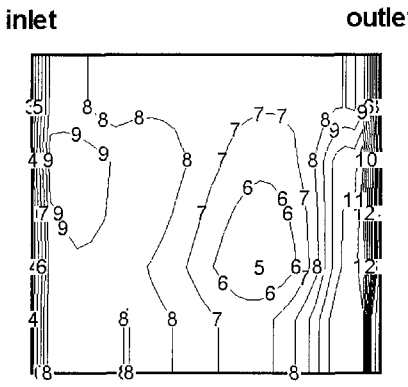

level	Er
13	7.93518E-09
12	7.32479E-09
11	6.71439E-09
10	6.10399E-09
9	5.49359E-09
8	4.88319E-09
7	4.27279E-09
6	3.66239E-09
5	3.05199E-09
4	2.4416E-09
3	1.8312E-09
2	1.2208E-09
1	6.10399E-10

(a) Abrasion on suction side

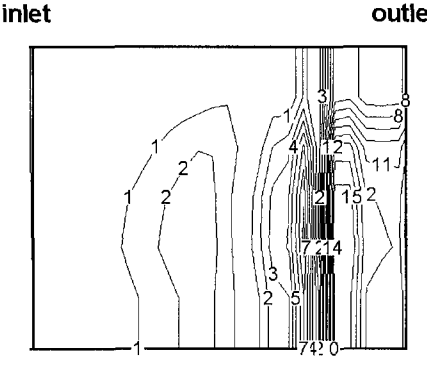

level	Er
15	9.15621E-09
14	8.54603E-09
13	7.93586E-09
12	7.32569E-09
11	6.71551E-09
10	6.10534E-09
9	5.49516E-09
8	4.88499E-09
7	4.27482E-09
6	3.66464E-09
5	3.05447E-09
4	2.4443E-09
3	1.83412E-09
2	1.22395E-09
1	6.13776E-10

(b) Abrasion on pressure side

Figure 2.3 Abrasion rate on the vane surfaces

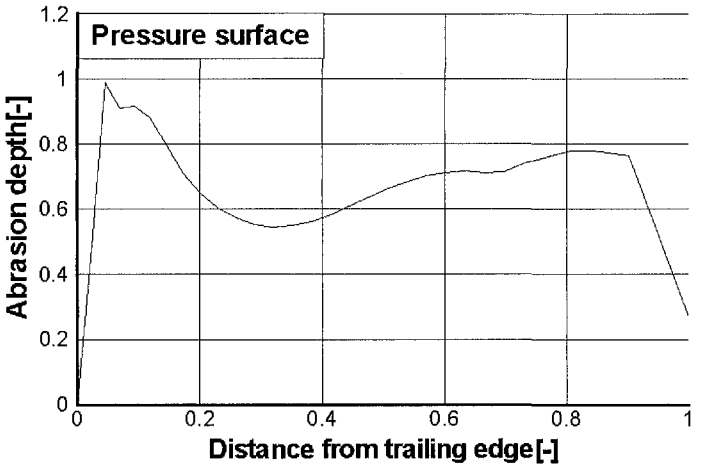

(a) On pressure surface

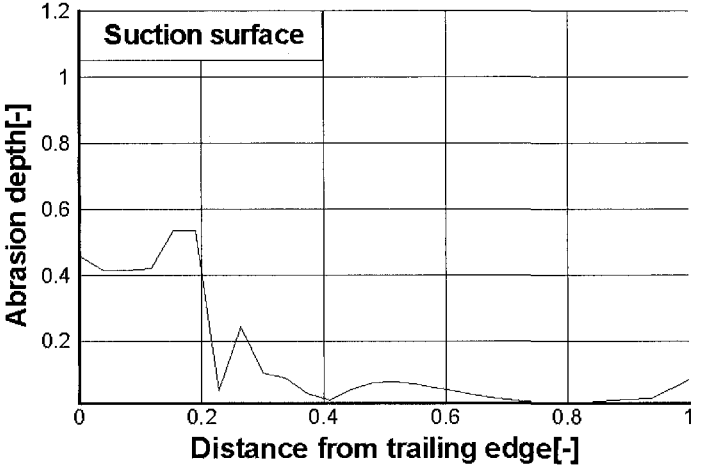

(b) On suction surface

Figure 2.4 Predicted results of guide vane silt abrasion

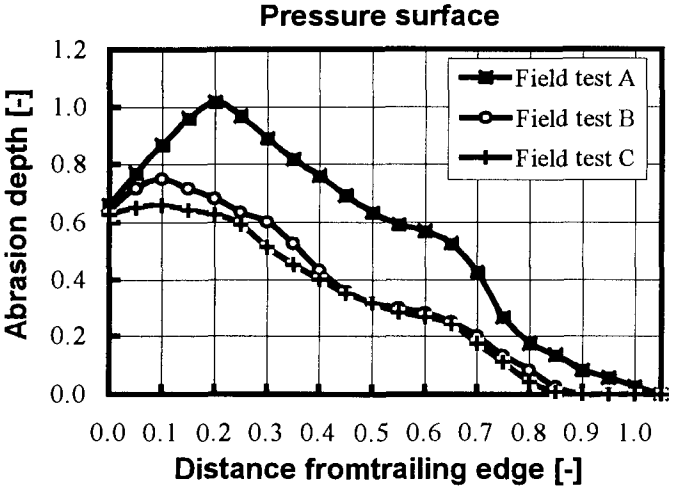

(a) On pressure surface

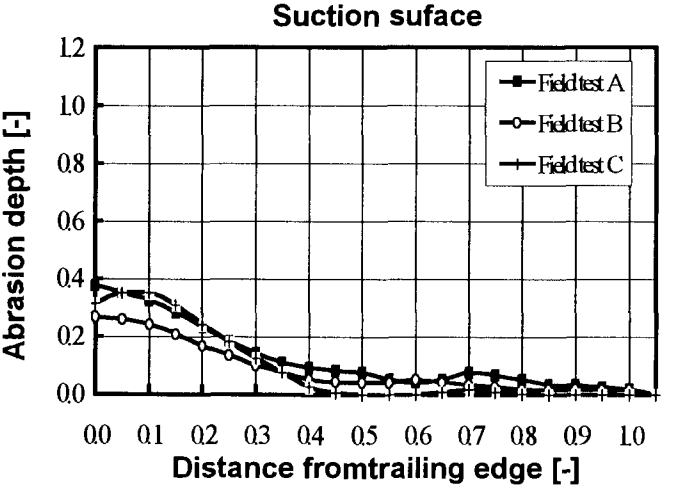

(b) On suction surface

Figure 2.5 Tested results of guide vane silt abrasion

2.2.2 Mechanistic Model Developed by The Erosion/Corrosion Research Center

In an effort to provide an erosion model that was applicable for a broad range of production situation, a mechanistic model for abrasion was developed by The Erosion/Corrosion Research Center, the University of Tulsa. The mechanistic model accounts for flow velocity, fluid viscosity and density, sand size and density as well as shape, pipe size and material, and flowing geometry. Another mechanistic model is being created that will include the abrasion due to random impingement.

To compute the abrasion ratio, a semi-empirical relation for sand erosion is used as follows (Ahlert 1994) [2.8]:

$$ER = A V_p^{1.73} f(\beta_1) \tag{2.40}$$

where B is the Brinell Hardness number of the target material, and $f(\beta_1)$ is the angle function, β_1 is the angle between the impinging velocity of particle to wall and the tangential of the wall, and $A = 1.95 \times 10^{-5}$. $f(\beta_1)$ is defined as:

$$f(\beta_1) = [a\beta_1^2 + b\beta_1]_{0^o}^{\delta^o} + [X\cos^2\beta_1 \sin(w\beta_1) + Y\sin^2\beta_1 + Z]_{\delta^o}^{90^o}$$

The constants a, b, X, Y and Z have different values for dry and wet surfaces. These values were given by Ahlert (1994) [2.8] as follows:

Table 2.1 Empirical constants for abrasion

Material	Carbon steel	Aluminum
A	$1.95\times10^{-5} \times B^{-0.59}$	2.388×10^{-7}
δ	15	10
a	-3.84×10^{-8}	-34.79
b	2.27×10^{-8}	12.3
w	1.0	5.205
X	3.147×10^{-9}	0.147
Y	3.609×10^{-10}	-0.745
Z	2.532×10^{-9}	1.0

This abrasion model is used to predict the silt erosion on the blade surface of hydraulic machinery in the present work by Yulin Wu. In most of other predictions of erosion, the Eulerian-Lagrangian method is used to calculate the particle trajectories and velocities. But in the present work, the Eulerian-Eulerian method of two-fluid model for silt-laden flow in hydraulic turbines proposed in Chapter 3 is used and the second type of boundary conditions for particle flow velocities is applied. The parameters of the Francis turbine are as follows:

Hydraulic runner diameter $D1$ = 2180 mm

Number of runner blades N = 17

Rotating speed of runner n = 450 rpm

Discharge of calculation condition Q = 23.08 m^3/s

Flow angle at the leading edge of blade $\beta_l = 30°$

Sand characters of silt phase in silt-laden flow through the runner

Sand diameter d_p = 0.1 mm

Sand density ρ_p = 2300 kg/m^3

Silt-phase volumetric concentration Cv = 0.032%.

The calculated results of the present computation show the relative velocity distributions of liquid phase in Figure 2.6 and the velocity distributions of silt phase in Figure 2.7.

There is a difference between relative velocities of water phase and silt phase. Near the inlet of runner the two phase's velocities only have a little difference. On the following areas of runner the particle velocity is smaller than the water velocity fore large inertia of sands. At the exit of runner, the velocity of sands increases and has the nearly same value as the water velocity. Figure 2.8 shows the erosion rate of silt to surfaces of this runner by using the prediction model. The prediction depth of erosion from the results in the present computation has indicated the agreement with the date of prototype turbine observation in Japan.

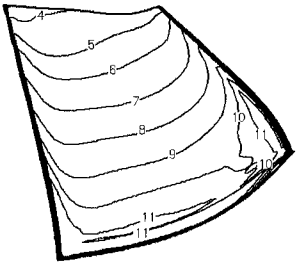

(a) On suction surface

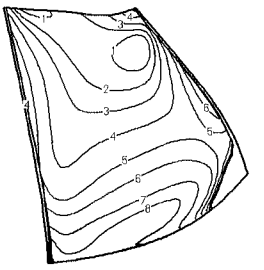

(b) On middle surface

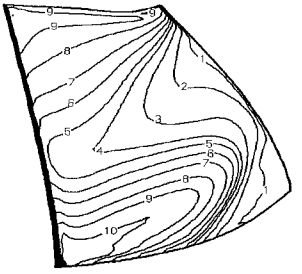

(c) On pressure surface

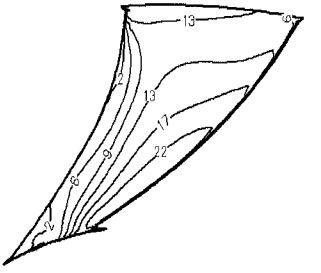

(d) On crown surface

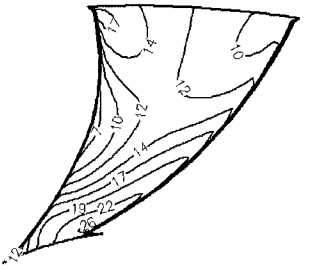

(e) On middle surface

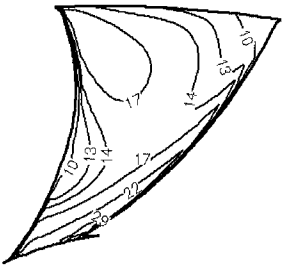

(f) On band surface

Figure 2.6 Relative velocity distribution of water phase through turbine runner (Velocity unit: m/s)

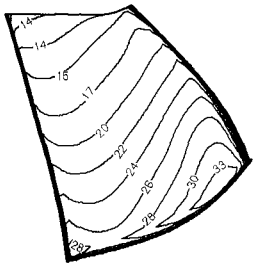

(a) On suction surface

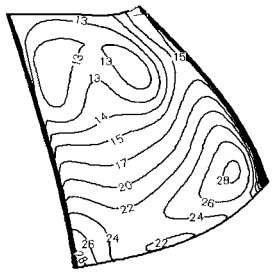

(b) On middle surface

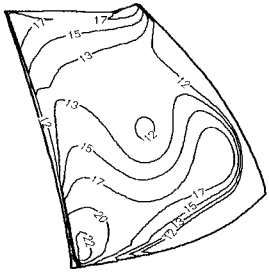

(c) On pressure surface

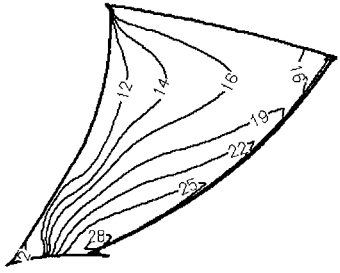

(d) On crown surface

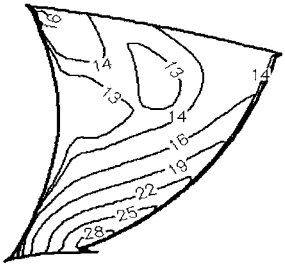

(e) On middle surface

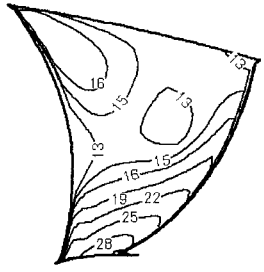

(f) On band surface

Figure 2.7 Relative velocity distribution of silt phase through turbine runner (Velocity unit: m/s)

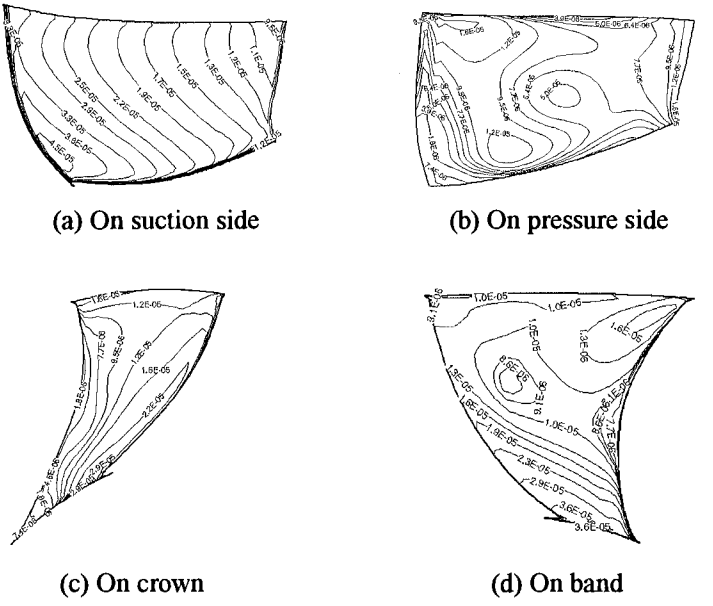

(a) On suction side (b) On pressure side

(c) On crown (d) On band

Figure 2.8 Prediction of erosion rate of silt on surfaces of hydraulic runner

2.2.3 Prediction Erosion Model Proposed by McLaury et al

McLaury et al. (1996) [2.10, 2.11] presented several models for the computation of solid particle erosion. The model equations vary depending upon the type of material being used. These models are based on direct impingement tests at various angles and impingement velocities. These erosion models consist of the following equations, where *ER* is the erosion ratio (kg/kg). The erosion ratio is defined as the amount of mass lost by the pipe wall divided by the mass of particles that cause the erosion. Other variables involved are the particle impingement angle θ (radians), the pipe material Brinell hardness factor B, and the particle impingement velocity V (m/s). Erosion equations have been developed for two materials: carbon steel and aluminum based on existing data in the literature and taken at The University of Tulsa [2.9]. Slight modifications to the carbon steel erosion model are required for the analysis of other steel alloys (e.g., stainless).

For carbon steel:

$$ER = \left[\frac{1559}{B^{0.59}}\left(\frac{V}{0.3048}\right)^{1.73} f(\theta)\right] \times 10^{-9} \tag{2.41}$$

where, for $\theta < 15°$

$$f(\theta) = 2.27\theta - 3.84\theta^2$$

for $\theta > 15°$

$$f(\theta) = 3.147\cos^2\theta\sin\theta + 0.3609\sin^2\theta + 2.532$$

For aluminum:

$$ER = (2.388 \times 10^{-7})\left(\frac{V}{0.3048}\right)^{1.73} f(\theta) \tag{2.42}$$

where, for $\theta < 10°$

$$f(\theta) = 12.3\theta - 34.79\theta^2$$

for $\theta > 10°$

$$f(\theta) = 1 + 0.147\cos^2\theta\sin(5.205\theta) - 0.745\sin\theta$$

The benchmark case for the erosion prediction method is the aluminum choke geometry presented by McLaury *et al.* (1992) [2.10]. This geometry consists of a sudden contraction, followed by a short straight throat section, and a sudden expansion. This geometry was used to verify the integrity of the erosion model by Jeremy K. Edwards et al [2.12] as shown in Figures 2.9.

In the erosion prediction procedure, the diffuser section (downstream of the sudden expansion) is sliced into "wafers" that are equally spaced along the pipe axis. The thickness of each wafer is Δx. Assuming that the mass lost by the pipe is distributed evenly around the circumference of the pipe wall, and

that the reduction in wall thickness due to erosion is much less than the inside pipe radius, the penetration rate P is given by:

$$P = \frac{m_w}{\pi \rho_w d \Delta x}(3.1536 \times 10^{10}) \tag{2.43}$$

where m_w is the pipe wall material mass loss rate (kg/s), ρ_w is the pipe wall material density (kg/m^3), and d is the pipe diameter (m) at the impact location. Eq. (2.43) gives the penetration rate in millimeters per year (mm/yr) if the prescribed units are used. Multiplying the result by 39.37 mil/mm converts the penetration rate to mils per year (mpy).

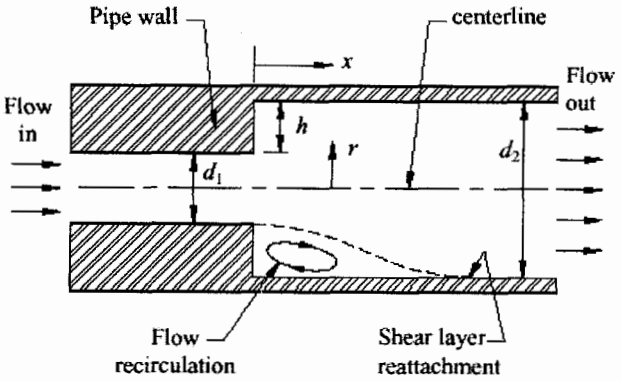

Figure 2.9 Sudden pipe expansion geometry

Results of the three-dimensional flow model were in close agreement with the experimental results of Stieglmeier et al (1989) [2.13]. Input data for the prediction erosion studied is as follows:

Inlet pipe diameter 6.5 mm
Outlet (diffuser) pipe diameter 15.9 mm
Inlet fluid velocity (centerline) 19.82 m/s
Inlet reynolds number 128,830
Entrance length (small diameter) 65 mm

Diffuser length (large diameter) 240 mm
Sand diameter 150 μm

Figure 2.10 (a) shows the variation of penetration rate with axial distance downstream of the expansion for both the experimental data and the erosion prediction up to 8 step heights downstream of the expansion. The erosion was computed based on a wafer thickness Δx = 5 mm. The point x/h = 0 corresponds to the location of the expansion. The erosion profile shows good agreement in both trend and magnitude with the experimental data for the steady state penetration rate. Even though experimental data is only available up to 8 step heights downstream of the expansion, the simulation was performed up to 30 step heights downstream.

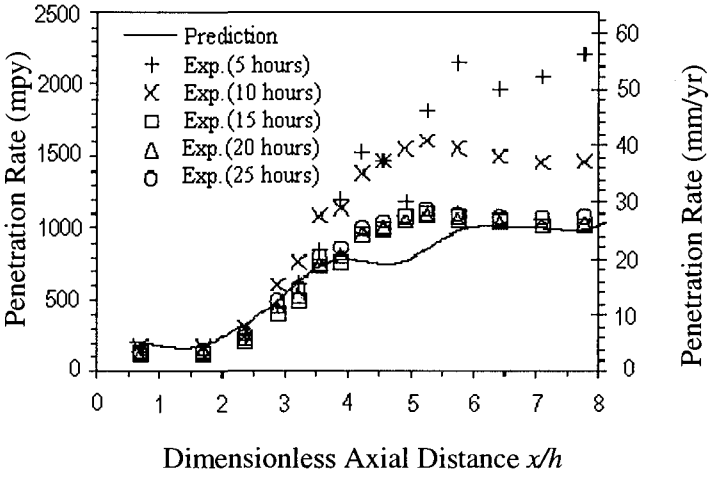

Figure 2.10 (a) Erosion profile in choke geometry

The erosion predictions for the entire simulated range are shown in Figure 2.10 (b). These results show a maximum penetration rate at approximately 13 step heights downstream of the expansion. The reattachment location for this case was determined to be approximately 10.5 step heights from the expansion. This indicates that the maximum penetration rate for this case occurs slightly downstream from the reattachment location. Further experimental investigation is required to verify the predicted results.

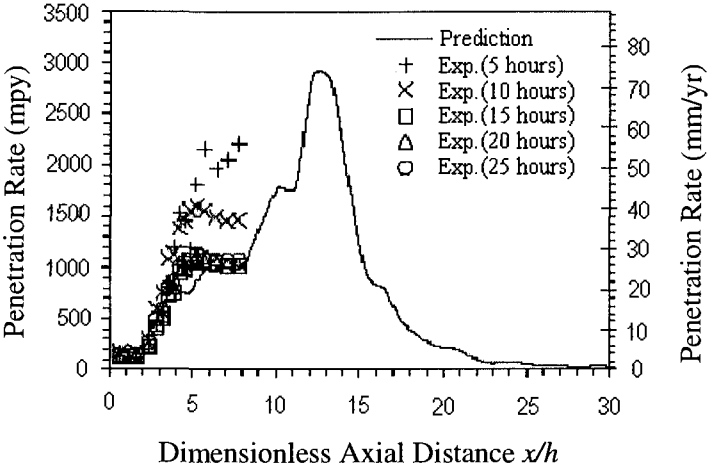

Figure 2.10 (b) Erosion profile in choke geometry

References

2. 1 Karelin V.Ya, (1983). 'Silt Abrasion of Turbo-pumps', Machinery Engineering Press, Moscow (in Russian).

2. 2 Elkholy A., (1983). 'Prediction of abrasion erosion for slurry pump materials'. *Erosion*, Vol. 84, No. 1.

2. 3 Graber P., (1983). 'Solids Handling Pumps'. *World Pumps*, No. 197.

2. 4 Bitter, J. G. A., (1963). 'A study of erosion phenomena (Part I)', *Wear*, Vol.6, 5.

2. 5 Bitter, J. G. A., (1963). 'A study of erosion phenomena (Part II)', *Wear,* Vol. 6, 169.

2. 6 Finnie, I., (1972). 'Some observations on the erosion of ductile metals', *Wear,* Vol.19, 81.

2. 7 Takehiko Yokomine, et al, (1997). 'Numerical simulation of erosion of gas-solid suspension flow in a pipe with a twisted-tape insert', *ASME Fluids Engineering Division Summer Meeting,* June 22~26, 1997, FEDSM97-3638.

2. 8 Drtina P. and Krause M., 'Abrasion on a Francis turbine guide vaneNumerical simulation and field tsts-', *Procs. of IAHR 1994,* Beijing, 713~724.

2. 9 Ahlert, K., (1994). 'Effects of Particle Impingement Angle and Surface Wetting on Solid Particle Erosion of AISI 1018 Steel', *M.S. Thesis*, The University of Tulsa.

2. 10 McLaury, B.S., (1996). 'Prediction of Solid Particle Erosion Resulting From Turbulent Fluctuations in Oilfield Geometries', *Ph.D. Thesis*, The University of Tulsa.

2. 11 McLaury, B.S., Shirazi, S.A., Shadley, J., and Rybicki, E., (1996,). 'Modeling Erosion in Chokes', *ASME FED* Vol. 236, San Diego, CA, pp. 773-781.

2. 12 Edwards, J.K., McLaury, B.S., and Shirazi S.A., (1998). 'Sopplemeting a CFD Code with Erosion Prediction Capabilities',

ASME Fluids Engineering Summer Meeting, June 21~25, 1998, Washington, DC, FEDSM98-5229

2. 13 Stieglmeier, M., Tropea, C., Weiser, N. and Nitsche, W., (1989). 'Experimental Investigation of Turbulent Flow through Axisymmetric Expansions', *ASME Journal of Fluids Engineering*, Vol. 111, pp. 464~471.

Chapter 3

Analysis and Numerical Simulation of Liquid-Solid Two-Phase Flow

Y. L. Wu

3.1 Basic Equations of Liquid-Solid Two-Phase Flow through Hydraulic Machinery

3.1.1 Introduction

Several theoretical and experimental techniques for investigation of multiphase flow are available. Basically, there are two fundamental theories for two-phase flow, namely, the macroscopic continuum mechanics theory and the microscopic kinetic theory. Marble (1963) [3.1] was one of pioneer researchers to describe basic equations of two-phase flow. From the sixties to seventies, general governing equations of two phase flow for the two fluid model and the mixture model based on the continuum mechanics theory were set up by Drew (1971) [3.2], Ishii (1975) [3.3] and others by using different average methods. In the mixture model, it is assumed that there exists only one type of mixture in fluid-dispersed flow, and that the whole flow space is full of the mixture. The mixture flow is described by using a set of unique characters. Roco & Reinhart (1980) [3.4] applied this model to calculate the liquid-particle mixture flow through centrifugal pump impellers.

In the two-fluid model, the dispersed phase is treated as a pseudo-fluid. In the Eulerian approach, the flow of the dispersed phase is described by conservation equations of mass, momentum and energy in continuum mechanics. In this model, there exists the slip of parameters between the carrier fluid and the dispersed phase. Based on the two-fluid model, increasing interest in the prediction of turbulent multi-phase flow has been noticed during the last twenty years, such as Danon et al (1974) [3.5], Al Taweel & Landau (1977) [3.6], Genchiev & Karpuzov (1980) [3.7], Melville et al (1979) [3.8], Sharma & Crowe (1978) [3.9], Michaelides & Farmer (1984) [3.10] and Shuen et al (1983) [3.11]. Danon et al (1974) tried to develop the one-equation turbulence model by adding a length scale determined experimentally to the turbulent kinetic energy equation for calculating two-phase round jet-turbulent-flow. Al Taweel & Landau (1977) deduced an energy spectrum equation at the transient frequency band, adding a supplement dissipation term to consider appearance of the dispersed phase. Calculated results show that the increase of volumetric density of the dispersed phase causes the turbulence intensity at the high frequency band decrease. Genchiev & Karpuzov (1980) proposed that a sink term has to be added to the single phase turbulent kinetic energy k equation to simulate the influence of the disperse phase. These authors applied the two-equation turbulence model to calculate two-phase turbulent flow. Two-equation turbulence models also have been proposed for dilute fluid-particle flow by Elghobashi & Abou-Arab (1983) [3.12] and Crowder et al (1984) [3.13]. Algebraic and one equation turbulence models have been suggested for the dense liquid-solid interaction by Roco & Shook (1983) [3.14]. Bertodano et al (1990) [3.15] applied the two-fluid model combined with the Reynolds stress turbulence model to analyze water-bubble flow. L.X. Zhou (1994) [3.16] suggested the $k - \varepsilon - k_p$ gas-particulate two-phase turbulence model (and other models) to calculate the gas-dispersed flow. Most of existing models are suitable only for relatively dilute mixtures, in which the particle-particle collision effect and the fluctuation energy interaction between the liquid and the particulate phases are negligible. During the last decade, there has been an interesting development in modeling dense solid-liquid flow, as shown, in references of Ma & Roco (1988) [3.17], Ahmadi & Abu-Zaid (1990) [3.18] and Gidaspow et al (1991) [3.19]. As mentioned above, Roco & Shook (1983) applied the macroscopic continuum theory and the one-equation turbulence model with double averaging to calculate dense liquid-particle flow. A probabilistic

microscopic model for solving shear motion of spherical particles dominated by friction and lubrication force was proposed by Ma & Roco (1988) to slow granular flow and high dense coal slurry. Gidaspow et al (1991) have developed a computer code that solves a generalization of N-S equations for multiphase flow. Particulate phase viscosity and pressure were derived by using the mathematical techniques of the dense gas kinetic theory.

3.1.2 General Concepts of Multiphase Flow

Basic Parameters of Multiphase Flow

The flow pattern of multiphase flow can be determined by the relations of following characteristic times:

(1) The flow characteristic time t_f:

$$\tau_f = L / v_r$$

where L is the character length of the flow domain and v_r is the reference velocity of the flow.

(2) The particle response time t_r, which is the measure of the dynamic response of particles.

$$\tau_r = \frac{d_p^2 \bar{\rho}_p}{18\mu}$$

where d_p is the particle diameter, $\bar{\rho}_p$ is the particle material density, and μ is the fluid viscosity. The subscript p indicates the particle phase.

(3) The mean particle response time t_{rl}:

$$\tau_{rl} = \tau_r (1 + R_{ep}^{2/3} / 6)^{-1}$$

where R_{ep} is particle Reynolds number $R_{ep} = |\vec{u} - \vec{u}_p| \frac{d_p}{\nu}$.

(4) The fluctuation time τ_T of fluid flow:

$$\tau_T = \frac{l}{u'} = \frac{k}{\varepsilon}$$

where l is the fluid turbulence length, and u' is the fluctuation velocity of the flow. And k is the turbulent kinetic energy of the flow and ε is the turbulent energy dispassion rate.

(5) The particle collision time t_p

$$\tau_p = \frac{l_p}{u'_p}$$

which is like t_T, is expressed by using the particle characters.

The flow patterns of multiphase flow can be determined according to the relation between the foregoing characteristic measures in the following extreme conditions.

If $\tau_{rl}/\tau_f << 1$ Non-slip flow (equilibrium flow)

If $\tau_{rl}/\tau_f >> 1$ Strong-slip flow (frozen flow)

If $\tau_r/\tau_T >> 1$ Diffusive-frozen flow (ignoring particle turbulent diffusion)

If $\tau_r/\tau_T << 1$ Diffusive-equilibrium flow (particle turbulent diffusion is comparative with that of liquid flow)

If $\tau_{rl}/\tau_p << 1$ (that is, the stokes number $S_t = \frac{\tau_{rl}}{\tau_p} << 1$) Dilute suspending flow

If $\tau_{rl}/\tau_p >> 1$ Dense suspending flow

And the stokes number τ_{rl} / τ_p is proportional to the $(\frac{u'_p d_p}{\nu} C)$. C_v is the particle volume fraction.

Density and Volume Fraction

Relations between deferent density determinations of multiphase flow are as follows:

$$\rho_m = \rho_f + \rho_p = \rho_f + \sum \rho_k = \rho_f + \sum n_k m_k = \rho_f + \overline{\rho}_p \sum n_k \frac{\pi d_k^3}{6}$$

where ρ_m is the density of mixture, ρ_f is the fluid bulk density, ρ_k, ρ_p are the particle bulk densities, and $\overline{\rho}_p$ is the particle material density. And n_k is the particle number in the unit volume.

The volume fractions of the fluid phase C_f and the particle phase C_p are defined as:

$$C_p = \rho_p / \overline{\rho}_p$$

$$C_f = \rho_f / \overline{\rho}_f = 1 - C_p = 1 - \rho_p / \overline{\rho}_p$$

For dilute two phase flow:

$$\rho_f = \overline{\rho}_f (1 - \rho_p / \overline{\rho}_p) \approx \rho_f$$

The mass loading is defined as $\rho_{p0} u_{p0} / \rho_{f0} u_{f0}$, where the subscript "0" is the values at the entrance condition.

Volumetric Averaging of Multiphase Flow

A control volume has the surface dA, where there are several types (phases) of particles. For each phase, the occupying volume is dv_k with surface area dA_k. Then the local volumetric fraction of kth phase particle can be expressed as:

$$C_k = dv_k / dv \tag{3.1}$$

where the relation between the length of the control volume l, flow system character length L and the particle diameter are as follows:

$$d_k << l << L \tag{3.2}$$

Then multiphase flow can be described by the Euler system of a multi-fluids model, in which the suspending particle phases are assumed to be a pseudo fluid and are also described by the fluid flow control equation. When describing the multiphase flow, the volumetric averaging method must be used at the control volume. If the mark "~" is applied to expressed the microscopic real value of a physical variable φ in a phase, that is $\widetilde{\varphi}_k$ (the subscript "k" represents k th phase), and the notation "< >" represents the volume averaging process in a control volume dv. The volume averaging value of $\widetilde{\varphi}_k$ is regarded as φ_k in the following forms:

$$\varphi_k = \langle \widetilde{\varphi}_k \rangle = \frac{1}{dv} \int_{dv_k} \widetilde{\varphi}_k \, d\widetilde{v} \tag{3.3}$$

and $$dv = \sum dv_k \quad (k=1, 2, 3,.....f).$$

where $k = 1, 2, 3,...f$, is the case of multi-phase flow containing f phases.

For example, the bulk density of kth phase ρ_k is the mass of this phase material in per unit volume of the mixture, that is:

$$\rho_k = \langle \widetilde{\rho}_k \rangle = \frac{1}{dv} \int_{dv_k} \overline{\rho} \cdot dv_k \tag{3.4}$$

also

$$\rho_k = \frac{dv_k}{dv} \frac{1}{dv_k} \int_{dv_k} \overline{\rho} \cdot dv_k = C_k \overline{\rho}_k$$

where $\overline{\rho}_k$ is the material density of this phase.

3.1.3 Basic Equations of Multiphase Flow

Microscopic Conservative Equations for Each Phase

Basic conservative equations of single-phase continual material on the continuum mechanics are now applied to kth phase in its control volume dv_k. Then basic conservative equations of the kth phase in the instantaneous form are obtained as follows:

(1) Continuity equation:

$$\frac{\partial \widetilde{\rho}_k}{\partial t} + \frac{\widetilde{\partial}}{\partial x_j}(\widetilde{\rho}_k \widetilde{u}_{kj}) = 0 \tag{3.5}$$

(2) Momentum equations:

$$\frac{\partial}{\partial t}(\widetilde{\rho}_k \widetilde{u}_{ki}) + \frac{\widetilde{\partial}}{dx_j}(\widetilde{\rho}_k \widetilde{u}_{kj} \widetilde{u}_{ki}) = -\frac{\partial \widetilde{p}_k}{\partial x_i} + \frac{\widetilde{\partial}}{\partial x_j}(\widetilde{\tau}_{k.ji}) + \widetilde{\rho}_k g_i \tag{3.6}$$

(3) Energy equations:

$$\frac{\partial}{\partial t}(\widetilde{\rho}_k \widetilde{C}_k \widetilde{T}_k) + \frac{\widetilde{\partial}}{\partial x_j}(\widetilde{\rho}_k \widetilde{u}_{kj} C_k \widetilde{T}_k) = \frac{\widetilde{\partial}}{\partial x_j}(\lambda_k \frac{\widetilde{\partial} \widetilde{T}_k}{\partial x_j}) + \widetilde{q}_c - \widetilde{q}_r \tag{3.7}$$

(4) Component equations

$$\frac{\partial}{\partial t}(\widetilde{\rho}_k \widetilde{Y}_{ki}) + \frac{\widetilde{\partial}}{\partial x_j}(\widetilde{\rho}_k \widetilde{u}_{kj} \widetilde{Y}_{ki}) = \frac{\widetilde{\partial}}{\partial x_j}(D_\rho \frac{\widetilde{\partial} \widetilde{Y}_{ki}}{\partial x_j}) - \widetilde{\omega}_{ks} \tag{3.8}$$

where, u is velocity, p is pressure, t is stress, g is volumetric force acting on the unit volume of fluid, C is specific heat, T is temperature, λ is thermal conductivity, q_e is radiation heat, q_r is reactive heat, Y_{ki} is mass fraction of ith

component in kth phase, ω_{ks} is chemical reactive rate of kth phase, and D_ρ is the material conductivity of kth phase.

Volumetrically Averaged Basic Equation of Two-Phase Laminar Flow

The volume averaging method, defined as foregoing, is applied to derive out the volumetric averaged basic equation of two-phase laminar flow, which are comparative to N-S equation in single-phase laminar flow.

The averaged value of differential of instantaneous variable $\tilde{\varphi}$ is in the following forms.

$$\left\langle \frac{\tilde{\partial}\tilde{\varphi}_k}{\partial x_i} \right\rangle = \frac{\partial \langle \tilde{\varphi}_k \rangle}{\partial x_i} + \frac{1}{dv}\int_{dA_k} \tilde{\varphi}_k n_{ki} d\tilde{A}$$
$$\left\langle \frac{\tilde{\partial}\tilde{\varphi}_{ki}}{\partial x_j} \right\rangle = \frac{\partial \langle \tilde{\varphi}_{ki} \rangle}{\partial x_j} + \frac{1}{dv}\int_{dA_k} \tilde{\varphi}_{ki} n_{kj} d\tilde{A} \tag{3.9}$$

where $\tilde{u}_s$ is the displacement velocity of interfaces; n_{ki} is the unit vector of outward normal on interface of kth phase.

By using equation (3.9) the volumetric averaged basic equation of kth phase laminar flow can be obtained.

(1) Continuity equations

$$\frac{\partial \rho_k}{\partial t} + \frac{\partial}{\partial x_j}(\rho_k u_{kj}) = S_k \quad (\mathrm{k} = 1,2\cdots\mathrm{f}) \tag{3.10}$$

where ρ_k is the bulk density of kth phase, and S_k is kth phase mass source term is as follows:

$$S_k = -\frac{1}{dv}\int_{dA_k} \tilde{\rho}_k (\tilde{u}_{kj} - \tilde{u}_{sj}) n_{kj} d\tilde{A} \tag{3.11}$$

For the dilute concentration multi-phase flow, the continuity equation for liquid is as follows:

$$\frac{\partial \rho}{\partial t} + \frac{\partial}{\partial x_j}(\rho u_j) = S \tag{3.12}$$

where

$$S = -\sum_k S_k = -\sum_k \dot{m}_k n_k \tag{3.13}$$

$$S_k = \dot{m}_k n_k$$

$$m_k = \frac{\pi d_k^3}{6}\bar{\rho}_k$$

$$\dot{m}_k = \frac{dm_k}{dt}$$

Equation (3.13) are used in the particulate phase, and m_k is the mass of an individual particle, n_k is the particle number in unit volume.

(2) Momentum equations:

$$\frac{\partial(\rho_k u_{ki})}{\partial t} + \frac{\partial}{\partial x_j}(\rho_k u_{ki} u_{kj}) = \rho_k g_i - \frac{\partial(C_k p)}{\partial x_i}$$
$$+ \sum_k \frac{\rho_k}{\tau_{rk}}(u_{ki} - u_i) + u_i S + F_{Mi} + \frac{\partial(C_k \tau_{kji})}{\partial x_j} \tag{3.14}$$

where

$$\tau_{rk} = \frac{d_k^2 \bar{\rho}_k}{18\mu}\left(1 + \frac{R_{ek}^{2/3}}{6}\right)^{-1}$$
$$R_{ek} = |\vec{u}_k - \vec{u}|\frac{d_k}{\nu} \tag{3.15}$$

$$u_i S_k = -\frac{1}{dv}\int_{dA_k} \tilde{\rho}_k \tilde{u}_{ki}(\tilde{u}_{kj} - \tilde{u}_{sj}) n_{kj} d\tilde{A} \tag{3.16}$$

And F_{Mi} is the Magnus force. The drag term expressed in Equation (3.15) also can include effects of the added mass force and the Basset force, which is discussed in the section 3.2.4 for the unsteady particle motion.

For the two-phase flow at the dilute concentration condition the momentum equations for of liquid phase are in the following form:

$$\frac{\partial(\rho u_i)}{\partial t}+\frac{\partial}{\partial x_j}\left(\rho u_j u_i\right)=\rho_k g_i-\frac{\partial p}{\partial x_i}+\frac{\partial \tau_{ji}}{\partial x_i}+\sum_k \frac{\rho_k}{\tau_{rk}}\left(u_{ki}-u_i\right)+u_i S+F_{Mi} \tag{3.17}$$

And momentum equations for particulate phases are as follows:

$$\frac{\partial(\rho_k u_{ki})}{\partial t}+\frac{\partial}{\partial x_j}(\rho_k u_{kj} u_{ki})=\rho_k g_i+\frac{\rho_k}{\tau_{rk}}(u_i-u_{ki})+u_i S_k+F_{kMi} \tag{3.18}$$

In Equation (3.18) it is assumed that pressure and viscosity stresses are zero, that is, $\langle \tilde{p}_k \rangle = 0$, $\langle \tilde{\tau}_{k,ji} \rangle = 0$, for dilute concentration particulate phase.

The energy equation and the component equation also can be obtained in similar forms.

Basic Equations by Using an Expression of Particle Number n_k in a Unit Volume.

By using Equation (3.11), Equations (3.10) and (3.18) have the following form

$$\frac{\partial n_k}{\partial t}+\frac{\partial}{\partial x_j}(n_k u_{kj})=0 \tag{3.19}$$

$$\frac{\partial(n_k u_{ki})}{\partial t}+\frac{\partial}{\partial x_j}(n_k u_{kj} u_{ki})=n_k g_i+\frac{n_k}{\tau_{rk}}(u_i-u_{ki})+\frac{n_k m_k}{m_k}(u_i-u_{ki})+\frac{F_{kMi}}{m_k} \tag{3.20}$$

Basic Conservative Reynolds Averaged Equations for Turbulent Two-Phase Flow

By using Reynolds averaging method to average basic equations of laminar two phase flow, i.e., equation (3.14) to equation (3.20), the basic equations of turbulent dilute liquid-particulate two-phase flow can be obtained as follows.

(1) Continue equation for liquid phase

$$\frac{\partial \rho}{\partial t}+\frac{\partial}{\partial x_j}(\rho u_j)=S-\sum \overline{n_p' \dot{m}_p'} \tag{3.21}$$

(2) Continue equation for kth particulate phase

$$\frac{\partial \rho_p}{\partial t}+\frac{\partial}{\partial x_j}(\rho_p u_{pj})=\overline{n_p' \dot{m}_p'}+S_p \tag{3.22}$$

where the averaging note ' $\overline{\quad}$ ' for every variable has been removed off for simplicity. And the superscript ' $'$ ' represents fluctuate value of turbulence $\overline{\rho' u_j'}, \overline{\rho_k' u_{kj}'}, \overline{n_k' m_k'}$ and so on are correlative terms in turbulence. Equation (3.22) is expressed in the form of particle number in equation (3.23).

$$\frac{\partial n_k}{\partial t}+\frac{\partial}{\partial x_j}\left(n_k u_{kj}\right)=-\frac{\partial}{\partial x_j}\overline{n_k' u_{kj}'}+S_k \tag{3.23}$$

(3) Momentum equations for liquid phase

$$\begin{aligned}
&\frac{\partial}{\partial t}(\rho u_i)+\frac{\partial}{\partial x_j}(\rho u_j u_i)=-\frac{\partial P}{\partial x_i}+\frac{\partial}{\partial x_j}\left[\mu\left(\frac{\partial u_j}{\partial x_i}+\frac{\partial u_i}{\partial x_j}\right)-\frac{2}{3}\left(\mu \frac{\partial u_i}{\partial x_j}\right)\delta_y\right] \\
&+\Delta \rho g_i+\sum \frac{\rho_p}{\tau_{rp}}(u_{pi}-u_i)+F_{ci}+u_i S-\frac{\partial(\rho \overline{u_j' u_i'})}{\partial x_j}+\sum \frac{m_p}{\tau_{rp}}(\overline{n_p' u_{pi}'}-\overline{n_p' u_i'}) \\
&-\left(u_i \sum \overline{n_p' \dot{m}_p'}+\sum n_p \overline{u_i' \dot{m}_p'}+\sum \dot{m}_p \overline{u_i' n_p'}+\sum \overline{u_i' \dot{m}_p' n_p'}\right)
\end{aligned} \tag{3.24}$$

(4) Momentum equations for particle phase:

$$\frac{\partial(n_p u_{pi})}{\partial t}+\frac{\partial(n_p u_{pj} u_{pi})}{\partial x_j}=n_p g_i+\frac{n_p}{\tau_{rp}}(u_i-u_{pi})+\frac{F_{p,ci}}{m_p}-\frac{\partial}{\partial t}(\overline{n'_p u'_{pi}})$$

$$+n_p\cdot(u_i-u_{pi})\frac{\dot{m}_p}{m_p}-\frac{\partial}{\partial x_j}(n_p\overline{u'_{pj}u'_{pi}}+u_{pj}\overline{n'_p u'_{pi}}+u_{pi}\overline{n'_p u'_{pj}}+\overline{n'_p u'_{pj}u'_{pi}})$$

$$+\frac{(\overline{n'_p u'_i}-\overline{n'_p u'_{pi}})}{\tau_{rp}}+\frac{1}{m_p}(u_i\overline{n'_p\dot{m}'_p}+n_p\overline{u'_i\dot{m}'_p}+\dot{m}_p\overline{n'_p u'_i}+\overline{n'_p\dot{m}'_p u'_i}$$

$$-u_{pi}\overline{n'_p\dot{m}'_p}-n_p\overline{u'_{pi}\dot{m}'_p}-\dot{m}_p\overline{n'_p u'_{pi}}-\overline{n'_p\dot{m}'_p u'_{pi}}) \qquad (3.25)$$

where, the Coriolis force is in the following relation:

$$F_{ci}=-\sum F_{p,ci}.$$

And τ_{rp} is the particle dynamic response time, which can be expressed in the following Wallis-Kiliachko drag formula,

$$\tau_{rp}=\frac{d^2{}_p\rho_p}{18\mu}\left(1+R_e^{\frac{2}{3}}/6\right)^{-1} \qquad (3.1<R_e<1000)$$

and R_e is the relative Reynolds number:

$$R_e=d_p\left|u-u_p\right|/\nu$$

(5) Energy equations of liquid phase

$$\frac{\partial(\rho c_p T)}{\partial t}+\frac{\partial}{\partial x_j}(\rho c_p u_j T)=\frac{\partial}{\partial x_j}(\lambda\frac{\partial T}{\partial x_j})+\omega_s Q_s-q_r+\sum m_k Q_k+c_p T s$$

$$-c_p T\sum\overline{\dot{m}_k' n_k'} - c_p\sum n_k\overline{T'\dot{m}_k'} - c_p\sum\dot{m}_k\overline{n_k' T'} - \frac{\partial}{\partial t}(c_p\overline{\rho' T'})$$

$$-\frac{\partial}{\partial x_j}(\rho c_p\overline{u_j' T'} + u_j c_p\overline{\rho' T'} + c_p T\overline{u_j'\rho'} + c_p\overline{\rho' u_j' T'} \tag{3.26}$$

where Q_k is the heat transfer caused by convection between liquid phase and particulate phases for every particle.

$$Q_k = \pi d_k N_u \lambda (T_k - T)^{ln(1+B)}/_B$$

where Q_h is the heat reaction on particle surface. And Q_s is the heat of a particle produced in chemical reaction.

(6) Energy equation of kth particulate phase

$$\frac{\partial(n_k c_k T_k)}{\partial t} + \frac{\partial}{\partial x_j}(n_k u_{kj} c_k T_k) = {n_k(Q_h - Q_k - Q_{rk})}/_{m_k} + {(c_p T - c_k T_k)n_k\dot{m}_k}/_m$$

$$-\frac{\partial}{\partial t}(c_k\overline{n_k' T'}_k) - \frac{\partial}{\partial x_j}(n_k c_k\overline{T_k' u'}_{kj} + c_k u_{kj}\overline{n_k' T_k'} + c_k T_k\overline{n_k' u_{kj}'} + c_k\overline{n_k' T_k' u'}_{kj})$$

$$+(c_p T\overline{n_k'\dot{m}'}_k + c_p n_k\overline{T'\dot{m}'}_k + c_p\dot{m}_k\overline{n_k' T'} + c_p\overline{\dot{m}_k' T' n'}_k + c_k\overline{T n_k'\dot{m}_k}$$

$$-c_p\overline{T_k'\dot{m}_k' n_k} + c_k T_k\overline{n_k'\dot{m}_k'} - c_k\overline{n_k'\dot{m}_k' T_k'}){/}_{m_k} \tag{3.27}$$

(7) The turbulent Reynolds stresses equations for liquid phase

$$\frac{\partial}{\partial t}(\rho\overline{u_i' u_j'} + \frac{\partial}{\partial x_k}(\rho u_k\overline{u_i' u_j'}) = -\frac{\partial}{\partial x_k}\Big[\rho\overline{u_k' u_i' u_j'} + \overline{p' u_j'}\delta_{ik} + \overline{p' u_i'}\delta_{jk}$$

$$+\mu\frac{\partial}{\partial x_k}(\overline{u_i' u_j'})\Big] - \rho(\overline{u_i' u_k'}\frac{\partial u_j}{\partial x_k} + \overline{u_j' u_k'}\frac{\partial u_i}{\partial x_k}) - 2\mu(\overline{\frac{\partial u_i'}{\partial x_k}\cdot\frac{\partial u_j'}{\partial x_k}})$$

$$+\overline{p'(\frac{\partial u_i'}{\partial x_j}\cdot\frac{\partial u_j'}{\partial x_i})}+\sum\frac{n_p m_p}{\tau_{rp}}(\overline{u_i'u_{pj}'}+\overline{u_j'u_{pi}'}-2\overline{u_i'u_j'})+2\overline{u_i'u_j'}+S \tag{3.28}$$

(8) The turbulent Reynolds stresses equations for particle phase

$$\frac{\partial}{\partial t}(n_p\overline{u_{pi}'u_{pj}'})+\frac{\partial}{\partial x_k}(n_p u_{pk}\overline{u_{pi}'u_{pj}'})=-(n_p\overline{u_{pk}'u_{pj}'}+u_{pk}\overline{n_p'u_{pj}'})\frac{\partial u_{pi}}{\partial x_k}$$

$$-(n_p\overline{u_{pk}'u_{pi}'}+u_{pk}\overline{n_p'u_{pi}'})\frac{\partial u_{pj}}{\partial x_k}-\overline{n_p'u_{pk}'u_{pj}'}\frac{\partial u_{pi}}{\partial x_k}-\overline{n_p'u_{pk}'u_{pi}'}\frac{\partial u_{pj}}{\partial x_k}$$

$$-\frac{\partial}{\partial x_k}(n_p\overline{u_{pk}'u_{pi}'u_{pj}'}+u_{pk}\overline{n_p'u_{pi}'u_{pj}'}+\overline{n_p'u_{pk}'u_{pi}'u_{pj}'})$$

$$+\frac{m_p+\dot{m}_p\tau_{rp}}{m_p\tau_{rp}}\left[n_p(\overline{u_i'u_{pj}'}+\overline{u_j'u_{pi}'}-2\overline{u_{pi}'u_{pj}'})+u_i\overline{n_p'u_{pj}'}\right.$$

$$\left.+u_j\overline{n_p'u_{pi}'}+\overline{n_p'u_i'u_{pj}'}\right]+\frac{m_p+\dot{m}_p\tau_{rp}}{m_p\tau_{rp}}\left[\overline{n_p'u_j'u_{pi}'}-\overline{2n_p'u_{pi}'u_{pj}'}\right]$$

$$-\overline{n_p'u_{pj}'}\frac{\partial u_{pi}}{\partial t}-\overline{n_p'u_{pi}'}\frac{\partial u_{pj}}{\partial t}-\frac{\partial}{\partial t}(\overline{n_p'u_{pi}'u_{pj}'}) \tag{3.29}$$

(9) The equations of correlation terms between the particle number density fluctuation and the velocity fluctuation, $\overline{n_g'v_{gi'}'}$, for particle phase

$$\frac{\partial}{\partial t}(n_p\overline{n_p'u_{pi}'})+\frac{\partial}{\partial x_k}(n_p u_{pk}\overline{n_p'u_{pi}'})=-(n_p\overline{n_p'u_{pk}'}+u_{pk}\overline{n_p'n_p'}+\overline{n_p'n_p'u_{pk}'})$$

$$\times\frac{\partial u_{pi}}{\partial x_k}-(2u_{pi}\overline{n_p'u_{pk}'}+n_p\overline{u_{pk}'u_{pi}'}+u_{pk}\overline{n_p'u_{pi}'}+\overline{n_p'u_{pk}'u_{pi}'}+\overline{n_p'u_{pk}'u_{pj}'})\frac{\partial n_p}{\partial x_k}$$

$$-(2n_p\overline{n_p'u_{pt}'}+2u_{pi}\overline{n_p'n_p'}+2\overline{n_p'n_p'u_{pi}'})\frac{\partial u_{pk}}{\partial x_k}-\frac{\partial}{\partial x_k}(\overline{n_p'n_p'u_{pk}'u_{pi}'})$$

$$+\frac{m_p+\dot{m}_p\tau_{rp}}{m_p\tau_{rp}}\left[\overline{n'_p n'_p}(u_i-u_{pi})-n_p(\overline{n'_p u'_{pi}})-\overline{n'_p n'_p u'_{pi}}\right]-u_{pi}\overline{n'_p n'_p}\frac{\partial u'_{pk}}{\partial x_k}$$

$$-\frac{\partial}{\partial t}(u_{pi}\overline{n'_p n'_p})-\frac{\partial}{\partial t}(\overline{n'_p n'_p u'_{pi}})-\overline{n'_p u'_{pt}}\frac{\partial n_p}{\partial t}-\overline{n'_p n'_p u'_{pi}}\frac{\partial u'_{pk}}{\partial x_k}$$

$$-u_{pk}u_{pi}\frac{\partial}{\partial x_k}(\overline{n'_p n'_p})-u_{pi}\frac{\partial}{\partial x_k}(\overline{n'_p n'_p u'_{pk}})-u_{pk}\frac{\partial}{\partial x_k}(\overline{n'_p n'_p u'_{pi}})$$

$$-n_p n_p\overline{u'_{pi}\frac{\partial u'_{pk}}{\partial x_k}}-2n_p u_{pi}\overline{n'_p\frac{\partial u'_{pk}}{\partial x_k}}-2n_p\overline{n'_p u'_{pi}\frac{\partial u'_{pk}}{\partial x_k}} \tag{3.30}$$

(10) The equation of correlation term of the particle number density fluctuation, $\overline{n'^2_g}$, for particle phase

$$\frac{\partial}{\partial t}(n_p\overline{n'^2_p})+\frac{\partial}{\partial x_k}(n_p u_{pk}\overline{n'^2_p})=-\frac{\partial}{\partial x_k}(n_p\overline{n'^2_p u'_{pk}})-(2n_p\overline{n'_p\frac{\partial}{\partial x_k}u'_{pk}})$$

$$-2n_p\overline{n'^2_p}\frac{\partial}{\partial x_k}u_{pk}-2n_p\overline{n'_p u'_{pk}}\frac{\partial n_p}{\partial x_k}-2n_p^2\overline{n'_p\frac{\partial}{\partial x_k}u'_{pk}}$$

$$-\overline{n'^3_p}\frac{\partial u_{pk}}{\partial x_k}-\frac{1}{3}u_{pk}\overline{\frac{\partial n'^3_p}{\partial x_k}}-\overline{n'^2_p\frac{\partial n'_p u'_{pk}}{\partial x_k}}-\frac{1}{3}\frac{\partial}{\partial t}(\overline{n'^3_p}) \tag{3.31}$$

(11) The turbulent energy dispassion equation for liquid phase

$$\frac{\partial}{\partial t}(\rho\varepsilon)+\frac{\partial}{\partial x_j}(\rho u_j\varepsilon)=-2\mu\frac{\partial^2 u_i}{\partial x_j\partial x_k}\overline{u'_j\frac{\partial u'_i}{\partial x_j}}-2\mu\overline{\frac{\partial u'_j}{\partial x_k}\frac{\partial u'_i}{\partial x_k}}\frac{\partial u_i}{\partial x_j}$$

$$-2\mu\frac{\partial u_j}{\partial x_k}\overline{\frac{\partial u'_i}{\partial x_k}\frac{\partial u'_i}{\partial x_j}}-2\mu\overline{\frac{\partial u'_j}{\partial x_k}\frac{\partial u'_i}{\partial x_k}\frac{\partial u'_i}{\partial x_j}}-\mu\frac{\partial}{\partial x_j}\left[\overline{u'_j\left(\frac{\partial u'_i}{\partial x_k}\right)^2}\right]$$

$$-2\nu\frac{\partial}{\partial x_i}\left(\overline{\frac{\partial u_i'}{\partial x_k}\frac{\partial p'}{\partial x_k}}\right)+\frac{\partial}{\partial x_j}(p\varepsilon)-2\rho\overline{\left(\nu\frac{\partial^2 u_i'}{\partial x_j\partial x_k}\right)^2}$$
$$+\sum\frac{1}{\tau_{rp}}\left[2\nu\frac{\partial}{\partial x_k}\left(\rho_p\overline{u_{pi}'\frac{\partial u_i'}{\partial x_j}}\right)+2\nu\frac{\partial}{\partial x_k}\left(\overline{\rho_p' u_{pi}'\frac{\partial u_i'}{\partial x_k}}\right)\right.$$
$$\left.-2\nu\rho_p\overline{u_{pi}'\frac{\partial^2 u_i'}{\partial x_k^2}}-2\nu\overline{u_j'\frac{\partial u_i'}{\partial x_k}\frac{\partial \rho_k}{\partial x_k}}-2\rho_p\varepsilon\right]$$
$$+2S\varepsilon+2\nu\overline{u_i'\frac{\partial u_i'}{\partial x_k}}+\frac{\partial S}{\partial x_k} \tag{3.32}$$

3.2 Closed Turbulent Equations for Liquid-Solid Two-Phase Flow through Hydraulic Machinery

3.2.1 Closed Turbulence Model Using the Modeled Second Correlation

It is necessary to apply the turbulence model to close the foregoing equations of multiphase flow. In this session, the modeled second correlation terms are used to simulate the third order correlation term and others, such as, the term containing the fluctuate pressure, which results in closing of Reynolds stresses equations.

Modeled Turbulent Reynolds Stresses Equations for Liquid Phase

The modeled equations of the turbulent Reynolds stresses equations for the liquid phase, i.e., equation (3.28) is as follows:

$$\frac{\partial}{\partial t}(\rho\overline{u_i'u_j'})+\frac{\partial}{\partial x_k}(\rho u_k\overline{u_i'u_j'})=D_{ij}+P_{ij}+\Pi_{ij}-\varepsilon_{ij}+G_{p,ij}+G_{R,ij} \tag{3.33}$$

where the gradient model, i.e., the Daly-Harlow model is used for the turbulence diffusion term in the following form:

$$D_{ij} = -\frac{\partial}{\partial x_k}\left[\rho\overline{u_k' u_i' u_j'} + \overline{p' u_j'}\delta_{ik} + \overline{p' u_i'}\delta_{jk} + \mu\frac{\partial}{\partial x_k}\left(\overline{u_i' u_j'}\right)\right]$$

$$= \frac{\partial}{\partial x_k}\left[C_s \rho \frac{k}{\varepsilon}\overline{u_k' u_l'}\frac{\partial}{\partial x_l}(\overline{u_i' u_j'}) + \mu\frac{\partial}{\partial x_k}(\overline{u_i' u_j'})\right.$$

where the term, $\rho\frac{k}{\varepsilon}\overline{u_k' u_l'}$, has the same dimensions as that of the eddy viscosity, μ_T, which reflects its anisotropy. The constant C_s in this equation is taken as 0.24.

The turbulence posses the local isotropy at the high Reynolds number condition, the dissipation for different turbulence energy components are the same, that is, the term, $\overline{\frac{\partial u_i'}{\partial x_k}.\frac{\partial u_j'}{\partial x_k}}$, is zero at conditions of $i \neq j$. So the turbulent energy dissipation can be defined as follows:

$$\varepsilon_{ij} = 2\mu(\overline{\frac{\partial u_i'}{\partial x_k}.\frac{\partial u_j'}{\partial x_k}}) = \frac{2}{3}\delta_{ij}\rho\varepsilon$$

The correlation terms, which including the pressure fluctuation, can be divided into three parts: the correlation between fluctuate velocity components, the correlation between fluctuate velocity components and the mean strains and the correlation between fluctuate velocity components and buoyancy, which are modeled by the following $\Pi_{ij,1}$, $\Pi_{ij,2}$ and $\Pi_{ij,3}$ in the Launder-Rotta model:

$$\Pi_{ij} = \overline{p'\left(\frac{\partial u_j'}{\partial x_k} + \frac{\partial u_j'}{\partial x_k}\right)} = \Pi_{ij,1} + \Pi_{ij,2} + \Pi_{ij,3}$$

$$\Pi_{ij,1} = -C_1 \frac{\varepsilon}{k} \rho \left(\overline{u_i' u_j'} - \frac{2}{3} \delta_{ij} k \right)$$

$$\Pi_{ij,2} = -C_2 \left(P_{ij} - \frac{2}{3} \delta_{ij} G_k \right)$$

$$\Pi_{ij,3} = -C_3 \left(G_{ij} - \frac{2}{3} \delta_{ij} G_b \right)$$

where $G_k = -\rho \overline{u_i' u_k'} \frac{\partial v_i}{\partial x_k}$, and the constants C_1, C_2 and C_3 are taken in the values of 2.2, 0.55 and 0.55 respectively. Then productive term of turbulent stresses can be modeled in the following form:

$$P_{ij} = -\rho \left(\overline{u_i' u_k'} \frac{\partial v_j}{\partial x_k} + \overline{u_j' u_k'} \frac{\partial v_i}{\partial x_k} \right)$$

The production of particle drag is:

$$G_{p,ij} = \sum \frac{n_p m_p}{\tau_{rp}} (\overline{u_{pj}' u_i'} + \overline{u_{pi}' u_j'} - 2\overline{u_i' u_j'})$$

where $\overline{u_{pi}' u_j'}$ and $\overline{u_{pj}' u_i'}$ can be modeled according to the dimension analysis:

$$\overline{u_{pj}' u_i'} \propto \sqrt{k_p k \delta_{ij}}, \qquad \overline{u_{pi}' u_j'} \propto \sqrt{k_p k \delta_{ij}}$$

and $$\overline{u_{pj}' u_i'} + \overline{u_{pi}' u_j'} = 2C_p^k \sqrt{k_p k \delta_{ij}}$$

Then: $$G_{p,ij} = \sum \frac{2 n_p m_p}{\tau_{rp}} (C_p^k \sqrt{k_p k \delta_{ij}} - \overline{u_i' u_j'})$$

The source terms induced by phase transformation are as follows:

$$G_{R,ij} = 2\overline{u_i'u_j'} \cdot S$$

And the constant C_p^k can be taken as 0.11.

Modeled Turbulent Kinetic Energy Equation and Turbulent Energy Dissipation Rate Equation for Liquid Phase

The exact turbulent kinetic energy, k, equation for liquid phase can be obtained from equations (3.28) through adding $i = j$.

$$\frac{\partial}{\partial t}(\rho\overline{u_i'u_i'}) + \frac{\partial}{\partial x_k}(\rho v_k \overline{u_i'u_i'}) = \frac{\partial}{\partial x_k}\left[\rho\overline{u_k'u_i'u_i'} + 2\overline{p'u_i'} + \mu\frac{\partial}{\partial x_k}(\overline{u_i'u_i'})\right]$$

$$-2\rho\overline{u_k'u_i'}\frac{\partial u_i}{\partial x_k} - 2\mu\overline{\left(\frac{\partial u_i'}{\partial x_k}\right)^2} + \sum\frac{2n_p m_p}{\tau_{rp}}(\overline{u_{pi}'u_i'} - \overline{u_i'u_i'}) + 2\overline{u_i'u_i'} \cdot S \tag{3.34}$$

Defining the turbulent kinetic energy $k = \overline{v_i'v_i'}/2$, the modeled turbulent kinetic energy, i.e., k equation can be deduced through introducing the foregoing correlation terms:

$$\frac{\partial}{\partial t}(\rho k) + \frac{\partial}{\partial x_j}(\rho u_j k) = \frac{\partial}{\partial x_j}\left(\rho C_\varepsilon \frac{k}{\varepsilon}\overline{u_j'u_i'}\frac{\partial k}{\partial x_i}\right) - \rho\overline{u_j'u_i'}\frac{\partial u_i}{\partial x_j}$$

$$+\sum\frac{n_p m_p}{\tau_{rp}}(C_p^k\sqrt{k_p k} - k) + 2kS - \rho\varepsilon \tag{3.35}$$

where the constant C_k is taken as 0.24, and the constant $C_p^k = 0.11$.

The modeled turbulent energy dissipation rate, i.e., ε equation for liquid phase can be also obtained by using the same method:

$$\frac{\partial}{\partial t}(\rho\varepsilon) + \frac{\partial}{\partial x_j}(\rho u_j \varepsilon) = \frac{\partial}{\partial x_j}\left(\rho C_\varepsilon \frac{k}{\varepsilon}\overline{u_j'u_i'}\frac{\partial \varepsilon}{\partial x_i}\right) + \frac{\varepsilon}{k}\left[C_{s1}(-\rho\overline{u_j'u_i'}\frac{\partial v_i}{\partial x_j}\right.$$

$$+\sum \frac{n_p m_p}{\tau_{rp}}(C_p^k \sqrt{k_p k} - k) + 2kS) - C_{s2}\rho\varepsilon \Bigg] \tag{3.36}$$

where the constants have the following values:

$$C_\varepsilon = 0.15, \quad C_{s1} = 1.44, \quad C_{s2} = 1.9, \quad C_{s3} = 0.8 \text{ and } C_p^k = 0.11.$$

Modeled Turbulent Reynolds Stresses Equations for Particle Phase

By using the similar method, which is applied for the modulation of equation (3.28) for liquid phase and neglecting the third order correlation terms of n_p', the modeled turbulent Reynolds stresses equations for particle phase can be obtained:

$$\frac{\partial}{\partial t}(n_p \overline{u'_{pi}u'_{pj}} + \frac{\partial}{\partial x_k}(n_p u_{pk} \overline{u'_{pi}u'_{pj}}) = D_{p,ij} + G_{p,ij} + P_{p,ij} - n_p \varepsilon_{p,ij} \tag{3.37}$$

where the turbulent diffusion terms are:

$$D_{p,ij} = -\frac{\partial}{\partial x_k}(n_p \overline{u'_{pk}u'_{pi}u'_{pj}}) = \frac{\partial}{\partial x_k}\left[n_p C_{ps} \frac{k_p}{\varepsilon_p} \overline{u'_{pk}u'_{pl}} \frac{\partial}{\partial x_l}(\overline{u'_{pi}u'_{pj}}) \right]$$

where the constant C_{ps} may be taken the same value as that of C_s, that is, C_{ps} = 0.24.

The production of turbulent stresses:

$$P_{p,ij} = -\left(u_{pk} \overline{n'_p u'_{pj}} \frac{\partial u_{pi}}{\partial x_k} + u_{pk} \overline{n'_p u'_{pi}} \frac{\partial u_{pj}}{\partial x_k} \right) - \overline{n'_p u'_{pi}} \frac{\partial u_{pj}}{\partial t} - \overline{n'_p u'_{pj}} \frac{\partial u_{pi}}{\partial t}$$

The production caused by particle drag:

$$G_{p,ij} = -\left(n_p \overline{u'_{pi}u'_{pk}} \frac{\partial u_{pj}}{\partial x_k} + n_p \overline{u'_{pj}u'_{pk}} \frac{\partial u_{pi}}{\partial x_k} \right)$$

And the viscous dispassion:

$$\varepsilon_{p,ij} = -\frac{m_p + \dot{m}_p \tau_{rp}}{m_p \tau_{rp}} \left[\overline{(u'_{pj} u'_i + u'_{pi} u'_j - 2u'_i u'_j)} + \frac{u_i}{n_p} \overline{u'_{pj} n'_p} + \frac{u_j}{n_p} \overline{u'_{pi} n'_p} \right]$$

$$= -\frac{m_p + \dot{m}_p \tau_{rp}}{m_p \tau_{rp}} \left[2(C_p^k \sqrt{k_p k} \delta_{ij} - \overline{u'_{pi} u'_{pj}}) + \frac{1}{n_p} (u_i \overline{u'_{pj} n'_p} + u_j \overline{u'_{pi} n'_p}) \right]$$

where $C_p^k = 0.11$.

Modeled Turbulent Kinetic Energy Equation for Particle Phase

Letting $i = j$ in equation (3.29), and neglecting the third order correlation terms of n'_p, the following turbulent kinetic energy, k_p, equation for particle phase can be obtained:

$$\frac{\partial}{\partial t}(n_p \overline{u'^2_{pi}}) + \frac{\partial}{\partial x_k}(n_p u_{pk} \overline{u'^2_{pi}}) = -\frac{\partial}{\partial x_k}(n_p \overline{u'_{pk} u'^2_{pi}}) + 2G_p + 2P_p - 2n_p \varepsilon_p \tag{3.38}$$

where the turbulent kinetic energy k_p for particle phase is defined as: $k_p = \overline{u'_p u'_p} / 2$.

Then the modeled turbulent kinetic energy, k_p, equation for particle phase can be expressed in the form:

$$\frac{\partial}{\partial t}(n_p k_p) + \frac{\partial}{\partial x_j}(n_p u_{pj} k_p) = D_p + G_p + P_p - n_p \varepsilon_p \tag{3.39}$$

where:

$$D_p = \frac{\partial}{\partial x_j}\left(n_p C_p^k \frac{k_p}{\varepsilon} \overline{u'_{pj} u'_{pI}} \frac{\partial k_p}{\partial x_I} \right)$$

$$G_p = -n_p \overline{u'_{pi} u'_{pj}} \frac{\partial u_{pi}}{\partial x_j}$$

$$P_p = -v_{pj} \overline{n'_p u'_{pi}} \frac{\partial u_{pi}}{\partial x_j} - \overline{n'_p u'_{pi}} \frac{\partial u_{pi}}{\partial t}$$

where $C_p^k = 0.24$, and the turbulent kinetic energy dissipation rate for particle phase is expressed as:

$$\varepsilon_p = -\frac{m_p + \dot{m}_p \tau_{rp}}{m_p \tau_{rp}} \left[2(C_p^k \sqrt{k_p k} - k_p) + \frac{1}{n_p} (u_i \overline{n'_p u'_{pi}}) \right]$$

where $C_p^k = 0.11$.

Modeled Transport Equation of Correlation Term between Particle Number Fluctuation and Velocity Fluctuation, $\overline{n'_p u'_{pi}}$, for Particle Phase

The modeled transport equation of the correlation term between particle number fluctuation and velocity fluctuation, $\overline{n'_p u'_{pi}}$, for particle phase can be obtained by modeling the necessary terms in equation (3.30) as follows:

$$\frac{\partial}{\partial t}(n_p \overline{n'_p u'_{pi}}) + \frac{\partial}{\partial x_k}(n_p v_{pk} \overline{n'_p u'_{pi}}) = D_{NV,ij} + G_{NV,ij} + P_{NV,ij} - n_p \varepsilon_{NV,ij} \tag{3.40}$$

where

$$D_{NV,ij} = -\frac{\partial}{\partial x_k}(n_p \overline{u'_{pk} n'_p u'_{pi}}) = \frac{\partial}{\partial x_k}\left(n_p C_{NV}^p \cdot \frac{k_p}{\varepsilon_p} \overline{u'_{pk} u'_{pl}} \frac{\overline{\partial n'_p u'_{pi}}}{\partial x_l} \right)$$

$$G_{NV,ij} = -\left(2n_p \overline{n'_p u'_{pi}} \frac{\partial u_{pk}}{\partial x_k} + u_{pk} \overline{n'_p u'_{pi}} \frac{\partial n_p}{\partial x_k} + \overline{n'_p u'_{pi}} \frac{\partial n_p}{\partial t} \right)$$

$$P_{NV,ij} = -(2u_{pi} \overline{n'_p u'_{pk}} + n_p \overline{u'_{pk} u'_{pi}}) \frac{\partial n_p}{\partial x_k} - (n_p \overline{n'_p u'_{pk}} + u_{pk} \overline{n'^2_p}) \frac{\partial u_{pi}}{\partial x_k}$$

$$- 2u_{pi} \overline{n'^2_p} \frac{\partial u_{pk}}{\partial x_k} - \overline{n'^2_p} \frac{\partial u_{pi}}{\partial t}$$

$$\varepsilon_{NV,ij} = -\frac{m_p + \dot{m}_p \tau_{rp}}{m_p \tau_{rp}} \left[(u_i - u_{pi}) \overline{n_p'^2} / n_p - \overline{n_p' u_{pi}'} \right]$$

where $C_{NV}^p = 0.24$.

Modeled Transport Equation of Auto Correlation Term of Particle Number Fluctuation

$$\frac{\partial}{\partial t}(n_p \overline{n_p'^2}) + \frac{\partial}{\partial x_k}(n_p u_{pk} \overline{n_p'^2}) = D_{NN,ij} + G_{NN,ij} - n_p \varepsilon_{NN,ij} \tag{3.41}$$

where $$D_{NN,ij} = -\frac{\partial}{\partial x_k}(n_p \overline{n_p'^2 u_{pk}'}) = \frac{\partial}{\partial x_k}\left(n_p C_{NN}^p \frac{k_p}{\varepsilon_p} \overline{u_{pk}' u_{pl}'} \frac{\overline{\partial n_p'^2}}{\partial x_l} \right)$$

$$G_{NV,ij} = -2 n_p \overline{n_p'^2} \frac{\partial u_{pk}}{\partial x_k}$$

$$\varepsilon_{NV,ij} = 2 n_p \overline{n_p' u_{pk}'} \frac{\partial n_p}{\partial x_k}$$

where $C_{NN}^p = 0.24$. The foregoing time-meaning equations (3.21) to (3.25) of two-phase turbulent flow and the transport equations (3.33) to (3.41) of two-phase turbulent characteristics form the close turbulence model of second order correlation for two-phase flow.

3.2.2 The Algebraic Turbulence Stresses Model of Two-Phase Flow

The Reynolds stresses turbulence model (RSM) is much complicated than the standard k - ε turbulence model for engineering applications. But the later is not general for different conditions. The algebraic Reynolds stresses turbulence model (ASM) is not complicated and can be applied at different condition, such as, at anisotropy condition, which consists of simplified algebraic equations of Reynolds stresses and the standard k and ε equations.

In the algebraic Reynolds stresses model, two approximations are made by Professor Rodi. The first one is to assume that the convection and the diffusion of Reynolds stresses $\overline{u_i'u_j'}$ are approximately in direct proposition to those of turbulent kinetic energy k. In the second approximation, there is a local equilibrium between the dissipation and the production of the stresses, that is,

Production + Diffusion = Zero and Production = Dissipation

The Algebraic Reynolds Stresses Equations for Liquid Phase

Based on the foregoing approximations, the simplified stresses equations can be obtained from equation (3.23) as follows:

$$P_{ij} + \Pi_{ij} + G_{p,ij} + G_{R,ij} - \varepsilon_{ij} = 0 \tag{3.42}$$

The expressions of the foregoing terms are introduced into equation (3.42), and lets $G_k = \rho\varepsilon$, then the algebraic equations of Reynolds stresses are expressed in the following form:

$$\overline{u_i'u_j'} = \frac{2}{3}\delta_{ij}k\frac{(c_1 + c_2 - 1)}{c_1} - \frac{k}{\varepsilon}\cdot\frac{1-c_2}{c_1}\left[\overline{u_i'u_k'}\frac{\partial u_j}{\partial x_k} + \overline{u_j'u_k'}\frac{\partial u_i}{\partial x_k}\right]$$
$$+\frac{k}{c_1\rho\varepsilon}\left[\sum\frac{2n_p m_p}{\tau_{rp}}(C_p^k\sqrt{kk_p}\delta_{ij} - \overline{u_i'u_j'}) + 2\overline{u_i'u_j'}\cdot S\right] \tag{3.43}$$

where $c_1 = 2.2$, $c_2 = 0.55$ and $C_p^k = 0.11$.

The Algebraic Reynold Stresses Equations for Particle Phase

The following equation (3.44) can be deduced from equation (3.37) by using Rodi's approximations:

$$G_{p,ij} + P_{p,ij} - n_p\varepsilon_{p,ij} = 0 \tag{3.44}$$

Then introducing the expressions of all terms of it, the equation (3.45), i.e., the algebraic equation of Reynolds stresses can be obtained in the following form:

$$\overline{u'_{pi}u'_{pj}} = C_p^k \sqrt{kk_p}\delta_{ij} + \frac{1}{n_p}(u_i \overline{n'_p u'_{pj}} + u_j \overline{n'_p u'_{pi}})$$
$$+ (n_p \overline{u'_{pj}u'_{pk}} + u_{pk}\overline{n'_p u'_{pj}})\frac{\partial u_{pi}}{\partial x_k} + \overline{n'_p u'_{pi}}\frac{\partial u_{pj}}{\partial t} + \overline{n'_p u'_{pj}}\frac{\partial u_{pi}}{\partial t}$$
$$- \frac{\tau_{rp}}{2n_p}\left[n_p \overline{u'_{pi}u'_{pk}} + u_{pk}\overline{n'_p u'_{pi}}\right)\frac{\partial u_{pj}}{\partial x_k} \qquad (3.45)$$

where $C_p^k = 0.11$.

The Algebraic Model Transport Equation of Correlation Term between Particle Number Fluctuation and Velocity Fluctuation, $\overline{n'_p u'_{pi}}$, for Particle Phase

The following equation (3.46) can be deduced from equation (3.40) by using the same way as that of equation (3.44):

$$G_{Nv,ij} + P_{Nv,ij} - n_p \varepsilon_{NV,ij} = 0 \qquad (3.46)$$

Then introducing the expressions of all terms of it, such as, $G_{NN,\,ij}$, $P_{NN,\,ij}$ and $\varepsilon_{NN,\,ij}$, the equation (3.47), i.e., the algebraic equation of the correlation term between particle number fluctuation and velocity fluctuation, $\overline{n'_p u'_{pi}}$, for particle phase can be obtained in the following form:

$$\overline{n'_p u'_{pi}} = \frac{\overline{n'_p n'_p}}{n_p}(u_i - u_{pi}) - \frac{c_{n1}\tau_{rp}}{n_p}\Bigg[(u_{pk}\overline{n'_p u'_{pi}} + 2v_{pi}\overline{n'_p u'_{pk}}$$
$$+ n_p \overline{u'_{pi}u'_{pk}})\frac{\partial n_p}{\partial x_k} + c_{n2}(2n_p \overline{n'_p u'_{pi}} + 2v_{pi}\overline{n'_p n'_p})\frac{\partial u_{pk}}{\partial x_k} + c_{n3}(n_p \overline{n'_p u'_{pk}}$$
$$+ v_{pk}\overline{n'_p n'_p})\frac{\partial u_{pi}}{\partial x_k} + \overline{n'_p u'_{pi}}\frac{\partial n_p}{\partial t} + \overline{n'_p n'_p}\frac{\partial u_{pi}}{\partial t} \Bigg] \qquad (3.47)$$

where $c_{n1} = 2.2$, $c_{n2} = 0.55$ and $c_{n3} = 0.55$.

The Algebraic Model Transport Equation of Auto Correlation Term of Particle Number Fluctuation, $\overline{n_p'^2}$, for Particle Phase

The following equation (3.48) can be deduced from equation (3.41) by using the same method as that of equation (3.44):

$$G_{NN,ij} - n_p \varepsilon_{NN,ij} = 0 \tag{3.48}$$

Then introducing the expressions of all terms of it, such as $G_{NN,ij}$ & $\varepsilon_{NN,ij}$, the equation (3.49), i.e, the algebraic equation of the auto correlation term of particle number fluctuation , $\overline{n_p'^2}$, for particle phase can be obtained in the following form:

$$\overline{n_p'^2} = C_{nn} \overline{n_p' u_{pk}'} \frac{\partial n_p}{\partial x_k} / \frac{\partial u_{pk}}{\partial x_{lk}} \tag{3.49}$$

where $C_{nn} = 0.24$.

The time-meaning turbulent equations (3.22) to (3.27) of two-phase flow and the algebraic equations (3.42) to (3.49) of turbulent characteristics the flows, and the turbulent kinetic energy k equation (3.35) and the turbulent energy dissipation rate ε equation (3.36) for liquid phase, as well as the turbulent kinetic energy K_p equation for particle phase (3.39) form up the algebraic turbulence model with second order correlation of liquid-particle two-phase flow in engineering based on the two-fluid model assumption.

3.2.3 The k – ε - k_p Turbulence Model of Two-Phase Flow

The k - ε - k_p turbulence model of two-phase flow has the isotropic characteristics and may be applied at the conditions of small circulation flow and the flow with small buoyancy forces. This model is actually the combination between the standard k - ε turbulence model for liquid phase and the k_p turbulence model for particle phase, in which the Boussinesq expressions are used to indicate the second order correlation terms in transporting equations.

Turbulence Model for Liquid Phase in the k - ε - k_p Turbulence Model

By using the Boussinesq expressions, the following correlation term can be simplified in the following equation [3.16]:

$$-\overline{u_i'u_j'} = \nu_T\left(\frac{\partial u_j}{\partial x_i}+\frac{\partial u_i}{\partial x_j}\right)+\frac{2}{3}k\delta_{ij}, \qquad -\overline{n_p'u_{pi}'} = \frac{\nu_p}{\sigma_p}\cdot\frac{\partial n_p}{\partial x_i},$$

$$-\overline{\rho u_k'u_i'u_j'} = \frac{\mu_e}{\sigma_k}\cdot\frac{\partial k}{\partial x_k}, \qquad -\overline{n_p'u_{pj}'} = \frac{\nu_p}{\sigma_p}\cdot\frac{\partial n_p}{\partial x_j},$$

$$D_{\varepsilon,ij} = \frac{\partial}{\partial x_k}\left(\frac{\mu_e}{\sigma_\varepsilon}\cdot\frac{\partial \varepsilon}{\partial x_k}\right), \qquad -\overline{n_p'u_{pk}'} = \frac{\nu_p}{\sigma_p}\cdot\frac{\partial n_p}{\partial x_k},$$

where $\sigma_k = 1.0$ and $\sigma_p = 1.5$.

The continuity equations and the momentum equations of liquid phase then can be deduced in this turbulence model:

$$\frac{\partial \rho}{\partial t}+\frac{\partial}{\partial x_j}(\rho u_j) = S = -\sum n_p \dot{m}_p$$

$$\frac{\partial}{\partial t}(\rho u_i)+\frac{\partial}{\partial x_j}(\rho u_j u_i) = -\frac{\partial P}{\partial x_i}+\frac{\partial}{\partial x_j}\left[\mu_e\left(\frac{\partial u_i}{\partial x_j}+\frac{\partial u_j}{\partial x_i}\right)\right]$$

$$+\sum\frac{n_p m_p}{\tau_{rp}}(u_{pi}-u_i)+\sum\frac{m_p}{\tau_{rp}}\left(\frac{\nu_p}{\sigma_p}\cdot\frac{\partial n_p}{\partial x_i}\right) \tag{3.50}$$

And the turbulent kinetic energy k equation and the turbulent energy dissipation rate ε equation for liquid phase are as follows:

$$\frac{\partial}{\partial t}(\rho k)+\frac{\partial}{\partial x_j}(\rho u_j k) = \frac{\partial}{\partial x_j}\left(\frac{\mu_e}{\sigma_k}\cdot\frac{\partial k}{\partial x_j}\right)+G_k+G_p+G_R-\rho\varepsilon \tag{3.51}$$

$$\frac{\partial}{\partial t}(\rho\varepsilon)+\frac{\partial}{\partial x_j}(\rho u_j\varepsilon)=\frac{\partial}{\partial x_j}\left(\frac{\mu_e}{\sigma_\varepsilon}\cdot\frac{\partial\varepsilon}{\partial x_j}\right)+\frac{\varepsilon}{k}\left[C_{\varepsilon 1}(G_k+G_p)-C_{\varepsilon 2}\rho\varepsilon\right] \tag{3.52}$$

where: $\mu_e=\mu+\mu_T$ $\quad G_k=\mu_T\left(\frac{\partial u_i}{\partial x_j}+\frac{\partial u_j}{\partial x_i}\right)\frac{\partial u_i}{\partial x_j}$

$\mu_T=C_\mu\rho k^2/\varepsilon$ $\quad G_p=-\sum\frac{n_p m_p}{\tau_{rp}}\left[2(k-C_p^k\sqrt{kk_p})\right]$

where $C_\mu=0.09$, $\sigma_k=1.0$, $\sigma_\varepsilon=1.3$, $C_{\varepsilon 1}=1.44$ and $C_{\varepsilon 2}=1.9$,

Turbulence Model for Particle Phase in the k - ε - k_p Turbulence Model

By using the Boussinesq expressions, the following correlation terms of particle phase can be simplified in the following equations:

$$-\overline{u'_{pi}u'_{pj}}=\nu_p\left(\frac{\partial u_{pi}}{\partial x_j}+\frac{\partial u_{pj}}{\partial x_i}\right), \qquad -\overline{n'_p u'_{pi}}=\frac{\nu_p}{\sigma_p}\cdot\frac{\partial n_p}{\partial x_i},$$

$$-\overline{u'_{pk}u'_{pi}}=\nu_p\left(\frac{\partial u_{pk}}{\partial x_i}+\frac{\partial u_{pi}}{\partial x_k}\right), \qquad -\overline{n'_p u'_{pj}}=\frac{\nu_p}{\sigma_p}\cdot\frac{\partial n_p}{\partial x_j},$$

$$-\overline{u'_{pk}u'_{pi}u'_{pj}}=\frac{\nu_p}{\sigma_p}\cdot\frac{\partial k_p}{\partial x_k}, \qquad -\overline{n'_p u'_{pk}}=\frac{\nu_p}{\sigma_p}\cdot\frac{\partial n_p}{\partial x_k},$$

where $\sigma_p=1.5$ and $C_p^k=0.11$.

The continuity equations and the momentum equations of particle phase then can be deduced in this turbulence model:

$$\frac{\partial n_p}{\partial t}+\frac{\partial}{\partial x_j}(n_p u_{pj})=\frac{\partial}{\partial x_j}\left(\frac{\nu_p}{\sigma_p}\cdot\frac{\partial n_p}{\partial x_j}\right) \tag{3.53}$$

$$\frac{\partial}{\partial t}(n_p u_{pi}) + \frac{\partial}{\partial x_j}(n_p u_{pj} u_{pi}) = \frac{\partial}{\partial x_j}\left[n_p \nu_p \left(\frac{\partial u_{pi}}{\partial x_j} + \frac{\partial u_{pj}}{\partial x_i} \right) \right]$$
$$+ \frac{m_p + \dot{m}_p \tau_{rp}}{m_p \tau_{rp}} n_p (u_i - u_{pi}) + \frac{\partial}{\partial x_j}\left(u_{pj} \frac{\nu_p}{\sigma_p} \cdot \frac{\partial n_p}{\partial x_i} + u_{pi} \frac{\nu_p}{\sigma_p} \cdot \frac{\partial n_p}{\partial x_j} \right)$$
$$- \frac{m_p + \dot{m}_p \tau_{rp}}{m_p \tau_{rp}} \cdot \frac{\nu_p}{\sigma_p} \cdot \frac{\partial n_p}{\partial x_i} + \frac{\partial}{\partial t}\left(\frac{\nu_p}{\sigma_p} \cdot \frac{\partial n_p}{\partial x_i} \right) \tag{3.54}$$

And the turbulent kinetic energy k_p transporting equation and for particle phase is as follows:

$$\frac{\partial}{\partial t}(n_p k_p) + \frac{\partial}{\partial x_j}(n_p u_{pj} k_p) = \frac{\partial}{\partial x_j}\left(n_p \frac{\nu_p}{\sigma_p} \cdot \frac{\partial k_p}{\partial x_j} \right) + G_{kp} + G_{pp} - n_p \varepsilon_p \tag{3.55}$$

where: $G_{kp} = n_p \nu_p \left(\frac{\partial u_{pj}}{\partial x_j} + \frac{\partial u_{pi}}{\partial x_j} \right) \frac{\partial u_{pi}}{\partial x_j}$,

$$G_{pp} = \frac{\nu_p}{\sigma_p}\left(\frac{\partial n_p}{\partial x_i} \cdot \frac{\partial u_{pi}}{\partial x_j} \right)$$

$$\varepsilon_p = -\frac{m_p + \dot{m}_p \tau_{rp}}{m_p \tau_{rp}} \left[2(C_p^k \sqrt{k k_p} - k_p) + \frac{u_i}{n_p} \cdot \frac{\nu_p}{\sigma_p} \cdot \frac{\partial n_p}{\partial x_i} \right]$$

where $\sigma_p = 1.5$ and $C_p^k = 0.11$. Equations (3.40) to (3.55) form the isotropic k - ε - k_p turbulence model of two-phase flow. Dai and Wu (3.1993) applied this k - ε - k_p turbulence model to calculate the liquid-particle two-phase flow through a centrifugal pump impeller [3.20].

The Algebraic Turbulence Model A_p for Particle Phase

The much more simple model to close the turbulent flow governing equations (3.54 ~ 3.55) of particle phase is to use the algebraic turbulence model - A_p model, that is, to use the Hinze-Tchen formula for particle phase eddy viscosity. The k - ε - A_p turbulence model of two-phase flow is the combination of the standard k - ε turbulence model for liquid phase and the algebraic turbulence model - A_p for particle phase, in which the ratio of the turbulent kinetic energy k_p for particle phase to this energy k for liquid phase equals to the ratio of the particle phase eddy viscosity ν_p to the liquid eddy viscosity ν_t, that is,

$$\frac{\nu_p}{\nu_t} = \frac{k_p}{k} = \frac{D_p}{D} = \left[1 + \frac{\tau_{rp}}{\tau_t}\right]^{-1} \tag{3.56}$$

where τ_{rp} is particle response time, according to the Stokes drag formula, it is indicated in the equation (3.57).

$$\tau_{rp} = \frac{\rho_p d_p^2}{18\mu} \tag{3.57}$$

The less the time τ_{rp} is the closer the particle follows the fluid motion. τ_t is the fluctuation time of liquid flow. According to the isotropic assumption of liquid turbulent flow and the assumption that the distribution of liquid flow velocity fluctuation accords with the Gaussian statistic distribution, it is obtained as follows:

$$\tau_{rp} = \frac{l}{u'} = \sqrt{3/2}\frac{C_\mu^{3/4} k}{\varepsilon} \tag{3.58}$$

from which it is clear that the fluctuation of particles is less than that of liquid based on the present turbulence model. In equation (3.55) neglecting the productive and the diffusive terms, as well as the second part of the ε_p

expression, and assuming that C_p^k equals to one, then the following equation can be obtained:

$$\frac{dk_p}{dt} = \frac{2}{\tau_{rp}}(\sqrt{kk_p} - k_p) \tag{3.59}$$

Integrating equation (3.59) in the period of t_t, and at the same time letting the turbulent kinetic energy k and k_p equal to constants, then we can get:

$$\frac{k_p}{k} = \left(1 + \frac{\tau_{rp}}{2\tau_t}\right)^{-2}$$

which is much similar to the Hinze-Tchen expression. Wu et al (1994) applied this k - ε - A_p turbulence model to calculate the liquid-particle two-phase flow at dilute concentration conditions through a centrifugal pump impeller [3.21].

3.2.4 Lagrangian-Eulerian Model for Liquid-Particle Two-Phase Flow

Lagrangian-Eulerian model for particle-laden two-phase flow is increasingly becoming a powerful tool to predict dilute turbulent two-phase flow of engineering significance. This hybrid model consists of the Eulerian formulation of the liquid phase and the Lagrangian formulation of the particle phase together with a stochastic dispersion model to account for the influence of liquid-phase turbulence on the particle phase. Most of existing Lagrangian stochastic models, in which the particles are individually treated and a representative number of particle trajectories are calculated and have adopted the fundamental method pioneered by Peskin and Kau (1976), Yuu et al (1978) and Gosman and Ioannides (1981) [3.22] to account for the effects of the liquid phase turbulence on the particle phase dispersion. Many authors have conducted in common that detailed inlet conditions play an important role in accurate Lagrangian predictions, and that a large number of particle trajectories are required to achieve a stochastically significant solution [3.23].

In Lagrangian stochastic computations, particle properties are determined using an ensemble averaging of many individual particle trajectories, such as,

10^4 particle trajectories, which requires consuming a great amount of computer CPU time. The stochastic dispersed-width transport (SDWT) model was presented to provide reduced sampling requirements.

Lagrangian Equation for Particles

In the Eulerian-Lagrangian model, the liquid flow is simulated by using the same Eulerian conservative equations as indicated in last session. But in the Lagrangian approach, the equation of motion for each of the particle parcel can be written as

$$\frac{d\tilde{U}_{pk}}{dt} = \frac{\tilde{U}_k - \tilde{U}_{pk}}{\tau_p} + F_{pk} \tag{3.60}$$

where $\tilde{U}_k = U_k + u_k$ is the instantaneous liquid velocity, F_{pk} is an external force. The response time of particle, τ_p, is defined as

$$\tau_p = \frac{\rho_p D_p^2}{18\mu f_p}$$

$$f_p = 1 + 0.15\mathrm{Re}_p^{0.687}$$

$$(0 < \mathrm{Re}_p < 1000)$$

The particle trajectories are computed by

$$\frac{dx_{pk}}{dt} = \tilde{U}_{pk} \tag{3.61}$$

The two-way coupling sources between the liquid- and particle-phases are given by

$$S_{Uk}^p = -\sum \frac{\pi}{6} \rho_p D_p^3 \dot{N} \Delta t \left(\frac{\tilde{U}_k - \tilde{U}_{pk}}{\tau_p} \right)$$

$$S_{\overline{u_j u_i}}^p = 2\left(\overline{U_j S_{Ui}^p} - U_j S_{Ui}^p \right) \delta_{ji}$$

$$S_{\varepsilon}^{p} = \frac{\varepsilon}{2k} S_{ujui}^{p}$$

where the summation is carried out over all droplet trajectories crossing the control volume.

Dispersion-Width Transport Model for Particle Phase

To obtain the instantaneous liquid velocity in equation (3.60), an improved model dispersion-width transport model can be used to determine the fluctuating liquid velocity as follows:

$$u_i = \sqrt{\overline{u_i^2}}\,\xi_i \delta_{ij} \tag{3.62}$$

where ξ_j is a Gaussian random variable having zero mean and unity deviation. In order to account for the anisotropic effects of liquid turbulence on particle dispersion, the normal stresses, $\overline{u_i^2}$, have been used here. The transverse component in equation (3. 62) is determined by

$$\xi_v = \xi_v + \frac{\sqrt{\overline{v^2}}}{r_p} \tau_p \alpha_p \tag{3.63}$$

where ξ_v is a Gaussian variable having zero meaning and unity deviation, r_p the particle radial position, and α_p a controlling parameter, being either zero or unity, to switch on or off this modification. In the dispersion-width transport model, both particle mean position and its variance are computed for each particle trajectory. Particle means position can be obtained by Lagrangian tracking of a computational parcel through a sequence of eddy. Simultaneously, the particle dispersion-width induced by liquid turbulence is determined and used as the standard deviation of the computational parcel's PDF after each interaction. The overall mean square dispersion corresponding to the variance of the parcel PDF after n-th interaction is determined by

$$\sigma_{pn}^2 = \sum_{k=1}^{n} \left(v_{rms} T_k\right)^2 \tag{3.64}$$

where

$$T_k = \Delta t_k - \tau_{pk} A_k + \begin{cases} A_k \sum_{i=k+1}^{n} \begin{cases} \tau_{pi} A_i Exp\left[- \sum_{j=k+1}^{i-1} \frac{\Delta t_j}{\tau_{pj}} \right] & i > k+1 \\ & k < n \\ \tau_{pi} A_i & i = k+1 \\ 0 & k = n \end{cases} \end{cases}$$

with A_k defined by

$$A_k = 1 - Exp\left[- \frac{\Delta t_j}{\tau_{pj}} \right]$$

In addition, the above-computed variance for each PDF should be normalized by the total number of computational parcels; that is,

$$\sigma_T = K \frac{\sigma_{pn}}{\sqrt{N_{cp}}} \tag{3.65}$$

where k is introduced as a correction factor account for undersampling, and N_{cp} is the number of computational parcels. It is clear that the normalization of equation (3.65) can recover the conventional discrete delta-function dispersion model as the number of computational parcels increases. However, according to this normalization, use of more computational parcels does not pay off as regard to the smoothing of Lagrangian computations. Obviously, $k = \sqrt{N_{cp}}$ corresponds to the situation that no normalization is used. The probability distribution function for a simplified isosceles triangle PDF can be obtained by

$$P(r)=\begin{cases}P_A & 0<r<w-r_p\\ P_C & w-r_p<r<r_p\\ P_D & w-r_p<r<w+r_p\\ 1 & r>w+r_p\end{cases}$$

$$(w/2<r_p<w)$$

$$P(r)=\begin{cases}P_A & 0<r<r_p\\ P_B & r_p<r<w-r_p\\ P_D & w-r_p<r<w+r_p\\ 1 & r\geq w+r_p\end{cases}$$

$$(0<r_p<w/2)$$

$$P(r)=\begin{cases}0 & 0<r<r_p-w\\ P_C & r_p-w<r<r_p\\ P_E & r_p<r<w+r_p\\ 1 & r\geq w+r_p\end{cases}$$

$$(r_p>w)$$

where $w=2\sqrt{3}\sigma_r$ is the PDF half-width, and the terms P_A, P_B, P_C, PD and P_E are defined by

$$P_A=\frac{6|w-r_p|\,r^2}{-2r_p^3+(w+r_p)^3+|w-r_p|^3}$$

$$P_B=\frac{-4r^3+6wr^3-2r_p^3}{-2r_p^3+(w+r_p)^3+|w-r_p|^3}$$

$$P_C = \frac{2r^3 + 3|w - r_p|r^2 + |w - r_p|^3}{-2r_p^3 + (w + r_p)^3 + |w - r_p|^3}$$

$$P_D = \frac{-2r^3 + 3(w + r_p)r^2 - 2r_p^3 + |w - r_p|^3}{-2r_p^3 + (w + r_p)^3 + |w - r_p|^3}$$

$$P_E = \frac{2r^3 - 3(w + r_p)r^2 - 2r_p^3 + |w - r_p|^3}{-2r_p^3 + (w + r_p)^3 + |w - r_p|^3}$$

Particle Motion Equation Disscussion

The equation of motion for each particle written in equation (3.60), like equations for most of engineering practice only includes the main force, such as, the drag force. But the drag coefficient C_D includes the effects of the drag force, the Basset force and the added mass force. The following equation is the general one of motion of the unsteady acceleration particle in liquid flow, called as the Basset - Boussinesque - Oseen equation, as follows:

$$\frac{\pi}{6}\rho_p d_p^3 \frac{du_p}{dt} = -\frac{1}{2}C_d \frac{\pi d_p^2}{4}\rho |u_p - u|(u_p - u) + \frac{\pi d_p^3}{6}\rho \frac{Du}{Dt} + C_a \frac{\pi d_p^3}{6} \times \rho\left(\frac{du}{dt} - \frac{du_p}{dt}\right) + \frac{\pi d_p^3}{6}(\rho_p - \rho)g - C_h \frac{d_p^2}{4}\rho(\pi\nu)^{1/2}\int_0 \frac{d}{d\tau}(u_p - u)\frac{d\tau}{\sqrt{t - \tau}} \tag{3.66}$$

where

$$\frac{d}{dt} = \left(\frac{\partial}{\partial t} + u_{pj}\frac{\partial}{\partial x_j}\right) \quad \text{and} \quad \frac{D}{Dt} = \left(\frac{\partial}{\partial t} + u_j \frac{\partial}{\partial x_j}\right)$$

and C_d is the drag coefficient at the steady motion, C_a the mass coefficient and C_h is the Basset term coefficient. The Basset term can be calculated by the following integration:

$$I = \int_0^t \left[\frac{du_p}{d\tau} - \frac{du}{d\tau} \right] \frac{d\tau}{\sqrt{t-\tau}} = I_1 - I_2 =$$

$$\int_0^{t-\Delta t} \frac{du_p}{d\tau} \frac{d\tau}{\sqrt{t-\tau}} + 2\sqrt{\Delta t} \left[\frac{du_p}{dt} \right]_{t-\Delta t} - \sum_i^n \frac{(u_i - u_{i-1})}{\sqrt{t-t_i}}$$

Many theoretical and experimental studies have been undertaken on the transient effects on drag coefficient [3.28]. Odar and Hamilton (1964) proposed an equation for the unsteady drag force exerted by a viscous fluid in a sphere which was accelerating arbitrarily and moving rectilinear in an otherwise quiet flow:

$$C_D = C_d + C_a \left(\frac{4}{3} \frac{d_p}{u_p^2} \right) \frac{du_p}{dt} + C_h \frac{2}{u_p^2} \sqrt{\frac{\mu}{\pi \rho}} \int_0^t \frac{\frac{du_p}{dt}}{\sqrt{t-\tau}} d\tau \qquad (3.67)$$

where C_D is the drag coefficient at unsteady motion.

Karanfilian and Kotas (1978) conducted a series of similar experiments with the condition of $10^2 < R_{ep} < 10^4$ and the acceleration number $0 < A_n < 10.5$. They reformed all the terms in the right hand side of equation (3.67) in to a single empirical term as follows:

$$C_D = (1 + A_n)^{\beta} C_d$$

where $\beta = 1.2 \pm 0.03$, U is the velocity of water flow and the acceleration number is:

$$A_n = \frac{U^2}{d_p \left| \frac{D\vec{U}}{Dt} \right|}$$

Sano (1981) considered the problem of unsteady viscous incompressible flow past a sphere. The unsteady drag coefficient of a sphere for different time domains is expressed as:

(1) small time domain:

$$C_D = C_d\left[H(t)+\frac{1}{3}\delta(t)+(\pi t)^{-1/2}\right]$$

(2) large time domain:

$$C_D = C_d\left\{1+\frac{3}{8}R_{ep}\left[\left(1+\frac{4}{t^2R_{ep}^{\ 4}}\right)erf\left(\frac{1}{2}t^{1/2}R_{ep}\right)+\frac{2}{\sqrt{\pi t}R_{ep}}\left(1-\frac{2}{tR_{ep}^{\ 2}}\right)\exp\left(-\frac{tR_{ep}^{\ 2}}{4}\right)\right]+\frac{9}{40}R_{ep}^{\ 2}\ln(R_{ep})\right\}$$

The similar relationships for steady drag coefficient C_d, like that in equation (3.14) are as follows:

$$C_d = \frac{24}{R_{ep}}\left(1+0.15R_{ep}^{\ 0.687}\right) \qquad R_{ep}<800$$

$$C_d = \frac{24}{R_{ep}}\left(1+0.125R_{ep}^{\ 0.72}\right) \qquad R_{ep}<1000$$

3.3 Numerical Simulation of Liquid-Particle Two-Phase Flow through Hydraulic Machinery by Two-Fluid Model

3.3.1 Numerical Method for Simulating Liquid-Particle Two-Phase Flow

Several numerical methods have been developed for solving the incompressible N-S equations by using the primitive variables, i.e., velocities and pressure. The main difference between these methods lies in the way of

finding a pressure field such that the flow field can be as close to divergence-free as possible (in order to satisfy the mass conservation equation). This is the main feature and difficulty for solving the incompressible viscous/turbulent flow problem, in which there is no obvious equation to obtain the unknown pressure. The pressure gradients only form a part of source terms of momentum equations. The main numerical approaches for solving this problem include:

1) The pseudo-compressibility method;
2) The approximate factorization scheme (the fractional step scheme);
3) The block-implicit finite difference method and the block-implicit finite element method;
4) The successive pressure-velocity correction scheme. The original version of the Semi-Implicit Method for Pressure Linked Equation (SIMPLE) was proposed by Patanker and Spalding (1972), which overcome the difficulty of solving pressure field by using the continuity equation and new variables, i.e., velocity and pressure corrections. This procedure has been widely used to solve many incompressible flow problems. A version of SIMPLE methods improved by Y.S. Chen (1986), SIMPLEC, will introduce to solve incompressible two-phase turbulent flow in this section [3.24].

Numerical Approach of SIMPLEC in Body-Fitted Coordinates

* Transformation of equations

In many flow problems, the geometry's boundaries are very complex, especially for internal flow problems with complicated boundaries, such as those of centrifugal impeller and hydraulic turbine. So the use of non-orthogonal body-fitted coordinates (BFC) can be beneficial in many aspects. It is not only why the boundary geometry can be represented closely using BFC systems, but also why the grid-refined solution can be easily obtained.

The governing equations of two-phase turbulent flow, expressed in the BFC system (ξ, η, ζ), can be represented by the following transport model equation (3.68) in the conservative form, in which ϕ denotes all the dependent variables respectively and Γ is the diffusion coefficient:

$$\frac{\partial(U_1\phi)}{\partial\xi}+\frac{\partial(U_2\phi)}{\partial\eta}+\frac{\partial(U_3\phi)}{\partial\zeta}=\frac{\partial}{\partial\xi}\left(J\alpha_1\Gamma\frac{\partial\phi}{\partial\xi}\right)+\frac{\partial}{\partial\eta}\left(J\alpha_2\Gamma\frac{\partial\phi}{\partial\eta}\right)$$
$$+\frac{\partial}{\partial\zeta}\left(J\alpha_3\Gamma\frac{\partial\phi}{\partial\zeta}\right)+\left(S_d+JS_\phi\right) \tag{3.68}$$

where S_ϕ is the source term indicated on the right side of governing equations. S_d is the extra source term resulting from non-orthogonality, that is,

$$S_d=\frac{\partial}{\partial\xi}\left(J\alpha_4\Gamma\frac{\partial\phi}{\partial\eta}\right)+\frac{\partial}{\partial\eta}\left(J\alpha_4\Gamma\frac{\partial\phi}{\partial\xi}\right)+\frac{\partial}{\partial\zeta}\left(J\alpha_5\Gamma\frac{\partial\phi}{\partial\eta}\right)+\frac{\partial}{\partial\eta}\left(J\alpha_5\Gamma\frac{\partial\phi}{\partial\zeta}\right)$$
$$+\frac{\partial}{\partial\xi}\left(J\alpha_6\Gamma\frac{\partial\phi}{\partial\zeta}\right)+\frac{\partial}{\partial\zeta}\left(J\alpha_6\Gamma\frac{\partial\phi}{\partial\xi}\right)$$

where U_1, U_2 and U_3 are contravariant velocity components in the body-fitted coordinates.

$$U_1=J\left(\xi_x u+\xi_y v+\xi_z w\right)$$
$$U_2=J\left(\eta_x u+\eta_y v+\eta_z w\right)$$
$$U_3=J\left(\zeta_x u+\zeta_y v+\zeta_z w\right)$$

where α_1, α_2, α_3, α_4, α_5 and α_6 are transformation coefficients.

$$\alpha_1=\xi_x'^2+\xi_y'^2+\xi_z'^2$$
$$\alpha_2=\eta_x'^2+\eta_y'^2+\eta_z'^2$$
$$\alpha_3=\zeta_x'^2+\zeta_y'^2+\zeta_z'^2$$
$$\alpha_4=\xi'_x\eta'_x+\xi'_y\eta'_y+\xi'_z\eta'_z$$
$$\alpha_5=\eta'_x\zeta'_x+\eta'_y\zeta'_y+\eta'_z\zeta'_z$$
$$\alpha_6=\xi'_x\zeta'_x+\xi'_y\zeta'_y+\xi'_z\zeta'_z$$

and

$$\xi'_x = J\xi_x = y_\eta z_\zeta - y_\zeta z_\eta$$
$$\xi'_y = J\xi_y = x_\zeta z_\eta - x_\eta z_\zeta$$
$$\xi'_z = J\xi_z = x_\eta y_\zeta - x_\zeta y_\eta$$

$$\eta'_x = J\eta_x = y_\zeta z_\xi - y_\xi z_\zeta$$
$$\eta'_y = J\eta_y = x_\xi z_\zeta - x_\zeta z_\xi$$
$$\eta'_z = J\eta_z = x_\xi y_\zeta - x_\zeta y_\xi$$

$$\zeta'_x = J\zeta_x = y_\xi z_\eta - y_\eta z_\xi$$
$$\zeta'_y = J\zeta_y = x_\eta z_\xi - x_\xi z_\eta$$
$$\zeta'_z = J\zeta_z = x_\xi y_\eta - x_\eta y_\xi$$

And J is the Jacobia of the coordinate transformation.

$$J = \partial(x,y,z)/\partial(\xi,\eta,\zeta) = \begin{vmatrix} x_\xi & y_\xi & z_\xi \\ x_\eta & y_\eta & z_\eta \\ x_\zeta & y_\zeta & z_\zeta \end{vmatrix} = x_\xi \cdot \xi'_x + y_\xi \cdot \xi'_y + z_\xi \cdot \xi'$$

* Discretization of equations

Discretization of governing equation (3.66) is performed by using finite difference approximations in the transformed domain. The second order central differencing is used for approximating the diffusion and the source terms. For the convective terms, the hybrid differencing scheme is employed, that is, using central differecing for cell Peclet number less than or equal to two and switching to upwind differencing when the cell Peclet number is greater than two. The finite difference equation is arranged by collecting terms according to the grid nodes around a central volume as shown in Figure 3.1.The final expression is given by equation (3.67) in which A represents the link coefficients between the grid nodes P, E, W, N, S, T, B, WE, NW, NT, NB, SE, SW, ST, SB, ET, EB, WT and WB.

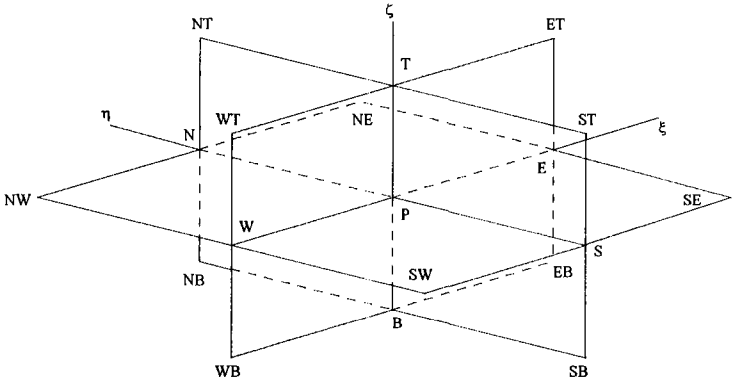

Figure 3.1 Three-dimensional grid system

$$A_P\phi_P = A_E\phi_E + A_W\phi_W + A_N\phi_N + A_S\phi_S + A_T\phi_T + A_B\phi_B + S_1 \tag{3.69}$$

where

$$\begin{aligned} S_1 = S &+ A_{NE}\phi_{NE} + A_{NW}\phi_{NW} + A_{NT}\phi_{NT} + A_{NB}\phi_{NB} \\ &+ A_{SE}\phi_{SE} + A_{SW}\phi_{SW} + A_{ST}\phi_{ST} + A_{SB}\phi_{SB} \\ &+ A_{ET}\phi_{ET} + A_{EB}\phi_{EB} + A_{WT}\phi_{WT} + A_{WB}\phi_{WB} \end{aligned}$$

$$A_P = A_E + A_W + A_N + A_S + A_T + A_B$$

$$A_E = \left\langle \left|\frac{F_e}{2}\right|, D_e\left\langle -\frac{F_e}{2} = D_e\left\{\left\langle \left|\frac{P_{\Delta e}}{2}\right|, 1\left\langle -\frac{P_{\Delta e}}{2}\right.\right.\right.\right.$$

$$A_W = \left\langle \left|\frac{F_w}{2}\right|, D_w\left\langle +\frac{F_w}{2} = D_w\left\{\left\langle \left|\frac{P_{\Delta w}}{2}\right|, 1\left\langle +\frac{P_{\Delta w}}{2}\right.\right.\right.\right.$$

$$A_N = \left\langle \left|\frac{F_n}{2}\right|, D_n\left\langle -\frac{F_n}{2} = D_n\left\{\left\langle \left|\frac{P_{\Delta n}}{2}\right|, 1\left\langle -\frac{P_{\Delta n}}{2}\right.\right.\right.\right.$$

$$A_S = \left\langle \left| \frac{F_s}{2} \right|, D_s \right\rangle + \frac{F_s}{2} = D_s \left\{ \left\langle \left| \frac{P_{\Delta s}}{2} \right|, 1 \right\rangle + \frac{P_{\Delta s}}{2} \right\}$$

$$A_T = \left\langle \left| \frac{F_t}{2} \right|, D_t \right\rangle - \frac{F_t}{2} = D_t \left\{ \left\langle \left| \frac{P_{\Delta t}}{2} \right|, 1 \right\rangle - \frac{P_{\Delta t}}{2} \right\}$$

$$A_B = \left\langle \left| \frac{F_b}{2} \right|, D_b \right\rangle + \frac{F_b}{2} = D_b \left\{ \left\langle \left| \frac{P_{\Delta b}}{2} \right|, 1 \right\rangle + \frac{P_{\Delta b}}{2} \right\}$$

where F is the convective coefficients and D the conductive coefficients as follows,

$$F_e = (\rho U \Delta\xi)_e \qquad F_w = (\rho U \Delta\xi)_w \qquad F_n = (\rho V \Delta\eta)_n$$
$$F_s = (\rho V \Delta\eta)_s \qquad F_t = (\rho W \Delta\zeta)_t \qquad F_b = (\rho W \Delta\zeta)_b$$

$$P_{\Delta e} = \frac{F_e}{D_e},\ P_{\Delta w} = \frac{F_w}{D_w},\ P_{\Delta n} = \frac{F_n}{D_n},\ P_{\Delta s} = \frac{F_s}{D_s},\ P_{\Delta t} = \frac{F_t}{D_t},\ P_{\Delta b} = \frac{F_b}{D_b}$$

$$D_e = \left[\frac{\Gamma_\varphi}{J} \alpha_1 \right]_e, \quad D_w = \left[\frac{\Gamma_\varphi}{J} \alpha_2 \right]_w, \quad D_n = \left[\frac{\Gamma_\varphi}{J} \alpha_3 \right]_n$$
$$D_s = \left[\frac{\Gamma_\varphi}{J} \alpha_4 \right]_s, \quad D_t = \left[\frac{\Gamma_\varphi}{J} \alpha_5 \right]_t, \quad D_b = \left[\frac{\Gamma_\varphi}{J} \alpha_6 \right]_b$$

where the <,> represents taking the maximum values, P_Δ is the grid Reynolds number. The hybrid-differencing scheme can be indicated as follows,

$$P_{\Delta e} > 2 \left. A_E \right/ D_e = 0$$
$$-2 \le P_{\Delta e} \le 2 \left. A_E \right/ D_e = 1 - \frac{1}{2} P_{\Delta e}$$
$$P_{\Delta e} < -2 \left. A_E \right/ D_e = -P_{\Delta e}$$

SIMPLEC solver for incompressible flow

The SIMPLEC algorithm is applied to drive the pressure field and the velocity field to be divergence free and convergence.

At first, the finite difference momentum equations for velocity components u, v, w can be written as

$$\begin{aligned} A_p^u\ u_p^* &= \sum_i A_i^u\ u_i^* - P_x^* + S_u \\ A_p^v\ v_p^* &= \sum_i A_i^v\ v_i^* - P_y^* + S_v \\ A_p^w\ w_p^* &= \sum_i A_i^w\ w_i^* - P_z^* + S_w \end{aligned} \tag{3.70}$$

where u^*, v^* and w^* are the solutions of equation (3.70), in order to satisfy the continuity equation, the velocity and the pressure are corrected according to the following relations:

$$\begin{aligned} u &= u^* + u' \\ v &= v^* + v' \\ w &= w^* + w' \\ p &= p^* + p' \end{aligned} \tag{3.71}$$

Then a new set of momentum equations can then be approximately constructed using the divergence-free flow field u, v, w and p

$$\begin{aligned} A_p^u u_p &= \sum_i A_i^u u_i - P_x + S_u \\ A_p^v v_p &= \sum_i A_i^v v_i - P_y + S_v \\ A_p^w w_p &= \sum_i A_i^w w_i - P_z + S_w \end{aligned} \tag{3.72}$$

By subtracting equation (3.70) from equation (3.72), respectively, the following equations are resulted

$$\begin{aligned} A_p^u u_p' &= \sum_i A_i^u u_i' - P_x' \\ A_p^v v_p' &= \sum_i A_i^v v_i' - P_y' \\ A_p^w w_p' &= \sum_i A_i^w w_i' - P_z' \end{aligned} \tag{3.73}$$

According to the SIMPLEC algorithm, equation (3.73) are rearranged by subtracting terms, $\sum A_i^u u_p$ from both sides to be as,

$$\begin{aligned} \left[A_p'' - \sum_i A_i''\right] u_p &= \sum_i A_i'' \left(u_i - u_p\right) - p_x \\ \left[A_p'' - \sum_i A_i''\right] v_p &= \sum_i A_i'' \left(v_i - v_p\right) - p_y \\ \left[A_p'' - \sum_i A_i''\right] w_p &= \sum_i A_i'' \left(w_i - w_p\right) - p_z \end{aligned} \tag{3.74}$$

The first terms on the right-hand sides of equation (3.74) are neglected to simplify the formulation. Thus

$$\begin{aligned} u_p &= -\left(\frac{1}{A_p^u - \sum_i A_i^u}\right) p_x = -D_u P_x \\ v_p &= -\left(\frac{1}{A_p^v - \sum_i A_i^v}\right) p_y = -D_v P_y \end{aligned} \tag{3.75}$$

$$w_p = -\left(\frac{1}{A_p^w - \sum_i A_i^w}\right) p_z = -D_w P_z$$

By equation (3.72), the continuity equation can be written as

$$u_x + v_y + w_z = \left(u_x^* + v_y^* + w_z^*\right) + \left(u_x + v_y + w_z\right) = 0 \tag{3.76}$$

Substituting equation (3.75) into equation (3.76), the following pressure correction equation can be obtained:

$$-\left[\left(D_u P_x\right)_x + \left(D_v P_y\right)_y + \left(D_w P_z\right)_z\right] = -\left(u_x^* + v_y^* + w_z^*\right) \tag{3.77}$$

Solution Procedures of Two-Phase Flow

The present numerical method for solving liquid-particulate two-phase flow contains the following steps:

1) Estimate the initial velocity and the pressure field of a single liquid phase flow in the computational domain.
2) Solve for the velocity, the pressure and the turbulent characters k and ε in the single phase flow, by using the SIMPLEC method, to get coarse convergence solution of the flow.
3) Based on the single phase flow solution, we solve for the particulate turbulent flow field, by using the algebraic particulate phase turbulence model.
4) Calculate the interaction terms between the liquid- and the particulate-phases to get some source terms in the control equations for the liquid flow.
5) Solve again the momentum equations, the turbulent energy and its dissipation rate equation for single phase flow, but including the interaction terms.
6) Set the new variables and return to step 3); repeat the process until it converges.

3.3.2 Calculated Examples of Two-Turbulent Flow by Using Two-Fluid Model

Numerical Simulation of Liquid-Particle (or Gas) Two-Phase Turbulent Flow through a Centrifugal Pump Impeller

The numerical approaches and the computer program has been applied to calculate the single-phase incompressible turbulent flow through a rectangular region with backward-facing step with comparison to the measured data [3.25], where the maximum differences between calculated- and measured-data is less than 7%, and through a centrifugal impeller with comparison to the experimental results by the PIV technique [3.26].

On the bases of the theory of two-fluid model for multiphase flow, the dispersed phase in these flow, at dilute concentration conditions, can be assumed to be a pseudo-fluid, which occupies a certain fraction volume in the whole flow domain shared with the continuum phase, i.e., the real fluid phase. According to this assumption, the simulation of two-dimensional two-phase flow through a centrifugal pump impeller has been conducted by using the $k-\varepsilon-A_p$ turbulence model and the SIMPLEC algorithm at dilute concentration conditions, for example, *Cv* (volume concentration) is less than 5%.

Boundary Conditions for Calculations of Liquid-Particle Two-Phase Turbulent Flow through a Centrifugal Pump Impeller

* Flow in liquid phase

(a) Inlet boundary. The inlet values of the radial velocity component u_{r1} and the circumferential one $u_{\theta 1} = \omega_{r1}$ are directly specified and easily altered. The inlet value of turbulent kinetic energy k_{in} adopts 0.5 ~ 1.5% of the inlet mean kinetic energy of flow, that is,

$$k_{in} = 0.005u_{r1}^2$$
$$\mu_{tin} = \rho u_{r1} l / 100.0$$
$$\varepsilon_{in} = C_\mu k_{in}^{3/2} / l$$

where l is the specific length of the inlet boundary, μ_t the eddy viscosity. The values of k_{in}, μ_{tin} and ε_{in} do not severely affect on the final results.

(b) Outlet boundary. The velocity components at the outlet of the calculated domain are deduced from their immediate upstream values by adding a fixed overall mass, whose amount is calculated to ensure overall mass conservation. The outlet values of k and ε are unimportant, because limited effects of the upstream are known at high Reynolds number and zero gradient is specified.

(c) Solid walls. In the near wall regions, to avoid the need for detailed calculations the wall functions are introduced and are used in the finite difference calculations. That is, the total tangential velocity V_B at the point B near the wall is corrected by velocity profile

$$V_B^+ = \begin{cases} Y_B^+ & Y_B^+ < 11.63 \\ \left(\frac{1}{\lambda}\right)\ln\left(EY_B^+\right) & Y_B^+ > 11.63 \end{cases} \tag{3.78}$$

where $\lambda = 0.41$ and $E = 9.0$. And

$$\begin{aligned} {}_B^+ &= V_B / u_\tau \\ u_\tau &= \sqrt{\tau_w / \rho} \\ Y_B^+ &= Y_B u_\tau / \nu = \rho C_\mu^{1/4} k_B^{1/2} Y_B / \mu \end{aligned}$$

where Y_B is the normal distance from the point B to the wall, τ_B is an approximation for wall stress τ_w near the wall and is formulated by neglecting the convection and the diffusion of the turbulent kinetic energy equation in this region.

$$\tau_B = C_\mu^{1/2} \rho k_B$$

Then, we obtain

$$\tau_w = \rho V_B C_\mu^{1/4} k_B^{1/2} \lambda / \ln\left(EY_B^+\right) \tag{3.79}$$

From the foregoing equation, then

$$k_B / \tau_B = C_\mu^{-1/2} / \rho = \text{constant}$$

which implies that the wall flux of k is zero. Accordingly, zero normal gradient prescription rate near the wall, the length scale is assumed to be proportional to the normal distance from the wall, then the turbulent energy dissipation rate ε_B and the generation term of turbulent kinetic energy G_w in this region is as

$$\begin{aligned} \varepsilon_B &= \frac{C_\mu^{3/4} k_B^{3/2}}{\lambda Y_B} \\ G_w &= \tau_w \frac{\partial u}{\partial y}\Big|_B \end{aligned} \tag{3.80}$$

(d) Boundary condition of pressure. The correction values p' of SIMPLEC scheme possess zero gradient specification every where except at a point is then required to all the pressure to be calculated.

(e) Periodic condition. On the pairs of upstream and downstream boundaries extending from the blade leading edge and the trailing edge respectively, the period conditions must satisfied, that is,

$$\phi_{right} = \phi_{left}$$

* Particulate phase

Variables in the particulate phase also possess zero normal gradient specification everywhere except the inlet. At the inlet particle velocity components are assumed to have the same values as those in liquid flow for simplicity. And the bulk density of particle phase (or particle number) at the inlet can be easy determined according to the known volumetric condition. The velocity components and the bulk density (or the particle number) at the outlet must be calculated to ensure overall mass conservation also by adding fixed numbers from their immediately upstream values. The particle (or bubble) number flux is defined as

$$Q_p = \sum_{i=1}^{n} N_{pi} A_i V_{pi}$$

where n is the number of grid stations in a section of the domain, N_{pi} is the particle number at the station, V_{pi} is velocity and A_i the area at the station. And N_p is defined as the particle number in the unit volume, that is,

$$N_p = \frac{6C_v}{\pi d_p^3} \tag{3.81}$$

where C_v is the volumetric concentration and d_p the particle diameter.

* Conditions for gas phase flow.

For the gas-liquid two-phase flow, at this dilute condition the flow pattern is the bubble flow in the liquid. The diameter of gas bubble is assumed to be 1.0 mm at the inlet of impeller, which will change according to the equi-thermal process equation.

Calculated Results of Centrifugal Pump Impellers

The calculation was conducted through a centrifugal pump impeller. The geometrical and flow parameters of the impeller are as follows:

Inlet diameter:	$D1 = 130\ mm$
Outlet diameter:	$D2 = 330\ mm$
Inlet angle:	$\beta 1 = 45°$
Outlet angle:	$\beta 2 = 18°$
Particle density:	$\rho_p = 1.295\ kg/m^3$
Volume concentration:	$C_v = 5\%$
Particle diameter:	$d_p = 1\ mm$
Gas density:	$\rho_g = 1.295\ kg/m^3$
Volume concentration:	$C_v = 5\%$
Gas bubble diameter:	$d_p = 1\ mm$
Liquid density:	$\rho_g = 1.0 \times 10^3\ kg/m^3$
Inlet velocity of liquid and gas:	$V_{in} = 6\ m/s$
Rotating speed of impeller:	$n = 1450\ rpm.$

Figure 3.2 shows the velocity fields of continuum phase through the impeller, at different flow conditions, such as in Figure 3.2 (a) at the particle-

liquid flow condition, (b) at the gas-liquid flow condition and (c) at the single phase flow condition. From these figures it is clear that the gas-liquid flow has a little influence on the liquid phase flow, and that on the contrary, the particle -liquid flow has a definite influence on the liquid flow.

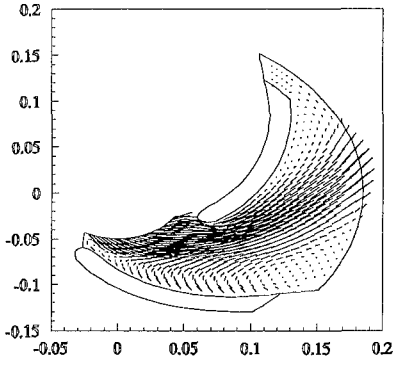

[The continuous phase (liquid) velocity profile (S-L)]

(a)

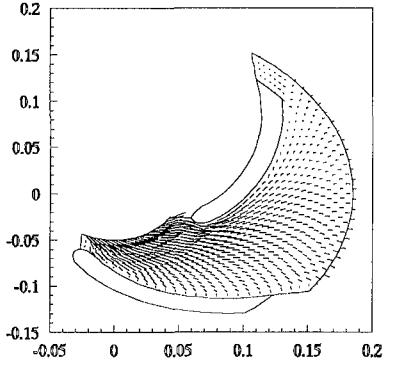

[The continuous phase (liquid) velocity profile (G-L)]

(b)

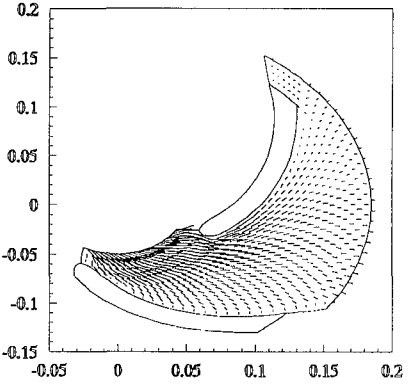

(c)

(a) At particle-liquid two phase flow
(b) At gas-liquid two-phase flow
(c) At single liquid phase flow

Figure 3.2 Velocity field of liquid phase

Figure 3.3 is the slip velocity distributions between the liquid phase and the particle phase (in Figure 3.3 (a)), and between the liquid phase and the gas phase (in Figure 3.3 (b)). The slip velocity $\Delta\vec{u}$ between two phases can be defined as

$$\Delta\vec{u} = \vec{u}_d - \vec{u}_c \tag{3.82}$$

where $\vec{u}_d$ is the velocity of dispersed phase, and $\vec{u}_c$ that of continuous phase.

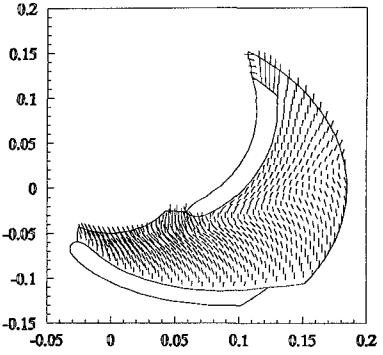

[The velocity difference of two phases (S-L)]

(a) At particle-liquid condition

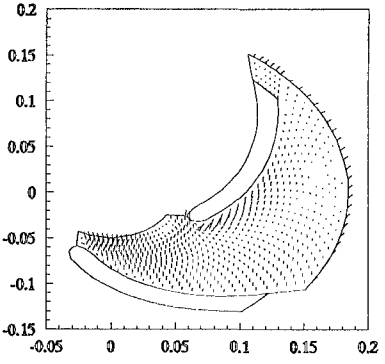

[The velocity difference of two phases (G-L)]

(b) At gas-liquid condition

Figure 3.3 Slip velocity between two phases

The velocities between gas- phases and liquid-phases are not too much difference. But the velocity difference between particle and liquid is large because of large response time of particles, which results in the increase of particle velocities at the outlet of centrifugal impeller.

Figure 3.4 is the pressure distribution through the impeller, which is not much difference with that of pure liquid flow. The same pressure distribution for liquid particle flow can be found in references [3.21, 3.27]. Figure 3.5 is distributions of the particle number (a) and the gas bubble number (b), which is the relative number to the number at inlet. The particle number at the inlet is $N_p = 9.55 \times 10^7$ at the condition $C_v = 5\%$ and $d_p = 1.0$ mm. From these figures, it is shown the particle number is denser than that at the inlet, and also denser near blade surfaces than that at the middle part of the flow passage. From the results it can be obtained that the calculation model and the computer program can be used to predict the main flow characters of gas-liquid flow through the impeller.

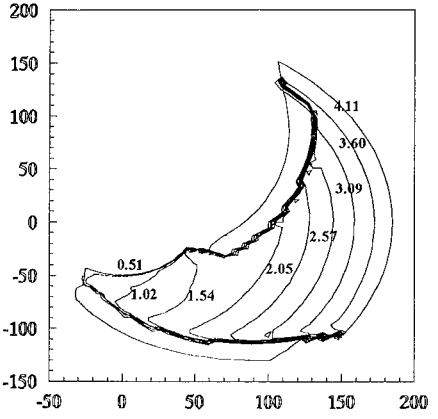

Figure 3.4 Pressure distribution at gas-liquid condition

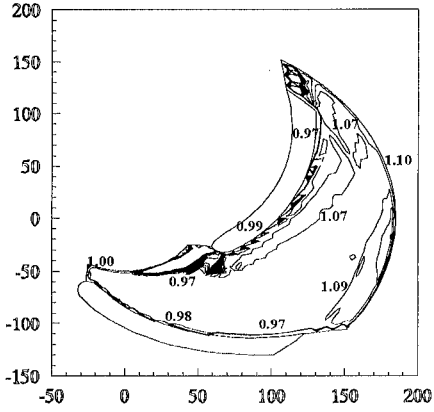

(a) Particle phases

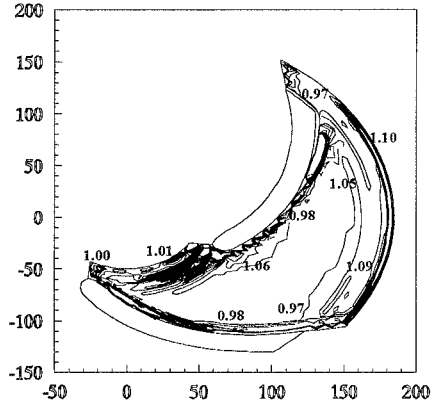

(b) Gas bubble

Figure 3.5 Number distribution

Three-Dimensional Particle-Liquid Two-Phase Turbulent Flow Calculation through a Hydraulic Turbine Runner

The three-dimensional turbulent particulate-liquid two-phase flow have been simulated through a hydraulic Francis turbine runner by using the k- ε -A_p turbulence model and the SIMPLEC algorithm on the bases of the theory of two-fluid model for multiphase flow.

Parameters of the turbine runner and boundary conditions

Parameters of the turbine runner are as follows

Diameter of runner:	$D = 1$ m
Head:	$H = 1$ m
Rotating speed:	$n = 82$ rpm
Discharge:	$Q = 0.98$ m^3/s
Blade number:	$Z = 14$
Particle diameter:	$d_p = 1.0$ mm
Particle volume concentration:	$C_v = 5\%$

The boundary conditions at the inlet of runner, for example, the inlet velocities of the continuous phase and dispersed phase, the particle number, the turbulent kinetic energy and the turbulent energy dissipation rate, are specified according to the known conditions. The outlet conditions are given as the Neumann condition. The velocity of continuous phase near walls and so on is determined according to the wall function. For the pressure and the particle number on other boundaries the Neumann condition is also specified except one station in the domain, where the value of pressure is fixed in order to get a definite solution.

Calculated Results of Turbine Runners

In the grid system of the runner, the flow passage through the runner is divided several parts from the blade pressure side to the suction side. The surface $K = 2$ is the geometrical surface close to the pressure side. And from the crown (hub) to the band (shroud) of the runner, the passage also is divided, for example, $J = 2$ indicates the surface close to the crown. Figure 3.6 shows the relative velocity distribution on the surfaces of $J = 6$ and $J = 14$. The velocity increases from the pressure side to the suction side, except near the trailing edge of the blade. And so does it from the inlet to the outlet (*L/L0* from 0 to 1) of the runner.

As in Figure 3.6, the same relative velocity distribution of dispersed phase is shown in Figure 3.7. This velocity is much smaller than the continuous phase velocity, because the velocity increases from the inlet to the outlet, the friction drag and other forces between two phase resist the increase of the continuous phase velocity. Figure 3.8 shows the pressure distributions through the runner on different surfaces, i.e., $J = 2$, 6, 14 and 18. It increases from suction side to pressure side, and decreases from inlet to outlet.

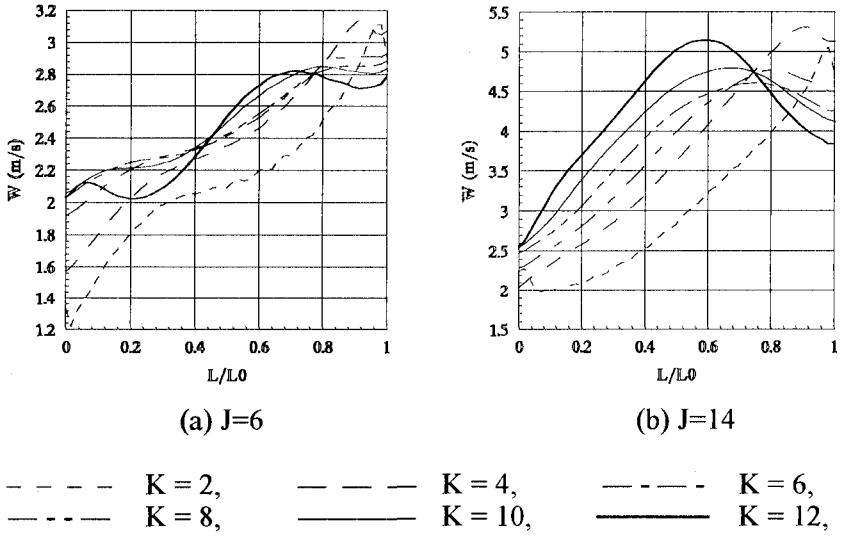

Figure 3.6 Velocity distribution of continuous phase

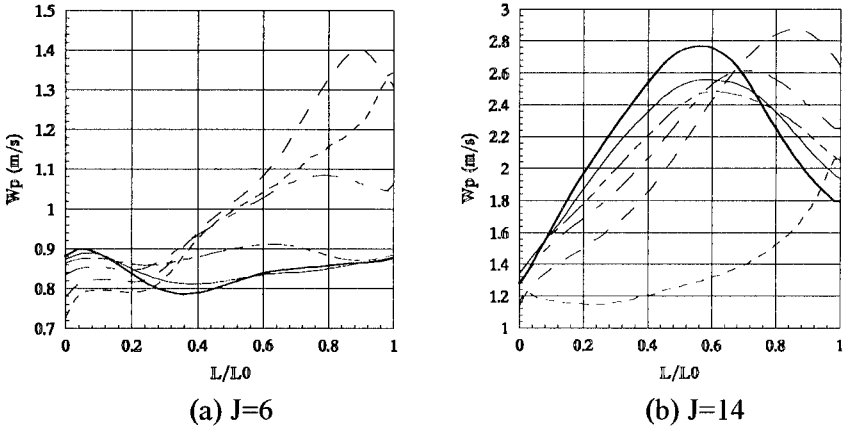

Figure 3.7 Velocity distribution of particulate phase

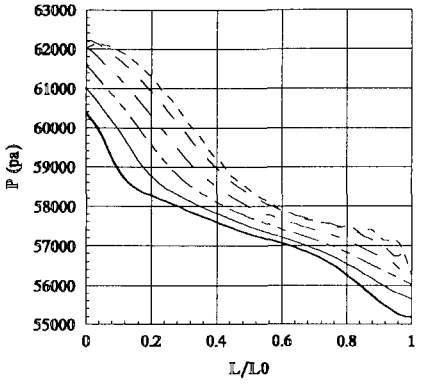

(a) J=2

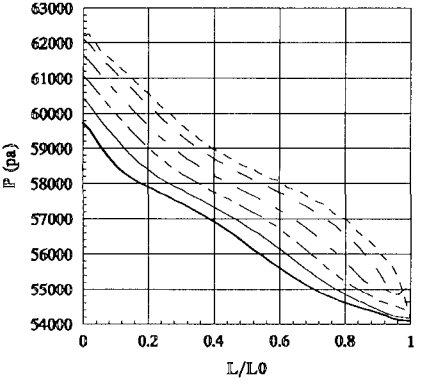

(b) J=6

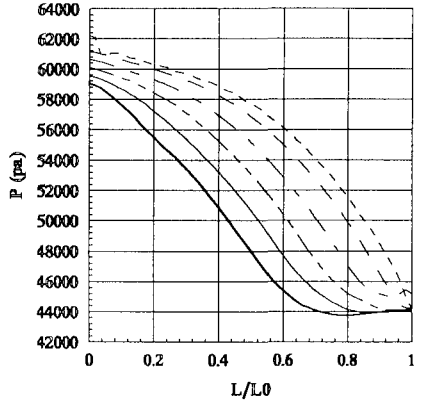

(c) J=14

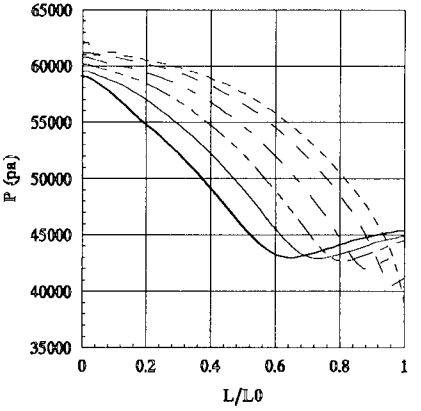

(d) J=18

Figure 3.8 Pressure distribution

References

3. 1 Marble, F.E., (1963). 'Dynamics of a gas containing small solid particles', Proc. of 5th *AGARD Combustion and Propulsion Colloquium*, Pergamon Press, London.

3. 2 Drew, D.A. and Segal, L.A., (1971). 'Averaged equation for two-phase flow', *Studies in Applied Math*, Vol. 50, 205-231

3. 3 Ishii, M., (1975). *Thermo-fluid dynamic theory of two-phase flow*, Eyrolles, Paris.

3. 4 Roco, M.C. and Reinhart, E., (1980). 'Calculation of solid particles concentration in centrifugal pump impeller using finite element technique', *7th Hydrotransport*, 359-376.

3. 5 Danon, H., Wolfshtein, M. and Hetsroni, G., (1974). 'Numerical calculations of two-phase turbulent round Jets', *Int. J. Multiphase Flow*, Vol. 3, 223-234.

3. 6 Al Taweel, A.M. and Landau, J., 1977, 'Turbulence modulation in two-phase jets', *Int. J. Multiphase Flow*, Vol. 3, 341-351.

3. 7 Genchiev, Zh.D. and Karpuzov, D.S., (1980). 'Effects of motion of dust particles on turbulence transport equations', *J. Fluid Mech.*, Vol. 103, 833-842.

3. 8 Melville, W.K. and Bray, K.N.C., (1979). 'A model of the two-phase turbulent jet', *Int. J. Heat Mass Transfer*, Vol. 22, 647-656.

3. 9 Sharma, M.P. and Crowe, C.T., (1978). 'A novel physico-computational model for quasi one-dimensional gas particle flow', *Trans. ASME, J. Fluids Engng.*, Vol. 100, 343-349.

3. 10 Michaelides, E.E. and Farmer, L.K., (1984). 'A model for slurry flow based on the equation of turbulence', *ASME FED*-Vol. 13, Liquid-Solid Flow and Erosion Wear in Industrial Equipment, 27-32.

3. 11 Shuen, J.S., Chen, L.D. and Faeth, G.M., (1983). 'Prediction of the structure of turbulent particle laden in rounded jet', *AIAA J.*, Vol. 21, 1480-1483.

3. 12 Crowder, R.S., Daily, J.W. and Humphrey, J.A.C., (1984). 'Numerical calculation of particle dispersion in a turbulent mixing layer flow', *J. Pipelines,* Vol. 4, 3 , 159-170.

3. 13 Roco, M.C. and Shook C.A., (1983). 'Modeling slurry flow: The effect of particle size', *Canadian J. Chem. Engng.*, Vol. 61, 4, 494-504.

3. 14 Bertodano, M.L., Lee S-J., Lahey, R.T. and Drew, D.A., (1990). 'The prediction of two-phase turbulence and phase distribution phenomena using a Reynolds stress model', *Trans. ASME, J. Fluid Engng.*, Vol. 112, 107-113.

3. 15 Zhou L. X., (1994). 'Theory of gas-particle two-phase flow and combustion and its numerical simulation', Publisher of Sciences in China, 1994.

3. 16 Ma, D.N. and Roco, M.C., 1988, 'Probabilistic three-dimensional model for slow shearing particulate flow: wet friction', *ASME* FED-Vol. 55, 53-60.

3. 17 Ahmadi, G. and Abou-Zaid, S., (1990). 'A Rate-dependent hermodynamical model for rapid granular flow', *Int. J. Non-Newtonian Fluid Mechanics*, Vol. 35, 15-30.

3. 18 Gidaspow, D., Jayaswal, U.K. and Ding, J., (1991). 'Navier-Stokes equation model for liquid solid flow using kinetic theory', *ASME* FED-Vol. 118, *Liquid-Solid Flow*, 165-172.

3. 19 Dai, J. and Wu, Y.L., (1993). 'Numerical simulation of turbulent liquid-particle flow in centrifugal impeller', *Proc. Int. Symp. on Aerospace and Fluid Science*, Sendai, 401-410.

3. 20 Wu, Y.L., Oba, R. and T. Ikohagi, (1994). 'Computation on turbulent dilute liquid-particle flow through a centrifugal impeller', *Japenese J. of Muliphase Flow*, Vol. 8, No. 2, 118-125.

3. 21 Gosman, A.D. and Ioannides, E., (1981). 'Aspects of computer simulation of liquid-fuelled combustors', AIAA paper 81-0323.

3. 22 Chen, X.Q. and Pereira J.C.F., (1996). 'Numerical study of a onevaporating polydispersed turbulent hollow-cone spray', *ASME* FED-Vol. 236, *Fluid Engineering Division Conference*, Vol. 1, 41-50.

3. 23 Chen, Y.S., (1986). 'Computer code for three-dimensional incompressible flow using nonorthoganal body-fitted coordinate systems', NASA CR-178818.

3. 24 Wu, Y.L., Dai, J., Oba, R., Ikohagi, T., (1995). 'Turbulent flow simulation through centrifugal pump impeller at design and off-design conditions', *Proc. of 2nd ICPF*, Tsinghua University, Beijing, 155-167.

3. 25 Wu Y.L., Sun Z.X., Oba, R., Ikohagi, T., (1995). 'Study on flow through centrifugal impeller by turbulent simulation', *ASME* FED-Vol. 222, *Fluid Machinery*, 63-68.

3. 26 Wu, Y.L., (1996). 'Computation on turbulent dilute liquid-particle flow through a centrifugal impeller by using the turbulence model', *ASME* FED-Vol. 236, *Proc. of the Fluids Eng. Division Summer Meeting*, 1996, Vol. 1, 265-270.

3. 27 Chang, K.C. and Yang J.C., (1996). 'Transient effects of drag coefficient in the Eulerian-Lagrangian calculation of two-phase flow', *ASME* FED-Vol. 236, *Fluid Engineering Division Conference*, Vol. 1, 5-10.

3. 28 Elghobashi, S.E. and Abou-Arab, T.W., (1983). 'A two-equation turbulence closure for two-phase flow', *Phys. Fluids*, Vol. 26, 931-938.

Chapter 4

Design of Hydraulic Machinery Working in Sand Laden Water

H. Brekke, Y.L. Wu and B.Y. Cai

4.1 Hydraulic Design of Turbines

H. Brekke

4.1.1 Introduction

Sand erosion in turbomachines in general may be divided into three categories:

1. Micro erosion which may be found on surfaces exposed to very high velocities where silt or sand grains of magnitude 60 μm and smaller are given a high rotational velocity by the turbulence in the boundary layers and thus causing a relatively strong abrasive erosion.

2. Secondary flow vortex erosion, which you may find in a so-called horseshoe vortex in corners of conduits, or other places where vortex and secondary flow are caused by combined effect from boundary layers and/or decelerated or accelerated flow.

3. Accelerations normal to streamlines, which will separate the sand grains and bring the sand grains to follow a path different from the water flow and in collision with the walls of the conduits. Sand grains with sizes from 0.5 mm and up will normally cause severe damage in flow with acceleration normal to the streamlines.

The conduits may be formed by blades in runners, guide vanes etc.

The design of hydraulic machinery working with Reynolds numbers, Re, from 10^6 to 10^8 will normally be exposed to flow conditions of all three categories.

The damage will depend on the hardness of the sand, the shape and grain size and naturally of the amount of sand as well as the absolute velocity and the hydraulic radius of the regarded conduit.

Special caution must be taken in design of labyrinth seals in turbines or so called wear rings in pumps as well as shaft seals due to very small hydraulic radii and possible direct abrasive erosion due to direct simultaneous contact between the sand grains and the rotational and stationary parts. It should also be emphasized that small turbines will get a more severe damage from sand than larger turbines of the same specific speed because of smaller hydraulic radii and smaller radii in the curvature which brings a relatively larger amount of sand in contact with the surface and cause a higher acceleration normal to the stream lines.

The design of hydraulic turbines may be divided into following categories with a significant different pattern of erosion.

- Impulse turbines
- High-head reaction turbines (Low specific speed Francis Turbines)
- Low-head reaction turbines (High specific speed Francis and Kaplan turbines)

4.1.2 Impulse Turbines

The most commonly used impulse turbine is the Pelton turbine. The classic type with horizontal shaft is shown in Figure 4.1 and the later developed vertical shaft type is shown in Figure 4.2. The less known Turgo turbine which is an axial flow machine with jets inclined relatively to the a plane normal to the shaft is shown Figure 4.3.

Because the nature of sand erosion will be the same for both types of these turbines and because very little information exits on sand erosion in Turgo turbines the discussion in this chapter will deal with Pelton turbines only. Also the low head type of impulse machine, the Ritmeyer turbines will not be described for two reasons. At first, it is not quite clear if this turbine type is classified as an impulse machine. Secondly, the Ritmeyer turbines are designed for low heads and thus the sand erosion will be less severe than machine types like Pelton turbines for high head.

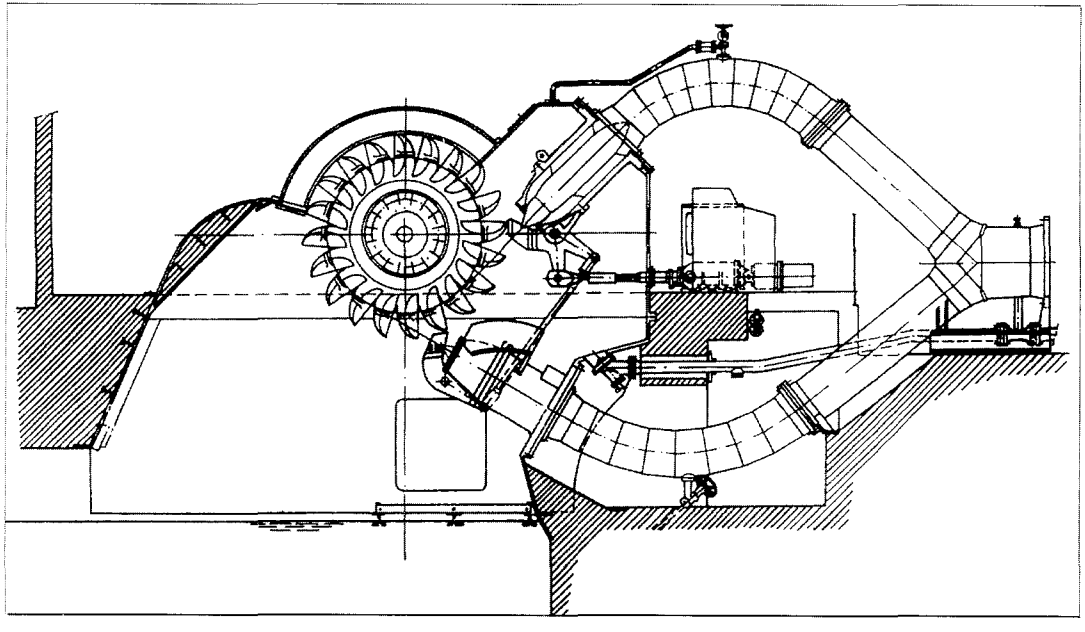

Figure 4.1 Horizontal Pelton turbine

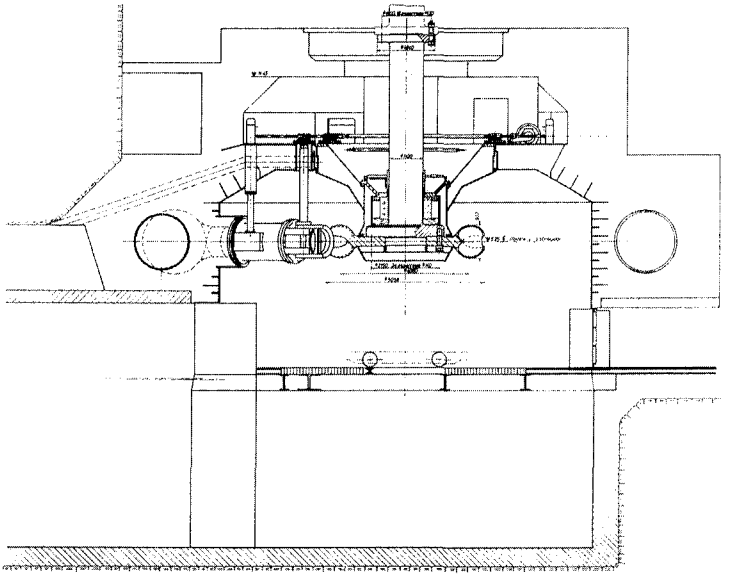

Figure 4.2 Vertical Pelton trubine

Because the Pelton turbines normally are designed for heads above 600 m, the velocity in the jets will be higher than 100 m/sec and the maximum acceleration of the particles in the buckets will normally be more than 50000 m/sec^2 depending on the size of the buckets and head of the plant.

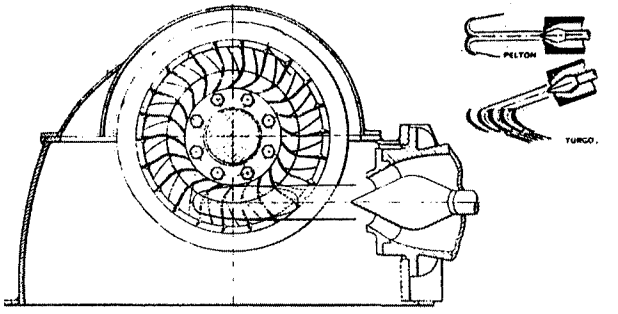

Figure 4.3 Turgo impulse turbine

In order to study the parameters or to determine which have influence on the sand erosion, it is necessary to divide the design into following portions:

- The inlet including the inlet valve
- The nozzles
- The runner of Pelton wheel
- The wheel pit

The Inlet and Valve

For a horizontal Pelton turbine and especially for a vertical multijet turbine the length/diameter ratio will be approximately 3 times longer than for a Francis turbine designed for the same head.

Because of this the velocity will normally be kept moderate and following formula may be used for normal turbines(except minihydro turbines).

$$C = K_i (2gHe)^{0.5}, \quad (0.08 < K_i < 0.1) \tag{4.1}$$

In the bifurcation sections the flow is accelerated towards the inlet in front of the nozzles after a local deceleration.

A typical design of a manifoil of a Pelton turbine is shown in Figure 4.4.

The velocities in the inlet will then be from 10 m/sec to 15 m/sec for heads from 600 ~ 1500 m, which is the normal range of head for Pelton turbines.

Because of the moderate relative velocities in the inlet section the sand erosion will be moderate and normal modern high resistant paint (epoxy based or others) will meet the requirement of erosion resistance with normal periodic maintenance.

Special heavy content of gravel or sand may require special maintenance with special paint soft rubber based coating or equivalent. In such cases a low velocity should be chosen in the inlet portion.

The velocity in the inlet valve is for economical and constructional reasons (maximum weight limitation) normally chosen somewhat higher than in the inlet manifoil or distributor. After the inlet valve a conical section with decelerated flow must then be installed.

The velocity in the inlet valve may be expressed by following formula

$$C = K_v (2gHe)^{0.5}, \quad (0.095 < K_v < 0.12) \tag{4.2}$$

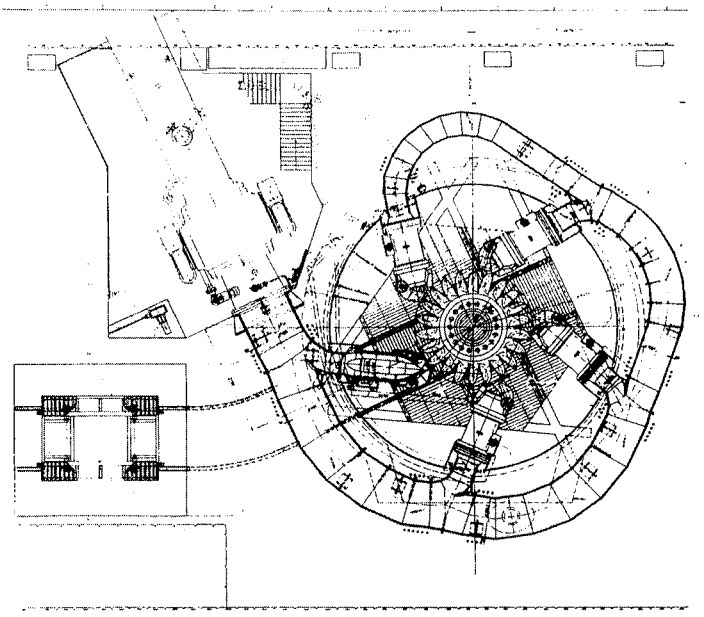

Figure 4.4 Manifoil for 5 jet turbine

In the by pass pipe the velocity in the bends should be chosen below 25 m/sec if sand laden water is expected. (The operational time for filling of the distributor through the by pass pipe normally is relatively short and thus the erosion will be reduced and a higher velocity than in the inlet has been chosen for this reason. Inspection for erosion should however be made as part of the maintenance program.)

The valve seals in the by pass system are exposed to heavy erosion during the closing period in the same way as the seals on the main valve during emergency closure with open needles. For Pelton turbines rubber seal has not sufficient strength to withstand an emergency closing sequence without being damaged by touring when the steel is approaching the rubber during the closure with full pressure difference across the seal.

Also seals completely made of steel are exposed to damage during emergency closure, but also during normal closure because of sand jammed between the movable and stationary part during closure.

Because of the high pressure any leakage caused by sand will cause serious damage of a closed seal due to cavitation when the turbine is stopped if also the nozzles are leaking and the valve is exposed to full pressure difference.

Because of this the inlet valve and by pass system should be regularly inspected for leakage if the turbine is operating in sand laden water. The valve system should also be closed before long stopping periods in order to avoid cavitation damage.

The main purpose for a maintenance seal however is to allow for repair of the main seals if leakage has occurred.

The Nozzle System

Through the nozzles of a Pelton turbine the flow is normally accelerated from 0.12 to 0.15 × $(2gH_n)^{0.5}$ to 0.99 × $(2gH_n)^{0.5}$ which will be the jet velocity.

Because of the extreme high velocity on the nozzle outlet and the needle surface a strong turbulent effect occurs on the needle surface. We are here talking about velocities up to 150 m/sec (nozzle diameters are normally between 170 ~ 300 mm). In order to obtain highest possible efficiency and to reduce damage by cavitation the nozzle is normally made with a relatively sharp or very short (less than 1 mm) contact against the needle tip in closed position.

From the outlet of the fins for the needle guidance the flow as described above is exposed to a very strong acceleration towards the nozzle converting all energy into "velocity energy". It is important that no rotational velocity component occurs in order to obtain a uniform velocity profile with minimum loss in the jet and avoid splitting of the jet.

However, the boundary layer on the needle tip creates a lower velocity in the center of the jet.

This is clearly illustrated in Figure 4.5 showing measured energy over the cross section in a jet.

The high velocity creates a strong turbulence in the boundary layer close to the surface of the needle tip. Observations of needle tips operating in water with hard fine grain sand or silt with grain size less than 60 μm for the majority of the content show a severe sand erosion after short time operation.

In Figure 4.6 is shown a typical erosion pattern from the start of the fine grain turbulence erosion on a needle tip.

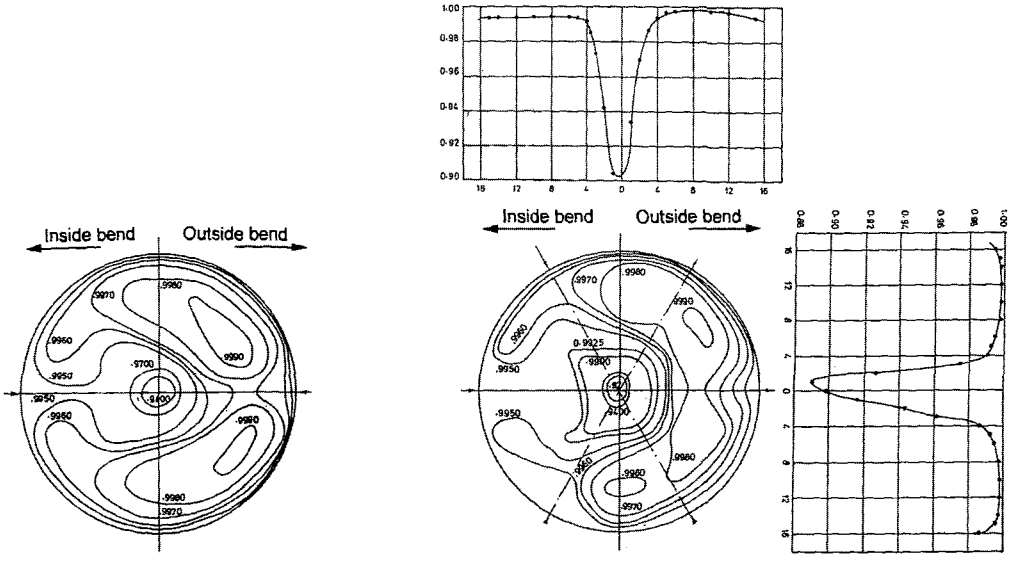

Figure 4.5 Velocity distribution in a jet of a Pelton turbine

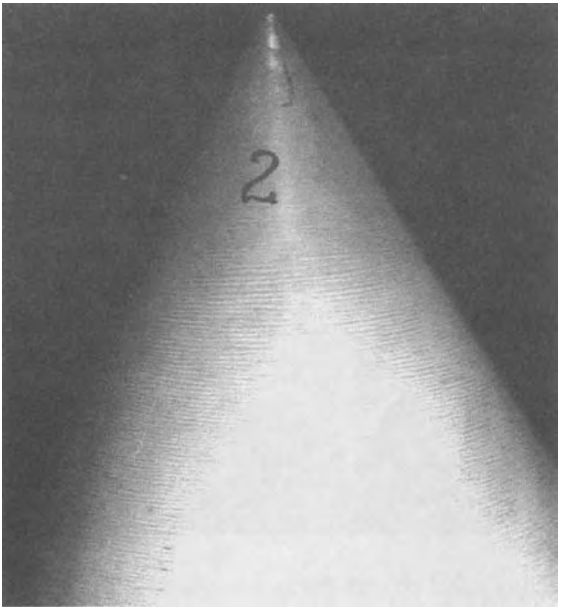

Figure 4.6 Beginning of fine grain sand erosion of a needle tip for a Pelton turbine

In Figure 4.7 is shown a severe erosion followed by cavitation for a high head 5 jets vertical Pelton turbine after 600 hours of operating at 920 m net head. The material of needle and nozzle were of the 13 % Cr 4% Ni type with hardness BH ≈ 300. The sand or silt was in this case very fine grain size with composition as shown in Table 4.1.

Table 4.1 (a) Grain size

Grain size	% Larger than	% Smaller than
0.500	0.00	100.00
0.250	0.07	99.93
0.125	1.01	98.99
0.063	23.03	76.97

This table shows that 76.97% of grains were smaller than diameter 0.063 mm.

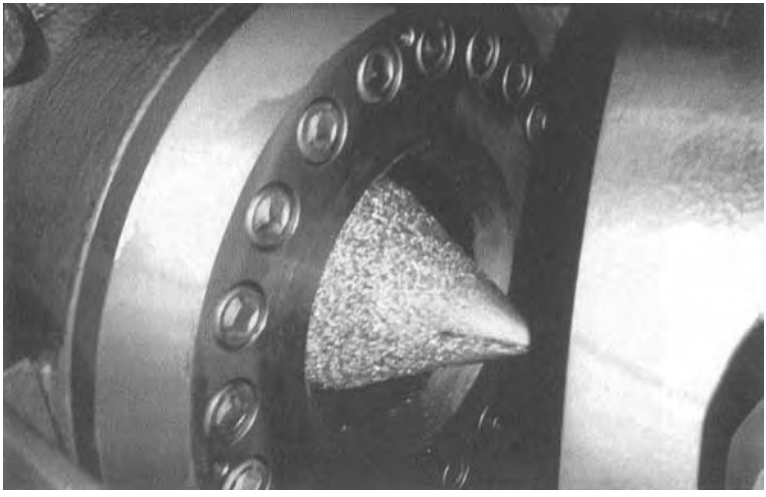

Figure 4.7 (a) Sand eroded Pelton needle after operation in water with fine grain hard sand (Grain size less than 60 μm)

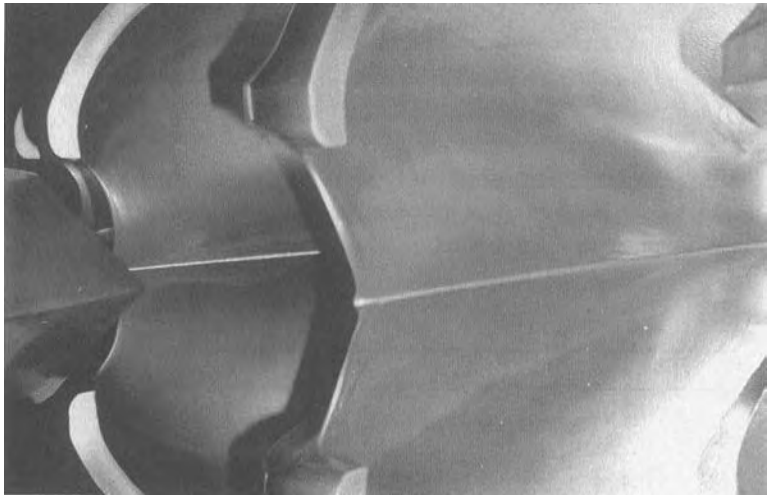

Figure 4.7 (b) The Pelton buckets which were not severely damaged by the fine grain sand refereed to in Figure 4.7 (a)

Table 4.1 (b) Composition

	Quantity %	Hardness	Density
Quartz	17	7	2.65
Kalifelspat	15	6	2.5
Plagioklas-feldpar	38	6	2.6
Slimmer	10	2	2.7
Clorit	2.5	2	2.9
Amfibal	1.5	5	3.0
Epidot	8.5	6.5	3.4
Magntite	7.5	6.0	5.2

This table shows that 86% of the sand had hardness 6 or over.

The amount of silt content in the water was not measured. But the water was colored by sand. It is in this case important to note that only minor erosion damage was observed on the Pelton runner. The possible reason for this will be explained later in the next chapter.

The conclusion for the erosion damage problem of needles caused by hard fine grain sand may be that the erosion cannot be solved by a hydraulic design. However, the new ceramic materials with surface hardness close to quartzite seem to be the solution of the sand erosion problem of a Pelton turbine nozzle. The lifetime obtained has been proven to be acceptable for certain chromic materials. Tests has been made is Switzerland and recently started in Norway. It should be emphasized that such materials are under testing also for guide vanes and facing plates in Francis turbines, but the task is more complicated than for Pelton runners due to more complex geometry.

The Pelton Runner

The hydraulic analysis of the flow over a Pelton bucket may be solve by a combines graphical and computerized method. The analysis is based on the assumption that the resultant acceleration vector must be normal to the surface of the water.

By assuming the shape of the water surface on the bucket at each step in time based on stroboscopic photo studies and assuming the particle path from time step to time step the acceleration components in radial direction = x, tangential direction = y and axial direction = z can be found by differentiating

twice the particle path. The resultant acceleration can be determined. If the resultant acceleration is not normal to the surface, the particle path and/or the surface contour or the water must be corrected by iteration until the resultant acceleration finally will be normal to the surface. In Figure 4.8 is shown the result of particle paths through all time steps together with the surface of the water for one step in time. The result of such analysis shown that the maximum absolute acceleration normal to the surface will be between 50000 and 100000 m/sec^2. This acceleration will have a strong effect by separating the sand grains and bringing them in a collision course towards the buckets surface. The pressure from one gram grain will then be 50 ~ 100 N against the surface.

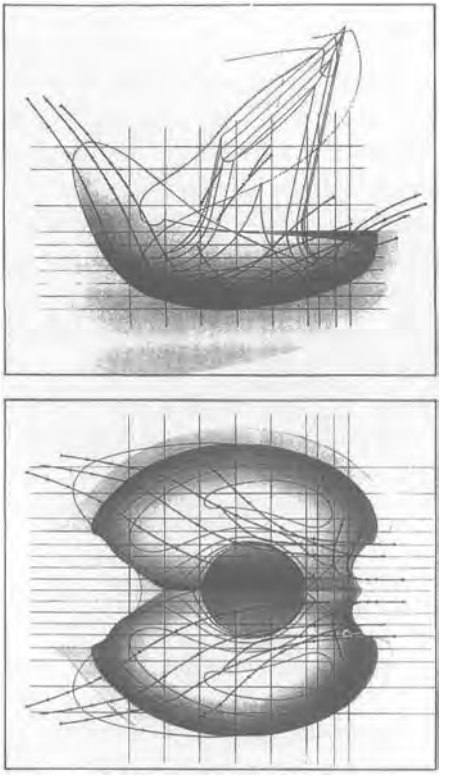

Figure 4.8 Particle paths on the water surface in Pelton bucket found by theoretical analysis

Because of the very strong acceleration of the flow over a Pelton bucket the curvature are of great importance. The most severe damage one will find from the bottom towards the outlet where the sand has been separated and brought in touch with the steel combined with small radii in the curvature. Other places exposed to the most severe erosion are the inlet region and at the splitter top when direct collision of the incoming sand in the jet occurs. In Figure 4.9 and Figure 4.10 the loss in efficiency, with and illustration of the corresponding buckets are shown. As a rule of the thumb one may estimate that the erosion can be measured by the thickness of the splitter, which will be gradually worn down proportional to the erosion depth in the bucket.

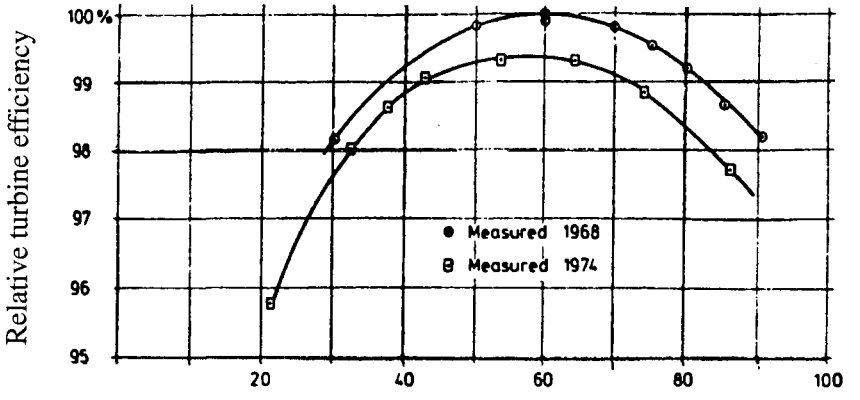

Figure 4.9 Loss in efficiency of a 6-jet turbine caused by sand erosion as shown in Figure 4.10, i.e. splitter width is approximately 1% of the bucket width.

The rule of the thumb then yields:

When the thickness of the splitter has been increased to be 1% of the bucket with the efficiency drops at 1% at full load.

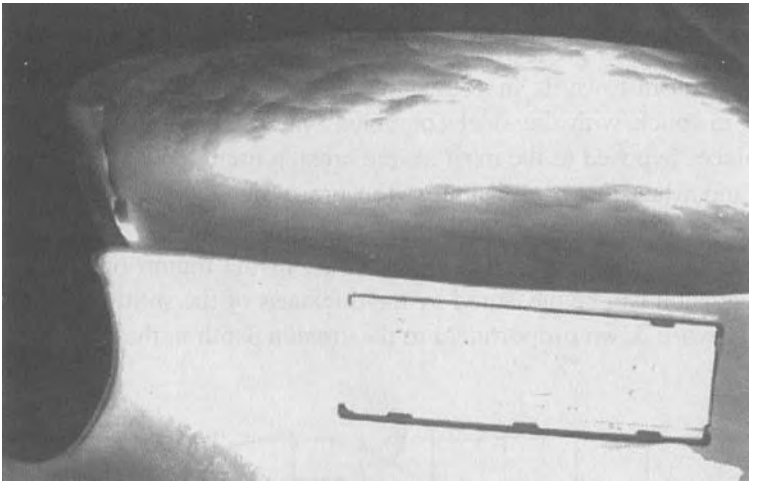

Figure 4.10 Sand erosion in Pelton bucket with refereed to Figure 4.9

The reason for the larger drop in efficiency at full load compared with the smaller drop at part load can be explained in the following way. The sand erosion follows the magnitude of the acceleration causing heavy erosion due to the curvature below the outlet edge. At the outlet edge the acceleration vanish and so the erosion. This leads to a decrease in the outlet angle, which in turn brings the outlet water in touch with the backside of the next following bucket, which will decrease the efficiency more at maximum flow than at reduced flow where the thickness of the water flow is reduced.

For the design of a Pelton runner, which is going to be in operation in sand laden water the radii of the curvature (where the flow direction is changed) should be largest possible. It is also obvious that the number of jets on a runner should be lowest possible to reduce the erosion and increase the lifetime.

The third statement will be that large buckets and nozzles with large hydraulic radii bring relatively less sand in contact with the surfaces.

These three statements lead to lowest erosion on large units with lowest possible number of jets on each unit.

However, the time needed for exchange of the runner is also an important factor for the availability of the unit. The vertical units with access for

dismounting of the runner without dismounting any adjacent parts is in favor of vertical units. The conclusion will be that large vertical units with 4 nozzles are the right chose even if horizontal units with 1 or 2 nozzles and larger buckets have a longer lifetime.

This is partly because of longer dismantling time of the runner, and in addition the price of the runner will be higher due to the size and a spare runner which normally must be available in case of fatigue problems with the runner in operation, will also represent a relatively high cost. The compatible life time factor for a runner for a 4-jet turbine versus a 6-jet turbine and the same speed and output per unit at a certain head can be found by the following formula:

$$T_4/T_6 = K - acceleration \times K - size \times K - jet\ number$$

which will be

$$T_4/T_6 = \sqrt{6/4} \times \sqrt{6/4} \times 6/4 = 2.5$$

(Note: often the speed will be lower for a 4-jet unit than a 6-jet unit which will increase the life time concerning fatigue due to decrease number of impacts per unit).

The lifetime may also be based upon the relative erosion depth, which will be a realistic measure of the absolute life time before the bucket will be too thin for safe operation instead of limit of maximum acceptable absolute roughness before cavitation occurs.

The lifetime ration based upon the relative erosion depth yields:

$$T_4 / T_6 = \sqrt{6/4 \times} \times \sqrt{6/4} \times 6/4 \times \sqrt{6/4} = 3.06$$

This formula is based on the bucket size found by following ratio

$$B_n/B_m = \sqrt{Z_n/Z_m} \qquad (4.3)$$

where Z_n and Z_m are the number of jets and B_n and B_m are the respective buckets widths.

From this formula one can determine the relative lifetime of the runner depending on the number of jets. The lifetime is larger for a large unit with a low number of jets and it will be more economic to install one or two bigger units instead of a higher number of smaller units if more than one unit are going to be installed. Then the question for the designer will be:

How big units can be built with the material technology of 1991. The limitation will be the material thickness of the manifoil and valve as well as the weight of the runner. Based on the experience from the turbines in Sima Power Plant in Norway units of 750 MW may be built for 1000 m head. For higher heads up to 2000 m units with output of 1000 MW may be built. In both cases the runners must be welded by sections because at present time no foundary to be able to cast these big runners in one piece in quality 13% Cr 4% Ni.

The technology of runner welding from sections is known. In Figure 4.11 is shown the dimensions of a unit, which may be built. However, it is important to have a foundry with high quality for runners experience in vacuum method or Argon desoxidation method (AOD method). It is important to avoid internal defects larger than 2 × 2 mm in the buckets roots to avoid fatigue problems (The content of Sulfur, Nitrogen, Oxygen and Hydrogen should be kept on a controlled minimum to avoid defects formed by inclusions of MnS and Mitrides etc.). With modern casting technique and welding procedures large Pelton turbines can be built for safety operation and prolonged lifetime in sand laden water. Additional thickness of 5 ~ 10 mm of the buckets may also be done without a large drop in efficiency. Ceramic or other hard surface materials are also in the developing stage and may be commercialized within few years.

Such materials may increase the lifetime with acceptable maintenance periods also for runners in smaller multijet units where repair work must be carried out in periods of approximately 1000 hours with stainless steel surfaces today. However, due to the fatigue problem of Pelton buckets caused by the pulsating hydraulic load one must be very careful with a brittle surface coating. Special care must be taken if heating of the surface material is necessary because brittleness may occur also in the base material and this may be fatal concerning fatigue resistance. Fatigue problems may give a limitation for a successful use of ceramic coating, but so far this possible problem has not been proven.

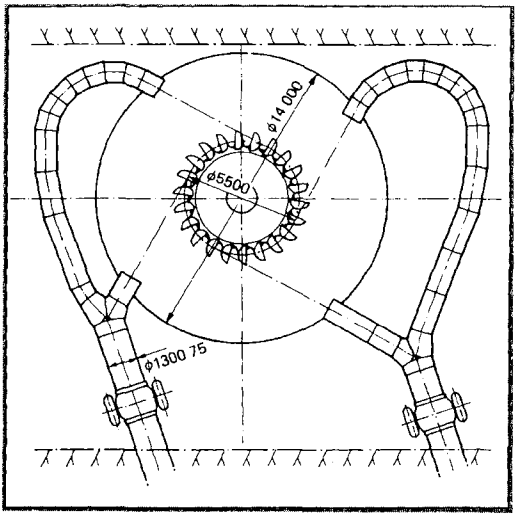

Figure 4.11 Draft of an 860 MW Pelton turbine for 2000 m net head

The Turbine Pit

Sand erosion in the turbine pit is normally not a big problem. In 6-jet machines erosion of baffles or guiding plats close to the runner exposed to outlet water will of course occur and such parts may be worn down quickly. However, these machines can be easily exchanged and are not very important to the operation except for gaining some permillage of efficiency in a new machine. These parts are also suitable for ceramic coating. The turbine housing is also exposed to light erosion, but severe damage on the plating has not been observed on vertical units.

The plates surrounding the runner on the upper part on horizontal units may of course be inspected for erosion and protected by special paint if necessary for high head machines (Rubber based coating or equivalent).

The conclusion concerning erosion in the turbine pit will be that the parts normally can be protected for acceptable life time by paint or soft coating and baffles and guidance plates close to the runner may be protected by ceramics if the time between necessary repairs is shorter than the normal maintenance periods.

General Conclusion

The time needed for exchanging runner and nozzles in a Pelton turbine is much shorter than changing guide vanes, seal rings and runner in a Francis turbine. Because of this the Pelton turbine is normally chosen instead of Francis turbines for high head operation i.e. over 400 ~ 450 m net head if heavy sand erosion is expected. (Changing runner and nozzles in a vertical multijet Pelton unit may be made in 4 days, while the work of exchanging and repairing a Francis unit will require approximately 4 weeks).

4.1.3 Reaction Turbines

The Francis turbines and the Reversible Pump turbines cover the high head range of the reaction turbines, which will get the most serious damage from sand erosion due to the high velocities and accelerations. This chapter will because of this cover for these turbines only.

The highest absolute velocities and accelerations one will find in the guide vane cascade outlet and at the pressure side of the runner. The highest relative velocities, however, one will find in the runner outlet regions for Francis turbines .In a reversible pump turbine one will find high relative velocities also on the pressure side of the runner (turbine inlet or pump outlet).

Because relatively high acceleration occurs in the runner together with high velocities one will also find sand erosion here. Horseshoe vortex acceleration occurs at the blades inlet and trenches from the inlet and along the blades junction to hub and ring may be found as described later. However, the most severe sand erosion damage in a Francis turbine occurs in the guide vane cascade. The design of the high head reaction turbines which will have a significant influence on the sand erosion in the different portions will be described as follows in the following chapters.

The inlet valve system
The spiral casing
The pressure relief and/or by pass system
The guide vane system
The runner and runner seals
The draft tube
The shaft seal

The Inlet Valve System

The inlet valves for Francis turbines or reversible pump turbines may be furnished with rubber seals. The reason is that the pressure drop across the valve will be reduced to approximately 50% during closure with open guide vanes because of the pressure created on the runner inlet by the rotation speed.

Rubber of strong quality shows a good resistance against sand erosion and rubbing by sand between movable steal part and the stationary rubber valve seat is reduced due to the soft rubber. An example of such valve seal (made by Kvaerner, Norway) is shown in Figure 4.12.

It is important to made the by pass system large in order to create highest possible pressure in the spiral casing before opening the valve seals and rotate the valve plug. A low pressure in the spiral casing during opening will increase the damage of the valve seals and the by-pass valve seats.

A minimum starting pressure indication system on the spiral casing will give a warning of increased leakage in the guide vane system from sand erosion. Such system or flow meter system on the by pass pipe should be used as indication for planning of the maintenance work on the turbine.

The Spiral Casing

The velocity in a spiral casing is normally relatively higher than in a manifoil of a Pelton turbine because of a shorter distance between the inlet valve and the guide vanes compared with the distance from valve to nozzle on a Pelton turbine.

The velocity in the inlet of the spiral case will normally be the same of magnitude as the runner outlet meridional velocity. The velocity through the inlet valve will normally be equal to the inlet velocity in the spiral case and the connecting pipe between turbine and valve is normally cylindrical. Because of the secondary flow in the spiral case an incorrect flow angle towards the stay vanes inlet often occur at the top and bottom regions of these. For high head turbines (heads above 500 m) turbulent erosion has occurred and removes paint and caused deep corrosion on top and bottom regions of stay vanes of traditional design as shown in Figure 4.13. In such case sand erosion will cause severe damage by increasing the speed of destruction of the paint and the turbulence corrosion erosion.

However, the modern design of stay vanes, with parallel stay ring facing, effectively reduces the incorrect inflow angle at the top and bottom of the stay vanes. The reason for this is that the inlet ends of the parallel stay ring plates

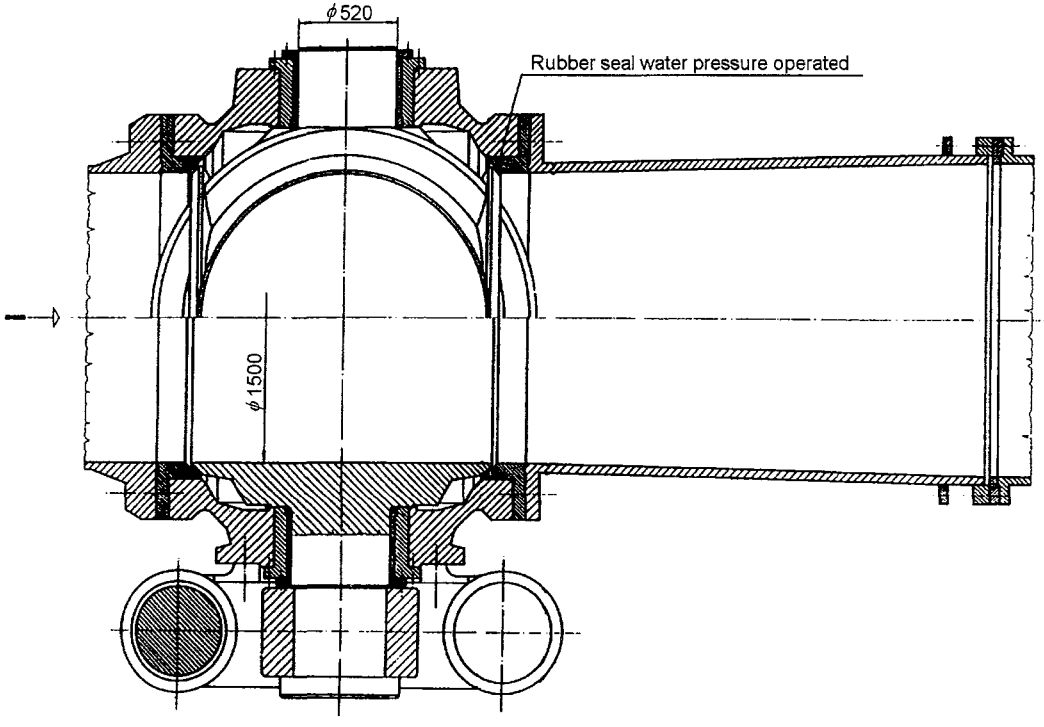

Figure 4.12 Spherical valve with main seal of water pressure operated rubber profile; Maintenance seal is of the traditional steel type

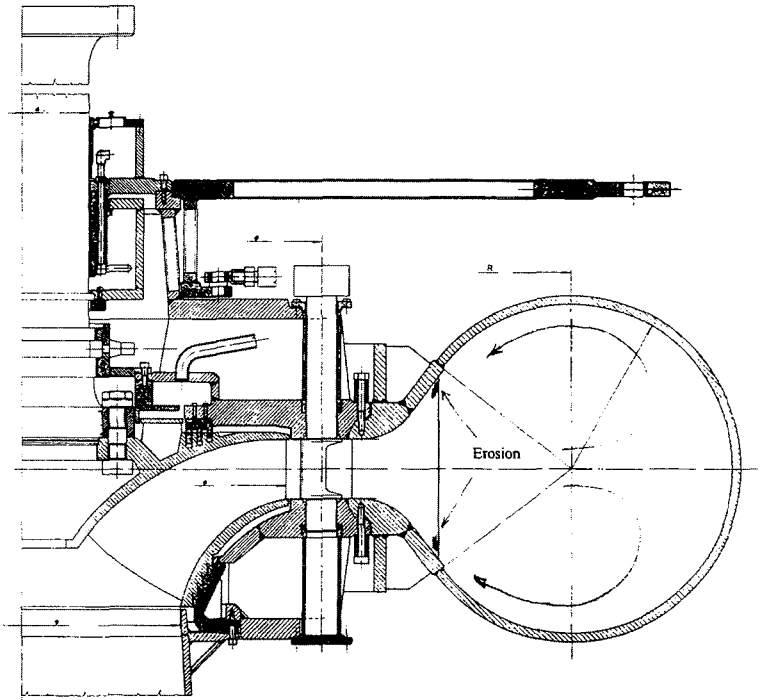

Figure 4.13 Secondary flow in a Francis turbine spiral case

prevent direct inflow of the boundary layer water caused by the secondary flow along the wall of the spiral casing. A modern design of stay ring for Francis turbines is shown in Figure 4.14. The velocity profile out of the stay vanes towards the guide vane inlet will also be more uniform with the modern design. This effect may also be favorable for the sand erosion, but a clear conclusion cannot be drawn. A normal paint will under normal conditions be sufficient to protect the steel.

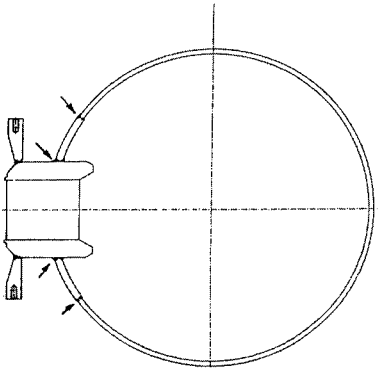

Figure 4.14 Modern design of stay ring for Francis turbines

For sand laden water rubber based paint in the spiral casing of high head turbines has been used and successfully tested in Switzerland by Sulzer. Special care should be taken of the stay ring. For ultra high head pump turbines stainless steel may be used in the stay vanes to prevent turbulence erosion and or sand erosion followed by cavitation damage.

The Guide Vane System

In the guide vane cascade one will find the highest acceleration and the highest absolute velocity in a Francis turbine. The relative velocity head $(C^2/2g)/H_n$ increases from about 0.1 to approximately 0.5 from the guide vanes inlet to the runner inlet for a high head turbine. At normal speed the pressure drop across the guide vanes will be approximately 40% of Hn at full load and 50% of Hn at small openings and in closed position.

Following effects create sand erosion in the guide vane cascade

(1) Turbulence erosion
Turbulence erosion occurs specially in the outlet region caused by high velocity and fine grain sand. Heavy erosion is observed on facing plates.

(2) Secondary flow
Secondary flow erosion occurs in the corners between facing plates and guide vanes due to the horse shoe vortex along point on the inlet end. Fine grain sand and medium size sand causes this erosion. Heavy erosion is observed on facing plates along the guide vane contours.

(3) Leakage erosion
The leakage through the small clearance between the guide vanes and the facing plates increases the horseshoe vortex on the suction side. In addition this leakage flow creates also heavy erosion at the inlet pressure side and the outlet suction side due to local separation and turbulence. Fine grain sand creates often-severe damage caused by this leakage flow in high head turbines.

(4) Acceleration
The acceleration of the main flow creating the rotation of the water in front of the runner and creates an acceleration normal to the stream lines and guide vane blade surfaces and separates sand and gravel to give impacts of the steel surfaces. If large grain size composites exist in the water heavy destruction of the guide vanes occurs. Secondary flow created by the acceleration normal to the streamlines also creates erosion by fine grain sand especially in the corners between guide vanes and facing plates.

* Design

It is not possible to avoid erosion by means of design only. Smoothest possible acceleration, reduction of the clearance gaps between guide vanes and the facing plates as well as a careful choice of the stay vane outlet angles bringing the guide vane in neutral position at the normal operation point could be recommended in general. Guide vane sealing to prevent the leakage flow will also reduce the erosion until the turbulence and secondary flow erosion has created waviness on the facing plates. Such waviness may cause dangerous galling between the seals and the facing plates and this guide vane seals may cause a reduction of the reliability of the turbine.

The conclusion will be that the designer's best weapon against sand erosion will be new material and in particular the new ceramic material that is

now under development also for complicated geometry like the guide vane system.

* Material development for guide vane system

For the guide vanes ceramic coating has been developed for high head turbines. This coating is the same quality, which has been, describes for Pelton needle and nozzles in this chapter.

* Loss in efficiency due to abrasive erosion

Abrasive erosion of the facing plates on head cover and lower cover leads to an increased leakage between the guide vane facings and the covers.

The increased loss in efficiency caused by abrasive erosion of 2 mm in a high head turbine operating at 540-m net head is shown in Figure 4.15. An eroded facing plate is shown in Figure 4.16.

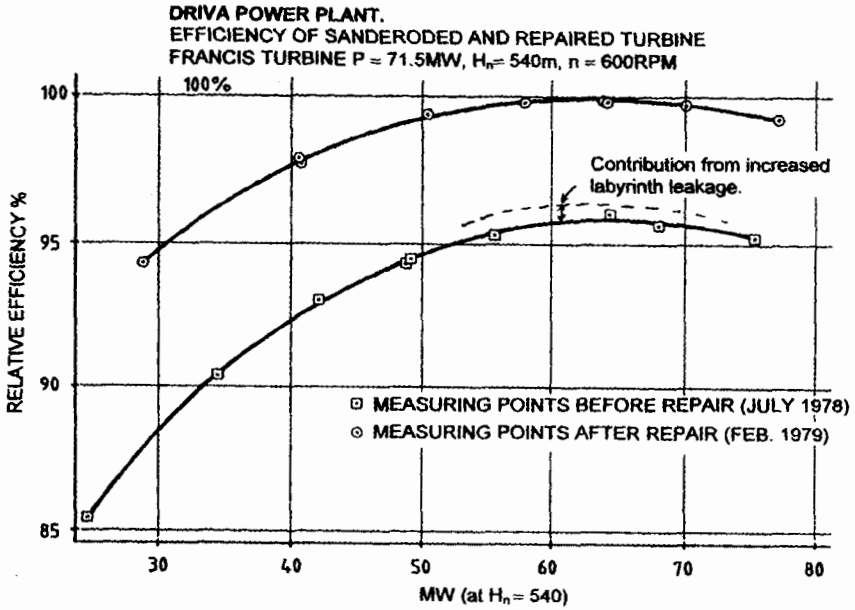

Figure 4.15 Efficiency loss corresponding to the erosion shown in Figure 4.16

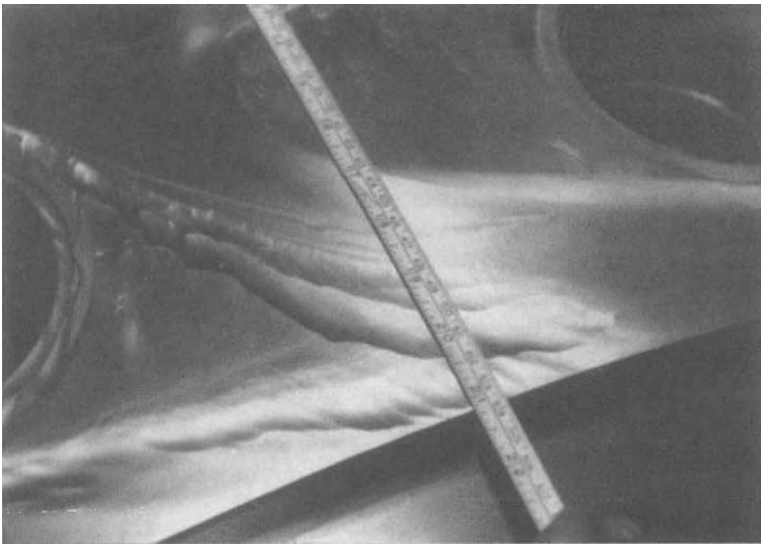

Figure 4.16 Eroded facing plate for Driva Francis turbine, average depth = 2 mm

It should however be emphasized that for a new turbine the clearance in a pressurized turbine will be approximately 0.5 mm on each side. The dry clearance (without pressure) will be 0.05 mm to 0.1 mm on each side.

Because of the small clearance one must be careful when coating the facing plates in order to obtain the necessary tolerances and surface finish.

The Runner

In the runner the highest relative velocities occur at the outlet regions while the highest accelerations may be found at or close to the blade inlet. At off design operation very high local accelerations may occur at the inlet edge of the blades.

Turbulence erosion from fine grain sand or silt may then be the reason for outlet erosion together with erosion from coarse sand while the acceleration at the inlet is mainly caused by coarse sand which may cause severe erosion specially at off design operation.

In any case the inlet region will be sensitive to incorrect pressure distribution and large difference in pressure between pressure and suction

sides. Splitter blades will reduce the pressure difference from pressure side to suction side and thus reduce the damage of flow around the inlet edge in off design point operation, which may cause severe local sand erosion.

Cross flow from hub to shroud caused by incorrect blade leaning will also increase the so-called horseshoe vortex in the blade roots. At the inlet of the blade horseshoe vortices may create sand erosion groves in a similar way as around the guide vanes.

Labyrinth Seals

The velocity of the labyrinth seals on the runner is in the order of 45 m/sec in a high head turbine. Turbulence erosion from silt laden water and sand erosion from coarse sand will always to some extent occur in this region. The clearance between the stationary and rotating parts is between 0.5 ~ 1.5 mm depending on the size of the turbine. A strong turbulence occurs in the flow making the sand erosion severe in this region. However, the efficiency loss caused by the increasing leakage will be small. The efficiency loss due to erosion of labyrinth seals was only 0.5% or approximately 10% of the efficiency loss shown in Figure 4.15.

The Draft Tube

Except for the portion of the draft tube closest to the runner outlet where the highest absolute velocities occurring sand erosion is normally not a problem in this part of the turbine. The section closest to the runner will normally be made of stainless steel, which is more resistant to abrasive erosion than carbon steel.

The Shaft Seal

Mechanical shaft seals with carbon rings may be damaged by silt and sand if the water running through the turbine reaches this part.

Clean pressurized water injected to the seal with overpressure higher than the water from the turbine flow may save this part from damage. Labyrinth seals, which allow for an arrangement to let the shaft seal from any sand erosion under operation at normal speed. Such arrangement has been used successfully in a large number of high head turbines operating in sand-laden water (Lubuge Power Plant in China is one example of this type).

Concluding Remarks

Sand erosion cannot be avoided in turbines because sedimentation of the silt with grain size less than 0.1 or 0.06 mm is not possible in majority of cases.

By careful design of the blade loading and by using dry running shaft seals of labyrinth type a safe running may be obtained.

The best weapon against sand erosion however, may be the development of the ceramic coating which increase the time between necessary repair by one or two decades compared with the surfaces of hardened stainless steel.

4.2 Effects of Silt-Laden Flow on Cavitation Performances and Geometric Parameters of Hydraulic Turbines

Y. L. Wu

4.2.1 Effects of Silt-Laden Flow on Cavitation Performances of Hydrauliv Turbines

A large number of hydraulic turbines working in silt-laden rivers encounters serious problems of silt abrasion and aggravated cavitaion. In lighter cases machine performances are impaired and in serious cases structural damages may result. In recent years, many hydraulic engineers are faced with the serious challenge of solving the problems of silt-laden flow in the many hydro projects on the silt-laden rivers.

Effect of Sand Content on the Cavitation Process

* Incipient cavitation number

The existence of silt in water flow has a definite influence on the inception of cavitation and its behavior in bubble growth. Liu, Y.X. (1983) did the first tests to study the incipient cavitation number in silt-laden flow in China [4.1, 4.2]. His experiment was carried out in a water tunnel with a test section of 8 × 20 mm^2 and the flow velocity of 12 to 23 m/s to measure the cavitation bubbles following a cavitation generator (a cylinder of diameter D = 15 mm). Tests were made with sand from the Huanghe River with grain size of 0.014 ~ 0.018 mm and sand content of 187 kg/m^3. The incipient cavitation number is defined as

$$k_i = 2(P_o - P_v)/(\rho U_o^2) \tag{4.4}$$

where P_O and U_O are the reference pressure and velocity at the inlet of the water tunnel. Figure 4.17 shows the experimental results of the variation of incipient cavitation number obtained by observing the bubble inception and the experimental results of the status cavitation number K_m for maximum sound intensity of cavitation noise. The inception cavitation was determined by measurement of the cavity length, here λ = 0.5 mm. Another group of experimental results were obtained by using a NASA 4412 airfoil in another water tunnel with plastic sand of d_{50} = 0.165 mm and density ρ = 1070 kg/m^3, as shown in Figure 4.18. From these two experimental results, it is very clear that there exists a critical concentration of S_{cr} = 10 ~ 13 kg/m^3 at which the incipient cavitation number K_i reaches a maximum value. For the consentration, S, less than 10 ~ 13 kg/m^3 the sand plays a role of inducing cavitation whereas for S greater than 10 ~ 13 kg/m^3 it has a retarding effect.

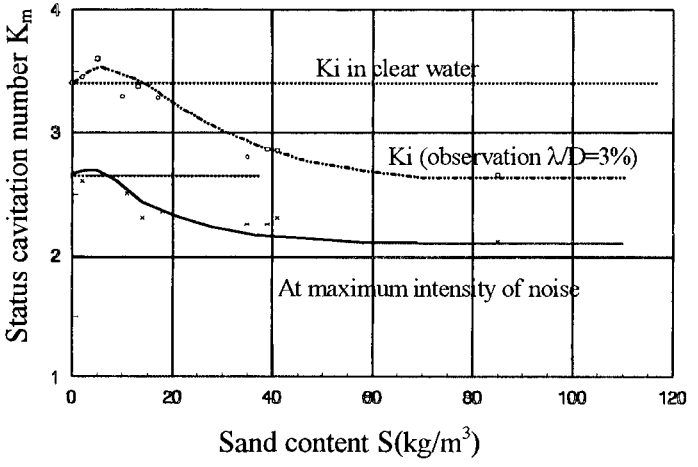

Figure 4.17 Effects of solid content on incipient cavitation number for a cylinder

* Cavity length

In clear water, the cavity length does not change for a given cavitation number. But for the test with silt-laden flow, the status cavitation number K_m for a certain cavity length changes with variation of sand concentration, as shown in Figure 4.19. Figure 4.20 shows the results of variation of cavity length with sand concentration, S, at the fixed value of K_m, which are taken in the values from 2.2 to 3.0. Figure 4.21 is the results of the same experiment as that for Figure 4.18. Figure 4.21 shows the variation of of cavity length with sand concentration at a fixed value of several cavitation numbers, K_m. For a definite cavity length, the critical concentration S_{cr} (for which the cavitation number is highest) may be 5 ~ 8 kg/m^3 for Figure 4.19 and 10 ~ 13 kg/m^3 for Figure 4.21.

* Cavitation Fluctuation

There is a critical concentration value S_{cr} for the variation of cavity fluctuation length ΔL_{max} as shown in Figure 4.22, where the S_{cr} is 10 ~ 13 kg/m^3 for NASA 4412 airfoil.

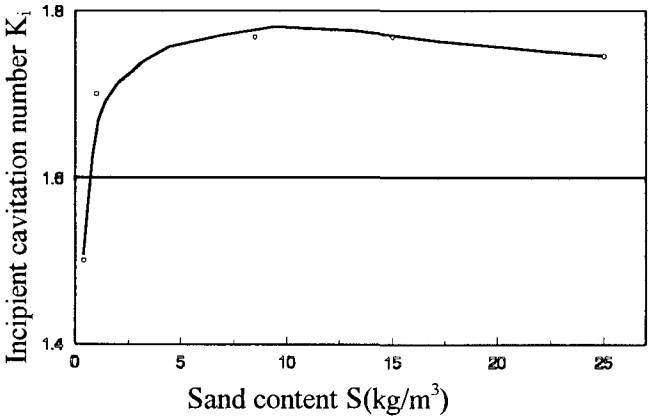

Figure 4.18 Relation between sand contents and Ki for NACA4412

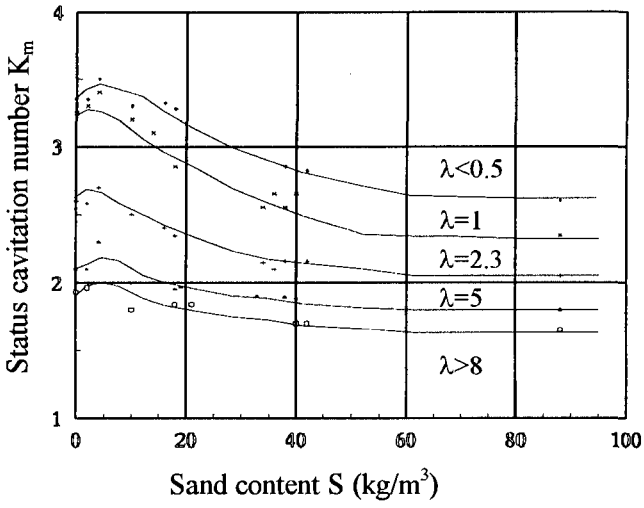

Figure 4.19 Effects of sand content S on K_m for different length λ

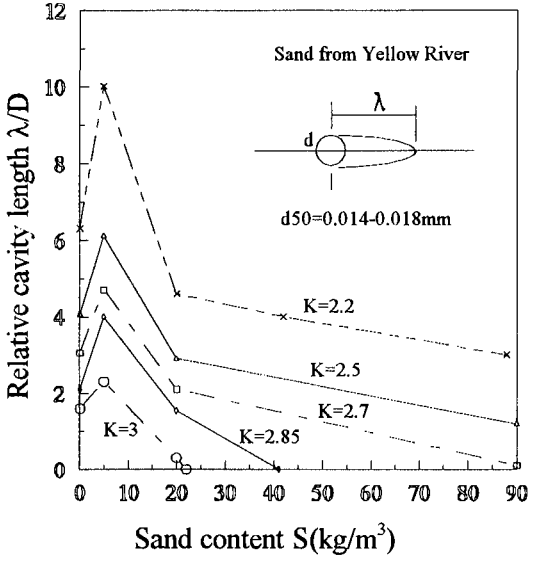

Figure 4.20 Relation between sand content *S* and cavity length

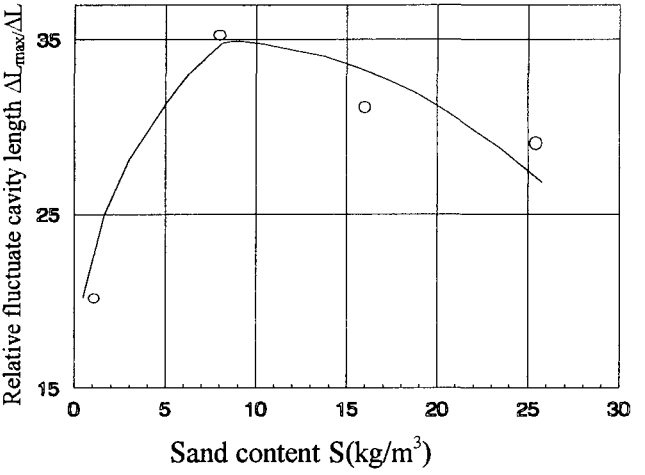

Figure 4.21 Relation between sand content and cavity length for NACA 4412 (d_{50} = 0.165 mm, ρ_s = 1070 kg/m^3, α = 4°)

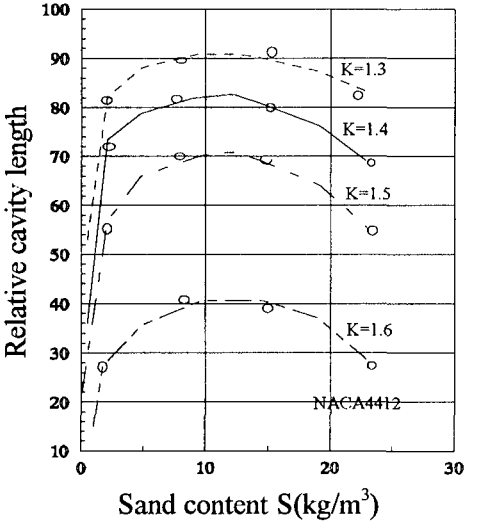

Figure 4.22 Relation between sand contents and relative fluctuate cavity length (NACA4412, α = 4°, d_{50} = 0.165 mm, ρ_s = 1070 kg/m^3)

4.2.2 Model Experiments on Cavitation of Turbines in Silt-Laden Flow

Results of two test of model turbines conducted in closed circuit test stands with silt-laden flow have been reported (Huang S.H., 1994) [4.3]. Figure 4.23 shows the variation of relative cavitation coefficients σ_c / σ_{co} versus sand concentration from a test of an HL001-LJ-25 model turbine designed for the Liujiaxia Power Station with the unit speed n_{11} = 68.75 rpm and the unit discharge Q_{11} = 600 l/s at the design condition.

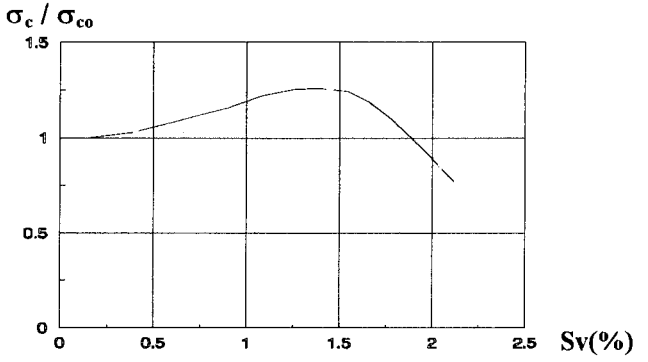

Figure 4.23 Relation between critical cavitation coefficient and sand concentration

Table 4.2 Test data of variation of σ_c / σ_{co} (Figure 4.23)

Test	S_v (%)	S_w (%)	Sand type	Density	d_{50} mm	σ_c/σ_{co}
1 o	0.0	0.0	Pure water	1.00	-	1.0
2 Δ	1.37	1.47	Plastic	1.07	0.25	1.20
3 V	2.01	2.15	Plastic	1.07	0.25	0.86
4 ×	0.35	0.85	Huanghe sand	2.37	0.06	1.04

As shown in Figure 4.23, a critical concentration of S_{cr} = 1.5 kg/m^3 exists for the maximum cavitation coefficient σ_c which was measured by the energy

method according to IEC Standard 7.3.1.4. But Figure 4.24 shows a similar test result of a model turbine with parameter n_{11} = 70.8 rpm and Q_{11} = 990 l/s. In this test, with sand density of 2614 kg/m^3, cavitation coefficient $\sigma_{c\max}$ were determined by using the maximum acoustic energy measurement of cavitation noice.

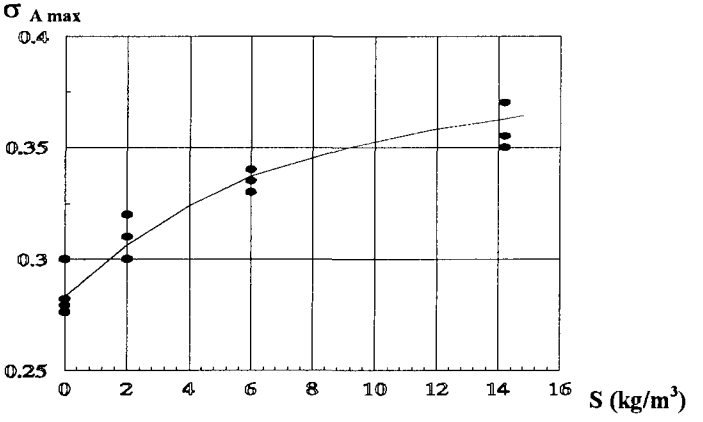

Figure 4.24 Effects of concentration on incipient cavitation coefficient

4.2.3 Selection of Geometric Parameters of Turbines Operating in Silt-Laden Flow

In order to reduce silt abrasion and cavitation erosion of the turbine, the properties of the flow must be taken into consideration in the hydraulic design of turbines.

Characteristic Velocity

It has been suggested that the peripheral velocity U_2 and the relative velocity W_2 at the outlet of turbine runners should be limited to [4.2]

$$\begin{aligned} &\text{For} \quad S_w < 5 \text{ kg/m}^3, \quad U_2 \text{ or } W_2 < 3840 \text{ m/s.} \\ &\text{For} \quad S_w < 12 \text{ kg/m}^3 \quad U_2 \text{ or } W_2 < 34 \text{ m/s.} \end{aligned} \tag{4.5}$$

Needless to say, the recommended limiting velocities are dependent on the runner material. For example, it is indicated by the turbine operation experience and the experimental data that for the stainless steel, Cr5Cu, the critical peripheral velocity U_{2cr} at the outlet of turbine runners working on silt-laden rivers is only 20 m/s. For another stainless steel 1Cr18Ni9Ti, it is 25 m/s. For common steel and other alloy, such as, 20SiMn, 0Cr13Ni4Mo, 0Cr13Ni6Mo, it is 35 m/s. The critical velocity, U_{2cr} or W_{2cr} is the limited velocity, if the velocity, U_2 or W_2 is larger than them, serious damage caused by sand abration and cavitation erosion will occuers.

Specific Speed and Geometrical Parameters of Turbine Runner

The specific speed n_s is defined as

$$n_s = 3.13 \cdot n_{11} \cdot \sqrt{Q_{11}\eta_T} \tag{4.6}$$

where η_T is the efficiency of the turbine. The unit speed n_{11} and the unit discharge are as

$$\begin{aligned} n_{11} &= \frac{nD_1}{\sqrt{H_r}} \\ Q_{11} &= \frac{Q}{D_1^2\sqrt{H_r}} \end{aligned} \tag{4.7}$$

where D_1 is the characteristic diameter of turbine runner at inlet, and D_2 is at outlet, Q the discharge of turbine and H_r the head at design condition.

If the discharge Q and the peripheral velocity coefficient K_{u1} at the runner inlet, as well as the meridional velocity coefficient K_{m2} at the outlet are expessed as

$$\begin{aligned} Q &= \frac{\pi}{4}D_1^2\left(1-k^2\right)\cdot V_{m2} \quad \text{For Kaplan turbine} \\ Q &= \frac{\pi}{4}D_2^2 \cdot V_{m2} \quad \text{For Francis turbine} \end{aligned} \tag{4.8}$$

where k is the ratio of the diameter of crown, d_h, to that of runner blade tip, D_1. And the velocitiy's coefficients k_{u1} and k_{m2}

$$k_{u1} = \frac{\pi \cdot D_1 \cdot n}{60} \cdot \frac{1}{\sqrt{2gH_r}}$$
$$k_{m1} = \frac{V_{m2}}{\sqrt{2gH_r}} \tag{4.9}$$

Then,

$$n_s = 493.5K_{u1}\sqrt{k_{m2}\left(1-k^2\right)\eta_T}\,(m \cdot kW) \quad \text{For Kaplan turbine}$$
$$n_s = 493.5K_{u1}\frac{D_2}{D_1}\sqrt{k_{m2}\eta_T}\,(m \cdot kW) \quad \text{For Francis turbine}$$

* Kaplan turbine runner

From the foregoing equations and the characteristic velocities for Kaplan turbine at the design condition, that is,

$$U_2 \leq 38 \text{ m/s} \quad \text{and} \quad V_{m2} = 11.5 \text{ m/s} \quad (< 12 \text{ m/s})$$

the suggested geometrical parameters of Kaplan turbine runners operating on silt-laden flow are as in the Table 4.3 by using the following velocity's relations

$$V_{u2} = V_{m2} \cdot ctg\alpha_2$$
$$V_2 = \sqrt{V_{u2}^2 + V_{m2}^2}$$
$$W_2 = \sqrt{\left(U_2 - V_{u2}\right)^2 + V_{m2}^2} \tag{4.10}$$
$$\sin\beta_2 = \frac{V_{m2}}{W_2}$$

Table 4.3 Suggested parameters of Kaplan turbine runners

H (m)	k	V_{m2} (m/s)	k_{m2}	k_{u1}	U_1 (m/s)	η_T	n_s (m.kw)	α_2 (°)	V_{u2} (m/s)	V_2 (m/s)	W_2 (m/s)	β_2 (°)
5	0.3	9.0	0.91	2.07	20.5	0.9	880	75	2.41	9.32	20.20	26.50
								80	1.59	9.14	20.90	25.50
10	0.4	10.5	0.75	1.89	26.5	0.9	700	75	2.81	10.87	25.90	23.90
								80	1.85	10.66	26.80	23.10
15	0.4	11.0	0.64	1.772	29.5	0.9	590	75	2.95	11.39	28.74	22.50
								80	1.94	11.17	19.67	21.80
20	0.4	11.5	0.58	1.58	31.3	0.9	515	75	3.08	11.90	30.47	22.20
								80	2.03	11.68	31.45	21.80
25	0.5	11.5	0.52	1.46	32.3	0.9	427	75	3.08	11.90	31.40	21.50
								80	2.03	11.68	32.40	10.80
30	0.5	11.5	0.474	1.37	33.2	0.9	382	75	3.08	11.90	32.24	10.90
								80	2.03	11.68	33.22	10.30
35	0.55	11.5	0.44	1.33	34.8	0.9	345	75	3.08	11.90	33.74	19.90
								80	2.03	11.68	34.73	19.34
40	0.55	11.5	0.41	1.31	36.7	0.9	328	75	3.08	11.90	35.53	18.90
								80	2.03	11.68	36.53	18.35

From these characteristic velocity values, the relation between the specific speed of Kaplan turbines operating in silt-laden rivers versus turbine head are expressed in Figure 4.25.

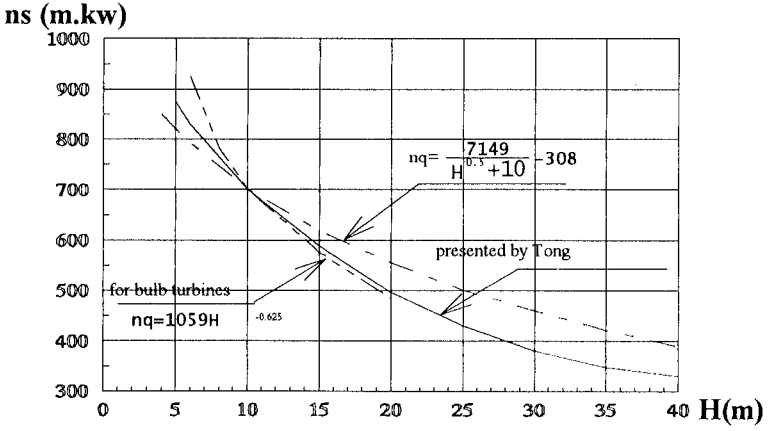

Figure 4.25 Relation between n_s and effective head for Kaplan turbines

In Figure 4.25, the statistical data for Kaplan turbines are indicated on the curver as

$$n_q = \frac{7149}{H^{0.5}+10} - 308 \tag{4.11}$$

for bulb turbines

$$n_q = 1059H^{-0.625} \tag{4.12}$$

* Francis turbine runner

For Francis turbines, the relative flow angle β_2 at the runner outlet does not change with variation of flow rates, the following relation can be obtained

$$\sin\beta_2 = \frac{V_{m2}}{W_2}$$

$$V_{u2} = U_2 - V_{m2}ctg\beta_2$$

$$tg\alpha_2 = \frac{V_{m2}}{V_{u2}}$$

$$V_2 = \sqrt{V_{u2}^2 + V_{m2}^2}$$

$$W_2 = \sqrt{(U_2 - V_{u2})^2 + V_{m2}^2}$$

From the foregoing equations and the characteristic velocities for Francis turbine at the design condition, and the peripheral velocity limits

When	$H<250$ *m,*	*then*	$U_2<40$ *m/s*
When	$H>250$ *m,*	*then*	$U_2=40$ *m/s*
When	$H<200$ *m,*	*then*	$U_2<38$ *m/s*
When	$H>200$ *m,*	*then*	$U_2=38$ *m/s*

the suggested geometrical parameters of Francis turbine runner operating on silt-laden flow are as in the Table 4.4

Table 4.4 Suggested parameters of Francis turbine runner

H (m)	35	50	70	100	120	150	180	200	250	300	350	400
U_2 (m/s)	29	30.5	33	36.5	38	38.5	39	39.5	39.8	40	40	40
W_2 (m/s)	25	28	29.5	32.5	34.2	36	37.7	38	38	38	38	38
$\frac{D_2}{D_1}$	1.18	1.15	1.11	1.06	1.03	0.98	0.93	0.90	0.84	0.79	0.74	0.70
U_1 (m/s)	24.60	26.54	29.70	34.42	36.90	39.27	41.93	43.85	47.36	50.64	54.04	57.16
k_{u1}	0.940	0.848	0.802	0.777	0.761	0.724	0.706	0.70	0.677	0.66	0.652	0.646
V_{m2} (m/s)	8.7	9.4	9.9	10.2	10.3	10.5	10.6	10.6	10.7	10.8	10.9	11.0
k_{m2}	0.332	0.300	0.267	0.230	0.212	0.194	0.178	0.169	0.153	0.141	0.132	0.124
β_2 (°)	20.36	19.62	19.60	18.30	17.53	16.96	16.33	16.20	16.35	16.51	16.67	16.83
V_{u2} (m/s)	5.56	4.13	5.20	5.65	5.39	4.07	2.82	3.02	3.33	3.57	3.60	3.64
α_2 (°)	57.40	66.30	62.30	61.02	62.38	69.00	75.10	74.12	72.73	71.74	71.72	71.69
V_2 (m/s)	10.32	10.27	11.18	11.66	11.63	11.26	0.97	11.02	11.21	11.37	11.48	11.59
α_1 (°)	28.0	26.5	25.5	24.0	23.8	22.0	21.8	21.0	19.5	18.0	16.5	15.5
V_{u1} (m/s)	16.36	18.85	20.76	22.91	23.35	25.99	26.50	27.61	30.20	33.24	36.80	39.66
V_1 (m/s)	18.53	21.07	23.00	25.08	25.52	28.03	28.54	29.58	32.05	34.95	38.38	41.16
W_1 (m/s)	11.98	12.15	11.95	15.18	17.02	16.90	18.72	19.40	20.22	20.48	20.40	20.67
n_s mkw	299.2	250.0	215.4	185.0	169.0	146.3	130.0	121.4	104.1	91.6	82.0	74.6

From table 4.4, it is obtained that the relative flow angle β_2 is in the range from 15° to 20°, the absolute velocity at the runner outlet at the design condition, V_2, is less than 15 m/s, and at the design condition, the peripheral component of absolute velocity at the runner outlet, V_{u2}, is positive.

The relation between the specific speed of turbines operating in silt-laden rivers and the turbine head are expressed in Figure 4.26 for Francis turbines. Statistical data are also plotted on these curves, such as (Tong, 1993) [4.4]

$$n_s = 2357H^{-0.538}$$
$$n_q = 638H^{-0.512} \tag{4.13}$$

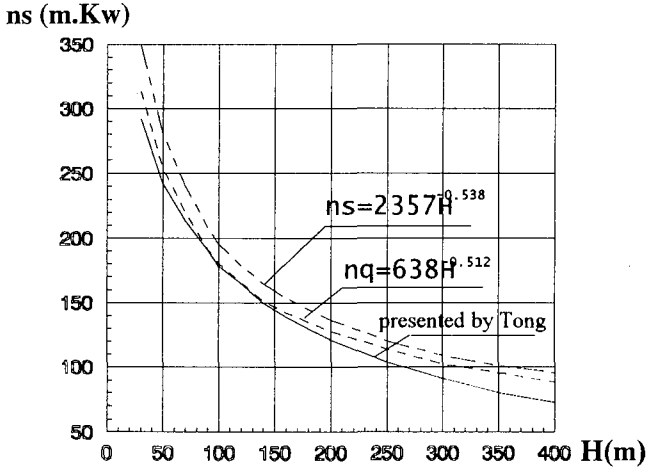

Figure 4.26 Relation between n_s and effective head for Francis turbines

Unit Speed and Unit Discharge

The unit speed n_{11} and the unit discharge Q_{11} can be expressed as follows:

For Kaplan turbines

$$n_{11} = \frac{60}{\pi}\frac{U_1}{\sqrt{H_r}}$$
$$Q_{11} = \frac{\pi}{4}\frac{\left(1-k^2\right)V_{m2}}{\sqrt{H_r}} \tag{4.14}$$

where H_r, U_1 and V_{m2} are all for design condition, and k is the ratio of the hub diameter to the diameter of the runner blade tip. The inlet diameter of runner equals to the outlet diameter of the runner, that is, $D_1 = D_2$.

For Francis turbines

$$n_{11} = \frac{60}{\pi}\frac{D_1}{D_2}\frac{U_1}{\sqrt{H_r}}$$
$$Q_{11} = \frac{\pi}{4}\frac{V_{m2}}{\sqrt{H_r}}\left(\frac{D_1}{D_2}\right)^2\frac{\varphi}{\eta_v} \tag{4.15}$$

where η_v is the volumetrc efficiency of Francis turbines, which is taken in the value of 0.995 to 0.997. And φ is the coeffient of blade thickness, which may be taken in the value of 0.98.

Suggested unit speed and unit discharge, as well as other coefficients are listed in Table 4.5 for Kaplan turbines operating on silt-laden rivers and in Table 4.6 for Francis turbines at the silt-laden flow condition.

Table 4.5 Unit speed and unit discharge for Kaplan turbines

Hr (m)	U_1(m/s)	n_{11} (rpm)	k	V_{m2} (m/s)	Q_{11} (m^3/s)
5.0	20.5	175	0.3	10.2	3.260
10.0	26.5	160	0.4	11.5	2.400
15.0	29.5	146	0.40~0.35	11.5	1.960~2.050
20.0	31.3	134	0.40~0.35	11.5	1.700~1.770
25.0	32.2	123	0.50~0.40	11.5	1.355~1.520
30.0	33.2	116	0.50~0.45	11.5	1.237~1.320
35.0	34.8	112	0.55~0.50	11.5	1.065~1.145
40.0	36.7	111	0.55~0.50	11.5	1.000~1.070

Table 4.6 Unit speed and unit discharge for Francis turbines

Hr (m)	U_2 (m/s)	U_1 (m/s)	n_{11} (rpm)	V_{m2} (m/s)	D_2/D_1	Q_{11} (m^3/s)
35	29.0	24.60	79.4	8.7	1.18	1.584
50	30.5	26.54	71.7	9.4	1.15	1.360
70	33.0	29.70	67.8	9.9	1.11	1.128
100	36.5	34.42	65.7	10.2	1.06	0.887
120	38.0	36.90	64.3	10.3	1.03	0.772
150	38.5	39.37	61.2	10.3	0.98	0.637
180	39.0	41.93	59.7	10.6	0.93	0.529
200	39.5	43.85	59.2	10.6	0.90	0.470
250	39.8	47.36	57.2	10.7	0.84	0.370
300	40.0	50.64	55.9	10.8	0.79	0.301
350	40.0	50.04	55.2	10.9	0.74	0.247
400	40.0	57.16	54.6	11.0	0.70	0.208

Selection of the Cavitation Coefficient of Hydraulic Turbine Working in Silt-Laden Rivers

A large number of hydraulic turbines working in silt-laden rivers encounters serious damage under the combination of silt abrasion and aggravated cavitaion erosion. In order to select the geometrical parameters and to determine the instalation level of the hydraulic turbines working in silt-laden flow, it is best to find the incipient cavitation number according to the model test results to ensure that the turbine will operate at the condition without cavitation and cavitation damage. The following statistic cavitation coefficients, σ_c, which are usally determined by the energy method, that is, by the reduction of turbine efficiency to 1% in experiments, can be refrenced when selecting some geometrical parameters for these turbines:

For Kaplan turbines: $\sigma_c = 3.04 \times 10^{-6} \cdot n_s^{1.74}$

For Francis turbines: $\sigma_c = 3.46 \times 10^{-6} \cdot n_s^2$

The safty factors K for different runner materials must be added, which are listed in Table 4.7, when doing the selection.

Table 4.7 Safty Factors K for cavitation

H (m)	30 ~ 100	101 ~ 250	>251
For 20SiMn	1.30	1.40	1.20
For 0Cr13Ni4 Mo	1.20	1.25	1.15
Stainless steel for Welding	1.25	1.35	1.20

Parameters of Guide Vanes

To reduce the damage of guide vanes of turbines working in silt-laden flow, the diameter of guide vanes, D_o must be larger than that for conventional turbines working on pure water rivers, such as.

$D_o = (1.16)\ D_1$ For high specific speed turbines
$D_o = (1.181.20)\ D_1$ For low and middle specific speed turbines
$D_o = (1.20)\ D_1$ For turbine working on silt-laden rivers

The larger diameter, D_o, will make the velocity decrease. The foils used in guide vane should be thin and with small curvature to minimize silt abration and cavitation erosion.

4.3 Hydraulic Design of Slurry Pump

Y.L. Wu

4.3.1 Internal Flow Characters through Slurry Pumps

Centrifugal slurry pumps have been proved to be useful and suitable both technical and economically in hydraulic transport of solids. Their use in mineral and chemical process industries, dredging and paper industries is quite extensive. The efficiency and erosion of through-flow passage of these pumps are the major consideration in their design and application.

Motion of Particles in Slurry Pumps

Several researchers have observed the motion of particles in centrifugal pump impellers experimentally and analyzed it numerically [4.5 ~ 4.10]. Herbich and Christopher (1963) at first observed the particle motion in dredge pump

impellers by using high-speed photograph and pointed out that particles in impeller were not slowed down appreciably at large cross section of the impeller discharge ring, and that their absolute tangential velocities did not increase to that of transporting liquid [4.5]. The observation of particle's movement through the centrifugal impeller were also made by Itaya And Nishikawa (1983) [4.6], Cynpyn B.K. (1975), and Zhao et al (1991) [4.9]. The computation of particle's trajectories were finished Zarya (1983) [4.7] and Menemura et al (1986) [4.8].

Gao et al (1992) [4.10] and Wu et al (1993) [4.11] have obtained the following remarks of particle movement through the slurry pump impellers by experiment and calculation:

(1) Along with the increase of density or diameter of a particle, its trajectory central angle of the relative motion through the impeller is enlarged, its exit velocity become large and its exit angle small. Then the particle having more inertia tends toward the pressure side of blade, which results in the erosion of the exit part of blade pressure side.

(2) The particle inlet velocity basically is proportional to the flow discharge of impeller and bears little relation with other factors. The particle inlet angle has mainly a relation with its impacting on the back cover of impeller. When the impeller speed increases, the impacting particle's number grows, which results in the discretization of particle's inlet angles.

(3) The particle exit angle at the impeller outlet only changes a little. Its values are basically in the range between $15° \sim 22°$ although a lot of factors affects the angle. The vane exit angle must bear on relation with this range when designing the impeller.

(4) The small value of geometric central angle of vane results in increase of chance of particle's impacting on blade pressure surface at the impeller exit part.

Particle's Number Distribution through Centrifugal Slurry Pumps

Recently attention has been paid to new development in flow visualization and image analysis of particulate-liquid two-phase flow. Elizabeth et al (1991) provided a comprehensive review on the state of the art of flow visualization of particulate two-phase flow, such as, visualization by direct photography, visualization by laser sheet, by holography, by speckle photography and by interferometry [4.12]. Besides the visualization technique other measuring techniques also are used. For example, by using the area type image sensor

and the high-speed image processing it may be possible to measure not only mean velocity but also liquid turbulence. The laser induced photochemical anemometry was used to measure velocity turbulence and Reynolds stresses in solid-liquid flow with concentration from 0 to 52% by volume. The ultrasonic technique is expected to determine the velocity of moving particle in two-phase flow.

In Wu et al [4.11] work, the test results on solid particle number distribution in centrifugal impeller at the dilute particle concentration conditions, that is, the volumetric fraction $C_v < 5\%$, are determined by using the direct flow visualization and the digital image processing. Experimental results gave the following remarks:

(1) At very dilute particle concentration, for example, $C_v = 2\%$ condition, particle numbers on the area near blade surfaces at the leading edge vicinity are very larger than those in the middle part between blades. This tendency also existed at other concentration conditions. As the C_v increase, particle number distribution at the inlet would be evened up. Nevertheless particles still concentrated near blade surfaces to a certain extent. This feature was caused by particle impacting against blade surfaces. The rebounded particles gathered in the area near these surfaces. At the same time, the area of dense particle concentration was rather larger near blade pressure surface than that near the suction one. So the chance of particle's impacting to the pressure surface was more than that to the suction one. In factor abrasion of blade pressure surface at the inlet was serious.

(2) In the intermediate part of flow passage of the impeller, particle number decreased from the pressure side of blade to its suction side. With increase of concentration this trend appeared more clear. It was obvious that particle number for unit area would decrease from the inlet to the outlet of impeller because of the mass conservation of particles.

(3) At the outlet of impeller particles gathered near the blade pressure surface. This phenomenon resulted in particle's impacting to this surface and in severe damage in the tailing edge of blade. But the concentration had little influence on the particle distribution at the outlet part. It was reasonable that the outlet blade angle remain between $18° \sim 22°$ at different dilute concentration conditions.

Recently, H. Tsukamoto and X.M. Wang in Kyushu Institute of Tech., Japan (1995) also observed the particles distribution and measured the pressure through the impeller.

Two-Phase Flow Pattern through Centrifugal Slurry Pumps

Up to now, many experimental investigations have been carried out on the connection between velocity distributions and parameters for conventional centrifugal pumps or high efficiency pimps. Velocity measurements for clean liquid flow have shown a non-uniform jet-wake flow pattern at the impeller outlet for shroud and enshroud impellers [4.13]. The cylindrical surface separating the impeller outlet and casing inlet has been as a representative area for understanding this connection. However, comparatively little is repeated so far on the flow through centrifugal slurry pumps. The late publications on the impeller outlet velocity of a slurry pump are the one by Cader et al (1992, 1993) [4.13,4.14], another by Hergt et al (1994) [4.15]. Sun et al (1995) measured the velocity distribution through a slurry pump impeller by using the direct flow visualization and the particle image velocimetry (PIV) technique [4.16].

Figure 4.27 shows three centrifugal pump impellers, where Figure 4.27 (a) is a the conventional pump design for high efficiency, Figure 4.27 (b) is a slurry pump impeller with three blades and is made by GIW, and (c) a Warmann Co. Design with 5 blades. Because the transported medium requires larger through-flow area, the main difference between the conventional design and the slurry-handling design is the meridional pattern and the number of blades. For example, the number of blades is usually smaller and passage wider in the axial direction, as well as, the blades have to be thicker to prevent erosion out. Impeller (c) is concave at the outlet radius compared to impeller (b). The designer of impeller (c) believed that this created a erosion reducing flow pattern in the form of a double inward spiral inside the casing and claimed to reduce casing wear by this special sort of secondary flow. Figure 4.28 shows the experimental results of radial velocity component at the impeller-casing interface and at the best efficiency point discharge (BEPQ) by Hergt et al (1994) [4.15].

Figure 4.28 indicates that for the slurry impeller (b) the outflow is concentrated near two shrouds above and all along the vane pressure side. It is slightly less developed near the vane suction side. The wake behind the vane itself is narrow. That means that two strong jets exist at the corners between the shrouds and the pressure side, and two weak jets locate at the other two corner between the shrouds and the suction side. For another slurry pump impeller (c) the results are similar, and show very uneven velocity distribution

over the outlet cross-section. The so-called four-jet-flow pattern has been observed at the outlet of slurry pump impeller.

Measurement of the liquid flow on the middle section through a centrifugal slurry pump impeller like Figure 4.27 (b) with four blades was completed by using PIV technique by Sun et al [4.16]. The obtained velocity distribution indicated that two separations occurred in the passage of the four blade impeller operated at optimum condition. The separation on the blade suction side mainly resulted from the inlet flow at a large positive attack angle. The recirculation on the blade pressure side was mainly due to the rapid expansion of the flow and insufficient constraint to flow in only four blade geometry.

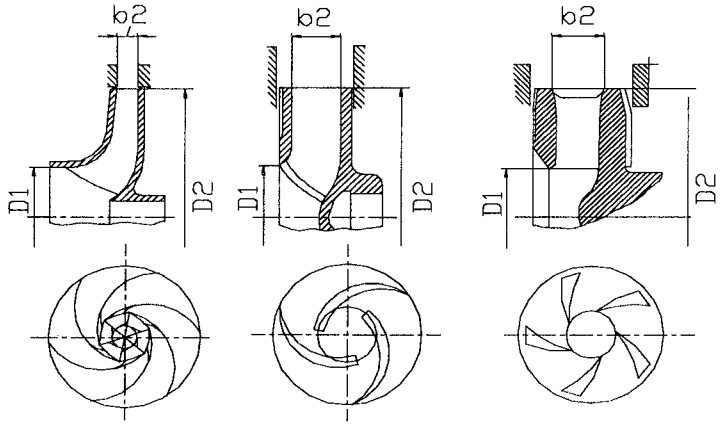

a. Conventional design | b. Slurry pump with 3 blades | c. Slurry pump with 5 blades

Figure 4.27 Meridional section of centrifugal impellers

Back-scattering LDV was used to investigate dilute particulate two-phase flow through a slurry impeller like Figure 4.27 (c) by Cader et al (1992, 1993) [4.13, 4.14]. Several qualitative aspects of the flow pattern were identified:

(1) Large-scale periodical, two-phase flow structures develop in the entire casing, and are dominated by stationary waves.

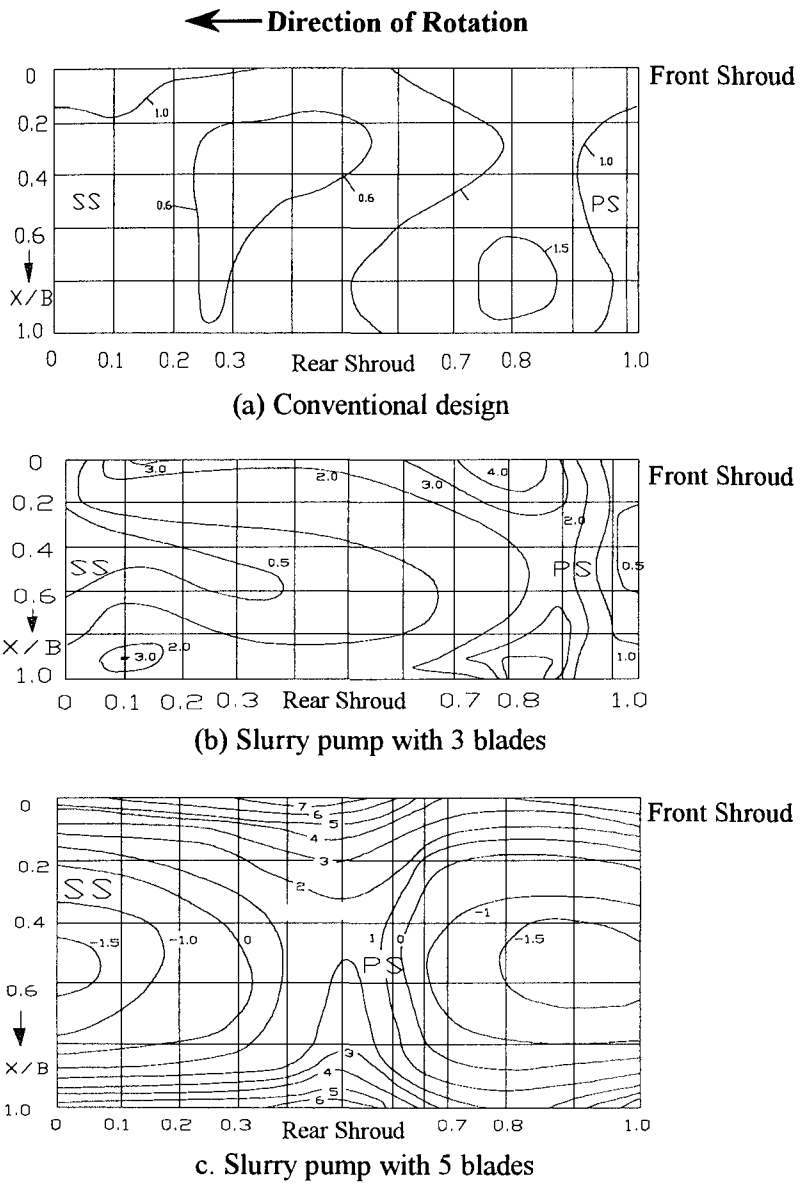

Figure 4.28 Distribution of radial discharge velocity component over one pitch by Hergt et al (1994) [4.15]
(SS:blade suction side, PS: blade pressure side)

(2) The particle generally lead the fluid in the radial direction and lag in the circumferential direction.

(3) The measured circumferential velocity distribution at the impeller casing flow interface, averaged over the bade width and pump circumferential correlates well with the head obtained from the pressure measurements over the pump inlet and outlet. The velocity averages over the casing width underestimate the pump head.

(4) The periodical and turbulent velocity fluctuations have a complexity which is not fully reflected in the present flow simulation.

(5) Particle slip velocities cause a change in the mixture velocity triangle and a supplementary energy loss because of the work performed by the drag forces. Slip velocity at a point is a function of the blade position.

4.3.2 Effects of Impeller Geometry on Performances of Slurry Pumps and Its Determination

The presence of solids in suspension causes the slurry performances of a centrifugal pump to differ from its performances when handling clear water. When pumping a slurry rather than clear water, the head decreases while power input to the pump increases. The influence of individual pump impeller geometry into the performances of a centrifugal pump handling sand slurry was specifically examined by Walker et al [4.17]. The test slurry impeller's patterns are like these shown in Figure 4.27 (b, c) with shroud and enshroud covers. The main trends to be drawn from the results of their experimental work are that:

(1) Vane pattern strongly influences the head ratio H_R of the head on slurry, H_s, to the head on water, H_w, and the efficiency ration E_R of the efficiency on slurry, η_s to the efficiency on water, η_w, such as,

$$H_R = \frac{H_s}{H_w} \tag{4.16}$$

$$E_r = \frac{\eta_s}{\eta_w} \tag{4.17}$$

(2) An increase in Froude number leads to numerically higher H_R and E_R.

(3) The inlet vane angle β_1 and the outlet vane angle β_2, the vane number Z, the outlet width b2 and the specific speed n_q, they all do not strongly influence performances of pumps over the range of geometry tested.

(4) The influence of particle size is different for H_R and E_R.

Main geometry of slurry centrifugal can be selected in the following.

Effects of Solids on Performances of Centrifugal Pumps

The relations between slurry characters, such as, the slurry weight fraction C_w, the slurry volumetric fraction C_v, the slurry density ratio S, and the solid density ratio S_s are as follows

$$C_w = \frac{S_s}{\frac{1}{C_v} + (S_s - 1)} = \frac{S_s}{S_s - 1}\left(1 - \frac{1}{S}\right)$$

$$C_v = \frac{C_w}{C_w + (1 - C_w)S_s} \tag{4.18}$$

$$S = 1 + C_v(S_s - 1) = \frac{1}{1 - C_w\left(\frac{S_s - 1}{S_s}\right)}$$

The head ratio H_R is the function of C_w, S_s and d_{50}, which is the mean diameter of solid, and is expressed in equation (4.19) or (4.20)

$$H_R = (1 - C_w)^{(0.21 + 0.06515 \ln d_{50})S_s} \tag{4.19}$$

or

$$H_R = 1 - 0.32C_w^{0.7}(S_s - 1)^{0.7}\overline{C}_D^{-0.25} \tag{4.20}$$

which has been suggested by A. Sellgren (1979) and where $\overline{C}_D$ is the characteristic drag coefficient, which is expressed by a weighted value:

$$\overline{C}_D = \frac{4}{3} g \frac{d_{50}(S_s - 1)}{\overline{w}^2}$$

where $\overline{w}$ is the weighted settling velocity.

The efficiency ration E_R was suggested by *K*. Holzenberger in equation (4.21)

$$E_R = 1 - 265.3C_v n_q^{-2.46} - (1 - 265.3C_v n_q^{-2.46}) \cdot 3.7 n_q^{-2} \qquad (4.21)$$

where n_q is the specific speed

$$n_q = n \frac{Q^{1/2}}{H^{3/4}}$$

where Q is capacity in m^3/s, H is head in m and n rotational speed in rpm. The simplified relations were given by Frazier and Kervrgessbe as follows:

$$E_R = H_R = (1 - C_w) \quad or \quad \frac{1 - C_v}{1 - C_v + S_s C_v} \qquad (4.22)$$

The hydraulic efficiency of slurry pumps can be estimated in the following statistic formula:

$$\eta_h = 1 - \frac{1.03}{n_q^{0.7}} = 1 - 0.010823 \left(\frac{n}{Q}\right)^{0.35} D_2^{1.05} \qquad (4.23)$$

where D_2 is the outlet diameter of impeller. For the volumetric efficiency:

$$\eta_v = 1 - \frac{5.79}{n_q^{1.4}} \qquad (4.24)$$

The transformation of efficiency from model (subscript: *m*) to prototype pump (*p*) can be performed by using the following efficiency difference:

$$\Delta\eta = K(1 - \eta_m)\left[1 - \left(\frac{R_{em}}{R_{ep}}\right)^{1/5}\right] \qquad (4.25)$$

where K is reference value, which may take the value of 0.4 to 0.6. And Reynolds number is:

$$\mathrm{Re} = \frac{D_1}{\nu}\sqrt{2gH_r}$$

where H_r is the head of pumps at the design condition.

The task of hydraulic design of slurry pumps is at first to selection of the geometry of their impellers, based on using the statistical formulas [4.18] as follows, or based on concerning the influence of existence of particles to the pumps [4.19, 4.20].

Diameters of Impeller

When designing a centrifugal slurry pump, the slurry head H_{sr} and capacity Q at the design condition must be given. At first, the suction diameter of the pump, d_0 should be chosen, then selection of the rotating speed, n, is need according to Table 4.8.

Table 4.8 Selection of rotating speed of slurry pump

Suction diameter d_o (mm)	<125	125~200	250~300	300~500	500~800	>800
Rotating speed n (rpm)	1470	1470~980	980~740	740~590	590~375	<375

The inlet diameter of the impeller D_0 can be chosen according to the following statistic formula:

$$D_0 = K_{D0}\sqrt[3]{\frac{Q}{n}} \quad or \quad D_0 = \sqrt{\frac{Q}{3.6 + 0.28Q}} \quad (m) \qquad (4.26)$$

where $K_{D0} = 3.5 \sim 4.5$.

The inlet diameter of impeller blade D_1 can be take in the same value as D_0 or can be calculated as

$$D_1 = (0.187 \ln n_q - 0.24)\, D_2 \qquad (4.27)$$

At the beginning of the design the outlet diameter of impeller can be estimated according to equation (4.28)

$$D_2 = \frac{1.91K_2}{n}\sqrt{H_r} \qquad (4.28\text{ a})$$

where

if $nq = 48 \sim 54.8$, $Z = 3$ and $\beta_2 = 20^0 - 35^0$, then $K_2 = 4.12 \sim 4.30$

if $nq = 43.8 \sim 71.2$, $Z = 5$ and $\beta_2 = 20^0 - 35^0$, then $K_2 = 3.90 \sim 4.96$

$$D_2 = 4.18\left(\frac{n_q}{100}\right)^{-0.585}\sqrt[3]{\frac{Q}{n}} \quad \text{for} \quad z = 5$$

$$D_2 = 5.00\left(\frac{n_q}{100}\right)^{-0.474}\sqrt[3]{\frac{Q}{n}} \quad \text{for} \quad z = 4 \qquad (4.28\text{ b})$$

$$D_2 = 4.86\left(\frac{n_q}{100}\right)^{-0.525}\sqrt[3]{\frac{Q}{n}} \quad \text{for} \quad z = 3$$

The final determination of the diameter D_2 must be calculated based on the head required and other geometrical parameters to be chosen. The ration of D_2 to D_1 should be chosen in the range of 2.25 to 2.8, That is,

$$D_2 / D_1 = 2.25 \sim 2.8$$

If it is larger than 2.8, the hydraulic efficiency of the pump may be higher, but the pump is too big to be repaired.

Vane Number (Z)

Three to five vanes should be chosen for slurry centrifugal pump impellers in order to transport solids. The vane number, Z, does not effect the performances of the pumps definitely in the above range, and it may be calculated according to the following formula:

$$Z \le INT\left[\frac{(1-\psi_2)\pi D_2}{S_{u2}}\right]$$

$$S_{u2mim} = 16.43 + 1.022 n_q \qquad (4.29)$$

$$S_{u2\max} = 5.12 n_q - 20.2$$

where ψ_2 is the vane coefficient at the impeller outlet, which is defined as:

$$\psi = 1 - \frac{Z\delta}{\pi D \cdot \sin \beta_A}$$

where δ is the thickness of the vane and ψ_2 can be estimated as follows:

$$\psi_2 = 0.954 - 0.774 \frac{n_q}{100}$$

Vane Angles (β_{A1} and β_{A2})

The inlet vane angle of impeller, β_{A1} can be estimated from the inlet flow angle, β_1 adding a angle of attack, α, that is

$$\beta_{A1} = \beta_1 + \alpha \qquad (4.30)$$

where

$$tg\beta_1 = {V_{m1}}/{U_1} = {6.08Q}/{D_1^2 b_1 \psi_1 \eta_v}$$

$$\alpha = 5^o - 15^o$$

$$\psi_1 = 1 - 0.04Z$$

or

$$\psi_1 = 0.479 n_q^{0.047}$$

where V_{m1} is the meridional component of absolute velocity at the inlet and b_1 is the width of impeller at the inlet, which may be estimated by the following:

$$b_1 = (0.06 \sim 0.20)D_2.$$

The outlet vane angle β_{A2} can be taken in the value of the range of

$$15^o \leq \beta_{A2} \leq 50^o.$$

For the transported solid particles with large diameters, β_{A2} is 30° to 35°, for small particles, about 10°. And the angle β_{A2} can also be estimated by using the following equation:

$$\beta_{A2} = 90\, Z^{-0.772} \tag{4.31}$$

Outlet Width (b_2)
The outlet width of slurry pumps is much larger than that of conventional pumps for transporting solids. It can be estimated in the following equation:

$$b_2 = K_{b2} D_2 \tag{4.32 a}$$

where K_{b2} = 0.12 ~ 0.18. If the specific speed is small or the particle concentration is dilute, it takes small value. It can also be calculated by using another equation:

$$b_2 = \left(0.08468 \ln n_q - 0.12096\right) D_2 \tag{4.32 b}$$

The inlet width of impeller can be estimated by the equation (4.33)

$$b_1 = (0.06 \sim 0.20)D_2 \tag{4.33}$$

4.3.3 Vane Pattern

The pattern of vanes of slurry centrifugal pumps, which possess the low specific speed, is basically two-dimensional. The logarithmoid is used to form

the vane pattern, because it was verified by Hebich's experiment that the impeller with the logarithmoid has higher efficiency than that with the circle-shaped vane. In the collar coordinate system (r, θ), the logarithmoid is described by equation (4.34)

$$r = r_1 e^{k\theta} \tag{4.34}$$

where r_1 is the radius at the leading edge of the logarithmoid, i.e., at the inlet of impeller vane, k is the coefficient and

$$k = ctg\alpha = tg\beta \tag{4.35}$$

where α is the angle of helix, and β the vane angle. Equation (4.34) will be a equal-angle logarithmoid if k is a constant. The differential equation of the vane pattern is as follows

$$\frac{d\theta}{dr} = \frac{1}{r \cdot tg\beta} \tag{4.36}$$

where variation of vane angle β from the impeller inlet to its outlet has three types of function, that is, the linear function, the convex and the concave as shown in Figure 4.29.

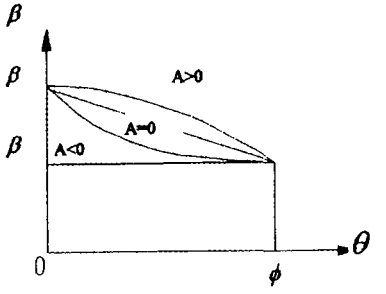

Figure 4.29 Three types of β distribution curves

The Pattern of Vane by Using Equation $\beta = f(\theta, \sin\theta)$

The variation of angle β is assumed to follow equation (4.37)

$$\beta = \beta_{A1} + \frac{\beta_{A2} - \beta_{A1}}{\phi}\theta + A \cdot \sin\left(\frac{\pi}{\phi}\theta\right) \tag{4.37}$$

where β_{A1} *and* β_{A2} are the inlet and outlet angles of vane, ϕ is the central angle of the vane, and A is the coefficient of the oscillation of sin function. The following two cases are used to form the vane pattern.

* The case of $A = 0$

If the coefficient A is zero, introducing equation (4.37) into the differential equation (4.36), then one integrates the equation to obtain the vane pattern equation (4.38 a):

$$r = r_1\left[\frac{\cos\beta_{A1}}{\cos\left(\beta_{A1} + \frac{\beta_{A2} - \beta_{A1}}{\phi}\theta\right)}\right]^{\frac{\phi}{\beta_{A2}-\beta_{A1}}} \tag{4.38 a}$$

where the central angle of vane is

$$\phi = \frac{\ln(r_2 / r_1)}{\ln(\cos\beta_{A1} / \cos\beta_{A2})}(\beta_{A2} - \beta_{A1})$$

and the curvature radius R of the vane pattern is calculated as follows:

$$R = r \cdot \sqrt{1 + \left\{\left(\frac{\phi}{\beta_{A2} - \beta_{A1}}\right)\frac{1}{\theta}\ln\left[\frac{\cos\beta_{A1}}{\cos\left(\beta_{A1} + \frac{\beta_{A2} - \beta_{A1}}{\phi}\theta\right)}\right]\right\}^2}$$

* The case of $A \neq 0$

When the coefficient A is a constant, then the similar equation can be obtained by integrating equation (4.36)

$$r = r_1 \cdot e^{\left(a + b\theta + c\theta^2 + d\theta^3 + e \sin \frac{\pi}{\phi}\theta + f\left(1 - \cos \frac{\pi}{\phi}\theta\right) + g \sin \frac{2\pi}{\phi}\theta + h \cdot \theta \cdot \cos \frac{\pi}{\phi}\theta \right)} \tag{4.38 b}$$

where

$$a = tg\beta_{A1}$$

$$b = \frac{A^2}{2} \frac{\sin \beta_{A1}}{\cos^3 \beta_{A1}}$$

$$c = \frac{1}{\cos^2 \beta_{A1}} \frac{(\beta_{A2} - \beta_{A1})}{2\phi}$$

$$d = \frac{\sin \beta_{A1}}{\cos^3 \beta_{A1}} \frac{(\beta_{A2} - \beta_{A1})}{\phi} \frac{1}{3}$$

$$e = \frac{\sin \beta_{A1}}{\cos^3 \beta_{A1}} \frac{2A\phi(\beta_{A2} - \beta_{A1})}{\pi^2}$$

$$f = \frac{A\phi}{\pi \cos^2 \beta_{A1}}$$

$$g = -\frac{\sin \beta_{A1}}{\cos^3 \beta_{A1}} \frac{A^2 \phi}{4\pi}$$

$$h = -\frac{\sin \beta_{A1}}{\cos^3 \beta_{A1}} \frac{2A(\beta_{A2} - \beta_{A1})}{\pi}$$

and

$$R = r\sqrt{1+\left[a+b+c\theta+d\theta^2+\frac{e}{\theta}\sin\frac{\pi}{\phi}\theta+\frac{f}{\theta}\left(1-\cos\frac{\pi}{\phi}\theta\right)+\frac{g}{\theta}\sin\frac{2\pi}{\phi}\theta+h\cos\frac{\pi}{\phi}\theta\right]^2}$$

The Pattern of Vane by Using Equation $\beta = f(\theta^b)$

The variation of angle β is assumed to follow equation (4.39)

$$\beta = arctg\left(a\theta^b + c\right) \tag{4.39}$$

where

$$c = tg\beta_{A1} \qquad a = \frac{tg\beta_{A2} - tg\beta_{A1}}{\phi^b}$$

then the function of the vane pattern is as follows:

$$r = r_1 e^{\theta\left[\frac{tg\beta_{A2}-tg\beta_{A1}}{1+b}\left(\frac{\theta}{\phi}\right)^b + tg\beta_{A1}\right]} \tag{4.40}$$

where

$$b = \frac{tg\beta_{A2} - tg\beta_{A1}}{\ln\left(\frac{r_2}{r_1}\right)^{1/\phi} - tg\beta_{A1}} - 1$$

$$\phi = \frac{\ln\left(r_2/r_1\right)}{\frac{tg\beta_{A2} - tg\beta_{A1}}{1+b} + tg\beta_{A1}}$$

4.3.4 Hydraulic Design of Centrifugal Slurry Pumps

Theoretical Head of Slurry Developed by Centrifugal Pumps

Based on the governing equation of particle-liquid two-phase flow, the theoretical head of slurry, H_{sth}, developed by a centrifugal pump impeller can be deduced as follows:

$$H_{sth} = \frac{C_w}{g}\left(U_2 V_{u2p} - U_1 V_{u1p}\right) + \frac{1-C_w}{g}\left(U_2 V_{u2f} - U_1 V_{u1f}\right) \tag{4.41}$$

where subscripts f and p indicate the fluid phase and the particle phase respectively, C_w is the weight fraction of solid particles, U_1 and U_2 are the peripheral velocities of impeller at the inlet and the outlet respectively, V_{u1} and V_{u2} are the circumferential components of absolute velocity at the inlet and outlet respectively, g is the gravity. If the inlet flow is meridional, the circumferential component of absolute velocity is zero, then

$$H_{sth} = \frac{U_2}{g}\left[C_w V_{u2p} + (1-C_w) V_{u2f}\right] \tag{4.42}$$

At the pure water operation condition, the theoretical head of the pump, H_{wth} can be got from the equation (4.42) as follows:

$$H_{wth} = \frac{U_2}{g} V_{u2p} \tag{4.43}$$

According to equation (4.16), the head ratio of the slurry theoretical head to one of water is

$$H_{Rth} = \frac{H_{sth}}{H_{wth}} = 1 - C_w\left(1 - \frac{V_{u2p}}{V_{u2f}}\right) \tag{4.44}$$

From the experimental results V_{u2p} is less than V_{u2f}, so that H_{Rth} is less than one.

The Active Slurry Head Developed by Centrifugal Pumps

If there are several groups (for example N groups) of solid particles, each group occupies X_i fraction of total weight of particles, then equation (4.44) has the following form

$$H_{Rth} = \frac{H_{sth}}{H_{wth}} = 1 - C_w(1 - \sum_{i=1}^{N} X_i \frac{V_{u2\,pi}}{V_{u2\,f}}) \tag{4.45}$$

The active head of slurry developed by the slurry pump, H_s, is deduced according to the hydraulic efficiency, η_h, and the slip factor, μ, caused by the limited vane number:

$$H_s = \left[1 - C_w(1 - \sum_{i=1}^{N} X_i \frac{V_{u2\,pi}}{V_{u2\,f}})\right] \cdot H_w \cdot \eta_h$$

$$H_s = \frac{\eta_h}{g}\left[1 - C_w(1 - \sum_{i=1}^{N} X_i \frac{V_{u2\,pi}}{V_{u2\,f}})\right] \cdot \left[\mu\left(\frac{\pi n}{30}\right)^2 r_2^2 - \frac{Qn}{60\eta_v b_2 \psi_2 tg\beta_{A2}}\right] \tag{4.46}$$

where the slip factorμis

$$\mu = 1 - \frac{\pi}{Z}\sin(\beta_{A2} - \Delta\beta_2)\psi_2$$

$$\Delta\beta_2 = \frac{1}{2} arctg\left(\frac{tg\beta_{A2} - \psi_2 tg\beta_{A2}}{1 + \psi_2 tg\beta_{A2}}\right)$$

and

$$\psi_2 = \sqrt{\frac{V_{m2} Z}{\pi U_2 \sin\beta_{A2} \cdot tg\beta_{A2}}}$$

The foregoing equation may have the simplified expression by using the statistic equations of H_R, such as, equation (4.19), (4.20) or (4.22) as follows:

$$H_s = H_R \cdot H_w \cdot \eta_h$$

$$H_s = \frac{\eta_h}{g} H_R \cdot \left[\mu \left(\frac{\pi n}{30} \right)^2 r_2^2 - \frac{Qn}{60 \eta_v b_2 \psi_2 tg\beta_{A2}} \right] \tag{4.47}$$

The Net Positive Suction Head of Centrifugal Slurry Pumps

Estimation of cavitation performances of slurry pumps is needed sometimes at the design condition, although most of them are used at the boosting conditions in industry.

The cavitation performance of slurry is not as good as that of pure water pumps, because the silt-laden flow may induce cavitation seriously. The inlet velocity of a slurry pump must be larger than 2.5 m/s to avoid particle's sediment. The required net positive suction head $NPSH_r$ for a slurry pump is defined as:

$$NPSH_r = \lambda_1 \frac{V_l^2}{2g} + \lambda \frac{W_l^2}{2g} \tag{4.48}$$

where the subscript l is at the leading edge of impeller vane. λ_1 and λ are the cavitation coefficients of the pump vane. The optimum $NPSH_r$ may be estimated by using equation (4.49)

$$NPSH_r = 0.0283 \omega^{4/3} \left(\frac{H_{sr} \nu^2}{1-\nu^2} \right)^{2/3} \left(\frac{Q}{\psi_1 \eta_v} \right)^{2/3} \cdot \left[\lambda^2 \left(\lambda_1 \psi_1^2 + \lambda \right) \right]^{1/2} \tag{4.49}$$

where ν is the radio of the hub diameter, d_h to the tip diameter, D_1 at the inlet, that is,

$$\nu = \frac{d_h}{D_1}$$

4.3.5 Hydraulic Design of Slurry Pump Casing

Three types of casings of centrifugal slurry pumps are used, as shown in Figure 4.30, these are, (a) spiral casing, (b) annular casing and (c) semi-spiral casing. The hydraulic design of the first type will be explained below

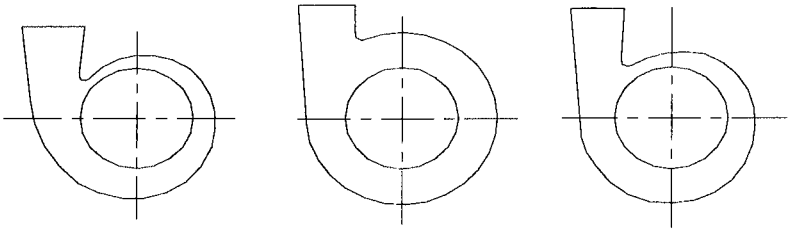

a. Spiral casing b. Annular casing c. Semi-spiral casing

Figure 4.30 Three types of casings of centrifugal slurry pumps

Nose of Spiral Casing

* Position angle of nose for spiral casings

The position angle of the casing nose along the circumferential direction, θ_n, which is measured from the largest section, i.e., the eighth section of the casing, is usually about 25° ~ 50° and may be determined by the following statistic equation (4.50),

$$\theta_n = 139\left(\frac{n_q}{19.9}\right)^{7.39} \cdot e^{-26.57\frac{n_q}{100}} \qquad (4.50)$$

$$n_q \in (16.4, 35.6)$$

* Gap between nose tip and impeller

For slurry pumps, the gap between the nose tip of spiral casing and the impeller, C_n, is usually large in order to transporting solid particles, which is estimated as follows:

(1) For transporting dense concentration particles

$$\frac{C_n}{D_2} = 13.748 d_o^{-0.422} \cdot e^{0.074 d_o} \ (\%) \qquad (4.51\ a)$$

$$d_o \in (1'', 14'')$$

where d_0 is the normal diameter of the pump suction pipe in inch.

(2) For transporting dilute concentration particles

$$\frac{C_n}{D_2} = 4.18 + 0.718 d_o \ (\%) \qquad (4.51\ b)$$

$$d_o \in (1'', 12'')$$

(3) For transporting sands

$$(\frac{C_n}{D_2})_{\min} = 40.35 \ln n_q - 106 \ (\%) \qquad (4.51\ c)$$

$$n_q \in (22, 35.6)$$

Area of the Eighth Section of Spiral Casing

If the specific speed of slurry pumps is less than 16.5, their performance, especially, the efficiency will be sensitive to the areas of spiral casing sections. If the areas are too small the efficiency of the pumps will decrease, and the optimum operation point will move to the small discharge condition, the performance curve of the pump also will be steeper. Otherwise, the curve will be flat, the optimum operation point will move to the large discharge condition. But if the areas are too large, the efficiency also will be down. The selection of the eighth section of the casing may be carried out on the following two methods.

* The characteristic velocity selection

The characteristic velocity of the casing, V_3, can be selected based on the velocity factor, K_{v3}, that is,

$$V_3 = K_{v3}\sqrt{2gH} \tag{4.52}$$

where

$$K_{v3} = 0.263\left(\frac{n_q}{100}\right)^{-.032}$$

Then the area of the largest section, the eighth section of the casing can be calculated as:

$$F_{eight} = \frac{Q_{eight}}{V_3} \tag{4.53}$$

where Q_{eight} is the flow rate through this section, and

$$Q_{eight} = \frac{360 - \theta_n^o}{360} Q$$

Other section's areas F_i can be followed the value of F_{eight}, that is,

$$F_i = \frac{\theta_i}{\theta_{eight}} F_{eight} \tag{4..54}$$

where θ_i and θ_{eight} are measured from the nose point. And $\theta_{eight}^o = 360^o - \theta_n^o$ if it is measured in degree. The dimensions of the casing can be selected according to the conventional pump casings from the data of section's areas.

* The area ratio method

The ratio of the area of impeller outlet to the area of the eighth section, Y, is referred as the area ratio for this eighth section, that is,

$$Y = \frac{F_{im,out}}{F_{eight}} = \frac{\psi_2 \pi D_2 b_2 \sin \beta_{A2}}{F_{eight}} \tag{4.55}$$

And the statistic formulas for Y are

$$\begin{aligned} Y_{\max} &= 2.496 - 2.606\frac{n_q}{100} \quad \text{For} \quad n_q \in (17.8, 35.6) \\ Y_{\min} &= 0.302 - 3.562\frac{n_q}{100} \quad \text{For} \quad n_q \in (21.9, 35.6) \end{aligned} \tag{4.56}$$

Function of Pattern of Inner Surface of Casings

In the spiral casing the logarithmoid is used for its inner surface, that is,

$$\rho = \rho_o e^{a\theta} \tag{4.57}$$

where ρ is the radius of the station on the surface, the factors, ρ_o and a may be determined according to the radius and the position angle of two known stations, these are, on the nose and in the eighth section. Dimensions of other type casing can be selected based on conventional pumps.

4.3.6 Hydraulic Design for Large-Scale Centrifugal Pumps in Silt-Laden Rivers

Large-scale pumps operating in silt-laden rivers suffer serious damage from the combination of cavitation erosion and silt abrasion. But , up to now, there is not any comprehensive hydraulic design method for these pumps. The equivalent pump operating in pure water is used for designing the silt-laden pump. The subscript p represents the design characteristics of the former, such as, the design head, H_p (m), the discharge Q_p (m^3/s), the efficiency η_p (%) and the suction head $H_{s,p}$ (m). The required performances of the silt-laden pump are expressed as H, Q, η and H_s at the operating condition when the pump is lasting at the middle of a repaired period. The design head, H' (m), the discharge Q' (m^3/s), the efficiency η'(%) and the suction head H'_s(m) are the performances of the pump designed for pure water operation, but working in silt-laden flow. The relations between them are as follows:

$$H' = 0.98H_p, \quad Q' = 0.97Q_p, \quad \eta' = \eta_p - 0.015, \quad H'_s = H_{s,p} + 1 \tag{4.58}$$

where

$$H_p = 1.041H, \quad Q_p = 1.074Q, \quad \eta_p = \eta + 0.04, \quad H_{s,p} = H_s - 2. \tag{4.59}$$

The parameters in equation (4.59) will be used in the design based on the conventional method and their data will be verified by the experiment. The manufactured pump will have the characteristics shown by equation (4.58) at silt-laden flow condition.

4.4 Hydraulic Design of Solid-Liquid Flow Pumps

B. Y. Cai

4.4.1 Working Condition of Solid-Liquid Flow Pumps

The performances of the conventional pumps, which are designed on the basis of the single-phase flow condition and are operating at the solid-liquid flow, differ greatly from those at pure liquid flow conditions. For example, Figure 4.31 to Figure 4.34 show the characteristics of the 10sh-13 type double suction centrifugal pump, which is operating at the clear water condition (the solid-phase weight content C_w= 0 kg/m^3) or at the slurry conditions (the solid-phase weight content are taken in the following values: C_w = 5, 20, 60, 100, 150, 200 and 300 kg/m^3) [4.22].

From these figures, it is clear that with the increase of the solid-phase content C_w, the head, the efficiency and the net positive suction head NPSH of the pump will decrease greatly, but the power N of the pump will increase, because the pump of type 10sh-13 was designed based on the pure water condition.

The similar situations are also can observed for the pumps, which are modified on aspects of the geometry of impeller and volute casing from the conventional pumps in order to be used at the solid-liquid flow conditions. The forgoing two types of pumps cannot be used at the slurry flow condition effectively. So that it is necessary to set up a design method of the solid-liquid flow pump based on the two-phase flow theory and on the flow structure of solid-liquid flow pumps.

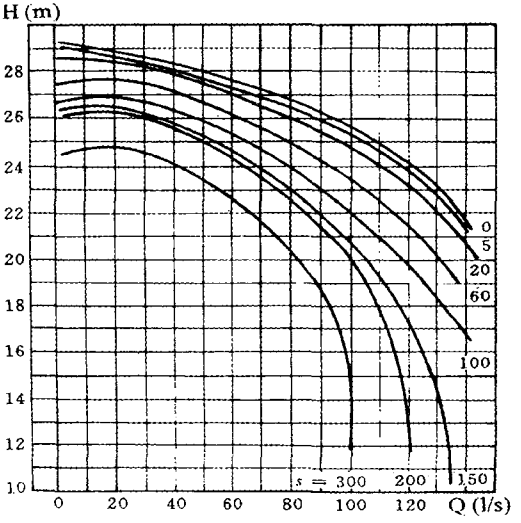

Figure 4.31 Characteristic curve of H(Q) of pump 10sh-13 at different solid-phase contents conditions s (kg/m^3)

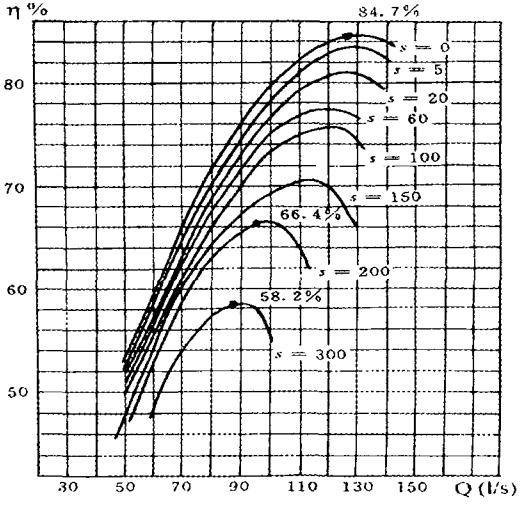

Figure 4.32 Characteristic curve of η(Q) of pump 10sh-13 at different solid contents conditions s (kg/m^3)

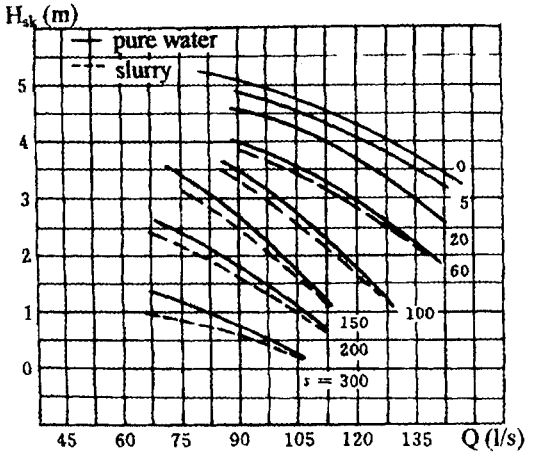

Figure 4.33 Characteristic curve of NPSH(Q) of pump 10sh-13 at different solid contents conditions s (kg/m^3)

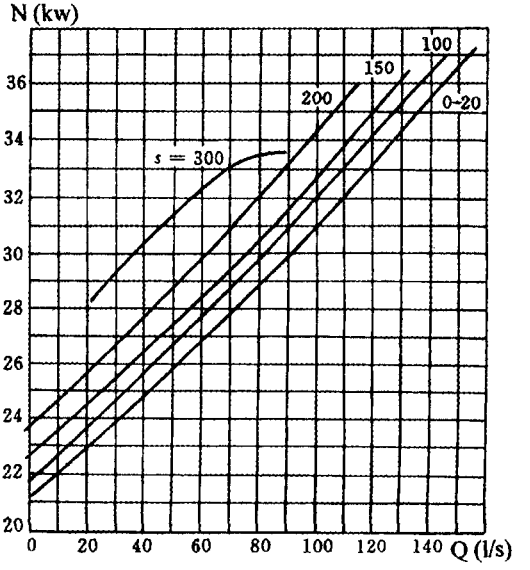

Figure 4.34 Characteristic curve of N(Q) of pump 10sh-13 at different solid contents conditions s (kg/m^3)

4.4.2 Hydraulic Design of Solid-Liquid Flow Pumps

The new hydraulic design method of solid-liquid two-phase flow pumps has been put forward in Ref. [4.20, 4.21] on the basis of experiences of test and design of a series of the new type of liquid-solid flow pumps. Their theoretical considerations for the design are as follows:

(1) Velocities of solid-liquid two-phase mediums are different all along because of the difference of the inertial forces.

(2) The fluid machine can only transfer the energy of the liquid phase and by no means can change the energy of the solid phase. The energy of solid phase is indirectly converted by the liquid phase in fact. Solid particles are in a by-force motion of liquid flow.

(3) The water flow is a function with respects of all kinds of physical characters and boundary conditions of flow domain. The pattern of the function depends upon mutual effects of the characters and the function solution is based on the boundary and initial conditions.

The new hydraulic design method of solid-liquid flow pump is based on the velocity distributions of the two phase flow structure in the pump. It is assumed that there exists a certain relation between the two-phase velocity fields. If the variation rate of the two-phase velocities gets a certain value and then most of solid particles may move along the streamlines of the liquid flow in the pump, the impact erosion of particles to pump walls may be reduced greatly and the friction erosion on the walls may increase, resulting in the extension of the service life of the solid-liquid pump. Therefore, the blade and flow passage designed according to the two-phase velocity distributions, not only can transfer the energy more effectively, but also can avoid the damage caused by the two-phase flow cavitation. And so far, the slurry pumps designed by using the new method has a higher efficiency and longer service time, as well as there is not any the erosion patterns, such as 'fish-scale pits' and 'honeycomb', but these pumps walls become brighter and smoother, as the results of frictional erosion, than those in the erosion pattern of other common slurry pumps.

It is possible that in the new method we do not need to change the design procedure and the design calculation method for conventional pumps, but need to add the consideration of the solid phase as movable and noncontinual boundary conditions in the liquid flow. The distortion of the velocity field of the liquid flow at the liquid-solid flow is the results of these boundary

conditions. That means, the velocity distribution of the clear water flow is regarded as the reference quantity and the solid particles are as boundary conditions, then the two-phase flow field can be calculated according to the Ref. [4.20].

Because of different inertial forces between solid and liquid through a pump, solid phase and liquid phase are moving with different velocities from its inlet to the outlet. While the velocity of solid particles is slower than that of water flow, particles effects are like a function of 'relative reduction' to the pump passage and a function of 'relative clog' to the water flow. Then in the liquid-solid flow there exists a velocity field distortion of the water flow compared with its original velocity field without particles. This type of the distortion makes the water velocity to be going up. Otherwise, if the velocity of particles is higher than that of water flow, there is a 'relative draw' effect of the particle to the water flow and the 'particle's existence is like a function of 'relative expansion' to the pump passage and makes the water velocity to be decreased.

The Suction Chamber of Pump

The distortion velocity of two phase flow in the suction chamber of a pump can be derived as follows. At first, the original energy head of clear water flow is H_c, that is,

$$H_c = z_c + \frac{p_c}{\gamma_L} + \frac{V_{cx}^2}{2g} \tag{4.60}$$

where the z is the height, p is the pressure and V_x is absolute velocity along the streamline x, γ is the gravity rate. The subscripts c are refereed to the clear water, and L and s to liquid and solid at the two phase condition respectively. Due to the influence of solid particles, the energy head of distortion of velocity and pressure fields H_1 is in the following form:

$$H_1 = z_L + \frac{p_L}{\gamma_L} + \frac{V_{Lx}^2}{2g} \tag{4.61}$$

If neglecting the difference between two potential, then $p_L = p_c$. And the input energy of the pump for both cases are the same, that is, $H_l = H_c$. So far, the distortion values of both velocity and pressure are as follows:

$$\frac{p_c - p_L}{\gamma_L} = \frac{V_{Lx}^2 - V_{cx}^2}{2g} \tag{4.62}$$

Then the distortion equation of the liquid flow velocity between the two-phase flow and the pure water flow can be obtained [4.20]:

$$V_{Lx}^2 - V_{cx}^2 = K_x^2 \tag{4.63}$$

where K_x is the velocity distortion coefficient

$$K_x = \sqrt{\frac{4gd(\gamma_s - \gamma_L)(\sin\theta + c_y \cos\theta)}{3C_x\gamma_L}}$$

And C_x is the drag coefficient along the flow direction, C_y is the drag coefficient in the direction perpendicular to the direction, θ is the angle between the flow direction and the horizontal direction, d is the diameter of particles.

According to the spherical particle motion equation, that is, the Bssinesque–Basset-Oseen equation, the following equation, so called as the transmission equation in two-phase flow, can be got at the steady flow condition:

$$V_{Lx} - V_{Sx} = K_x \tag{4.64}$$

which shows that if $V_{Lx} > K_x$, the particle can be transmitted by the liquid flow. If the velocity field at the clear water flow condition, V_{cx}, is known and the parameters of particle, such as, the diameter, the gravity rate and the drag coefficient, are given, the distortion velocity field, V_{Lx}, of the water phase and the particle-phase velocity, V_{Sx} at the liquid-solid flow, can be got by solving Equation. (4.63) and (4.64).

In engineering practice, particles should be considered as the spheroids with the equivalent diameter d_i, that is,

$$d_i = B_i N_i^{1/2} D_o \tag{4.65}$$

where N_i is the discharge percentage of the particle, B_i the transformation coefficient of particle and D_o the equivalent diameter of suction chamber of pump.

When the equivalent diameter is used in the calculation, the gravity rate of particles must be replaced by wet gravity rate, γ_w. If the liquid flow velocity field is distorted at the two-phase flow condition, the 'relative block' diameter of particles d_i' will be given in the following equation:

$$d_i' = \sqrt{2 - \left(\frac{V_{Lx}}{V_{Sx}}\right)^{\alpha}}\, d_i$$

Figure 4.35 shows the velocity triangle at the blade leading edge at the two-phase flow condition.

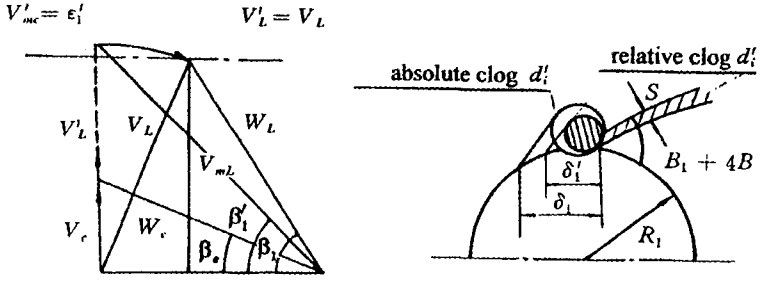

Figure 4.35 Calculation of velocity field at blade inlet

In Figure 4.35, V_c is the clear water flow velocity at the inlet. And the blade inlet jostle coefficient $\varepsilon_1' = 1.1 \sim 1.3$. At the two-phase flow condition, the distortion velocity of liquid flow V_L is larger than V_c. The velocity of

particles is zero because of their staying at the stationary point on the blade surface. The stationary particles make the flow passage be 'absolute block', then the blade jostle coefficient ε_1' and the blade thickness S_1' will be getting large. The attack angle at the inlet, β_e, is going up to the value of β_1 The inlet circulation is not zero any more and get a positive value, which results in the decrease of the head of pump.

Pump Impeller

The same consideration as in the last section can be used in a pump impeller. But the two-phase flow velocity distributions are complex through the pump impeller. Because the absolute velocity V is composed of relative velocity W and the rotational velocity $U = \omega^2 R$ (where ω is the rotational angular velocity of the impeller, R is a radius). Water and particles in the impeller are acted by the inertial, centrifugal and Coriolis forces in the coordinate system rotating with the impeller. As the results of the actions, particles move faster than the water flow gradually through the impeller, especially near its outlet. That means at the outlet the 'relative drawing' of the particles to the water flow appears. The difference between the of the two phases are as follows:

$$F_{r1} = \omega^2 R(m_S - m_L) \tag{4.66}$$

Then the relative drawing force by particles in meridional plane F_{r2} is expressed as:

$$F_{r2} = C_r \frac{\pi d_r^2}{4}\left[\frac{\gamma_L (V_{mS} - V_{mL})^2}{2g}\right] \tag{4.67}$$

where the subscripts m refers to the meridional plane, d_r is the particle diameter and Cr is the drag coefficient on this plane. Then the following equation is derived according to the mechanics basic equations:

$$V_{mS} - V_{mL} = K_r \tag{4.68}$$

where

$$K_r = \sqrt{\frac{4\omega^2 R d_r (\gamma_S - \gamma_L)}{3C_r \gamma_L}}$$

The diameter d_r will be replaced by the mean diameter d_{50} when considering infinite number of particles. The similar distortion equation of liquid flow on the meridional plane of the impeller is obtained as follows:

$$V_{mC}^2 - V_{mL}^2 = K_r^2 \tag{4.69}$$

If the liquid velocity at the two-phase flow condition is larger than zero, it is possible for the particles to transport through the impeller. In order to make the transporting effective, it is necessary to make V_{mL} larger than K_r, that is, $V_{mL} \geq K_r$. For getting the higher efficiency, the values of velocities at the impeller outlet should not be selected to be large.

The Coriolis force also make particles accumulate near the outlet, which results in change of the particle equivalent d_m, such as,

$$d_m = B_m \sqrt{\frac{\pi D_2 b_2 N_i}{Z \varepsilon_2}} \tag{4.70}$$

where D_2 and b_2 are the outlet diameter and the width of impeller respectively, Z is the number of blades, ε_2 is their displacement at the outlet, B_m the incorporate coefficient of particles there. The same 'absolute clog' also occurs at the outlet as at the inlet. The effects of blade thickness S_2 and the equivalent diameter of particles make the direction of water flow change, which gradually results in the transition of the flow to the state of 'the relative suction'. Then the distortion of particle diameter becomes:

$$\Delta d_m = \sqrt{1 - \left(\frac{V_{mL}}{V_{mS}}\right)^k} d_m \tag{4.71}$$

And the relative suction diameter of particle on the meridional section at the outlet is:

$$d_m = \sqrt{\left(\frac{V_{mL}}{V_{mS}}\right)^k}\, d_m \tag{4.72}$$

Therefore, regarding the liquid flow velocity on the meridional section at the outlet and at the clear water flow condition as the reference value, and the particles as the moving boundary layers, the velocity triangle at the outlet may be solved. The outlet circulation will decrease at the two-phase flow condition, which causes the pump head getting lower than that at the clear water condition. As mentioned before the increase of the inlet circulation make the head decrease too.

Volute Chamber of Pumps

At the clear water condition, the streamline equation of the pump volute casing is such as:

$$\tan\delta = \frac{V_r}{V_u} = const \tag{4.73}$$

where V_r and V_u are the radial and the circumferential velocity components. At the two-phase flow condition, the tangential velocity component V_{u2} at the impeller outlet will decrease. So will the tangential velocity V_u in the volute. And the particle velocity V_{ms} on the meridional section is larger than that of water flow, so that the discharge on a unit section of the volute, q, will also increase, the spiral angle of the volute should be large, then the width of volute should be greater than that of conventional pumps. In order to increase the hydraulic efficiency of slurry pumps, the two-phase flow design should be used to calculate the volute. At first, the distortional velocity in the volute chamber V_{3L} should be taken in the following values:

$$V_{3L} = K_{v3}\sqrt{2gH} - \Delta V_u \tag{4.74}$$

where K_{v3} is the velocity coefficient at the two-phase flow condition, ΔV_u is the value of decrease of V_u at the outlet at the condition. The area at the eighth section in the volute F'_{VIII} for the water flow at the two-phase flow condition should be indicated in the following equation:

$$F'_{VIII} = \frac{Q(1-N_i)}{V_{3L}\eta_v} \tag{4.75}$$

For the solid flow, the similar area F''_{VIII} also can be got:

$$F''_{VIII} = \frac{QN_i}{V_{3S}\eta_v} \tag{4.76}$$

where

$$V_{3S} = V_{3L} - K_3$$

$$K_3 = \sqrt{\frac{4gd_{i3}(\gamma_w - \gamma_L)(\sin\theta + C_y\cos\theta)}{3C_x\gamma_L}}$$

$$d_{i3} = \beta_3 N_i^{1/2} D_3$$

And D_3 is the discharge diameter of pump. The largest section area of the volute is F_{VIII},, that is,

$$F_{VIII} = F'_{VIII} + F''_{VIII} \tag{4.77}$$

Then all section areas of the volute can be calculated, as that:

$$F_{VII} = 7/8\ (F_{VIII})$$
$$F_{VI} = 6/8\ (F_{VIII})$$
$$F_V = 5/8\ (F_{VIII})$$
$$\cdots\cdots\cdots\cdots$$
$$F_I = 1/8\ (F_{VIII})$$

4.4.3 Examples of the Design

The foregoing design method has been used to design some types of slurry pumps. Table 4.9 and Table 4.10 show the performances of LXL-H-36 and

150 ND types of the slurry pump designed by using the method respectively. From the tables it is seen that at the two-phase flow condition the efficiency of the pump designed by the foregoing method could be higher than that at clear water condition. These types of pumps also get good cavitation performances.

Table 4.9 Performances of the slurry pump of LXL-H-36 type

Discharge Q (l/s)	Head H (m)	Shaft power N (kw)	Efficiency η (%)	Rotating speed n (r/min)	Solid weight content S (kg/m^3)	Gravity rate γ_m
65.72	39.19	38.16	66.10	1451		
60.03	40.10	36.55	64.50	1449	S = 0.0	1.0
55.31	40.74	35.59	62.70	1451		
63.29	39.20	39.08	73.40	1450		
52.05	39.60	36.14	66.00	1450	S = 235	1.18
44.07	39.00	33.66	59.00	1452		
64.82	26.10	47.48	68.20	1447		
62.04	35.80	46.72	65.70	1448	S = 538	1.41
58.57	36.30	45.98	63.90	1448		

Table 4.10 Performances of the slurry pump of 150 ND type

Discharge Q (l/s)	Head H (m)	Shaft power N (kw)	Efficiency η (%)	Rotating speed n (r/min)	Gravity rate γ_m
260.0	41.0	44.7	65.0	980	
320.0	40.0	51.3	68.0	980	1.0
382.0	39.5	58.4	70.5	980	
261.9	39.0	67.6	72.0	980	
321.3	37.4	76.6	75.0	980	1.75
382.4	36.5	86.4	77.0	980	
272.08	37.7	60.8	72.0	980	
314.1	36.8	78.1	74.2	980	1.83
372.4	34.7	84.6	76.5	980	

References

4. 1 Mei Z.Y. and Wu Y.L., (1996). 'Review of research on abrasion and cavitation of silt-laden flow through hydraulic turbine runner in China', Proc. of the 19th IAHR, Sectionof Hydraulic Machinery and Cavitation, 1996, Valencia, 641 ~ 650.

4. 2 Liu, Y.X., (1983). 'Effects of silt-laden flow on cavitation', *J. of Hydraulic Engineering*, 5, 55 ~ 58, (in Chinese).

4. 3 Huang, S.H. and Cheng, Z.J., (1994). 'Experimental study on critical cavitation coefficient of hydraulic turbines in silt-laden flow', *Technology of Hydraulic Machinery*, 5, 9 ~ 12, (in Chinese).

4. 4 Tong, W.M., (1993). 'Selection of objective parameter of hydraulic turbines on silt-laden river', *Proc. of Abrasion and Cavitation in Hydraulic Machinery*, 30 ~ 40, (in Chinese).

4. 5 Herbich, J. B. and Christopher, R. J., (1963). 'Use of high speed photography to analyze particle motion in a model dredge pump', *Proc. IAHR Congress*, London, 89 ~ 98.

4. 6 Itaya, T. And Nishikawa, T., (1983). 'Study on sand pumps', *Trans. JSME,* Vol. 29 ~ 27, B, 1786 ~ 1794.

4. 7 Zarya, A.N., (1983). 'Motion of phases of the mixture in acentrifugal impeller', *Fluid Mechanics-Soviet Research*, Vol. 17 ~ 3, 84 ~ 90.

4. 8 Menemura, K. et al, 1986, 'Behavior of solid particles in a radial-flow pump impeller', *Bulletin of JSME*, Vol. 29 ~ 253, 2101 ~ 2108.

4. 9 Zhao J.T., (1991). 'The movement of solid particles in centrifugal impeller', *Pump Technology*, No. 1, 1 ~ 6, (in Chinese)

4. 10 Guo, Z.Q., Xu, H.Y. and Wu, Y.L., (1992). 'Experimental study on motion of solid particles in centrifugal impeller', *Proc. of Intern. Conf. On Pumps and Systems*, Beijing, 504 ~ 512.

4. 11 Wu, Y.L., et al., (1993). 'Experiment on solid-liquid two-phase flow in centrifugal impeller', *Proc. Int. Symp. on Aerospace and Fluid Science*, Sendai, 379 ~ 387.

4. 12 Elizabeth, A.E. et al, (1991). 'Survey of literature on visualization of particulate two-phase flow', *ASME FED*-Vol. 118, *Liquid-Solid Flow*, 131-161.

4. 13 Carder, T., Masbernat, O. and Roco, M.C., (1991). 'Liquid-solid slip velocity around a centrifugal pump impeller', *ASME FED*-Vol. 118, Liquid-Solid Flow, 101.

4. 14 Carder, T., Masbernat, O. and Roco, M.C., (1993). 'Two-phase velocity distribution and overall performance of a centrifugal slurry pump', *ASME FED*-Vol. 154, *Pumping Machinery*, 177-185.

4. 15 Hergt, P. et al, (1994). 'A study of the outlet velocity characteristics of slurry pump impeller', *ASME FED*-Vol. 189, *Liquid-Solid Flow*, 197-205.

4. 16 Sun, Z.X. et al, (1995). 'Experimental investigation of the flow inside a model pump impeller by PIV measurement', *Proc. of Intern. Conf. of Pumps and Fans*, Beijing, 795-798.

4. 17 Walker, C.I., (1992). 'The effect of impeller geometry on the performance of centrifugal slurry pumps', *Proc. of Symposium on Freight Pipelines*, Wollogong, 97-101.

4. 18 He, X.J., (1994). 'Principles and design method of slurry pumps', *Fluid Machinery,* Vol. 22, No. 9, 17-22, (in Chinese).

4. 19 Xu, H.Y., (1992). 'Solid-liquid flow design principle on slurry pump', *J. of Engineering Thermophysics*, Vol. 13, No. 4, 389-394, (in Chinese).

4. 20 Cai , B.Y., (1984). 'Theory and design of two-phase flow of centrifugal pump', *Bulletin of Sciences*, Vol. 29, No. 3, 407-414.

4. 21 Cai, B.Y., (1985). 'A new pattern of energy transformation in two-phase flow', *Bulletin of Sciences*, Vol. 30, No. 6.

4. 22 Zhao, J.T., (1986). 'Experimental study of effects of solid material to performances of centrifugal pump', J. of Tsinghua University, Vol. 26, No. 1.

This page is intentionally left blank

Chapter 5

Erosion-Resistant Materials

M. Matsumura and B. E. Chen

5.1 Selection of Erosion-Resistant Materials

M. Matsumura

For hydraulic machine (turbine and pump) working in sand particles laden water, the selection of abrasive erosion resistant structural material or of protective surface coating is one of the most important issues in their design. For this the following points, although which make the selection quite difficult, should be considered:

(1) A material may show different sand erosion resistance for different erosion conditions.

(2) Test results obtained under accelerated erosion conditions in laboratory cannot be applied extended to real machines.

The erosion resistance of material will be discussed in the following sections successively.

5.1.1 Multi-posion Test of Erosion Resistance in a Real Water Turbine

A systemic research on the selection of erosion-resistant materials was made by Prof. Duan Chang Guo and his collaborators. They conducted a multi-position scheme of erosion testing to demonstrate that one material may show different silt erosion resistance at different positions in a water turbine because the components of the hydraulic machinery have different erosion

condition parameters such as the velocity and turbulence of flow. The material specimens were installed at all main components of flow passages of the water turbine, which used to be suffered from silt erosion, as follows:

1. Outlet edge of runner blades;
2. Outlet edge on water turbine's guide vanes;
3. Plane of guide vane;
4. Labyrinth ring (wearing ring);
5. Inlet wall of draft tube;
6. Wall of spiral case;

as shown in Figure 5.1.

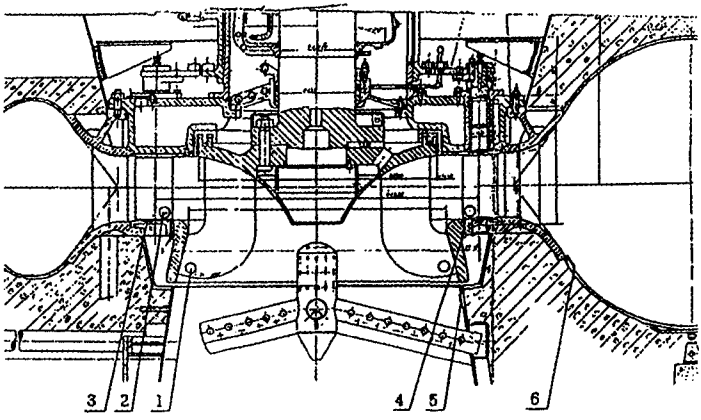

Figure 5.1 Positions where test specimens were installed

The parameters of the test turbine are shown in Table 5.1. 15 kinds of metallic and non-metallic materials shown in Table 5.2 were tested.

The testing materials include conventional cast stainless steels (SCS1, SCS5 and SCS13); low carbon cast steel (SC46); high nickel, high manganese chrome stainless steels (NMC and NMW); steel plates (SM4 and SM58Q); high manganese carbon steel (DFME); plasma spray coatings of ceramics of aluminum oxide (AL-203) and tungsten carbide (WC); Synthetic rubber coatings (S-61 and L-2710) and protective resin paint coatings (EPX and PUT).

Table 5.1 Parameters of the test turbine

Type	:	Vertical shaft Francis turbine
Maximum water head	:	71.1 m
Desing water head	:	61.0 m
Turbine output	:	8,800 kw
Flow discharge	:	17.1 m^3/s
Rotating speed	:	428.6 rpm
Draft head	:	1.0 m
Dia. of runner	:	1,400 mm

Table 5.2 Materials tested

No.	Material	Chemical composition (%)							
		C	Si	Mn	P	S	Ni	Cr	Mo
1	SCS1	0.10	0.39	0.72	0.022	0.013	0.89	12.24	0.34
2	SCS5	0.035	0.47	0.68	0.020	0.012	4.01	12.08	0.29
3	SCS13	0.040	0.99	1.00	0.023	0.010	9.54	19.52	-
4	SC46	0.19	0.40	0.78	0.020	0.009	-	-	-
5	NMC	0.042	0.43	2.54	0.020	0.013	5.56	13.27	0.60
6	SM41	0.17	0.20	0.85	0.023	0.006	-	-	-
7	SM58Q	0.10	0.24	1.34	0.014	0.003	0.20	0.07	0.12
8	NMW	0.07	0.35	5.60	0.010	0.003	6.50	12.40	1.24
9	DFME	0.14	0.56	17.05	0.017	0.001	2.16	15.19	-
10	AL-203	(Ceramic of aluminum oxide)							
11	WC	(Ceramic of tungsten carbide)							
12	S-61	(Synthetic rubber)							
13	L-2710	(Synthetic rubber)							
14	EPX	(Epoxy resin paint)							
15	PUT	(Polyurethane resin paint)							

The operating period of the test turbine was divided into three stages. Total testing duration was 1779 hours. To obtain consecutive data of the

variation of the silt content, water was sampled daily from the inlet of the test turbine. The average silt content was 1~3 kg/m^3; however, it reached 18.95 kg/m^3 maximum in a flood season. Grain size classification and mineral composition analysis were conducted. Though the results showed some scatter depending on the sampling date, the average values are shown in Table 5.3.

Table 5.3 Properties of silt

Grain size (μm)						
Range	<53	53-100	100-208	208-295	295-351	>351
Average	27	77	154	252	323	426
Mineral composition [relative content (%)]						
Quartz	15	20	30	35	35	30
Feldspar	20	30	35	35	30	30
Carbonate	40	20	10	5	5	5
Augite & hornblende	5	15	15	20	25	25
Chlorite	10	5	5	5	5	5
Mica	remainder	remainder	remainder	remainder	remainder	remainder

Weight loss of each specimen was measured by a precision balance scale at every inspection, and the average depth of erosion damage was calculated for each specimen by the following formula:

$$h = 10\,\Delta G / \gamma S \tag{5.1}$$

where,

h: average eroded depth [mm].
ΔG: weight loss of specimen at each inspection [g].
γ: specific weight of the test material [g/cm^3].
S: surface area of the test specimen subjected to silt erosion [cm^2].

Relative index of abrasive erosion resistance is defined by the following formula, in which abrasive erosion resistance of cast carbon steel SC46 is taken as a reference value, since it is most commonly used for water turbine components.

$$\varepsilon = h_R / h \tag{5.2}$$

where,

h: average eroded depth as calculated by equation (5.1) for each specimen at different position of the turbine [mm].

h_R: the same for SC46 specimen at each position of the turbine [mm].

ε: relative index of abrasive erosion resistance for each material at each position of the turbine.

An ε larger than 1.0 means that the material is more resistant against silt erosion than the SC46. Table 5.4 shows the value of relative erosion index of final measurement for each specimen at each test position

Table 5.4 Relative abrasive erosion indices

Position / Material	Runner blade	Guide vane	Bottom ring	Wearing ring	Draft tube	Spiral case
SCS1	1.91	1.97	0.46	1.24	-	-
SCS5	-	1.01	0.53	0.76	-	-
SCS13	1.09	1.17	0.40	0.93	-	-
SC46	1.00	1.00	1.00	1.00	1.00	1.00
NMC	1.42	1.24	0.88	-	-	-
SM41	-	-	-	-	1.43	1.03
SM58Q	-	-	-	-	1.45	0.68
NMW	1.44	1.27	1.42	2.44	-	-
DFME	0.93	0.92	1.43	-	-	-
AL-203	-	3.06	1.18	-	-	-
WC	-	2.59	2.42	-	-	-
S-61	-	-	-	-	-	7.29
L-2710	-	-	-	-	6.61	8.67
EPX	-	-	-	-	= 0	= 0
PUT	-	-	-	-	= 0	0.30

According to Table 5.4, a set of specimens of the same material does not show same degree of relative erosion resistance at different test positions. For

example, all the relative erosion resistance indices for cast stainless steels of SCS5 and of SCS13 on both runner blades and guide vane exceeds 1.0. This means they are both more resistant to silt erosion than SC46. However, those of the specimens on wearing ring and on bottom ring are far below 1.0 showing that is their erosion-resistance is poorer than SC46 at these positions. On the other hand, the relative erosion resistance indices of DFME for runner and guide vane positions are less than 1.0, while that for bottom ring position exceeds 1.0.

Prof. Duan and his collaborators attributed the aforementioned results to differences in erosion type with different hydroabrasive erosion conditions. Due to the difference in flow velocity and in impinging angle of sand particles the erosion conditions were classified as shown in Table 5.5.

Table 5.5 Classification of silt erosion

Test position	Flow velocity	Impinging angle	Type of erosion
Runner blade	High (22 ~ 27 m/s)	Small Larger in cavitation area	II
Guide vanes	High (18 m/s)	Small Larger near bottom end	II
Wearing ring	very high	Larger, due to vortex & turbulent	III
Cheek crevice plate	very high	Larger, due to vortex & turbulent (*)	III
Spiral case	low	Small	I
Draft tube	low	Small Larger near inlet	I

(*): Test specimens were placed under the bottom end of the guide vanes at their open position. where the classification is as the type III.

Figure 5.2 shows the relative erosion resistance indices of six different metallic materials for two different test positions with different erosion types, the type II and the type III. From this figure, it can be seen that the

relative erosion resistance indices of these materials fall on the opposite sides of the line of 1.0 for the two different testing positions. It is concluded that the order of the materials in silt erosion resistance varies depending on the condition and the type of erosion attack.

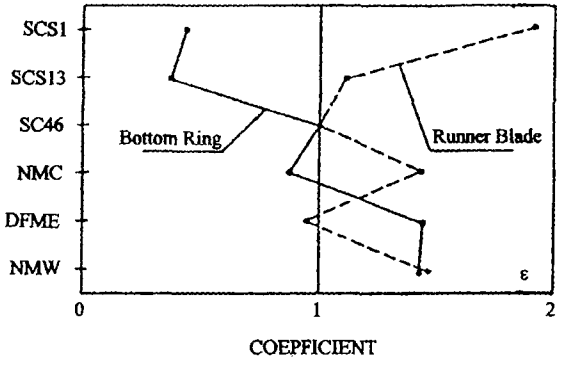

Figure 5.2 Relative erosion indices for two different positions

5.1.2 Laboratory Erosion Tests

The objects of laboratory erosion tests are generally

(1) Ranking the materials according to their resistance to erosion, or

(2) Estimation of the service life of a material, which is used for the construction of a hydraulic machine.

Measurement of a relative index proportional to the resistance, ε cited in the previous section for example, will accomplish the first object. An absolute numerical measurement, mm/year for example, will be required for the second object. In other words, a laboratory test with the second object is of a higher grade than the one with the first object. However, it has often been experienced by designers and engineers that any experimental result obtained by these laboratory erosion tests cannot be applied to the real machine. Even the ranking of materials hardly coincides with the order of their service life in the field. Reasons for this discrepancy are discussed below.

The discrepancy between a laboratory test result and the performance of the material in the field is totally attributed to the fact that the extent and

nature of the damage which is caused by the impingement of solid particles on a surface strongly depends on the impact angle, on the shape of the particle, on the impact velocity and on the material of the surface.

Figure 5.3 shows typical dependencies of erosion on impact angle for a ductile material (mild steel, aluminum etc.) and a brittle material (quenched steel, ceramic etc.). Here erosion is defined as the mass of material removed per unit mass of impinging particle. It should be noted that the ductile material exhibits the most severe damage at impact angles lying typically in the range 20° to 30°. In contrast with this, the brittle material is damaged most rapidly under conditions of large impingement angle, and minimally at shallow impact angles. Suppose particles were directed at a right angle against a test specimen in a laboratory test, a brittle material would suffer heavily and a ductile material slightly. This test result will nominate the ductile one for the construction material of a real machine. However if it were used for a pneumatic powder transport pipe wall, where solid particles impinge at shallow angles, a larger damage will result on the ductile material than on the brittle one. Thus, from this example it can be seen that the performance of the materials in the field is often clearly opposite to the indication of the laboratory test.

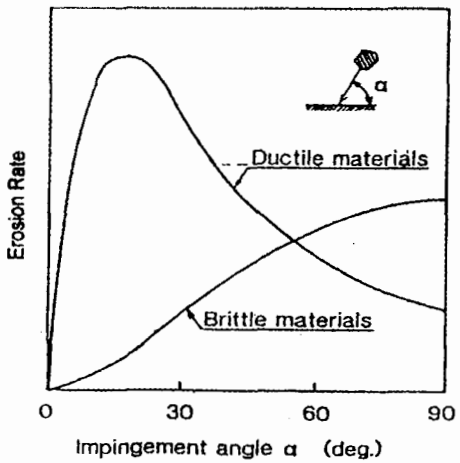

Figure 5.3 Schematic representation of erosion rate on impingement angle

Then, how about making the impact angle of particles in tests coincides with that in real machines, or conducting the erosion test at every impact angle? This would be successful provided that the impact angle in a real machine could be precisely predicted. The problem with this is that the particle impact angle is not clear in nearly all of laboratory testing machines. It will be surely much harder to predict it in a real machine.

Even if the prediction and the measurement of impact angle were successful in both the machines, the test results will still be far from predicting the real damage so long as exactly the same particles with those in the field were not used in the test.

Figure 5.4 shows the results of two series of erosion tests which were conducted by Sheldon and Finnie 1966, under the same impact velocity on the same group of materials but using two different grit mesh sizes of 120 (particle size of 127 μm in diameter) and 1000 (9 μm). If we make a comparison between the hardened steel and the plate glass in their resistance to erosion caused by the impact of 127 μm particles (Figure 5.4 (a)), the former will be naturally judged more resistant to erosion than the latter because it sustains a smaller erosion at every impact angle. In contrast with this, in the erosion test of 9 μm particle resulted the typical variation for the same materials now behaving in a ductile or more ductile manner in which erosion reached a maximum at an angle considerably less than 90 deg, and the hardened steel sustained a far larger erosion over all impact angles as compared with the plate glass. Thus, the conclusion from the result of laboratory test using 127 μm particles, would be the very reverse of the performance of the materials in a real machine if it were engaged with 9 μm particles. Some larger particles than those used in field are often adopted for laboratory tests in order to shorten the test duration through accelerating the erosion rate of the test specimen. The test results obtained under such accelerated test conditions cannot be extended to real machines even if the measurements were conducted at every impact angle.

How about now using the particles obtained in field for laboratory tests, and measuring the erosion rate at every impact angle? Under such test conditions the erosion rate of test specimens will be reduced to nearly the same level as those in field, and far longer test duration, say weeks or months possibly, will be required to cause some measurable weight losses to the specimen. This is not an exaggeration of the problem; the reduction of the particle diameter from 127 to 9 μm resulted in the damage rate being reduced

to one hundredth (compare the scales of ordinates of Figure 5.4). Particles impact velocity in laboratory tests has to be unavoidably raised in order to obtain test results within the limited duration of tests.

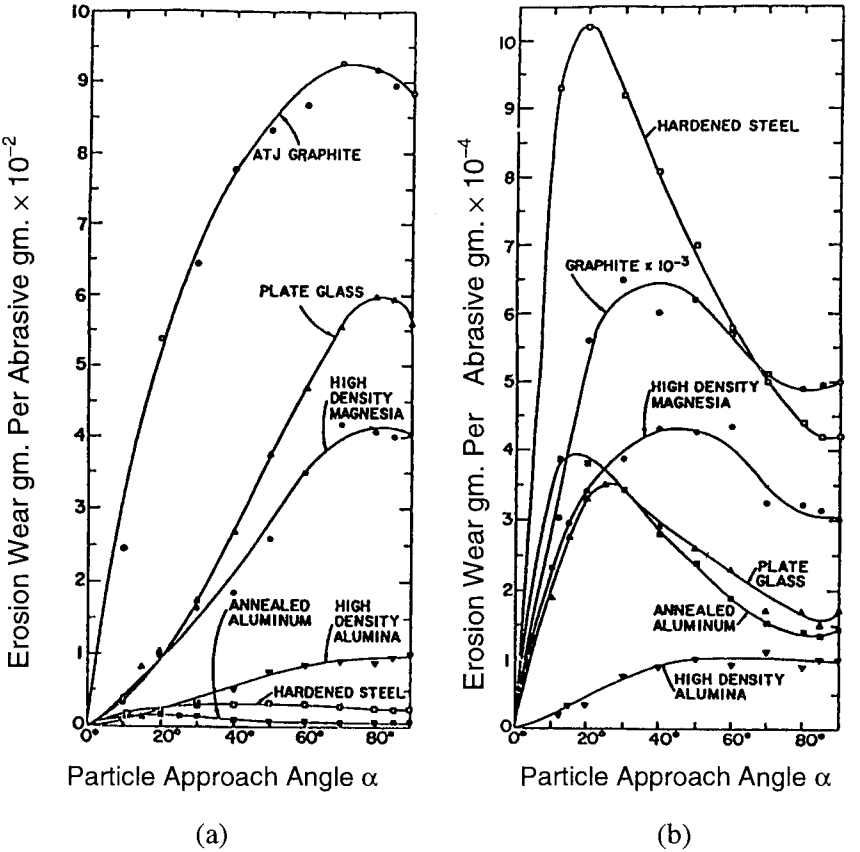

(a) Predominently brittle manner, grit mesh size = 120

(b) Predominently ductile manner, grit mesh size = 1000

Figure 5.4 Erosion of a number of materials versus the particle impact angle, particle velocity is 150 m/sec, SiC grit

Particle impact velocity has an influence of no less importance than particle size does on the extent of damage. This is also true regarding the brittle/ductile manner of the target material.

Figure 5.5 is an experimental result obtained by Prof. Hojo and his colleagues about the influence of the particle impact velocity on the erosion extent and the brittle/ductile manner of erosion damage of a methyl-methacrylate resin. At lower impact velocities, the maximum of erosion at shallow impact angles was larger than that at high angles, which indicated the ductile manner of the resin. The higher the impact velocity, the larger the maximum erosion at high impact angles, which is a typical variation for the same material from a ductile to a brittle manner. This variation of abrasive erosion manner surely depends on the characteristics of the material, namely it is different from one material to another. Therefore, the result of a laboratory erosion test which was obtained under a particle impact velocity different from that in the real machine cannot be expected to coincide with the real performance of the materials in field.

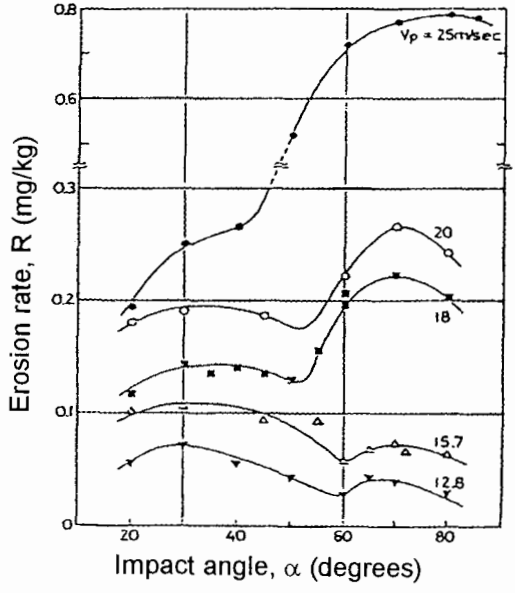

Figure 5.5 Effect of impact angle on erosion rate for various impact velocities

It is concluded as follows. The erosion extent and brittle/ductile manner of abrasive erosion damage depends strongly on the particle impact angle, on the particle size, on the impact velocity as well as on the characteristics of the target material. This fact leads to the realization that a laboratory erosion test result, even a ranking of materials, can not coincide with that of their performance in field, provided that all of these experimental conditions were not precisely coincided with those of the real machine. A laboratory test, however, which is conducted under the same condition, as the field is no more a laboratory test but a real machine test.

It will be discussed in 5.2, how we can still make use of laboratory tests in material selection for the construction of hydraulic machines.

5.1.3 Selection of Materials for Hydraulic Machines

Duan Chang Guo and his collaborators gave the following comments on the abrasion erosion resistance of the materials which were examined in the multi-position test described in 5.1.1.

(1) Low carbon cast steel (SC46):

SC46 is a kind of ordinary low carbon cast steel commonly used for hydraulic machinery. As is widely known, its erosion resistance is not satisfactorily high for the hydraulic machinery working in silt-laden water. Experimental results obtained this time also indicated that SC46 suffered heavy weight loss on various test positions of a water turbine.

(2) Conventional cast stainless steel (SCS1, SCS5 and SCS13):

These are also commonly used stainless steels for water turbine components, such as runners, guide vanes, etc.. Among them, SCS13 is an austenitic stainless steel and SCS1 and SCS5 are martensitic, of which SCS5 has higher nickel content.

Among these stainless steels, SCS13 has some cold hardening effect, and shows better cavitation erosion resistance than the other two. However, for silt erosion SCS13 was not so resistant as expected but SCS1 showed higher resistance. It's resistance is twice as much as that of SC46 for the type II erosion and was nearly identical to SC46 and the other two materials for the type III erosion.

These stainless steels revealed more resistance than SC46 for the type II erosion but less or identical for the type III erosion.

(3) *High nickel, high manganese chrome stainless steels (NMC and NMW):* These two alloys are newly developed metals having high cold hardening effect and, hence, high cavitation erosion resistance. NMC is the one suitable for casting and NMW is the one for protective overlay weldment.

Of these two alloy metals, NMW showed better resistance against both the type II and the type III erosion, especially for the type III. Since there are very few metals with enough resistant against the type III erosion, high resistance of NMW is noteworthy. The erosion resistance of NMC is identical to NMW for the type II erosion but it is much poorer than NMW or nearly equivalent to SC46 for the type III erosion.

(4) *High manganese carbon steel (DFME):*
This king of steel is prevalently used as a high resistant steel against dry sand abrasion. It showed higher resistance against the type III erosion as expected, but with almost the same degree of resistance as SC46 against the type II erosion. If we consider the difficulties in welding or in machining this kind of steel, its use for turbine components is hardly advantageous.

(5) *Steel plate (SM41 and SM58Q):*
They are expected to be used for manufacturing spiral case and draft tube, which would suffer rather light silt erosion.

The test results showed that erosion resistance of two tested materials is almost identical to each other. For both position of spiral case and draft tube, the absolute amount of erosion weight loss is small. Therefore, either of the steel plates can be used as the materials for these components.

(6) *Plasma spray coating (WC and AL-203):*
Specimens coated with two kinds of ceramic materials were tested. One ceramic material was WC, tungsten carbide, and the other was AL-203, ceramic of aluminum oxide. The coating layers were formed by the plasma spray method. The coated surface of these ceramics showed very high hardness, Vickers hardness of 570 for WC and 630 for AL-203.

These specimens were tested at two positions, guide vane and bottom ring. The results indicate that these two kinds of coating layer have very high silt erosion resistance, which corresponds 2.6 ~ 3.0 times as much as that of SC46. Of these two materials, AL-203 seems better. As can be seen from the result of the specimen on the bottom ring, however, it is so

brittle and easily cracked by rough impact that the coating layer may break off after a certain period of operation. WC seems less brittle than AL-203.

(7) *Protective resin coating by painting (EPX and PUT)*:
EPX is a epoxy resin paint and PUT is a polyurethane resin paint, both of which are claimed to be abrasion resistant. The thickness of the paint film was 0.3 mm for both. The specimens were placed on wall of the spiral case and the draft tube. The test results were quite disappointing. All paint films were eroded out and erosion progressed into matrix materials after the test. Visual observation revealed that the damage was not due to the poor cohesion of the paint film to the matrix metal but was due to poor erosion resistance of the coating film itself.

(8) *Rubber coating (S-61 and L-2710)*:
Specimens with two kinds of rubber coatings, S-61 and L-2710, were tested in the spiral case and in the draft tube. Erosion damage on these specimens was very slight. Their values of relative erosion resistance indices reached up to 7 to 9, representing very high resistance. Of these two kinds of rubber coatings, L-2710 was better and there were no scratches found on its surface by close visual inspection after the test. Such rubber coating may possibly be applied to the turbine components, which receive a higher flow velocity and rougher turbulence. The possibility should be verified by further prototype test on runner blades or guide vanes.

Prof. Duan's testing results and comments are very practical and useful for designers in selecting materials for hydraulic machines because the examination was conducted not in a laboratory-testing machine but in a real water turbine. It must, however, be reiterated, as is often pointed out in the comments, that each material tested did not compose any whole component or part of the water turbine, but was installed the specimen in it. Some basic mechanical properties other than the resistance to solid erosion will be requested for a material when it is used for the construction of a hydraulic machine.

Dr. Hashimoto, a veteran engineer with extensive experiences about abrasion during his work in a factory manufacturing solid particle-dealing machines such as mills, mullers, crushers and sand blasting machines. Basing on his experiences, he wrote in 1977 an excellent and practical manual on

how to cope with abrasion attack with reference to such machines. The following criteria for evaluation of material are cited here from his manual.

From an economic point of view, materials must be selected that minimize the cost ratio, which is defined as;

$$Cost\ ratio = \frac{Sum\ of\ costs}{Service\ life}$$

where the numerator includes the material cost, personnel expenses for exchanging worn parts, decrease in production during the exchange of the parts and warehouse charge for holding stock of parts. The denominator, the service life of the material is to be obtained from (1) a laboratory test, or from (2) the performance of the material in a real machine. As his experiences totally deny the reliability of the laboratory tests, he concluded that the service life of a material must be obtained from the performance of the material in a real machine. This cannot be obtained without constructing a real machine using the very material and running it for a long duration. The evaluation of materials from the economic side is, therefore, nothing but a "trial and error".

In the approach to the subject from the technical side, we have to strictly adhere to the necessary steps described below.

<1> Impulsive load:

If the machine has to carry a heavy impulsive load, reject cast iron and nonmetallics. High manganese cast steel and high-alloyed cast steel stand well against it. Low alloyed cast steel follows them. In the case of little or no impulsive load, introduce cast iron or nonmetallics. The choice between them depends on the intensity of abrasion attack. The former has the advantage in terms of economy.

<2> Static load:

Bracketing machines and rolls of compacting machine carry a hundred tons of static load. Nothing but cast steel can be used for these machines. Hard facing cannot be used because the base metal beneath the hard facing yields to the heavy static load. Cast iron bears medium static load, but nonmetallic materials should be avoided because some of them are too brittle and others bear too much deformation. In the case of very low static load, elastomers and plastics are applicable.

Sintered carbides and cast minerals stand well against the attack of hard and sharp edged particles.

<3> Temperature of environment:

Polymers are rejected at the temperatures higher than 50°C. At much higher temperatures sintered carbides and cast minerals perform better than other materials. They can stand 1000°C for a long duration so they are usually used as an excellent heat-resisting material.

<4> Corrosion:

In the case where the particles themselves or the particle-laden liquid is corrosive, corrosion-resisting materials have to be chosen. The oxidizing agent attacks metals that resulting an oxide layer on the surface, which is hard and brittle enough to flake off on particle impact. Thus metals will lose thickness rapidly. The choice must be made from cast nonmetallics, sintered carbides and polymers, considering the restrictions of <1>, <2> and <3> at the same time.

<5> Intensity of abrasion attack:

In the selection of materials to cope with abrasion attack, the abrasion resisting characteristics of materials is the last consideration among the requisites. As a general rule, a material harder than the particles should be used. If this is impossible, you should choose the hardest one among the materials, which get through the above mentioned restrictions.

Dr. Hashimoto concludes his suggestion for selecting material with an indication that hardened surface layers of cemented steel, nitriding steel or siliconizing steel have to be given enough thickness in order to exhibit their resistance to abrasion.

5.2 Metallic Materials

M. Matsumura

Among abrasive erosion resistant materials, metals take the most important position as bulk material for the construction of hydraulic machines. They have the erosion resistance to a certain extent when the coating or the hard facing over the surface is broken and the substructure is exposed to the erosion attack. In addition, they have good mechanical strength,

which is the most important requisite for the constructing materials of erosion-sustaining hydraulic machines.

In this paragraph, we will discuss the problem that is, how to assess their performance in field from laboratory test results. An approach to this may be comparing the ranking of several materials based on their performance in real machines with those in laboratory test, which were conducted under various conditions. Dr. Oka and his colleagues compared the actual service performance of metallic materials with their test results in laboratory, which is discussed below.

5.2.1 Testing Apparatus and Procedure

Two kinds of testing apparatuses have been used. One is the vibratory apparatus, which uses a magnetostriction vibratory unit.

Figure 5.6 shows the schematic diagram of the apparatus. Uniform slurry is set up in a fluidized-bed bath, i. e., solid particles are suspended uniformly in an upward flow of liquid. The test specimen is a column of $\Phi 16 \times 22$ mm with the side wall entirely covered by a vinyl tape except for the circular bottom of the test surface. It is vibrated axially at a high frequency of 19.9 kHz in the slurry. The peak-to-peak amplitude is 20 μm. The particle impact parameters were determined by inspecting the size and shape of the craters on the surface and are given in Table 5.6. It was also confirmed that no cavitation damage occurred on the test surface, provided that particles of over 50-μm diameter were used for the slurry.

Table 5.6 Test conditions

	Impact velocity m/s	Impact angle	Impact parameter	Slurry particles
Vibratory apparatus	2.2	90°	Frequency 19.9 kHz	Silica sand 60 wt%
Jet-in-slit apparatus	1.7	90°	Flow rate 2 L/min	Silica sand 6 wt% Gypsum 12 wt%

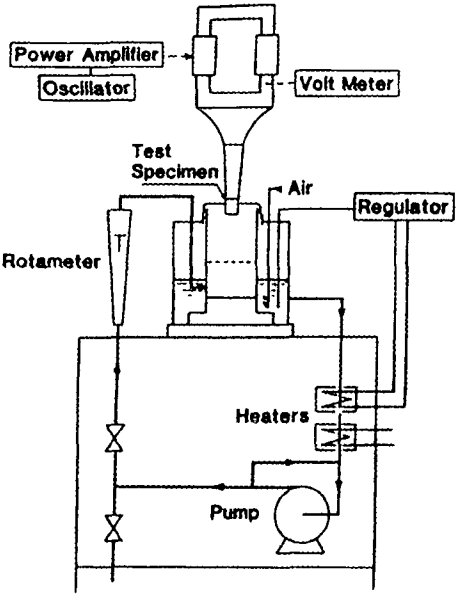

Figure 5.6 Schematic diagram of vibratory testing apparatus

The other is a jet-in-slit apparatus of which schematic diagram is shown in Figure 5.7.

The main tank of transparent polyvinyl chloride resin consists of two sections placed one over the other. In the lower section of smaller diameter, a fluidized-bed is set up. In the upper section of the tank, the slurry exhausted from the test section is separated into solid particles and clear liquid. Solid particles precipitate to fall down into the fluidized-bed below. The bulk of the clear liquid is circulated by the pump into the test section and the rest into the underside of the distributor to set up the fluidized-bed. The liquid jet from the nozzle (1.6 mm diameter) located in the center of the test section sucks up the slurry, which is mixed with the jet liquid to impinge upon the surface of the test specimen ($\Phi 18 \times 4$ mm) and thereafter exhausted radially through the slit between the specimen and guide plate. The damage occurs at the area of jet impingement on the specimen as well as on the surface outside of this area which is due to the radial flow. Four pieces of such test sections are installed in the tank.

Both the apparatuses have some common features:

* The damage develops only on the testing surface of the specimen, no other part of the apparatus is damaged,
* The amount of particles, the specimen size and the power consumption are all small, and
* The reproducibility of the test results is excellent.

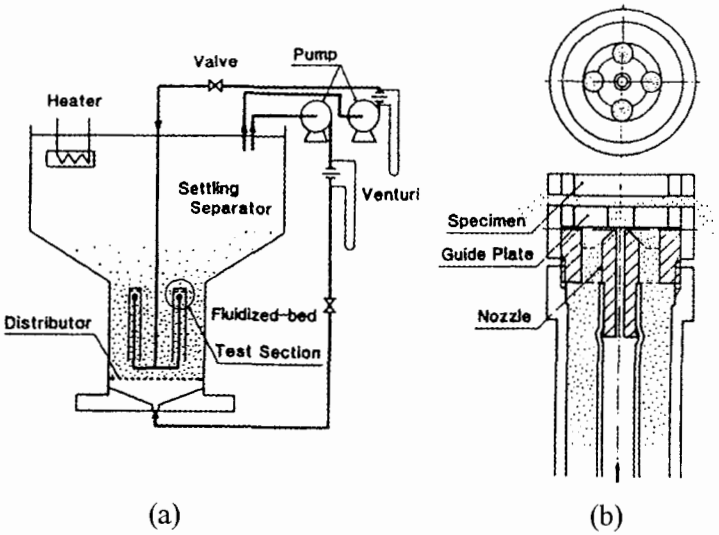

Figure 5.7 Schematic diagram
jet-in-slit testing apparatus (a) and test section (b)

The most important feature is that the whole of the test surface is subjected to erosion and corrosion at the same time. This is indispensable for obtaining reliable test results.

The chemical compositions and physical properties of the materials are listed in Table 5.7. They are stainless steel of type 316L and Hastelloy C as reference materials, and the material A and B which have been used for the pump components, It should be noted that material A and B have higher hardness than other materials, which was attained by precipitation-hardening.

Table 5.7 Chemical compositions and physical properties

Specimen	Chemical compositions (%)			Metallic structure	Physical properties	
	C	Ni	Cr		Vickers hardness	Specific gravity
Stainless Steel (316L)	0.03	13.5	17.0	Austenite	198	8.0
Hastelloy C	0.08	53.5	16.5	Austenite	210	8.7
Material A	0.05	5.5	25.5	Austenite and ferrite	280	7.7
Material B	0.03	6.0	28.0	Austenite and ferrite	500	7.7

Slurries were prepared from the particles and the corrosive liquids in Table 5.8. The liquids have nearly the same chemical compositions as those in an actual stack gas scrubber. Silica sand particles were used for the reference slurry. The gypsum particles were the same as that contained in the slurry of the scrubber.

Table 5.8 Slurries

Liquid of Slurry	Particles	Particle properties	
		Mean diameter, μm	Vickers hardness
Deionized water	Silica sand	77	1200
H_2SO_4 sol., pH 4			
H_2SO_4 sol., pH 4 Cl-(C_aCl_2), 200 ppm	Gypsum	40	20 ~ 50
H_2SO_4 sol., pH 2			

Corrosion tests were conducted in the jet-in-slit apparatus by corrosive liquids without particles. The slurries of the solid particles and deionized water were used for the erosion tests, and those of the solid particles and the corrosive liquids for the erosion-corrosion tests.

5.2.2 Test Results

Some results of the erosion test as well as the erosion-corrosion tests are shown in Figures 5.8 and 5.9. Fairly good linear relations existed between the volume loss of specimen and test duration, and constant damage rates independent of the test duration were obtained from the slopes of the lines.

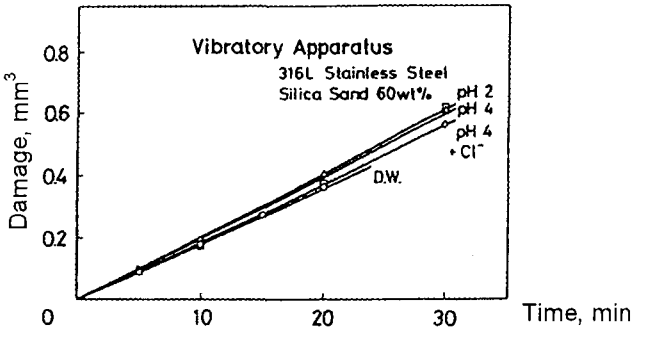

Figure 5.8 Erosion-corrosion damage versus testing time for 316L stainless steel
(frequency 19.9 kHz; amplitude 20 μm; silica sand 60 weight %; and respective liquids)

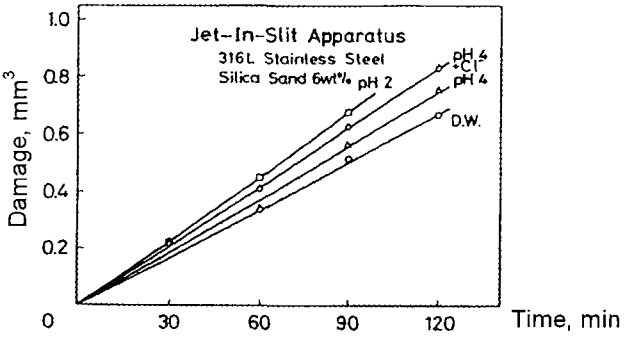

Figure 5.9 Erosion-corrosion damage versus testing time for 316L stainless steel
(jet velocity 1.7 m/s; silica sand 6 weight %; and respective liquids)

The results of erosion-corrosion tests in the slurries of silica sand and corrosive liquids are shown in Figure 5.10 (vibratory apparatus) and Figure 5.11 (jet-in-slit apparatus). Each apparatus has established the same order in damage rate, namely stainless steel > Hastelloy C > material A > material B.

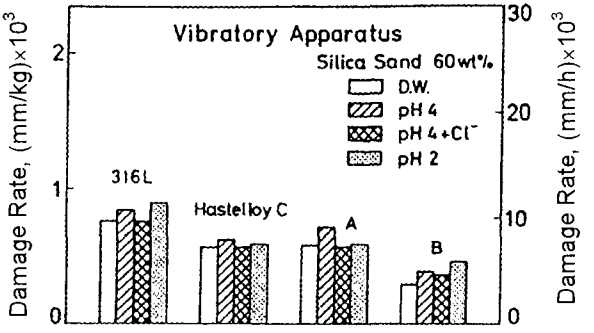

Figure 5.10 Damage rates of materials in vibratory apparatus (Frequency 19.9 kHz; amplitude 20 μm; silica sand 60 weight % and respective liquids)

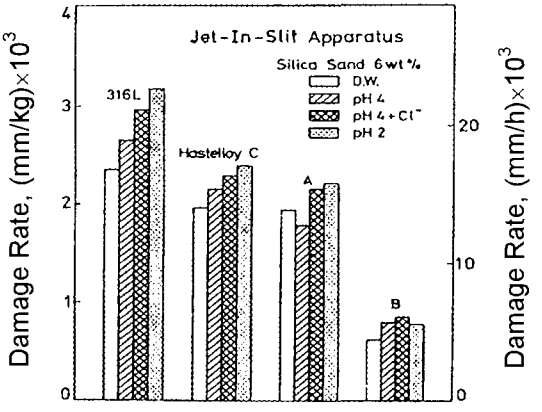

Figure 5.11 Damage rates of materials in jet-in-slit apparatus (jet velocity1.7 m/s; silica sand 6 weight % and respective liquids)

Erosion-corrosion tests in the gypsum slurry were conducted only in the jet-in-slit apparatus (the particle size was so small that cavitation occurred in the vibratory apparatus). The damage rates shown in Figure 5.12 are extremely small as compared with those in the silica sand slurry (Figure 5.11). This may be attributed to the size as well as to the hardness of the particle. As to the order in damage rate, stainless steel and Hastelloy have exchanged their positions, though material A and B stayed in the same position. The specimen surfaces showed a matted appearance as well.

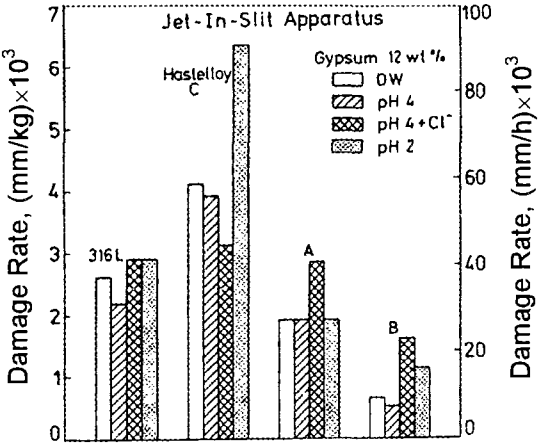

Figure 5.12 Damage rates of materials in jet-in-slit apparatus (jet velocity 1.7 m/s; gypsum 12 weight % and respective liquids)

5.2.3 Damage on Pump Components

The materials A and B had been used for the components of pumps A and B respectively, which had a common size: bore diameter, 125 mm; impeller diameter, 265 mm; revolution, 1750 rpm; discharge quantity, 85 m^3/h. They pumped gypsum slurry of sulfuric acidity at the same time under nearly the same condition: the solid particle concentration has ranged between 20 and 40 wt%, and pH value between 2 and 4.

The average depth of the damage on the blade top of the impellers and the surface of the casings has been measured at regular intervals. Figure 5.13

shows the results. It should be recognized that the damage depth increased linearly with the duration of the operation just as in the case of the test apparatuses. In each pump, the casing was damaged more deeply than the impeller, and the damages of pump B were one-half or one-third smaller than A which is in good agreement with the test results shown in Figures 5.11 and 5.12.

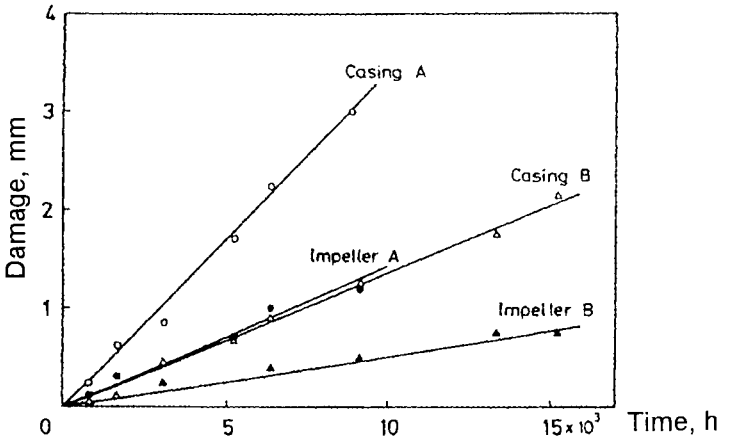

Figure 5.13 Erosion-corrosion damage versus operation time for pump components in actual service

5.2.4 Requisites for Laboratory Tests

The test results obtained by the jet-in-slit apparatus agreed well with the actual performance in the pumps not only on the order but also on the relative magnitude of the damage rate. In other words, a quantitative relationship has been established between the test result and the actual damage of the pump. By using the relationship, it is possible for the apparatus to assess quantitatively the damage rate of any material, which is to be used as pump components under the same operating condition.

It is, however, indispensable to know the effects of the test parameters on the test results for estimating the damage rate to any material which is to be used under some other conditions. With this object in mind, a quantitative comparison of the damage rate between the test results and the field

performance of the material *B* is given in Table 5.9, in which the damage rate in mm/h of the pump components was divided by the bulk particle flow rate to obtain the damage rate per unit mass of the particle i.e. mm/kg. It arouses interest that the damage rate in mm/h of the specimen in the gypsum slurry is of nearly the same magnitude as those of the pump components, though the rate in mm/kg is by 10^3 times larger than those of the components. On the contrary, the damage rates of specimen in the silica sand slurry are much larger than any damage rate of the actual pump.

Table 5.9 Comparison between test results and actual performance of material B

	Damage rate (mm/h)	Damage rate (mm/kg)
Jet-in-slit test		
Silica sand slurry	6.2×10^{-3}	8.6×10^{-4}
Gypsum slurry	2.3×10^{-5}	1.6×10^{-6}
Actual performance in pump		
Impeller	5.5×10^{-5}	3.2×10^{-9}
Casing	1.4×10^{-4}	8.2×10^{-9}

<1> Slurry particles:

A point of advantage in using the silica sand slurry is the shortening of the test duration. For example, it takes, at a minimum 20 h, to determine the damage rate of Hastelloy C in the gypsum slurry, but only 2 h is enough for precise measurements in the silica sand slurry. As to the test results, however, stainless steel and Hastelloy C have exchanged their positions in the order of damage rate when the silica sand slurry was used for the gypsum slurry (comp. Figure 5.11 with 5.12). This suggests that the actual slurry in question should be used even though the purpose of the test might be a rough selection of materials. In the tests for estimating the damage rate of a material in the actual plant, it is absolutely necessary to use the actual slurry.

<2> Slurry liquid:

Tests on a material in the vibratory apparatus by silica sand slurries have resulted in nearly the same magnitude of damage rates

independent of the slurry liquid (Figure 5.10). A similar tendency was recognized in the test results of the jet-in-slit apparatus where silica sand particles were used (Figure 5.11). In contrast to these, the damage rates of the material varied largely depending on the slurry liquid when gypsum particles were used (Figure 5.12). This is apparently because the erosiveness of gypsum particles is less intense than that of silica sand, and correspondingly, the effect of corrosion has appeared more distinctly on the test results. Thus, in this aspect as well, it is necessary to use the actual slurry in laboratory tests.

<3> Particle impact parameters:

The average velocity of slurry flow over the impeller surface is on the order of 1 m/s, which is the volumetric flow rate divided by the area of the flow cross section. Over the casing surface, it is on the order of 10 m/s on the assumption that the slurry is circulating at the same velocity as the impeller. It is generally recognized that the erosion rate by particles impingement is proportional to the 2.3th (ductile material) ~ 6th (brittle material) power of the impact velocity. The difference in the damage depth between the impeller and the casing is less than expected from the slurry flow velocities. This discrepancy may be attributed to the differences in the particle flow rate and their impact angle. These parameters are characteristic of each components and depend decisively on the operating conditions.

The particle's impact velocity in the jet-in-slit apparatus is 1.7 m/s as shown in Table 5.6, which is naturally not coincident with those in the pump. It is impossible and not necessary for them to coincide with each other, because the quantification of the impact velocity effect is possible, and hence the damage rate under any impact velocity may be easily estimated based on test results under known conditions.

The impact angle is the most important parameter that gives decisive influence not only on the extent of damage but also on its nature. In the jet-in-slit test, a slurry jet impacted on the disk-shaped specimen, and then the slurry run radially over the specimen surface to the periphery. Thus, the impact of particles was at a right angle in the central part of the specimen and, is oblique at its periphery. It was found, however, that the oblique impact of the particles barely contributed to the weight loss of the specimen because the damage (decrease in the thickness) was concentrated on the central part of it.

The damage of the specimen was consequently due to the particle impact at a right angle. In contrast with this, the particle impact angle on the impeller and casing surface was apparently oblique except for the small central portion of the impeller. Then a question arises why such an excellent coincidence could be obtained for the erosion behavior of the test specimen with that of pump impeller? An answer to this question is given by Figure 5.14 which was obtained for commercially pure iron using the slurry of silica sand and deionized water in fixed-bed type vibratory testing apparatus in which particle impact angle was precisely regulated (See Oka, 1986). You can see that erosion rate at the impact velocity of 1.4 m/sec depends greatly on the impact angle but it does not at all when the impact velocity was decreased to 0.4 m/sec. This behavior is explained as follows. The difference in the damage mechanism (deformation and cutting) originates itself in the shape of craters which were created on the metal surface by particle impact: the oblique impact of a particle causes a creator of slender shape due to some sliding of the particle following the impact and cutting is predominant on the crater surface. Whereas a particle impact at a right angle brings about a round crater where deformation is predominant. When a particle was impacted at a low velocity (0.4 m/sec for example), the particle possibly can not slide over the surface even though the impact angle was oblique. Or it can slide but without leaving any scratch on the surface. In other words, the damage mechanism will possibly be the same with that of a right angle impact irrespective of the impact angle of the particle provided that the impact velocity is lower than a certain critical velocity. In the case of Figure 5.14 the critical velocity lies between 1.4 and 0.4 m/sec. In the case of the slurry pump, the critical impact velocity is surely higher than this because a softer particle (gypsum) strikes a harder metal surface as compared to the experiment of Figure 5.14.

In conclusion, the point of reasons why the test results of the jet-in-slit apparatus have agreed with the actual performance of the material might be the low damage rate (mm/h) in the apparatus, which was inevitable in using the actual slurry in the field. The specimen with a large testing surface has achieved the measurement of such a low damage rate and yet of small weight, as well as by the stability of the apparatus which could bear the operation of such a long duration.

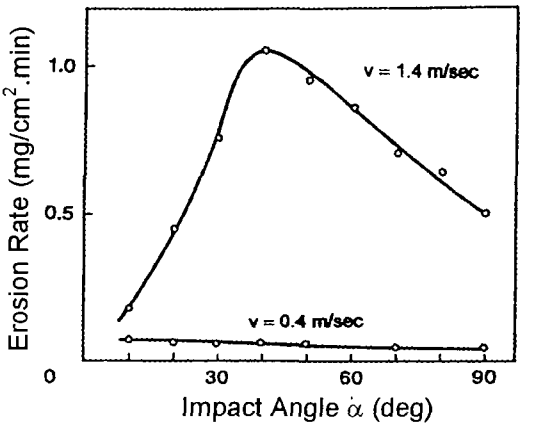

Figure 5.14 Effects of impact angle on erosion rate of iron specimen in fixed-bed facility (frequency 19.9 kHz; amplitude 24 μm and 8 μm; silica sand and deionized water, 40°C)

5.3 Organic Polymer Linings

M. Matsumura

Excellent ability to resist erosion is inherent in some organic polymers as is described in section 5.1 However, since they have certain weak points regarding mechanical strength and heat resistance, they are usually applied as lining to parts of machines and equipment used in ambient temperatures. For example, steel pipe lined with polyurethane was applied by a clay factory in England to a kaolin tailing pipeline in 1970. Currently it is being used successfully in a dam deposit pipeline in Japan. Its applications to mining and dredging operations are also being evaluated. For further applications and wider use, however, the following problems have to be resolved.

1> The manufacturing cost of polyurethane lined pipe is much higher than conventional steel pipe.

2> The flange joint and mechanical joint of the lined pipe are very expensive and troublesome. A welding joint has to be developed.

3> Experience in using polyurethane lined pipe is not extensive. Its long-term durability is as yet unknown.

To solve these problems, Kawasaki Steel Corporation and Mitsubishi Chemical Industries Co. Ltd. of Japan developed a system for room temperature curing of polyurethane (RTV) and established an economical manufacturing technique for RTV lined pipe (See Owada, 1986). In the following, new technical developments are discussed and compared with the conventional technique.

5.3.1 Conventional Polyurethane Lined Pipe

Conventional thermosetting polyurethane uses a polyether-polyurethane system which consists of Toluenediissocyanate (IDI) - polytetramethylene ether glycol (PTMG) as prepolymer and 4,4`-methylenebisorthochloroaniline (MOCA®, Dupont Company) as curing agent. Typical molding conditions and mechanical properties of thermosetting polyurethane are shown in Table 5.10. Heating treatment is indispensable for the mixing, casting and curing processes, for promoting chemical reaction and for obtaining the appropriate properties.

The manufacturing process of thermosetting polyurethane lined pipe is shown in Figure 5.15. The steel pipe is blasted and degreased to get a proper surface for the following primer application. The purpose of the primer application is to protect the pipe from corrosion and to bond polyurethane elastomer to the steel surface. Phenol-Polyvinyl (butyl alcohol) primer is commonly used. This primer has to be baked at nearly 100°C, and the optimum coating thickness is usually 20 to 50 μm when it is dried.

The prepolymer and the curing agent are separately melted and degassed at 80°C and 120°C respectively. Then, they are mixed in quantities of 12 (prepolymer) to 1 (curing agent).

Mixed polyurethane is poured into the steel pipe, which is preheated to between 100° and 110°C. After leveling the liquid polyurethane, centrifugal casting is performed for straight piping. For bend piping and other fittings, mold casting is used. The lining is cured at 100° and 110°C for 3 to 4 hours. Lastly, polyurethane lined pipes are usually aged for 1 to 2 weeks at room temperature before shipping.

There are the following problems with this conventional manufacturing technique.

1> Heating processes result in extensive energy consumption which together with heating equipment increases the cost of production.

Table 5.10 Typical molding conditions and mechanical properties of thermosetting polyurethane and RTV elastomer

Moulding condition	Thermosetting polyurethane	RTV
Prepolymer	TDL-PIMG	RTP
Viscosity (cps)	2000 (80°C)	3000 (25°C)
Curing agent	MOCA®	RTC
Viscosity (cps)	500 ~ 600 (120°C)	1000 (25°C)
Mixing ratio (parts by wt.)		
Prepolymer	12	3
Curing agent	1	2
Mixing temperature (°C)		
Prepolymer	80	R.T. (Room-temp.)
Curing agent	120	R.T.
Pot life (min.)	10	5.5
Curing temperature (°C)	100 ~ 110	R.T.
Curing time(hour)	3 ~ 4	1 ~ 2
Post cure temperature (°C)	R.T.	R.T.
Post cure time (week)	1 ~ 2	1 ~ 2
Mechanical property		
Hardness (Shore A)	87	83 (ASTM D2240)
100% modules (kg/cm^2)	41	43 (ASTM D412)
300% modules (kg/cm^2)	82	85 (ASTM D412)
Tensile strength (kg/cm^2)	306	387 (ASTM D412)
Elongation at break (%)	503	519 (ASTM D470)
Tear strength (kg/cm)	63	69 (ASTM D470)
Tabor abrasion loss (mm/1000 cycle) (H-18 wheel, 1kg)	42	40 (ASTM D1242)
Water absorption (%) (40°C×7 days)	1.4	1.6 (ASTM D690)

2> The size of product is limited because the scale of equipment for heating is limited.

3> Casting and curing at 100° to 110°C make it impossible to repair the polyurethane lining in the field.

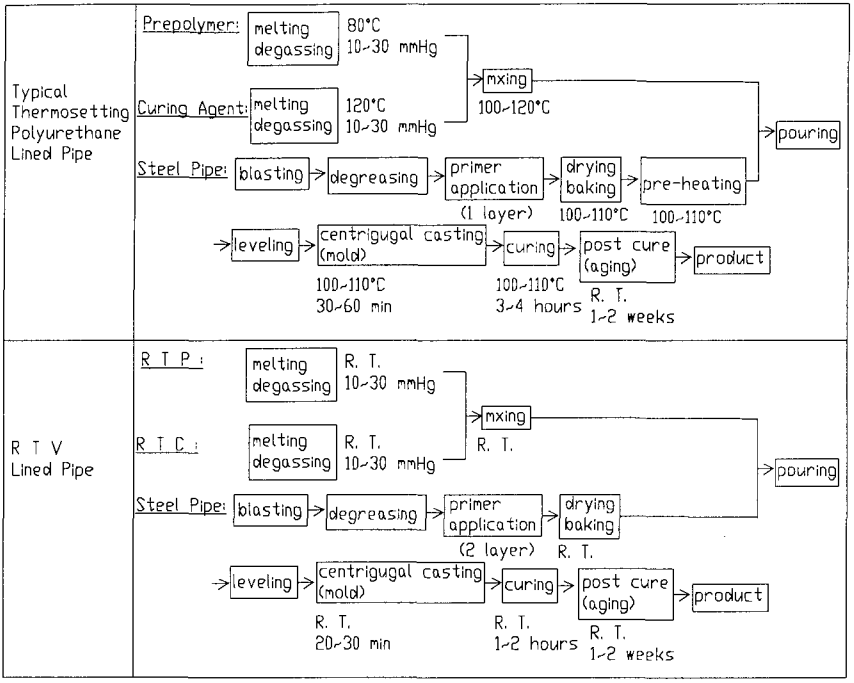

Figure 5.15. Manufacturing processes of typical thermosetting Polyurethane lined pipe and RTV lined pipe

5.3.2 Room-Temperature Curing Polyurethane (RTV)

(1) Improving polyurethane curing reaction characteristics:

To control the polyurethane curing reaction, it is necessary to modify the composition of functional groups. RTV chemistry is basically similar to conventional thermosetting polyurethane but special polymeric components are added to both prepolymer (RTP) and curing agent (RTC) in order to improve molecular cross-linking reactivity at room temperature. Modified points include the composition ratios of active-NCO, -OH, and -NH_2 groups in the prepolymer and curing agent, and the molecular weight

distribution of the polymer components. These changes create a new polyurethane system that can be cured at room temperature, RTV molding conditions and the initial properties of RTV are shown in Table 5.10. Physical properties of RTV bear some comparison with those of thermosetting polyurethane.

(2) Erosion resistance:

Erosion resistance is the most important characteristic for a lining material used in slurry transportation pipes. Slurry erosion tests were performed to compare the erosion resistance of RTV to other materials. Figure 5.16 shows test conditions and relative erosion resistance obtained in a rotary erosion testing apparatus (Figure 5.17). The erosion resistance of RTV to coarse silica stone was 10 to 12 times greater, and to fine silica stone 40 to 50 times greater than that of mild steel. Thermosetting polyurethane also showed good erosion resistance; to coarse silica stone 7 to 10 times greater, and to fine silica stone 30 to 40 times greater than mild steel.

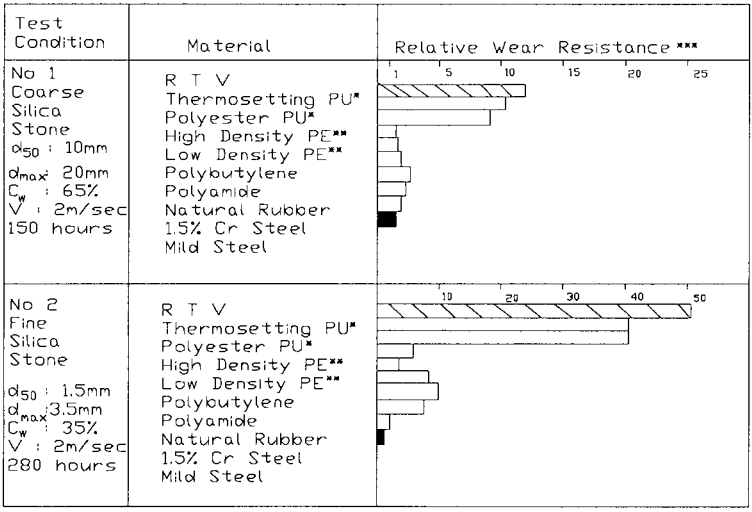

PU*: Polyurethane; PE**: Polyethylene

*** Wear resistance of mild steel is expressed as 1.

Figure 5.16 Chart of relative erosion resistance to mild steel by means of rotary erosion test

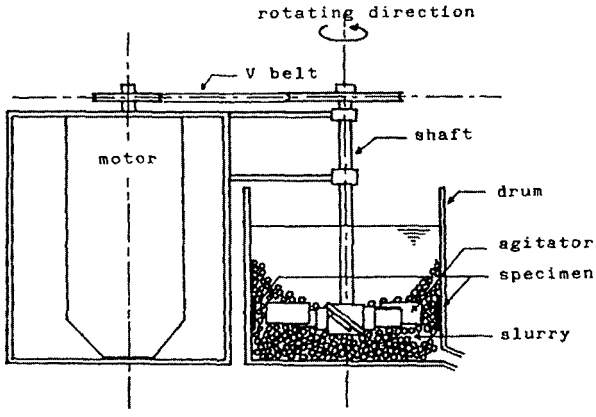

Figure 5.17 Schematic drawing of rotary erosion tester

(3) *Effects of mechanical properties of RTV on erosion resistance:*
Relationships between erosion resistance and mechanical properties are shown in Figs 5.18 (a) to (f) for RTV and other materials. These figures show the relative erosion resistance of materials as compared with mild steel, the figures being obtained from the rotary erosion tests using coarse silica stone. It can be seen that the erosion resistance of polyurethane elastomers increases with the increase in tensile strength, tensile elongation and tear strength. It also increases with the decrease in hardness and Tabor abrasion loss

These results may imply that the erosion process of these materials can be regarded as a mechanical fracture phenomenon, because the most erosion resistant polyurethane has the largest tensile strength multiplied by elongation among the materials tested (see Figure 5.18 (e)), and the mechanical fracture energy, which is an index of resistance to the mechanical fracture energy, which is an index of resistance to the mechanical fracture, is proportional to the tensile strength multiplied by elongation.

Lower hardness and larger tear strength are desirable for increasing the erosion resistance of RTV as shown in Figures 5.18 (a) and (b). But these properties are closely correlated with other properties. For example, lower hardness relates itself to reduced tensile strength, and increased tear strength leads to decrease in elongation. Therefore, we may conclude that a balance of properties is needed for the best results.

Tabor abrasion resistance showed a good correlation with slurry erosion resistance, as is shown in Figure 5.18 (f). This test may be usable for selecting materials.

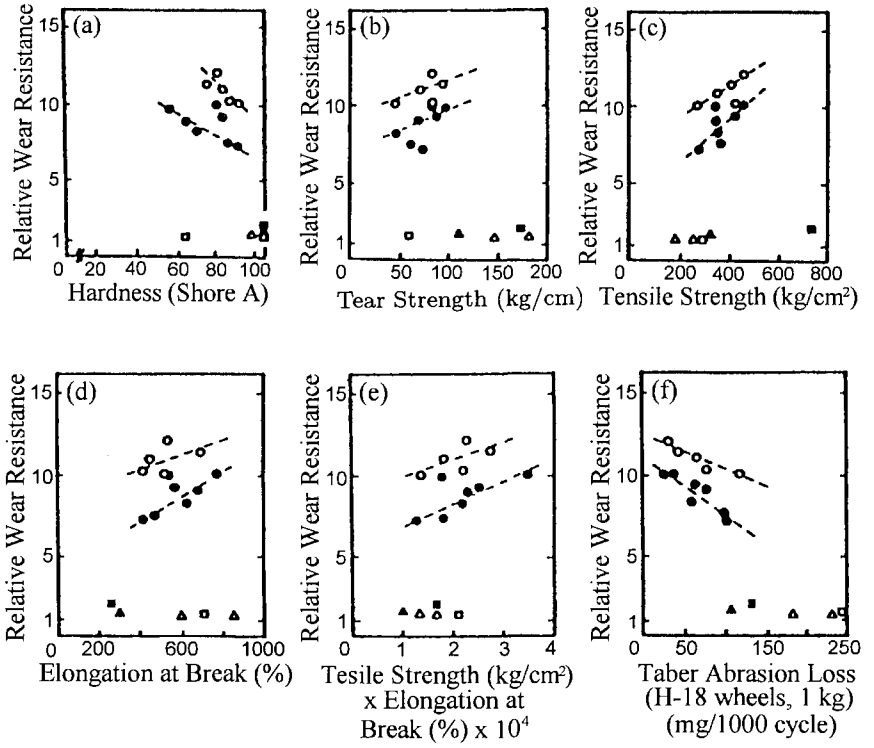

Wear test condition: Coarse silica stone; No.1 in Figure 4.2

Symbols: ○-RTV, ●-Thermosetting polyurethane, △-Polyethylene ▲-Polybutylene, -Natural rubber, ■-Polyamide

Figure 5.18 Relation between erosion resistance and mechanical property

(4) Hydrolytic stability:

The hydrolytic stability of polyure-thane is a major factor in ensuring the long-term durability of polyurethane lined pipe in slurry service. It is greatly affected by the composition of the prepolymer. Generally

speaking, polyether-polyurethane has a better hydrolytic stability than polyester-polyurethane does. The susceptibility to hydrolysis of ester linkage in polyurethane structure is far larger than that of ether, urethane, urea, biuret, or allophanate linkages. Cross-links of polyester-polyurethane are destroyed in a shorter time than polyether-polyurethane.

(5) Corrosion resistance:

Corrosion resistance of lining materials in the principal consideration in severely corrosive slurry environments. RTV is generally resistant to the mild conditions of common acids, bases, and organic reagents encountered in slurry environments.

5.3.3 Durability of RTV Lined Pipe

(1) Loop test:

The loop test was carried out using closed loop equipment totaling 35 m long. This loop is composed if 89 mm or 114 mm (O.D.) pipes, a slurry tank, a slurry pump, an electromagnetic flowmeter and a thermometer. The flow rate and the temperature of slurry were automatically monitored.

Table 5.11 shows the shape of specimens and materials tested. All pipe specimens had the same inside diameter and carefully joined using flange joints to avoid discrepancy in level.

Table 5.11 Specimens and materials used in closed loop test (mm)

Specimen		Material	
Straight pipe:		RTV lined pipe:	
dimater (O.D.)	89, 114	lining thickness	4
thiness	4	hardness (shore A)	80
length	500		
		Thermosetting:	
90° Bend pipe		lining thickness	4
dimater (O.D.)	89, 114	hardness (shore A)	80
thiness	4		
bending radius	450	Lined pipe	
		Steel pipe: ASTM A53-71a	
		thickness	8

Coarse silica stone, medium and fine silica stones, coarse and fine coals, and fine iron ore were used as abrasive particles to simulate dredging slurry, dam deposit slurry, coal slurry and iron ore slurry respectively. Table 5.12 shows. the testing conditions.

Table 5.12 Testing conditions of loop test

Specimen size (mm)	Slurry	Particle size (mm)	Concentration				
			C_w (wt%)	Velocity (m/sec)	Temperature (°C)	pH	Period (day)
89	silica stone	d_{50} 3 d_{max} 6	32	4	20~36	8.1~8.3	90
89	silica stone	d_{50} 1.5 d_{max} 2.5	45	4	5~19	8.1~8.2	90
114	silica	d_{50} 0.5	50	3	15~35	7.8~8.2	90
89	coal	d_{50} 4 d_{max} 10	35	4	6~34	7.7~8.1	120
114	coal	d_{max} 2.4	45	3	25~50	8.3~8.5	90
114	iron ore concentrate	d_{max} 15	50	3	25~45	7.3~7.6	90

Average erosion loss and maximum erosion loss were obtained respectively from the weight loss and the thickness loss of a specimen. Correction for water absorption was made by using a dummy specimen immersed in water at the same temperature during the same period as the loop erosion test. Table 5.13 shows the loop test results. The erosion loss of a straight pipe is the average erosion loss, and that of a bend pipe the maximum thickness loss. It also shows the relative erosion resistance of polyurethane lined pipe taking the erosion resistance of steel pipe as 1.

The test results in Table 5.13 are summarized as follows. The coarse silica stone slurry caused larger erosion than the medium one independent of the material tested and of the specimen shape. The fine silica stone (condition No. 3), fine coal (condition No. 5) and iron ore (condition No. 6) caused so little damage to lined pipes that their erosion resistance relative to the steel pipe could not be estimated. The bend specimens suffered larger erosion than the straight specimens, even though it was taken into account that the erosion

loss of the bend pipe was the maximum loss in thickness and, that of the straight pipe was the averaged loss. In every test condition, PTV polyurethane lining pipe exhibited better erosion resistance than thermosetting polyurethane lining pipe.

The adhesion strength of the RTV elastomer after the loop test was more than 20 kgf/cm at 90° peel-off. Thus, any deterioration in adhesion was not detected.

Table 5.13 Results of loop test

Testing condition	Specimen	Erosion loss (mm/year)			Relative erosion resistance		
		RTV	Thermosetting polyurethane	Steel pipe	RTV	Thermosetting polyurethane	Steel pipe
1	Straight	2.12	2.35	30.20	14	13	1
	Bend	23.60	30.70	201.40	9	7	1
2	Straight	1.64	1.64	18.70	11	11	1
	Bend	19.80	37.40	132.50	7	4	1
3	Straight	0.00	0.00	2.53	*	*	1
4	Straight	0.29	0.31	7.60	26	25	1
	Bend	1.50	1.50	21.30	14	14	1
5	Straight	0.00	0.00	1.46	*	*	1
6	Straight	0.00	0.00	1.66	*	*	1

*: Impossible to estimate the relative wear resistance.

(2) Field test:

Table 5.14 shows the field test results with RTV lined pipe installed in three slurry pipelines in practical use. In every environment, RTV lined pipe showed good erosion resistance and enough adhesion strength. Use of RTV lined pipe in the blastfurnace slag pipeline and the blastfurnace dust concentrate pipeline are continuing successfully.

Table 5.14 Results of field test

Slurry condition				Specimen (Pipe) (mm)	Erosion rate
Slurry	Particle size (mm)	C_w (wt%)	Velocity (m/sec)		
Dredging sand	d_{50}: 0.15 d_{max}:20	60	5.0	750 mm (I.D) 1000 mm long Steel thickness 12 mm RTV lining 7 mm	Steel: 4.7 mm/year; RTV: 0.7 mm/year;
Blast furnace slag	d_{max}: 25	45	4.2	300 mm (I.D) Steel 10 mm Natural rubber lining 20 mm RTV lining 10 mm	Steel: > 30 mm/year, life - 3 months; Rubber: 10 mm/year, life - 2 years RTV: 1.5 mm/year, predicted life - 5 years;
Blast fumace dust concentrate	d_{50}: 0.2 ~ 0.3	70	5.0	100 mm (I.D) Steel 8.6 mm RTV lining 5 mm	Steel: 2.3 mm/year, life - 3 years; RTV: no failure after 4 years;

5.3.4 Cost Estimation

In the cost estimation of polyurethane lined pipeline, we have to consider not only the initial cost but also maintenance and replacement costs, and service life as well. Because RTV lined pipe is manufactured by an energy-saving process the manufacturing cost is more than 20% lower than that of

thermosetting polyurethane lined pipe. Table 5.15 shows the relative cost and life expectancy in two slurry environments. The life/cost ratio may be a comprehensive measure to demonstrate the advantage of RTV lined pipe over other materials, even though it leaves the installation and maintenance costs out of account. It may be concluded that RTV lined pipe is the most economical material for pipelines which handle the abrasive and corrosive slurries of dam deposits, dredging sands and coarse coal. Considering maintenance and replacement costs, its advantages become even greater.

Table 5.15 Relative cost and life expectancy

Installation environment	Material (Pipe)	Relative cost	Relative life	Life/Cost ratio
1. Coarse silica stone	Steel pipe	1	1	1.0
	RTV lined pipe	4	14	3.5
	Th.PU* lined pipe	5	13	2.6
2. Coarse coal	Steel pipe	1	1	1.0
	RTV lined pipe	4	26	6.5
	Th.PU* lined pipe	5	25	5.0

Th.PU*: Thermosetting Polyurethane;
All relations based on 300 mm (O. D.), 6-m long flanged pipe.
Thickness: Steel pipe, 14 mm;
Polyurethane lined pipe, steel 8 mm + lining 6mm.

5.4 Ceramics

M. Matsumura

The important components in coal liquefaction plants are known to suffer severe damage due to the erosive nature of coal slurries as well as to the corrosive agents contained in them. Very short service lifetime (weeks) is experienced by the letdown valves trims and seats used to throttle high-temperature (350 ~ 450°C), high-pressure (30 ~ 140 kgf/cm^2) slurries. Block valves lose their tightness owing to the galling on their surface caused by coal

ash or catalyst particles. The critical parts of slurry flow meters suffer abrasive erosion and cannot indicate slurry flow rate correctly.

For the sound and stable operation of coal liquefaction plants, the development of materials, which are highly resistant to abrasive erosion, is indispensable. Several project teams were organized for investigating these problems and selecting suitable materials for the critical components in the demonstration plants of coal liquefaction. They reported some results of a primary investigation in which ceramics and their composites were nominated for parts of the plants as materials promising high erosion resistance.

Ceramics have a long career as useful materials for industry. They began to be utilized at about the same time as modern industry was born, and still now hold an important position together with metallic and organic materials. Ceramics in the past, familiar to us as tableware, were rather unsuitable for industrial use because they were brittle in nature and short of reliability in strength. Their use was, therefore, limited to concrete, brick or glass. With the recent technical progress in industry, the need has arisen for materials, which can be used in such severe environments, which even metallic materials can not bear, and also for those with special characteristics. In response to this demand, the strength of traditional ceramics has been greatly improved by selecting and preparing raw materials of high quality and high purity, and also by applying new manufacturing processes. In addition to the traditional ceramics of oxides such as SiO_2 and Al_2O_3 Ceramics of nitrides (Si_3N_4, TIN etc.), borides (AlB_2, TiB_2 etc.) and carbides (SiC, BC ect.) have been newly developed. These new ceramics (including the oxides) are endowed not only with inherent resistance to corrosion and to heat but also with outstanding electrical, optical and mechanical properties. They are called, therefore, fine ceramics. Among fine ceramics, those for structural use are called engineering ceramics (Table 5.16).

Table 5.16 Major engineering ceramics

Nitrides:	βSi_3N_4, AlN, BN, TiN
Carbides:	αSiC, SiC, B_4C, WC, TiC
Oxinitrides:	Sialon (Si-Al-O-N)
Oxides:	Al_2O_3, Zr-Y_2O_3, Al_2O_3-ZrO_2

As structural material, engineering ceramics have many advantages:

1> Many are highly resistant to oxidation and other forms of chemical attack.
2> Some are exceptionally hard and resistant to abrasive erosion.
3> They are usually lighter than metals.
4> They can maintain their mechanical strength at elevated temperature, and withstand heat.
5> They have small thermal conductivity, small thermal expansion and high resistance to thermal shock.

Despite their many virtues mentioned above, most ceramics have had their use greatly restricted in structural applications because of their most glaring defect, i.e. brittleness. Also, ceramics are often difficult to make in large complex shapes. Production of the final shape may require expensive grinding. The machining of some ceramics is difficult, time-consuming, and costly because of their exceptional hardness.

One of the ways used to cover up the brittleness, in other words to increase their fracture toughness was to combine a ceramic with another material. Such a combination is known as a composite material. Ceramic particles bounded together by metal film (typically consisting of 5 to 15% volume of the material) is called cermet. Cermet has larger fracture toughness and is shaped up more easily than bulk ceramics. Another type of composite is that of a ceramic coating over a substrate of metallic materials which are, as is well known, easily shaped to any configuration.

5.4.1 Bulk Ceramics

(1) Manufacturing process:

The manufacturing of bulk ceramics begins with the production of pure, uniform sized, submicron spherical particles of the ceramic material. They are usually made by a sol-gel process, a solution-precipitation process, or through vapor phase reaction. Once a ceramic powder is formed, it is mixed with deliberate additives to improve its strength and other properties. it is then compacted and shaped at the same time. Dry and wet processing, tape casting, plastic compaction, cold isostatic pressing, slip casting and injection molding are the usual processes for the compacting and shaping.

After the compacting and shaping it is densified through sintering at high temperature (about 1650°C for aluminum oxide, 1700°C for zirconium oxide,

2050°C for silicon carbide). During sintering, the ceramic particles coalesce without actually melting to build up a polycrystalline bulk material. The hot press (HP) process and the hot isostatic pressing (HIP) process are the processes in which the compaction and the densification are combined.

(2) Abrasive erosion resistance of bulk ceramics:

D.K. Shetty and his collaborators conducted abrasive erosion tests on a variety of bulk ceramics in 1983, such as those listed in Table 5.17, where their physical and mechanical properties are also given. Synthetic slurry consisting of silica particles (the median size, 10 ~ 15 μm) dispersed in a petroleum-based oil was heated to a temperature of 220°C. Tests were conducted by impacting the slurry at a jet velocity of 135 m/sec and a 90°C degree impingement angle. Test periods were typically 10 minutes in duration. Erosion rates were calculated from profilmeter traces of the craters produced on the target surfaces, and expressed as ($\Delta v/v$) where Δv was the volume of the crater and v was the volume of the target specimen used in the test.

Three different types of abrasive erosion were noted. A group of ceramics that included a hot pressed B_4C, a sintered α-SiC, a hot pressed Al_2O_3, a hot pressed AlN and a glass ceramic exhibited very low erosion rate, smooth transgranular erosion surface and an approximate inverse correlation of erosion rates and target hardness as shown in Figure 5.19.

The cemented carbides erosion rates were also plotted in the figure for the purpose of comparison. The broken lines qualitatively indicate the transition behavior of cemented carbides, i.e., both hard and brittle grades (low binder levels) and less hard tougher grades (high binder levels) erode more readily than do the optimum grades.

A second group of ceramics that included hot pressed grades of SiC and Si_3N_4 and a sintered grade of Al_2O_3, eroded by an intergranular failure mechanism, resulted in an order of magnitude increase in erosion rates relative to the first category.

A third group of ceramics, that is the soda-lime glass without crystalline grains, was eroded by indentation fracture (lateral cracking) near the center of craters formed and by microcutting near the periphery. Consistent with its low hardness (H = 5.2 GPa) and low fracture toughness (K_{IC} = 0.75 $MPam^{1/2}$) this ceramic material exhibited the highest erosion rate among all the materials tested.

Table 5.17 Properties and erosion rates of target materials eroded with silica slurry

Material	Source (Grade)	Young's modulus E (GPa)	Hard-ness H (GPa)	Fracture toughness K_{IC} 1/2 (MPam)	Erosion rate * $(\Delta v/v)\times10^{10}$	Erosion charac-teristics
Cemented WC 10% Co, 4% Cr	Kennametal (K701)	533	16.2	7.8	1.8±0.7	-
Cemented WC 5.5% Co, Cr	Kennametal (K703)	627	17.0	10.2	1.3	-
B_4C (HP)	Norton (Norbide)	448	31.0	-	0.3±0.15	Transgra-nular delaminatio n or microflaking $\frac{\Delta v}{v} \propto \frac{1}{H^n}$
SiC (S)	Carborundu m	406	26.1	2.7 (4.7**)	0.7±0.2	
Al_2O_3 (HP)	Avco	413	17.7	2.7 (4.7**)	1.4	
AlN (HP)	Battelle	-	10.9	2.9	1.6	
Glass-ceramic	Corning (Pyroceram)	116	6.6	2.4	210±10	
SiC (HP)	Norton (NC-203)	440	22.7	4.0	19±2	Inter-granular
SiC (HP)	Ceradyne	-	20.7	5.3	10±1	
Si_3N_4 (HP)	Norton (NC-132)	310	15.9	4.2	5±1	
Al_2O_3 (S)	3 M Co. (Alsimag 614)	316	9.4	4.0	6.5	
Soda–lime glass	PPG Ind. (Float glass)	72	5.2	0.75	2200±100	Micro-cutting indentation fracture

(HP): Hot pressed, (S): Sintered.

* Test conditions: jet velocity = 135 m/s, θ = 90, 8 percent silica slurry.

** High K_{IC} values reported in the literature.

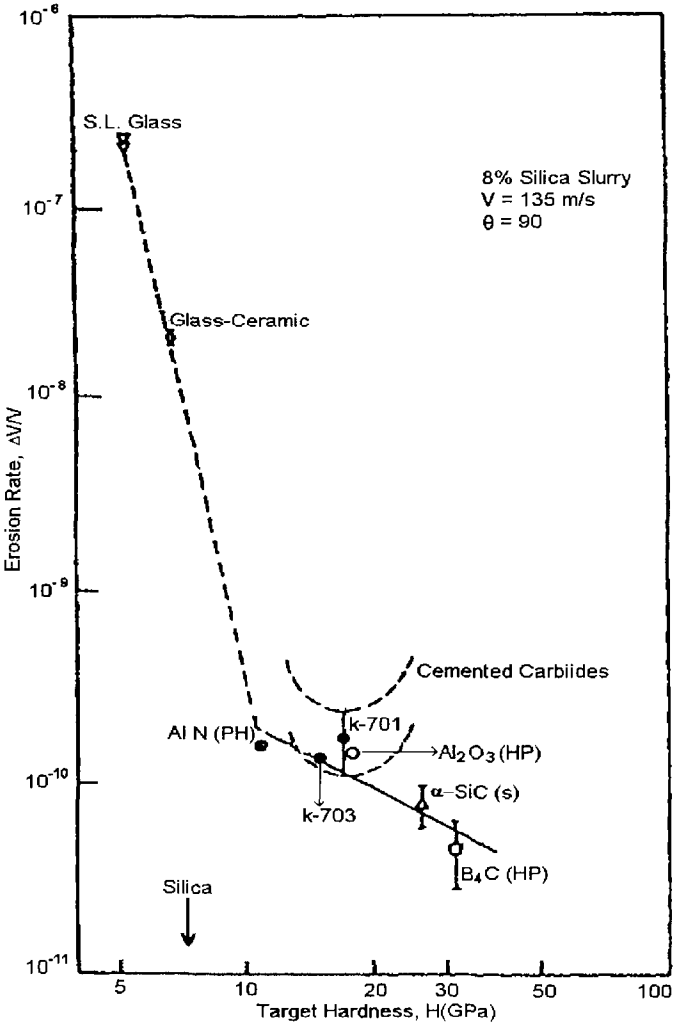

Figure 5.19 Erosion rate (Δv/v) - hardness (H) correlation for ceramic targets that eroded by the delamination of micro-flaking mechanism

The above test results may be summarized as follows. The bulk ceramics of polycrystalline structure erode by either of two mechanisms, transgranular or intergranular failure. The latter showed significantly higher erosion rates.

However, the fracture toughness value of the ceramics eroded by intergranular failure was in fact greater than the toughness value of the ceramics that eroded by transgranular failure. Thus bulk fracture toughness is not a good measure of a ceramic's resistance to erosion. On the other hand, hardness is a good measure of erosion resistance once the fracture category is decided.

Another problem in the erosion of bulk ceramics is that different grades of the same generic material can be eroded by the two different mechanisms showing an order of magnitude difference in erosion rates.

5.4.2 Cemented Carbides

(1) Manufacturing process

Cermet consists essentially of the particles of brittle but hard carbides, oxides or nitrides, contained in a ductile binder phase. In a broad sense, the carbide element may be one of those, which belong to the group IV_B, V_B, VI_B in the periodic table, and the binder metal is the iron group, namely Fe, Ni and Co. But at present, only two combinations, i.e., WC-Co and WC-TiC(TaC, Nbc)-Co are in practical use. These are usually called cemented carbides.

As shown in Figure 5.20, the standard manufacturing process of cemented carbides has already been established. Powdered tungsten carbide, cobalt metal and additions are mixed together, pressed to form a block, and then sintered at an elevated temperature. HIP (hot isostatic pressing) may be used instead of sintering. In the early stage of sintering, a liquid solution is created from the Co and WC at a certain temperature lower than the melting point of WC. Sintering, then, proceeds rapidly as the solution enfolds the WC particles. In the cooling process following the sintering, the tungsten and carbon elements in the solution precipitate on the surface of the WC as crystal, and cobalt increases its concentration in the solution. The nearly pure cobalt metal solidifies itself in the space between the WC particles and makes a strong bonding there. Formation of the liquid solution, to adequately cover the particle's surface, is indispensable for a strong bonding.

(2) Properties of cemented carbides:

It has been already made clear that the mechanical properties of cemented carbides depend on the composition and size of the carbide, and most strongly on WC/Co ratio. Generally a larger WC/Co ratio and smaller particle size brings about a lower toughness but a higher hardness. In an ideal condition

WC crystals develop themselves in a square pillar shape because they have a hexagonal lattice. Crystals in this shape increase the toughness of the material.

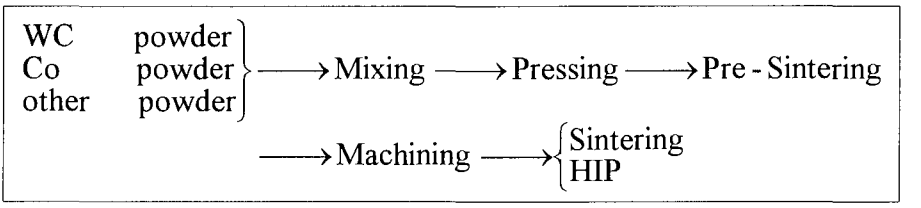

Figure 5.20 Manufacturing process of cemented carbides.

(3) Erosion resistance:

The chemical composition and the mechanical property of cemented carbide specified by JIS (Japanese Industrial Standard) are shown in Table 5.18. Erosion tests were conducted on these materials using a rotary type testing apparatus which is similar to the one shown in Figure 5.17 of the preceding paragraph, under the following conditions; abrasive particles, SiC (125 μm, # 120); particle concentration in slurry (water), 10 wt%; the maximum peripheral velocity at the tip of propeller, 10.3 m/sec; duration of test, 44 hours. Test results obtained are shown in Figure 5.21 as relationships between the hardness of material and the relative extent of damage, taking stainless steel (SUS 304) as the standard. Most materials fell on the line which indicated that the higher the hardness is, the smaller the extent of the damage. TF2, which is of the highest hardness among the materials tested shows the smallest extent of damage. Several materials, however, did not obey the hardness vs. damage relation. This may be partly attributed to the fact that those were mainly A - and p-type and they contained TiC and TaC. But, some materials without TiC or TaC did not obey the relation, and trials to relate the erosion resistance with other properties of the material such as WC/Co ratio or particle size also failed. Therefore, we cannot but conclude that it is impossible to relate the abrasive erosion resistance of cemented carbides with any single property of them. This conclusion is supported by another test results shown in Figure 5.19. Of course, we have to keep it in mind that as a general rule, erosion resistance depends decisively on the test conditions.

Table 5.18 Chemical composition and mechanical properties of cemented carbides

JIS specification	Material name		Chemical composition (%)			Mechanical property			Specific gravity
			Co	TiC + TaC	WC	Hardness		Deflective strength	
						HRa	Hv	(kg/mm^2)	
V1	MV1	DTi05	6	---	rest	91.0	1613	200	14.9
	TV1	D10	5.5	---	``	90.5	1483	200	14.9
V3	MT3	GTi20	11	---	``	89.0	1272	280	14.4
	TV3	D30	13	---	``	88.0	1158	300	14.1
V6	MV6	GTi40S	20	---	``	83.0	788	310	13.5
	TV6	D60	25	---	``	84.5	831	320	13.0
M10	MM1	UTi10T	6	31	``	92.0	1545	150	11.1
	TM1	TU40	6	17.7	``	92.5	1693	150	13.0
M40	MM4	UTi40T	15	6.5	``	89.0	1263	230	13.5
	TM4	TU40	18	9.5	``	89.0	1693	240	12.4
P10	MP1	STi10T	9	38	``	91.5	1532	160	10.4
	TP1	TX10	8	30.6	``	92.0	1651	150	10.5
P30	MP3	STi30	10	8	``	90.5	1495	200	13.0
	TP3	Tx30	9	10.5	``	90.5	1495	180	12.7
K20	MK2	HTi20	5.7	---	``	91.1	1583	220	14.9
Ultra fine	MF1	UF20	12	---	``	91.5	1570	250	14.2
	MF2	UF30	16	---	``	90.0	1382	300	13.8
	MF3	HF25	14	---	``	91.0	1651	300	14.0
	TF1	EM	13	2.0	``	91.0	1557	250	14.3
	TF2	F	6	2.0	``	93.0	1892	200	14.9
			Co Ni Cr						
	MR1	GTI30C	2 7 7	---	``	84.0	867	230	13.9
	MR2	GTI50C	2 11 11	---	``	80.0	744	250	13.5
	TR1	MS18	- 18 2	---	``	86.0	1037	180	13.6

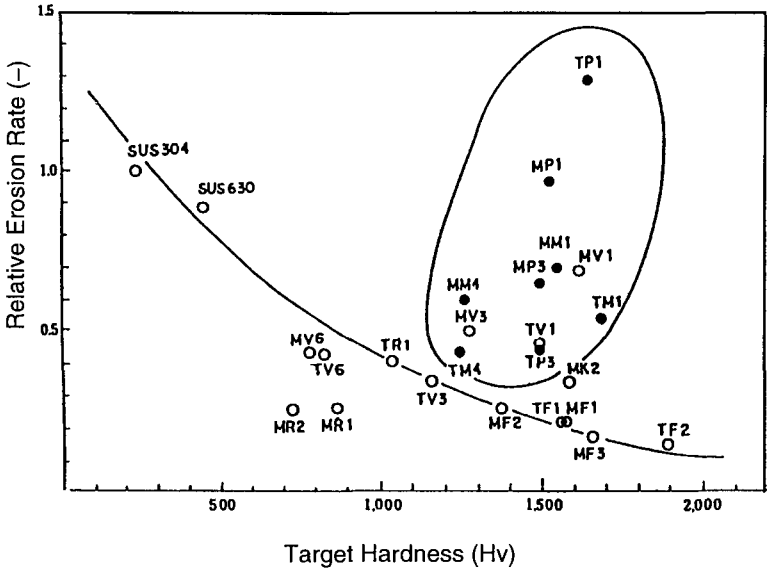

Figure 5.21 Target hardness vs relative erosion rate correlation for cemented carbides

5.4.3 Coatings

(1) Manufacturing process

Special techniques are required for the preparation of ceramic films and coatings. Figure 5.22 shows a classification of the techniques: In the chemical vapor deposition (CVD) method a gaseous or volatilized compound is transported by a pressure difference or by a carrier gas to the substrate surface which is maintained at a much higher temperature than the vapor source, but at a considerably lower temperature than the melting temperature of deposit compound. The deposition processes take place on the substrate surface in the form of decomposition or chemical reduction obeying the laws of thermodynamics and reaction kinetics. The following is an example of CVD reaction

$$3TiCl_4(g) + C_3H_8(g) + 2H_2(g) \xrightarrow[\text{on Fe}]{1000°C} 3TiC\,(S) + 12Hcl\,(g)$$

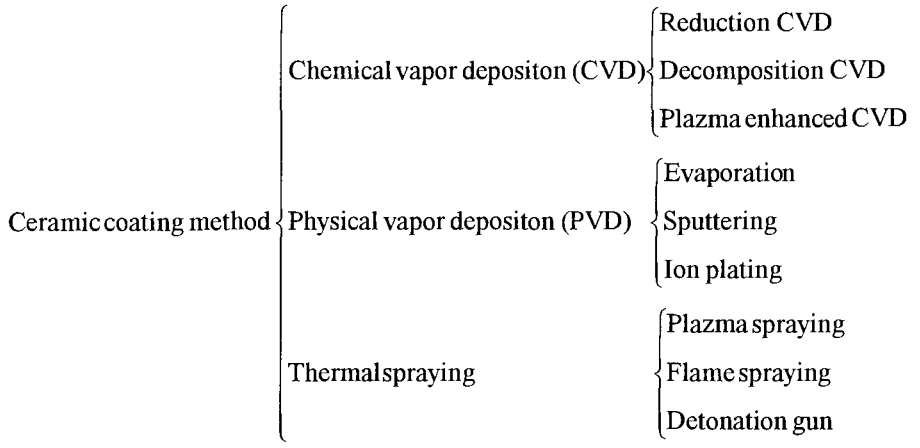

Figure 5.22 Ceramic coating methods

In physical vapor deposition (PVD) techniques, the material needing coating is placed in a high vacuum chamber (typically 10^{-6} torr) opposite the substrate and evaporated by heating or electron beam. Upon evaporation, atoms of coating material are ejected from the solid material, and impinge and condense on the substrate surface (Evaporation method). Or, the ejection of the source material is accomplished by the bombardment of the surface with gas ions accelerated by a high voltage (Sputtering method). When a high voltage is applied between the substrate (-) and the source material (+) in a vacuum but with some leaked gas (Ar, N_2) of $10^{-3} \sim 10^{-1}$ torr, a plasma state is established and the particles of atomic dimension from the source metal react with the gas to form a compound on the substrate surface (Ion plating method). An example of ion plating is

$$2T_i + N_2 \xrightarrow{6.0 \times 10^{-2}Pa} 2T_i N \quad 773k$$

The thermal spraying process is a technique that combines solid particle melting, quenching and consolidation all together. In plasma spraying, a plasma jet is created by electric heating an inert gas arc in a water-cooled

nozzle. The particles injected into the plasma jet undergo rapid melting and at the same time are accelerated toward the substrate surface. Upon impingement rapid quenching of molten particles occurs to form a fine-grained layer which may retain a substantial amount of porosity.

(2) Erosion resistance:

The thermal sprayed ceramic layer has a larger thickness (more than 100 μm) than that of CVD of PVD (less than 10 μm), but it may be more likely flaked off from the substrate surface when it is attacked by the repeated impingement of solid particles. On the other hand, CVD coatings have the disadvantage through the high temperature at which the substrate has to be heated during the application of coatings. The heating may exert unfavorable influences on the substrate material. In a PVD process, the substrate is not heated as in the CVD process and the thickness of the coating is thin enough to keep the precise measurements of the substrate as well as to stick itself to the surface. Thus as a promising method, PVD coatings are being applied to many parts of hydraulic machines which are usually damaged by the erosion of particle impingement. However, their performance not only in field, bur even in testing has scarcely been reported yet. Therefore a report on PVD coatings, not in the particles impingement test but in cavitation erosion test, is given below for a rough assessment of the coatings performance.

The cavitation-erosion tests on stainless steel (SUS 410JI) coated with an ion plating process (IP) were conducted using an ultrasonic cavitation-erosion testing facility based on the ASTM standard method (G.32). The resistance of materials to cavitation was evaluated by a weight loss vs. testing damage diagram. It was found that the erosion resistance of TIN-coated steel is superior to steel coated with the same film thickness of electroplated Cr, and of course to uncoated base metal. It is also to be noted in Figure 5.23 that Cr-Tin multilayered coating shows the most effective erosion resistance among the tested IP coating specimens. The reasons for this improvement in the erosion resistance of TiN-coated materials are as follows. First, the TiN layer did not peel off from the substrate surface, owing to its adhesion strength. Secondly, the erosion resistance of the layer itself was greater than that of the substrate material. In addition, it was confirmed that this erosion resistance is maintained even after the erosion damage has reached the substrate material in some parts, since the residual stress generated by the layer deposition improved durability of the substrate metal.

The application of PVD coating technique is not limited to ceramics. Amorphous metal coatings can be obtained by using a specially prepared target metal for sputtering. The amorphous metal layer thus obtained has a high hardness, a high corrosion resistance as well as a high erosion resistance, which may be suitable for anti-erosion-corrosion use.

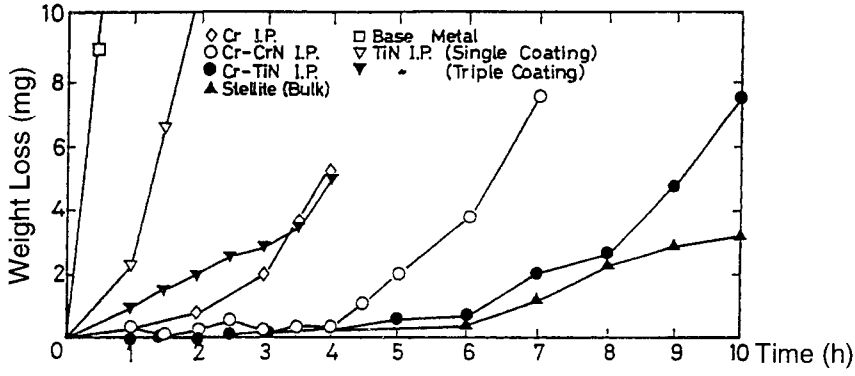

Figure 5.23 Cavitation-erosion test results of ion-plated multilayered coatings (frequency 18.3 kHz; amplitude, 40μm; deionized water, 290 k)

5.5 Metal Protective Coating

B. E. Chen

The surface protection from particles abrasive erosion damage includes metal coating and non-metal coating, as well as surface treatment used on the area of components of hydraulic machinery, which is easily damaged by abrasive erosion. The protection methods are economic and valid in the view of both saving on precious metal and protecting the portion from serious erosion, not only in manufacturing but also in repairing on site.

5.5.1 Bead Welding

Bead welding is generally used to protect the flow-passage portion of hydraulic machinery from erosion, which is applicable both for manufacturing of new unit and for overhaul of unit in operation.

(1) Clarification of the surface

As far as newly manufactured unit is concerned, bead welding area on surface is determined in accordance with the design theory and analysis on the information that shows the area which is easily worn out, and it is relatively simple to clarify the surface in this case. For overhaul of the unit in operation, the surface of component is damaged by erosion, on which there appear pinholes, honeycomb structure (also called sponge structure), fish-scale pits and grooves that are not usually treated if their depth is approximately 1 mm. For the deeper honeycomb structure, fish-scale pit and grooves, it is necessary to mark the area with chalk or paint, which is properly expanded by 30 ~ 35 mm as compared with the area. The expanding of the obviously damaged area is required in save side.

It is usually to clarify the damaged surface and bead welding area by carbon-arc method. Carbon-arc method with gas bubble is to melt the metal to be cut with high temperature (6000° ~ 7000°C) of electrical arc, and then to blow away the melted metal with compressed air of 39 ~ 59 Mpa. This measure is valid to cut not only the steel and the casting pig but also the stainless steel.

(2) Selection of material for bead welding

There exist two categories of material that are utilized in the erosion protection for hydraulic machinery. One is the welding rod of abrasive resistance widely used for many years, and another is the ceramal.

(a) Welding rod of abrasive resistance

Considering the excellent properties of abrasive resistance material are crucial for raising the longevity of the hydraulic machinery, the bead welding rods should satisfy the following technical specifications: good property of abrasive resistance; easy to strip scoria; steady arc and easy to operate; minimum toxic fog; and low cost. Though there exist many categories of welding rods of abrasive resistance and brands worldwide, the technical specifications mentioned above should be satisfied as far as possible.

Table 5.19 shows the experimental results for several welding rods of abrasive resistance.

From Table 5.19, it is shown that welding rod with high chromium alloy, i.e. F_1, has good property of resistance to erosion. The material

of welding rods is to be selected in accordance with the factors damaging the component by hydro abrasive erosion or cavitation.

Table 5.19 Experimental results of abrasive erosion resistant materials in hydraulic turbine

Material	Chemical component (%)			Hardness	Wear coefficient ε			
	C	Cr	Rest	(Hv)	20~40 mesh	140~200 mesh	Kashi River sand	Rushui River sand
F_1 (China)	3.510	29.98	-	671	3.79	11.34	6.28	4.28
F_5 (China)	0.770	22.75	B	505	3.01	13.55	4.85	4.02
Wear No. 1 (China)	2.770	28.90	-	611	2.95	7.60	4.89	3.93
2-14 (China)	0.250	12.71	Mo, Ni, B	613	2.28	5.04	3.20	2.49
Cr5Cu (China)	-	-	-	250	0.86	1.41	1.66	1.11
1Cr18Ni9Ti (China)	0.800	18.00	9Ni	232	1.00	1.00	1.00	1.00
A3 (China)	-	-	-	-	0.79	1.18	1.04	0.84
5006 (Swiss)	3.180	31.03	Mo, Si, Nb	601	3.18	10.26	5.36	4.13
5003 (Swiss)	0.067	13.29	Mo, Ni	471	1.41	2.01	1.06	1.42
W410 (Japan)	Stainless steel Cr13 electrode			412	1.46	2.18	1.58	1.51

(b) Ceramal for bead welding

Ceramal belongs to agglutinate that is made through metallurgical process of carbide, boride, silicide and nitride in which powder metal is added. Agglutinant is both of ceramal's high hardness, resistance to erosion and corrosion, high temperature resistance and of metal's plasticity, electrical conductivity and weldability. The experimental results obtained on the prototype demonstrate the abrasive resistance of

ceramal is excellent while its expense is much lower than stainless steel. In order to be convenient in the process of bead welding, the ceramals could be made into flakes which are fast in bead welding, high in strength, easy to melt and low-priced without pollution of forming agent.

(3) Technological process in bead welding

The welding area and quantity of bead welding in majority of the components for hydraulic machinery are relatively large, and the welding rod of resistance to erosion usually adopted belongs to high-chromium type or chromium type or chromium manganese type, which are more difficult to weld than ordinary welding rods of low carbon steel, the stress and deformation are obvious. Using the welding rods to guarantee the quality of bead welding, the following technological measures can be adopted.

(a) Temperature

The stress concentration and deformation are serious on the components that are welded because the sheet at bead welding is thick. The component to be welded should be preheated if possible .If the preheating is difficult in site, the temperature around the site should be raised to 20°C ~ 30°C for the sake of slow-cooling and temperature-maintaining in the process of welding.

(b) Electric currency of welding

High currency of welding will cause the melting zone deep enough to expand the heat-affected area, which is easy to appear the phenomenon of edge damaging. On the other side, carbon in the component to be welded possibly permeates into the welding, so the resistance to erosion is reduced in the sheet of bead welding. In the welding process, short arc and small electrical currency should be adopted as far as possible on the condition of satisfactory quality, which are also beneficial to reducing the cracks and pores.

(c) Order of welding

In order to make the heat not concentrated in local portion in large quantity with producing big stress and deformation, the measure of symmetric block jump welding is usually adopted. This measure should be especially utilized for blade of hydroturbines with large area. The number of blocks is determined according to the total to be welded, and the area of each block is suitable to be 80 × 100 mm or 150 × 200 mm

with the junctions in stagger. As shown in Figure 5.24, the minimum distance of stagger is one block or two to make the heat diffused away equally in all directions.

(d) Multilayer welding

In order to save on the consumption of abrasive welding rods in the case of thick layer in bead welding, carbon-welding rods can be used at the bottom of bead welding layer, and the abrasive welding rods are utilized at the top layer only. The bead on each layer of welding should be staggered in multilayer welding for reduction of heat deformation.

For the blades of mixed-flow turbine, it is easy to have the change on the trailing edge of blade and the deformation of flange on the crown; For the axial blades, distortion on the trailing edge is often found; So the unidirectional bead is suitable as welding the trailing edges, which is to say that the bead is taken from outside to inside, from thin to the thick instead of from the thick to the thin. Symmetric and jump regulations should be strictly carried out with welding of small quantity in every time.

(e) Treatment on the surface of bead welding

The rough surface of bead welding has significant effect on the properties of machines. The welded surface should be polished to satisfy the specifications of smoothness and concerning geometry. Tempering treatment is needed with temperature about 300° ~ 500°C to eliminate welding stress and raise the resistance to erosion.

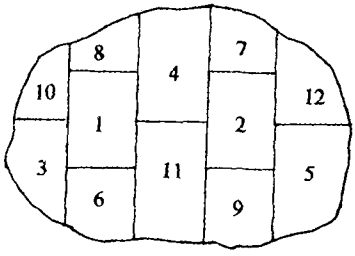

Figure 5.24 Block partition for bead welding

(4) Deformation of bead welding

Deformation is inevitable for the hydroturbine and pump with large size, complex geometry and considerable gradient of thickness. The following sorts of deformation can be produced for mixed-flow hydroturbines:

(a) Deformation in Radial Direction
With large quantity of bead welding and big gradient of thickness, radial deformation readily appears in the upper and lower armillary portions,which damages the shape and concentricity of the circles. This would give rise to the non-uniform clearance in the leakage-preventing circles, which leads to the pressure impulse and the increase of vibration of the machine and oscillation of the shaft system.

(b) Deformation in the axial direction
Non-uniform reduction of the distance between crown and rig may cause axial deformation when bead welding for protection is proceeding with on the conducting portion connecting blades with crown or rig as considerable thickness gradient on the two sides possesses.

(c) Deformation of blade
The main deformation in blade is the breakage on the trailing edge where the blade is relatively thin. In order to reduce the deformation, firstly, the technological process of welding should be strictly controlled; secondly, the component deformation should be supervised for changing the position of bead welding to maintain the homogeneous reversible deformation.

Different measures to counter deformation can be adopted for different portion if necessary, especially for the portion with large deformation. As shown in Figure 5.25, it is an example to use the crutches for eliminating the deformation on the trailing edge of blades. The crutches welded for connecting two blades are to be dismounted in the end of bead welding while the position of spot welding has to be polished.

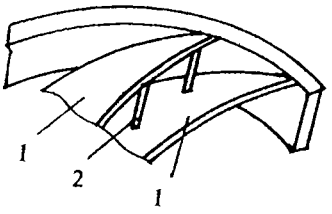

Figure 5.25 Crutches for preventing blades from deformation

(5) Evaluation on bead welding

The bead welding has simple technological process which is suitable for both flat and vertical welding. It is, especially, convenient for big components that are difficult to turn over when welding. And it is, generally, easy to firm up the conjunction between the welding layer and the component surface. The bead welding is mostly adapted for on-site overhaul on the hydroturbine components with rough surfaces and deep local grooves.

The shortage of bead welding is that the layer of welding is higher than original size, so the surface after bead welding should be polished to satisfy the requirement of previous size, which is a serious consumption of labor and welding rods.

5.5.2 Paving Welding

The anti-erosion materials are to be made to plate form that are adhered to the surface of components by spot or braze welding, called paving welding.

(1) The brief technology of paving welding

(a) In order to make the steel plates of paving welding closely adhered to the surface of component, the portion of paving welding should be smooth and clipping and polishing have to be made if it is rough.

(b) The size of anti-erosion steel plates and their arrangement are of great importance to the strength between components and steel plates of paving welding. Because blades of hydroturbine are curved in space, the plates cut into stripes are put on blades for paving welding, with more in quantity and small in size in the portion having big curvature. Figure 5.26 demonstrates the arrangement of anti-erosion steel plates of paving welding for blades of mixed-flow hydroturbine.

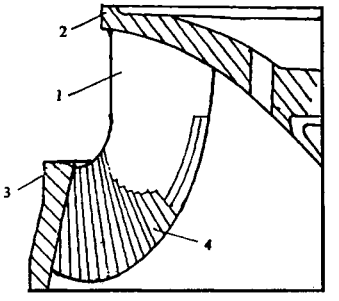

Figure 5.26 Arrangement of plates for paving welding on blades

(c) In order to guarantee the close bond between steel plates and components, a limited number of holes are drilled in steel plates. The welding seam should exist between the stripes plate.

(d) The technological process of paving welding is also strictly controlled to prevent the deformations as stated for the bead welding.

(2) Evaluation on paving welding

Paving welding is adaptive for components with large area and flat surface; the work load, deformation and residual stress are small, and polishing is not needed for the surface of paving welding is smooth. The consumption of metal and working time is less than bead welding.

The shortage of paving welding is the difficulty in satisfying the close bond between the steel plates and the components, especially for the large curvature on the surface of components clearance is inevitable. The convex closure that is easy to emerge during the operation leads to the separation of steal plates from components and erosion damage on the components, The paving welding is economic if it can definitely guarantee that steel plates do not separate from the component. At present, bead welding is widely used in the production.

5.5.3 Alloy Powder Spray Coating

There are various measures of thermal spray coating according to heat resources to be used. The main measures in hydraulic machinery are oxy-acetylene welding of thermal spray with alloy powder, plasma spray coating electric-arc spray coating, detonation spray and electron ray etc., their technology has been described in a series of monographs.

Thermal spray coating is made in the way of that briefly, the anti-erosion powder material is heated to melting or thermoplastic state by high-temperature resources and is sprayed upon the surface of components with the help of the fog produced by the jet gas, forming the protective coating.

Thermal spray coating can be adopted to form the protective coating of metal or non-metal anti-erosion materials. It is convenient to be used both in manufactures and at power plants site with its simple equipment, high efficiency and excellent quality of protective coating.

(1) Selection of powder for spray coating

The mechanism of erosion damage in hydraulic machinery is different from that in the general machinery, and it is not suitable to adopt ordinary alloy

powder for the thermal spray welding on the components that are readily damaged. The autolysis alloy powder is adaptable for the protection of hydraulic machinery from the erosion damage. A sort of special alloy powder is successfully developed and the alloy powder for anti-erosion requirement is also developed by Gansu University of Technology, China.

The specification for selecting the powder is as follows:

a) excellent ability of anti-erosion;
b) regular shape (sphere-like mostly);
c) low melting point;
d) excellent residue-precipitating property;
e) excellent moisture;
f) strong property of deoxidization;
g) delicate in the spraying layer;

Table 5.20 shows the basic prescription and physical properties of some powders used for thermal spray welding in the hydraulic machinery.

Table 5.20 Basic Prescription and physical property of powders for spray welding

Powder No.	TWT-67 (China)	16C Metco (USA)	No.6 Wall colmong (USA)	FP6m (Japan)
Chemical component(%)	C 0.8	0.5	0.75	0.5 ~ 0.7
	B 3.5	4.0	3	2.2 ~ 2.6
	Si 4.0	4.0	4.25	4 ~ 5
	Cr 16.0	16.0	13.57	12 ~ 16
	Ni 64.0	67.0	73	72 ~ 75
	Rest 11.0	5.5	4.75	3.5 ~ 5
Hardness (HRC)	55 ~ 60	58 ~ 62	56 ~ 61	55 ~ 60
Melting point (°C)	980~1050	-	1040	1040
Density of impressed powder (g/cm^3)	> 3.9	> 3.9	> 3.9	> 3.9
Flowing (s/100g)	< 26	< 25	< 25	< 26
Strength (kgf/mm^2)	30 ~ 50	30 ~ 50	30 ~ 50	30 ~ 50
Processing characteristic	Excellent	Excellent	Excellent	Excellent

(2) Process of spraying

(a) Pretreatment for the surface of component

It is quite important to clean the surface of components before spraying in order to form the close metallurgical combination with excellent spraying layer.

For the flow passage components of water turbine with grooves, fish-scale pits and honeycomb structure, it is necessary at first to grind them off with grinding wheel of other tools, and then to make the compensation with electric or gas welding and finally to smooth the surface by the grinding wheel. For the flow passage components of new water turbine, the above-mentioned treatment is also needed for the existence of rough surface in cast construction used for water turbine.

After the above treatment, another process, sand blast, is also required, which not only can make the surface a little bit rough for convenience of powder adhered to surface, but also can reduce the rust-cleaning labor to some extent.

(b) Preheating for the component

The purpose of preheating is to eradicate the moisture on surface of components, strengthening the combination between spraying layer and component, as well as reducing the stress for avoiding the peeling off of the spraying layer before re-melting.

The temperature for preheating is dependent on the size and properties of components. It is usually 250° ~ 300°C for carbon steel, and 350° ~ 400°C for stainless steel. Local symmetry preheating and heating stress-reducing method are usually adopted for components with large dimension, integral preheating is used for those with small dimension. The oxy-acetylene flame and muffle furnace are valid.

(c) Operational technology of thermal spray welding

There are two methods for thermal spray welding: the one-step method and the two-step method. The one-step means that thermal spray welding goes while the re-melting is proceeding with. Two-step means that thermal spray welding is prior to re-melting. The process technology is as follows:

One-step: Treatment for surface — Preheating — Powder pre-spraying-Powder-spraying and Re-melting — Cooling — Post treatment;

Two-step: Treatment for surface — Preheating — Powder-spaying — Re-melting — Cooling — Post treatment.

(3) Deformation control method

It is difficult to correct the deformation once it has taken place because of the complex construction in the flow passage components and the strict assembling size and shape for the runner and guide vanes. Deformation-controlling method is crucial to the spray welding.

The following measures have obtained good effect on controlling the deformation in spray welding for medium and small types of water turbine.

(a) Blades of Francis runner:
The main portion for thermal spraying is located on the trailing edge of suction side local leading edge and trailing edge of pressure side. Because the thickness of blades has got quite difference as compared with that of crown and lower ring, and the blade are closely ranked, symmetry thermal spray welding should be adopted to avoid the deformation in crown and lower ring.

(b) Upper and lower labyrinth in runner:
The runner is preheated to 150° ~ 180°C, and then is divided into four or eight portions according to the dimension of runner as shown in Figure 5.27. The flame should be used to maintain temperature at the position 1' while the thermal spray welding is proceeding at the position 1. The spray welding should be changed to the position 1' immediately after finishing the spray at the position 1. No stop is allowed until the job is completely finished. The runner should be wrapped up or put into the furnace for slowly-cooling.

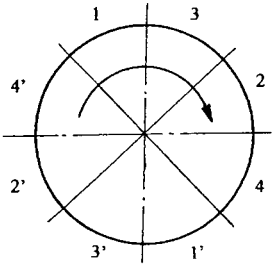

Figure 5.27 Process of thermal spraying welding in upper and lower labyrinth

(c) Guide vanes:
The main problem is to avoid the deformation when the thermal spray welding is going on. The guide vane is totally heated with oxy-acetylene flame, and powder is sprayed upon the surface with certain thickness, and finally one can start the re-melting treatment while the temperature keeps on the level of 400° ~ 500°C on the other side with oxy-acetylene flame. Because of the large coefficient of expansion in the spraying layer with large contraction as cooling, the other side should be cooled slowly at first, and then let the spraying layer cooling down slowly. This is the reasonable process of spraying , and it can be installed directly without shape-correcting process.

(d) Blades of axial Runner:
The portion that is readily worn out is mainly located on the leading and trailing edge and the outer edge of runner. In order to control the deformation, blade is preheated to 180° ~ 200°C and then thermal spray welding is done in different regions, as shown in Figure 5.28. The positions of 1 and 2 with relatively small constraints, are done at first and the direction for remelting is illustrated as the arrows in the figure. At this time when the integral temperature has increased to some extent, the positions of 3 and 4 are sprayed under such a higher temperature, getting less deformation and lower stress. The process of spraying is demonstrated in Figure 5.29. Spraying is done at first on the position of 1', and vice versa. After the spraying, certain level of temperature is kept and cooled down slowly.

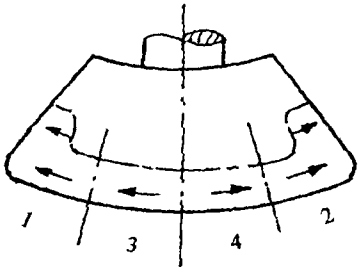

Figure 5.28 Process of thermal spray welding of axial runner blades

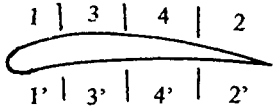

Figure 5.29 Process of thermal spray welding of runner blades

(4) Application in practice

Obvious achievements have been obtained after four-year operation of 12 water turbines from 8 hydro-electric power plants on which autolysis alloy powder developed by China Gansu University of Technology is adopted for erosion and cavitation resisting purpose [5.14]. Figure 5.30 shows the comparison of anti-erosion property between the blades without thermal spray welding and the blades that are sprayed with Ni37 autolysis powder of the Francis runner for Ba Jia Zui hydro-electric power plant. In order to guarantee the conditions of water quality and operation, the blades without spraying powder and blades with thermal spray welding are ranked alternatively, that is to say the blades with even number are all sprayed by autolysis powder. The big difference in erosion-resisting aspect is found for these two sorts of blades after 15,840 hours of operation. On the blades without spraying powder, one can find the serious damage and even holes on the trailing edge of suction side, while on the blades with thermal spray welding, one can just see the slight wear on the trailing edge of suction side without any deformation in its shape of geometry.

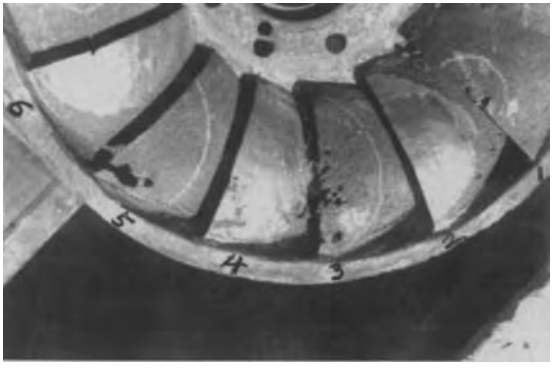

Figure 5.30 Comparison of spraying and non-spraying blades after 15,840 hours operation in Ba Jia Zui Power Plant

Figure 5.31 shows the picture of comparison experiments carried out in the wicked gates of water turbine in Hong Ya power plant, with the rated head is 93 m, the output is 1000 kw and the annual average density of sand is 5.3kg/m^3, the maximum density of sand 203 kg/m^3. Figure 5.31 (a) is the situation of the blades without protection of spraying powder while Figure 5.31 (b) is demonstrating the situation for blades with thermal spray welding of Ni37 alloy powder after one-year operation. One can find no damage in the blade with Ni37 alloy powder spray.

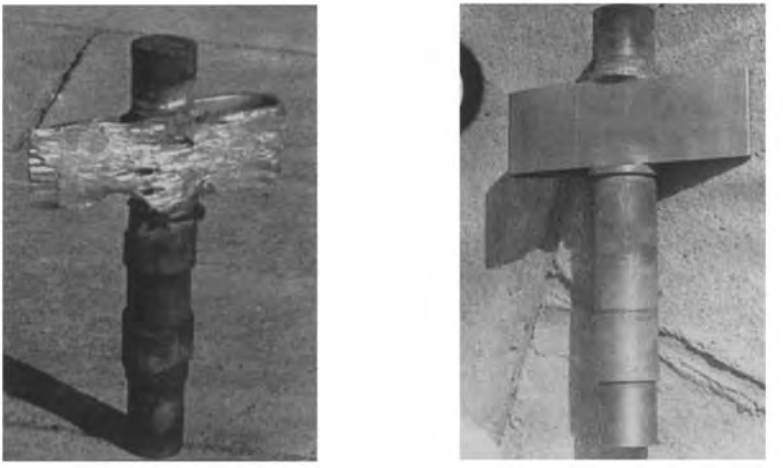

(a) Non-spraying blade (b) Spraying blade

Figure 5.31 Erosion of blades after a period of operation in muddy water

5.6 Non-Metallic Protection Coating

B. E. Chen

In the past thirty years, many researches and experiences have been accumulated worldwide in the aspect of adopting polymer coating to protect metal construction and devices of hydraulic engineering from cavitation and sand erosion. But only a few sorts of polymer coating material are adapted to the protection of hydraulic machinery working under the condition of siltladen water.

It is reported that non-metallic coating materials of erosion-resistance for hydraulic machinery have been developed in many countries. A lot of research works have been implemented with great achievements. Several sorts of non-metallic coating have obtained good results in prototype machines, some of which are epoxy emery coating, composite nylon coating, polyurethane coating and enamel coating.

5.6.1 Epoxy Emery Coating

It is reported that epoxy-made coating for erosion-resisting purpose was used for blades of water turbines more than thirty years ago in the United States, which was also used as erosion-resisting coating in hydraulic machinery and penstocks in USSR and F.R.G. In the past ten years, erosion-resisting epoxy emery coating has been developed and widely used in pumps, turbines and hydraulic buildings in China.

(1) Characteristics of epoxy emery coating

Epoxy emery coating consists of epoxy, curing agent, tenacity-increasing agent, filler and diluent, the properties of which are as follows:

(a) Epoxy:

Epoxy is a new kind of synthetic resin that is high-molecular polymer containing oxygen-group, which possesses various sorts. Epoxy propan-echloride is the main monomer for all sorts of epoxy resin, which can be condensed into epoxy resin while combined with polyhydric diphenol and alcohol, i.e. epoxy resin of diphenol propane, phenolic resin and glycerol epoxy resin. The diphenol propane epoxy resin, sometimes called A-diphenol epoxy resin, is mostly used, which is also adopted in the protection of hydraulic machinery from erosion. Ranking in order by molecular weight, A-diphenol epoxy resin has many types, i.e. 618, 619, 6101, 634, etc., the properties of which are as follows:

*High strength of adhesion: Strength of adhesion is dependent on curing agent, see Table 5.21.

*Good process for technology: At ordinary temperature, it possesses good fluidity. After being permeated among the filler, coating materials become plastics-like epoxy slurry, and the heated trowel can be readily utilized to form the shape.

*Small contractility: Epoxy resin has no by-products in solidifying, it therefore produces no gas bibles while the contraction rate is less than 2%, or even 0.1% after the emery is added, and its coefficient of thermal-expansion is quite small.

*Small absorbability: The absorbability for water is less than 0.5% at the temperature off housing, so it is impossible for coating materials to expand when it is in water for a long time besides its excellent steadiness and electricity-insulating ability.

Table 5.21 Adhesion strength of epoxy resin with different curing agents

Curing agent Name	Curing condition	Adhesion strength (kgf/cm^2)
Triethylene-tetramine	80°C, 4h	603
Tetraethylene-pentamine	80°C, 4h	545
Eurelon	100°C, 3h	503
Dimethyl imidazole	120°C, 4h	508
Dicyandiaminde	150°C, 4h	769
Butene dicarboxylie anhydride	200°C, 2h	582

(b) Curing agent:

Curing agent is a sort of hardening substance that makes the linear molecule of epoxy resin crossing in network structure. There are many sorts of curing agent and the ammonia curing agent is mostly used for the coating in water turbines and pumps, majority of which are triethylene tetramine, tetrethylene pentamine and polyamide. This sort of curing agent has the advantage of hardening at temperature of housing, low viscosity, fast hardening and little poison. In most cases, the main filler is emery with high hardness; its Mhos hardness reaches 11. In addition, small amount of alumna is added to increase the adhesion and some nylon yarn and nylon clothing are put into it to increase the integrity.

The prescription for coating materials is dependent on their purpose, condition of increasing temperature on site and resource of materials. The general prescription is demonstrated in Table 5.22.

Table 5.22 Prescription of epoxy emery coating materials in erosion-resisting composite layer for blades of hydraulic machinery

Material and its proportion	Prescription								
	A			B			C		
	BS	FS	SS	BS	FS	SS	BS	FS	SS
Epoxy 618	100		100	100		100	100		100
Epoxy 6101		100			100			100	
Amilan 200	40	60	30				40	60	30
Amilan 300				40	60	30			
Trierhylene-tetramine	7	6	11						
Dimethyl imidazale				5	5	5	5	5	5
Ethyl butyl ether (501)	20	20	10	24	24	16	24	24	16
Polyvinyl butyral	4	4		4	4		4	4	
Paracril	16	16		16	16		16	16	
Emery		375			375			375	
Porcelain powder	5	30		5	30		5	30	
Aluminum oxide	5	10		5	10	5	10		
Moly-sulfide			40			40			40
Nylon wire		10			10		10		
Acetone			65			65			65

Note: BS=bottom sheet, FS=fundamental sheet, SS=surface sheet

(2) Technology of operation

(a) Treatment for surface

Rust and oil residue on the surface of components can be erased by the method of sand blast until the original color appears on the surface.

(b) Heating the component

The component should be preheated to 50°C approximately before putting the coating material upon the surface.

(c) Allocation of coating materials

Prescription of coating material is usually made up of 5 ~ 10 materials, some of which will have the chemical reaction as encountering. So that, certain process must be followed in the allocation. The allocation for epoxy emery coating material is usually divided into three sheets,

bottom sheet, fundamental sheet (slurry sheet) and surface sheet. The function of bottom sheet is to increase the adhesion with the component and slurry sheet. The slurry sheet is mainly in charge of erosion-resisting function, and the surface sheet will make the slurry sheet smoothing. The steps of allocation are as follows:

To put epoxy resin and tenacity-increasing agent, diluent and curing agent, filler into three different containers. If the temperature is satisfactory with specific requirements, the materials in the two containers forwards are mixed together with fast stirring until it becomes homogeneity, and then the material in the third container is added into with stirring at once. Then coating jobs should start as soon as possible to avoid the solidification phenomenon.

(d) Making coating

*Bottom sheet: To paint the bottom sheet with the requirements of being thin and homogeneous, and the slurry sheet is then painted when the bottom sheet has been glued (after 10 minutes approximately).

*Slurry sheet: To make this sheet keeping the temperature at 80°C or so.

*Surface sheet: The slurry sheet is to be completely examined at its initial level of solidification, and then to paint the surface. For a small component, it is valid to paint for once or twice. For a large component, spray painting is available, but 60 percent of acetone must be added into the painting liquid for the purpose of dilution. The surface sheet should be painted twice, and the thickness in first spray painting should be very thin, otherwise flow of painting liquid appears, making the surface rough.

(e) Solidification and maintenance of coating

At the completion of epoxy emery coating , the full solidification is required to guarantee the adaptive strength and adhesion. In ordinary temperature the cringe agent will be cured completely at 25°C or so after one week, and will cured after four hours if the temperature is raised to 60°C. The latter is better in quality. For medium-temperature curing agent, three hours are enough to cure completely at the temperature of 120°C.

(3) Application in practice

Protection of epoxy emery was used in the runner blades of the turbine at San Men Xia Power Plant on the Yellow River, obtaining great achievements. After operation of 23,000 hours, the coating maintained more than 95% on the pressure surface, and 30% of coating was stripped away on the suction surface, mainly concentrated in the region with strong cavitation damage. With such methods of protection, the overhaul period is three times as much as that without protective coating. The similar test was done at the Tian Qiao Power Plant on the Yellow River, and after the accumulating operation time of 15,560 hours for three years, 99% of coating was not eroded on the non-cavitation region. This method was extended into other power plants and pump stations with serious erosion, and good achievement was also obtained.

According to our experience in application of epoxy emery resin coating, we have the conclusion that this sort of coating is good in erosion-resisting function but not superior in the cavitation-resisting aspect, and we find the coating on the cavitation region is all damaged which should be further improved in the future. So that, this sort of coating is mainly used in erosion-resisting aspect.

5.6.2 Composite Nylon Coating

(1) Prescription of nylon coating and its technical Specification

The prescription and physical-chemical properties of composite nylon are demonstrated in Table 5.23

Table 5.23 Prescription and properties of composite nylon

Name	Adhesive strength (kgf/cm^2)	Shearing strength (kgf/cm^2)	Tearing strength (kgf/cm^2)	Hygroscopicity (%)		
				1 day	30 days	180 days
Ternary system 171	637~716	428~468	582~606	0.62	2.91	3.31
Transformatio 1010-171	612	398	481	0.42	1.30	1.56
Ternary system H18-1	683	434	-	0.52	2.84	3.56
Transformation 1010-H18-1	691	424	-	0.30	1.30	1.93

(2) Technology of painting

(a) Preparation of composite nylon powder
Nylon Powder must be dried for 8 hours at the temperature ranging from 75°C to 80°C and epoxy powder has to be put on dried conditions.

(b) Clarification on the surface of component
The cleaning measure is the same as that adopted in epoxy emery coating.

(c) Preheating of components
The preheating is necessary also as above-mentioned

(d) Painting
Composite nylon coating materials are made to powder through grinding, and the flame spraying measure is used to implement the painting process. When the component is heated to 250°C, the composite nylon powder is quickly sprayed upon the component, and making to the formation of coating. The powder spraying duration should be short as much as possible from the thin position to the thick one. To the position where erosion is serious, the thickness of coating could be larger to certain extent which can be completed through two or three layers with spraying.

In order to improve the adhesive strength, the coating material in the bottom sheet should be selected from polymers possessing excellent adhesion with surface of metal, on which copolymers binary nylon with good tenacity is covered.

(e) Cure and anneal
For the component with large thermal capacity, curing temperature can be relatively low because it takes time to cool down.

Some of big molecule of the melted high polymer are forced to deform in the process of painting, and which, however, have the tendency to recover in aggregation freely at the formation of coating with the generation of contraction stress, and at this moment the thermal stress is produced because of non-coincidence of thermal expansive coefficient between the coating and the metal on the critical surface of adhesion while annealing treatment is available for internal stress reducing purpose.

(3) Application in practice

Composite nylon coating was tested in the pumps installed at the Jia Ma Kou Pumping Station on the Yellow River, and the coating in operation of more than 4,000 hours without damage. The same achievement have also been obtained in several other pumping stations.

According to the experience for years, it is quite valid to use composite nylon coating in pumping stations. But in the case of water turbine with big components, reparation readily appears at the position of strong cavitaition because of the affects resulting from the variation of temperature and the decline of adhesive strength. Powder with low melting point and local thermal spraying should be further studied.

5.6.3 Rubber Coating of Polyurethane

Many sorts of elastic coating materials exist for the erosion-resisting protection in hydraulic machinery. Simple introduction of a polyurethane rubber coating with good achievements in the operation of prototype machines is herewith given. The physic-mechanical property of J_2 polyurethane rubber is shown in Table 5.24.

Because this sort of Polyurethane rubber is obtained through pouring, the appropriate mould has to be manufactured, in which certain distance is required between the inner surface of the mould and the outer surface of the component, and the value of distance is determined by the thickness of rubber.

Table 5.24 Physical-chemical property of J_2 polyurethane rubber

Molecular weight	1000	1700	2000
Tensile strength (kgf/cm^2)	400 ± 40	300 ± 30	280 ± 30
Percentage elongation (%)	450 ~ 560	500 ~ 580	450 ~ 550
Stable percentage elongation (%)	90 ~ 170	80 ~ 130	80 ~ 130
Hardness	70 ~ 95	70 ~ 90	70 ~ 85
Tearing strength (kgf/cm^2)	50 ~ 80	60 ~ 80	50 ~ 75
Permanent deformation (%)	<10	<12	<14

The surface of blades should be treated carefully through shaping and manufacturing. And then clarify the surface of component: The solution containing 1.5 percent of KH-550 anhydrous ethanol with coupling agent is painted upon the surface of component. The mold-releasing agent of silicone grease is painted in the region where there is no requirement for rubber pouring process.

The component that has been clarified is put into the oven where the component is heated to the rated temperature and keeps this level for one hour, and then the adhesive of 821 that has been allocated is sprayed upon the surface of component with powder spraying gun. At this moment, the component is put into the mould and as the temperature of the mould reaches 80°C or so, the gluing material is poured into the void between the component and mould to form the composite layer.

After the pouring, the mould has to be heated to 120°C for vulcanization of rubber, and core of adhesive, and then the mould can be released. Finally, the component with the composite layer is heated to 120°C and kept in this temperature for 2 hours in order to make it vulcanized kept in further.

In order to examine the erosion and cavitation-resisting property of several metal and non-metal materials developed in recent years, Chinese Ministry of Water Conservancy and Electric Power has organized an industrial comparison experiment for erosion-resisting materials in a Hydro-electric Power Plant in Shanxi Province. Sixteen sorts of metal and non-metal materials are examined. In the year of 1980, the experiment started to test until the end of 1985. Three Kaplan water turbines are installed at this power plant with average sand content being 48.28 kg/m^3. The blades of water turbine that are cast by cast steel 2G30 are seriously damaged in after running for 1500 hours.

J_2 pouring polyurethane rubber composite coating obtained the best evaluating among all the materials that were tested. After running for 12,320 hours, the blades with the bottom sheet made up of SE 822 adhesive, was not damaged at all on the pressure side, and only 5 cm^2 was found to be damaged on the suction side, amounting to 0.2 percent of the total area.

It has to be pointed out that the application of this material is limited to some extent because of its pouring formation, complex technology and high costs for mould manufacturing aspect.

5.6.4 Composite Enamel Coating

(1) Characteristics and prescription

Composite enamel coating has high hardness, smooth surface and good property in anti-erosion and anti-cavitation. The enamel coating is hard and brittle, against that the collision should be avoided. The composite coating consists of bottom glaze and surface glaze, the prescription of which is shown in Table 5.25 and Table 5.26.

Table 5.25 Main composition for bottom glaze

Glaze No.	Percentage of raw material (%)								
	SiO_2	Al_2O_3	Na_2O_3	K_2O	B_2O_3	CaF_2	CoO	MnO	Na_3AlF_6
1	47	5	10.5	8.0	11.5	7	3	-	7
2	42.8	4.6	-	3.8	20.0	3.9	2	5.9	-
3	83.2	-	-	10.1	-	-	-	-	-
4	48	6.9	-	7.4	13.4	8.9	-	-	2
5	47.3	8.7	-	-	18.7	6.6	-	-	-

Table 5.26 Main composition for surface glaze

Raw material	SiO_2	Al_2O_3	Na_2O_2	K_2O
Percentage (%)	68.2	3.5	16.7	3.5

(2) Operation technology

(a) Treatment on the surface

The measure of treatment upon the surface is the same as that used in the epoxy emery coating.

(b) Preparation for glaze slurry of enamel

All the raw materials with appropriate proportion are put into the melting pot at the temperature that is higher than 1,350°C to be melted into glass-like liquid, and then quenched with water and finally grained into powder. Lapping materials, i.e. viscous soil, alumna and borax etc., are added to obtain the bottom glaze and surface glaze.

(c) Enamel

The surface of component has to be grained with abrasive cloth, on which the bottom glaze is sprayed, and is sent inside the flame separation furnace with the burning temperature being 900°C. The burning temperature for the slurry of surface glaze is about 850° ~ 900°C. The multi-burning technology should be adopted for components with large gradient of thickness, keeping the average temperature to avoid the phenomenon of over-burning or under-burning.

(3) Application in practice

After running for 5,520 hours at a power plant where axial-flow stables blade water turbines are installed with annual average silt content being 104 kg/m^3, the composite enamel coating on the runner blades are still perfect, except having slight damage at the outer rim of trailing edge. The composite enamel coating has not separated from trailing edge surface until the turbine operates for 22,515 hours. But the previous blades of cast steel 2G35 are seriously damaged after only running for 4,871 hours.

The application of composite enamel coating is limited to some extent because it's processing technology is some complicated for the component largess and it seems to be impossible to repair the damaged local composite coating at power plant site.

5.7 Surface Treatment against Erosion Damage

B. E. Chen

The heat treatment of component surface is one of the measures to raise the resistance to abrasive erosion and cavitation erosion of hydraulic machinery components. The heat treatment can increase the hardness of the surface of components in the erosion-resisting purpose.

There are various sorts of heat treatment, but few of them is adaptive for erosion protection in hydraulic machinery, because the requirements of not only high hardness and low brittleness but also that a certain thickness of resistant erosion layer on surface is required as well. The heat-treatment measures should satisfy this requirement for hydraulic machinery.

The adaptive heat treatment measures which can satisfy the above-mentioned requirements are briefly introduced in this section.

5.7.1 Quenching and Tempering

It is known that quenching makes the metal phase changing and obtains martensite and residual austenite. The erosion-resisting property of the treated metal can be increased with the rising of hardness. Main change in the tempering is the decomposition of martensite and the transform of residual austenite. Tempering can improve in the brittleness and eliminate the stress that is caused by quenching. Appropriate controlling on the tempering temperature can raise the erosion-resisting property for carbon steel, especially for alloy steel. Although the low temperature of tempering can raise hardness and anti-abrasiveness, it can also lead to increase of brittleness. The temperature of tempering, therefore, is ranging from 220°C to 600°C.

5.7.2 Diffusion Permeating Plating

The principle of diffusion permeating plating is as follows: high temperature (800° ~ 1000°C) treatment on the surface makes the metal or non-metal elements diffusing into the inner layer of component, forming the surface layer made up of these elements. One can obtain the various sorts of surface layer with the different elements permeated into the component, improving the erosion-resisting property. Carbon permeating, nitrogen permeating. Ion-bombarded heat treatment is used for increasing erosion resistance of hydraulic machinery.

(1) Carbon-permeating method.

Carbon-permeating method is a chemical measure that is widely used in the mechanical manufacture. In this measure, the component is put in the reducible CO gas, or in the carbonator, and is heated to 910° ~ 980°C, then to keep this temperature while the active carbon atoms produced on the surface of component by the permeated carbon medium, which will make carbon permeated into low carbon steel or low carbon alloy steel through the absorption and diffusion on the surface. After the permeation, quenching and tempering are required in order to guarantee high hardness, high abrasiveness and coordination of tenacity in the center for the permeated component. With this treatment, the component can reach 720 ~ 900 Hv in hardness and

abrasiveness can be greatly improved. The depths of carbonized layer is usually ranging from 0.5 ~ 2.5 mm, and even 4 ~ 10 mm for some special component.

(2) Co-permeation of carbon and nitrogen

Carbon and nitrogen can be permeated into metal at the same time, which possesses the following advantages as compared with carbonization: The surface of co-permeation has high hardness, abrasiveness and fatigue strength than carbonization, and at the same time nitrogen reduces austenite-forming temperature. Therefore, copermeation can be proceed with at low temperature keeping the component will not be overheated and direct quenching is valid with small deformation.

Now gas of carbon and nitrogen is widely used at co-permeation, in which ammonia gas is added and the component is heated and quenched in this medium. The hardness on the surface using this treatment can reach to Hrv 1580 ~ 1590, and with the depth of permeation being 1 mm.

(3) Ion-bombarded heat treatment

With the development of plasma physics and vacuum technology, the method of ion-bombarded heat treatment has appeared. This category of measures includes ion nitrogenation, ion permeation of carbon, ion co-permeation of carbon and nitrogen, ion copermeation of sulfur and nitrogen, and permeation of ion into metal, etc.

As compared with chemical heat treatment, ion-bombarded heat treatment has its own advantages: it shortens the production period and can control the phase construction on the surface, obtaining excellent properties; the bright surface, energy-saving purpose and harmlessness can be achieved because of sputtering phenomenon.

When the Gas of C-H series passes the furnace in which the component is put in and heated at pressure-reducing atmosphere, at the moment a high voltage is imposed between the positive polar and the component, glow discharge will rise with producing plasma. Rapid reduction of voltage around the component forces the carbon ions accelerated to bombard the surface of component that is then carbonized. This makes surface of component be clear, energy saving and harmless. The depth of permeation can reach 1mm.

Ionic carbonization is superior to traditional carbonization in mechanical performance if carbon density is constant throughout the depth of permeation. After experiencing 90 minutes of ionic carbonization, the surface hardness of

steel containing 0.3% of carbon, 0.69% of manganese, 1.15% of chrome and 0.24% of molybdenum can reach 900 Hv, which is 50 H_V higher than traditional gas co-permeation of carbon and nitrogen.

This new technology of ionic carbonization is at its primary stage in resisting erosion and cavitation of hydraulic machinery.

References

5. 1 Boldy A.P.and Duan C.G., (1990). 'The Current State of Technology in Hydraulic Machinery', Gower Technical.

5. 2 Duan, C.G., (1998). 'Approach to the Demand on Anti Abrasive Erosion from Hyduaulic Machinery Project', *Proceedings of 19th IAHR Symposium on Hydraulic Machinery and Cavitation*, World Scientific, Singapore, Volume 1, pp. 59 ~ 69.

5. 3 Duan, C.G., Tanaka, H., Zhao K., Han S.H., and Zhao, X.L., (1987). 'Multipositon and multimetering scheme for silt erosion test of hydraulic machinery', *Proceedings of the 2nd China-Japan Joint Conference on Fluid Machinery.*

5. 4 Duan, C.G., (1982). 'Sand Particles Erosion of Water Turbine', Press of Tsinghua Univ., (in Chinese)

5. 5 Ebata, M., (1988). 'Amorphous Alloys Coating', Maintenance, No.92, January, pp. 19 ~ 25.

5. 6 Hojo, H., Tsuda, K. and Cao M.T., (1980). 'Erosion Damage of Polymethy 1 Methacrylate', *Journal of the Society of Materials Science*, Japan, 1980, No.332, July, pp. 731 ~ 735.

5. 7 Matsumura, M., Oka, Y., Ebara, R., Kobayashi, T. Odohira, T., Wada, T. and Hatano, M., (1989). Submitted to ASTM.

5. 8 Mitsui SRC Development Co., LTD, Toyo Engineering Corporation and Yamatake Honeywell Co., LTD, (1988). Report on Coal Liquefaction Technology, Tokyo.

5. 9 Oka, y., Ogasahara, T., Yamawaki, M. and Matsumura, M., (1986). 'Slurry Erosion-Corrosion on Commercially Pure Iron in Vibratory Testing Facility', *Boshoku Gijutsu*, vol. 35, No.4, April, pp.223 ~ 229.

5. 10 Oka, Y., Matsumura, M., Yamawaki, M. and Sakai, M., (1987). 'Jet-in- Slit and Vibratory Methods for Slurry Erosion-Corrosion Tests of Materials', *Slurry Erosion: Uses, Applications and Test Methods*, ASTM STP 946, J. E. Miller and F. E. Schmidt, Jr., Eds., American Society for Testing and Materials, Philadelphia, pp. 141 ~ 154.

5. 11 Owada, S., Nakai, Y., Ikeda, Y., Nakarai, T. and Kobayashi, T., (1986). 'Manufacture and Property of Room-Temperature Curing Type of Polyurethane Lined Steel Pipe for Abrasive Slurry Transportation', *Proceedings of the Eleventh International Conference on Slurry Technology*, Hilton Head, South Carolina, USA, pp. 293 ~ 302.

5. 12 Sheldon, G.L. and Finnie, I., (1966). 'On the Ductile Behavior of Nominally Brittle Material during Erosive Cutting', *Journal of Engineering for Industry. Trans. ASME, Series B,* vol. 88, No. 4, November, pp. 387 ~ 392.

5. 13 Shetty, D.K., Wright, I.G. and Claver, A.H., (1983). 'Wear of Ceramics by Erosive Slurry', *Proc. 6th Int. Conf. on Erosion by Liquid and Solid Impact*, Cambridge, England, pp. 621 ~ 629.

This page is intentionally left blank

Chapter 6

Interaction between Cavitation and Abrasive Erosion Processes

V. Ya. Karelin, A. I. Denisov and Y.L. Wu

6.1 Effect of Suspended Particles on Incipient and Developed of Cavitation

In the study of the joint effect exerted by suspended particles and cavitation on working surface, there appear two problems of significant theoretical and practical interest. The first problem refers to determination of the effect produced by suspended matter on origin of cavity and development of cavitation in a liquid flow. The second problem deals with defining of cavitation-abrasive erosion intensity decided by ratio of these two deteriorating processes, each taken individually. Both problems have not been solved yet due to insufficiency of experimental data obtained and the difficulties in defining the influence produced by each of these processes separately in hydraulic machines.

The presence of sediments suspended in a flow results in alteration of the physical-chemical properties of this flow and, specifically, of its volumetric strength, which decides the ability of such a liquid to resist interruption of its discontinuity. In accordance with the theory, assuming existence of something like "weak points" or "nuclei" of cavitation in any volume of real liquid [6.1], the presence of solid particles in water should encourage much earlier emergence of cavitation and rapid development of the latter. V. Iterson was the first to confirm this phenomenon and to measure experimentally development of accelerated cavitation of water saturated with carbon powder

in a Venturi tube. With powder content of 0.5 g/l the pressure in the tube was 15% higher at cavitation incipience than in case of pure water. The same effect produced by solid particles is described in [6.2], when the cavitation developed was studied in the region behind a cylindrical model placed in a water tunnel.

To investigate this interesting problem a flat-shaped Venturi nozzle was used [6.3] which enabled the researchers to consider the basic factors influencing the intensity of hydroabrasive, cavitation and cavitation-abrasive erosion patterns: flow velocity, pressure values at the input and output, expansion angle of the diffusion region, different phases in development of the cavitation, abrasive particle sizes and their concentration, nature of the damage on surface being worn, temperature of the mixture etc.

Model 8 was installed in the modified section of the pressure piping constituting a part of the stand shown in Figure 6.1. The throat cross-sectional area in the Venturi tube having dimensions 30 × 30 mm is formed by two brass guides, the first one is placed parallel to the axis of the flow direction and the second one is positioned at angles of $\theta = 5°$, 10°, 15° and 20°. The transparent side walls allow observation of the moment of cavitation incipience, to follow its development and to measure precisely the length of the cavitation area. By use of a pump model 4K-8 it was possible to set the flow rate, in the throat of the Venturi tube, ranging up to 32 m/s, which is entirely in agreement with the liquid flow behaviour taking place within the flow-passages of modern pumps.

The experiments have shown that cavitation emergence occurs somewhat earlier, when using water with solid particles, and in doing so the advance of this cavitation origin in hydro-mixtures, as compared with pure water, increases with a rise of the sediment concentration [6.3]. With the solid particle content being $\rho = 16$ g/l, this advance within the throat of the nozzle is equal to about 15% of the flow velocity (or flow rate). When the sediment concentration is smaller than the indicated level, the effect of the solid particles on incipient cavitation is less evident. As an example, Figure 6.2 (a) illustrates the change in the cavitation area according to flow rate in the Venturi nozzle Q/Q_{in} (here Q_{in} is flow rate at the moment of cavitation origin in pure water), at the angle of $\theta = 5°$ input pressure being $H_{inp} = 42$ m and sediment concentration $\rho = 16$ g/l. This suggests that in case of hydromixture, a smaller flow rate Q/Q_{in} is required for development of, the same 5m long steady cavitation zone than in the event of pure water. In other words, the

presence of sediments serves to speed up cavitation emergence. In the course of further developed cavitation its length goes on to increase. However, the effect of the solid particles present in the flow gradually subsides. When the length of this cavitation zone comes to l_{cz} = 110 mm, the both curves are joined to form one curve (see Figure 6.2 a).

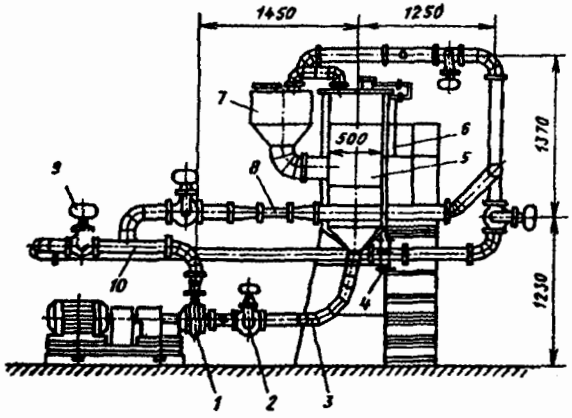

1-pump, **2**-intake valve, **3**-input pipe, **4**-by-pass pipe, **5**-inlet tank, **6**-level indicator, **7**-particles' input, **8**-Venturi tube, **9**-outlet valve, **10**-tube

Figure 6.1 Test stand for analysis of hydroabrasive erosion in centrifugal pumps

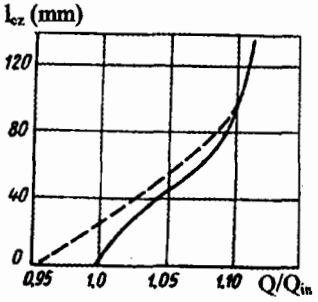

(solid line: pure water; dashed line: mixture with sand content ρ = 16 g/l)

Figure 6.2 a Alteration of cavitational zone length versus flow rate of a Venturi tube

Figure 6.2 b illustrates, for the same model, change of the cavitational zone length versus sediment content for given the cavitation number K, derived in accordance with the known formula (6.1), i.e.

$$K = \frac{p_0 - p_1}{\frac{1}{2}\rho v_0^2} \tag{6.1}$$

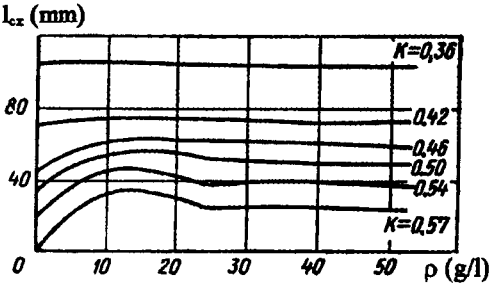

Figure 6.2 b Effect of sediment matter concentration on cavitational zone length at constant value of cavitation number K

It is inferred from the diagrams that with the flow being saturated up to 10 ~ 15 g/l the cavitation zone length l_{cz} increases from 5 to 35 mm at the initial stages of cavitation development (K = 0.57). The further rise of the sediment content results in certain drop of the l_{cz} value. Although these terms correspond to concentrations which are much higher than maximum values typical of natural water sources, it should be noted that the situation considered changes is most likely characterized by composite physical processes associated with changes of surface tension, viscosity, density, frictional forces and inertia, with the hydromixture being saturated by abrasive particles.

In transition to the more developed phases of cavitation (with decrease of K values) the stimulating effect of solid particles starts to reduce and when the cavitation number becomes K = 0.36 the presence of sediments in the flow having concentration of up to 50 g/l fails to determine the cavitational zone sizes. It is most likely that disturbance of the liquid continuity, under the

conditions of cavitation being strongly developed, is accompanied by the strength much greater than forces governing the liquid strength at the moment of its separation from a particle. Therefore, at this phase of cavitational development the solid particles fail to affect the cavitation.

The cavitation performance of centrifugal pumps using hydromixtures with solid particle density ρ_r exceeding the liquid density ρ_0 is amenable to theoretical treatment [6.1, 6.4].

It is most simple to assume that the mixture under consideration, at the leading edges of the impeller, acts as homogeneous liquid having density ρ_r. Such assumption holds true if the velocities of solid particles and those of the liquid are the same throughout the flow-passages in a pump. Since this is not the case, let us find out how the lag of the solid particles moving in the accelerated flow can affect the distribution of pressures in the flow direction.

Let us consider the hydromixture flow in the region restricted by two sections 0-0, upstream of the entrance leading to the impeller blade, and 1-1 positioned in the region of the minimum pressure. Let us also assume that, before the entrance to the blade, the velocities of the solid particles and those of the liquid are the same and equal to w_0. Within section 1-1 the liquid velocity has become equal to w_1, and that of the solid particles is equivalent to w_{1T}. Using the equation for energy, as applied to the hydromixture mass restricted between the cross-sections under review, and neglecting the losses, we shall have

$$(P_0 - P_1)Q_r = \rho_r Q_T \frac{w_{1T}^2 - w_0^2}{2} + \rho_0 Q_0 \frac{w_1^2 - w_0^2}{2} \qquad (6.2)$$

where Q_r, Q_T, and Q_0 are respectively flow rate of the hydromixture, solid particles and water.

Dividing the right and left hand sides of the equation (6.2) by the product $Q_r \rho_r g$, we shall obtain

$$\frac{P_0 - P_1}{\rho_r g} = \frac{\rho_T Q_T}{\rho_r Q_r} \frac{w_{1T}^2 - w_0^2}{2g} + \frac{\rho_0 Q_0}{\rho_r Q_r} \frac{w_1^2 - w_0^2}{2g} \qquad (6.3)$$

Taking into account that $Q_r\rho_r = Q_T\rho_T + Q_0\rho_0$, it is better to present equation (6.3) in a form more convenient for analysis

$$\frac{P_0 - P_1}{\rho_r g} = \frac{w_1^2 - w_0^2}{2g}\left[1 + \frac{\rho_T Q_T}{\rho_r Q_r}\left(\frac{w_{1T}^2 - w_0^2}{w_1^2 - w_0^2} - 1\right)\right] \qquad (6.4)$$

It is seen from the expression obtained that the differential pressures (heads) emerging in-between the cross-sections under consideration are equal to alterations of velocity heads, provided only that the velocities of solid particles w_{1T} and those of the water w_1 are the same. In reality, $w_{1T} < w_1$ due to the action of head resistance forces, which result in additional drop of pressure within the cross-section 1-1 and hence constitutes a great threat of cavitation emergence.

Even if we assume that, with small sediment concentrations and without particles of large sizes, as typical of natural waterways, $w_{1T} \approx w_1$, when the sediment carrying stream flow s around the blade leading edge, the additional drop of pressure based on equation (6.4), i.e. $\Delta p = p_0 - p_1$ will be the same as in case of pure water motion. However, the absolute pressure decrease in this case, in the region of the minimum pressure corresponding to the greatest hazard possible from the incipient cavitation viewpoint, will be greater than in the event of pure water transfer, since

$$\frac{\Delta P_r}{\rho_r g} = \frac{w_1^2 - w_0^2}{2g} = \frac{\Delta P_0}{\rho_0 g} \qquad \Delta P_r = \Delta P_0 \frac{\rho_r}{\rho_0}$$

Hence, cavitation in pumps dealing with hydromixtures begins earlier than it does in case of pure water.

The conclusion based on theoretical data is confirmed by the results obtained during experimental analyses and full-scale test observations. Figure 6.3 illustrates alteration of the feed at the moment of incipient cavitation in a centrifugal pump (impeller dia. is 268 mm, rotational speed is 1750 rev/min) as a function of the hydromixture density ρ_r. The increase in density apparently encourages earlier emergence of cavitation and can consequently become the cause for intensity rise of the cavitational erosion.

It should be noted that the influence of density upon cavitation emergence becomes noticeable at the concentration levels of solid particles which significantly exceed the sediment concentration existing in natural reservoirs. Consequently, for conventional pumps, the change in cavitation incipient conditions, due to presence of solid particles, seems hardly probable. But for custom-designed pumps, for transferring concentrated hydromixtures, this should be taken into account.

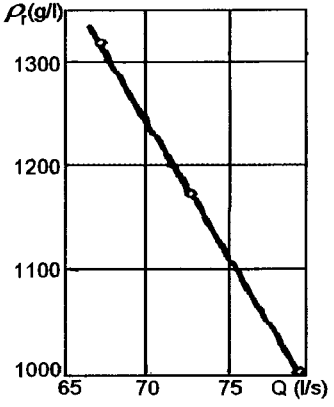

Figure 6.3 Dependence of critical (incipient cavitation) flow rate of a pump on density of transferred hydromixture

The problem of defining the total erosion intensity, including both cavitation and erosion effects of sediments, has a number of unsolved issues.

In the process of cavitation-abrasive erosion the joint hydrodynamic forces acting on the surfaces, hydraulic machines; are from bursting of cavitation bubbles and collision of sediment particles contained in the water. Because of difference in behavior of these two processes, dependent on the cavitation development degree, concentration of sediments contained in the water and erosion resistance of the material for operating components of the pump, such joint cavitation-abrasive erosion process will follow rules other than those described earlier.

The data obtained in multiple experimental studies indicate that there is a large number of alternatives in cavitational-abrasive erosion development.

Depending on a number of factors its intensity can either rise or drop, as compared with pure cavitational erosion.

In our researches aimed at studying the mechanism of the joint cavitational-abrasive erosion taking place in the diffusion area of a planar Venturi nozzle, the specimens used were fabricated from silumin Ал - 9B and had the working surface of 120 × 30 mm. The erosion was evaluated by loss in the mass of these specimens after 6 hours of testing. The tests were performed entirely with respect to the same phase of cavitational development defined by the cavitational zone of 110 mm in length. In this case the closure of the cavitational zone under review took place within the limits of the specimen. The hydroabrasive erosion conditions were created through suppressing the cavitation by means of raising the general pressure level in the installation system.

Figure 6.4 illustrates the effect produced by divergence angle θ of the nozzle diffusive area upon the erosion level in pure water and in water containing sediment matter (ρ = 5 g/l, diameter of particles d_h = 0.25 ~ 0.5 mm) with the cavitational zone length being l_{cz} = 110 mm. The presented data, in addition to characterizing the specific design features of the Venturi nozzle model used in these experiments, help to form conclusions concerning the effect of the by-passed surface shape on the erosion process. With the increase of angle θ, a gradual transition takes place from the surface cavitation to the hiding-off form of cavitation. While with θ = 5° the cavitational zone covers the whole surface of a specimen and collapses within its boundaries, at the angle values corresponding to θ >5 ° there begins to emerge, at the end area of the cavity, fluctuating flares which disappear without contacting the specimen surface. With further increase of angle θ and the permanent length of the cavitation zone being preserved, the thickness and volume of this zone become larger, while the intensity of the action produced by the spherical impact wave in the specimen surface diminishes, which is in agreement with principles of the cavitation erosion theory. Moreover, enlargement of the cavitational volume corresponds, strictly speaking, to an increase in development cavitation degree and hence, to a decrease of the cavitation erosion intensity, which is known to have its maximum level at the initial phases of the cavitation development.

Reduction of the cavitation-abrasive erosion, due to increase of angle θ, causes enlargement of cavitation zone sizes. But the latter moves away from

the deteriorated surface and deforming action on the solid particles penetrating through the depth of this zone.

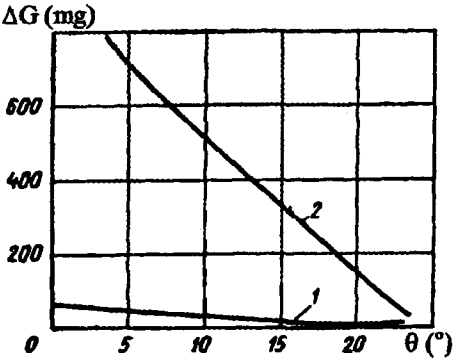

1. cavitation erosion; 2. cavitation-abrasive erosion

Figure 6.4 Effect of Venturi nozzle diffusion angle θ on erosion loss ΔG

Figure 6.5 shows specimen mass loss versus test duration at angles $\theta = 5°$ and 15° for two modes of erosion processes. The erosion line obtained during the cavitation process possesses several characteristic bends, which suggests for a certain incubation period, as well as for alterations in erosion intensity. During the combined effect produced by both cavitation and sedimentation, the bends in the erosion curve become smoother and the relationship comes closer to linear, the same as in the process of hydroabrasive erosion. But still, the absolute combined erosion level is much higher than the erosion from the cavitation effect and that of the sediments matter, exerted individually. Therefore, the test results given in Figure 6.5 are presented in a semilogarithmic coordinate system.

Sharp multiple amplification of the cavitation-abrasive erosion, as compared with separate forms of failure and their algebraic sum, has been experimentally demonstrated earlier [6.1, 6.2]. The surface reacts with the flow due to formation of water microstreams of spherical impact waves containing solid particles. Moreover, due to heavy velocity fluctuations accompanying development of cavitation, the abrasive particles present in the area of the cavitational zone acquire additional accelerations, thus enhancing

the erosion process under consideration. Consequently, the sediment particles perform a double effect: the first is developed within the cavitation zone limits, whereas the second acts throughout the adjacent regions.

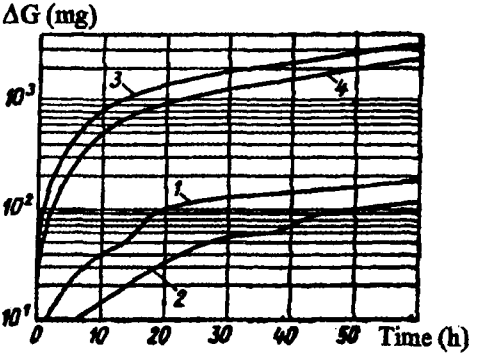

1. cavitation erosion, θ=5°; *2*. the same, at θ= 15°;
3. cavitation abrasive erosion, θ= 5°; *4*. the same, with θ= 15°

Figure 6.5 Loss in mass of specimens against test duration:

The influence of concentration and grain-sizes of the sediment matter on the cavitation-abrasive erosion behavior at a certain phase of cavitation development is illustrated by the relationship obtained experimentally (see Figure 6.6). Small sediment concentrations (ρ < 5 g/l), with particle diameter d_h = 0.1 ~ 0.25 mm, affect the erosion process insignificantly (Figure 6.6 (a)). When the concentration increases to 10 ~ 16 g/l, the erosion rate rises sufficiently due mainly to the hydroabrasive failure. The particle diameter factor (Figure 6.6 (b)) in this case is similar to its effect displayed in the hydroabrasive failure process (see Figure 6.4). When the particle size increases to the level above d_h = 0.35 ~ 0.4 mm, practically no increase the cavitation-abrasive erosion is observed.

In order to define the effect of the flow velocity upon the cavitation, hydroabrasive and cavitation-abrasive erosion processes, tests were run in a wide range of velocity values performed with the diffuser nozzle set at the divergence angle θ = 5° and with the other parameters being maintained constant, such as $l_{cz.}$ = 110 mm, ρ = 5 g/l, d = 0.1 ~ 0.25 mm (Figure 6.7 a).

Curve 3 in Figure 6.7 corresponds to the behavior of cavitation-abrasive erosion taking place at velocities v = 23 ~ 32 m/s, curve 2 is presented in accordance with the hydroabrasive erosion development shown in terms of non-cavitation streams. The different inclination angle at the initial portions of curves 2 and 3 reveals that these curves may cross each other at lower velocities. The point of their intersection is within the 14 ~ 16 m/s velocity range. This fact confirms existence of certain typical flow rate values at which the cavitation-abrasive flow intensity can be lower than that of the hydroabrasive erosion, i.e. the cavitation zone has the function of protecting the specimen surface from the solid particles.

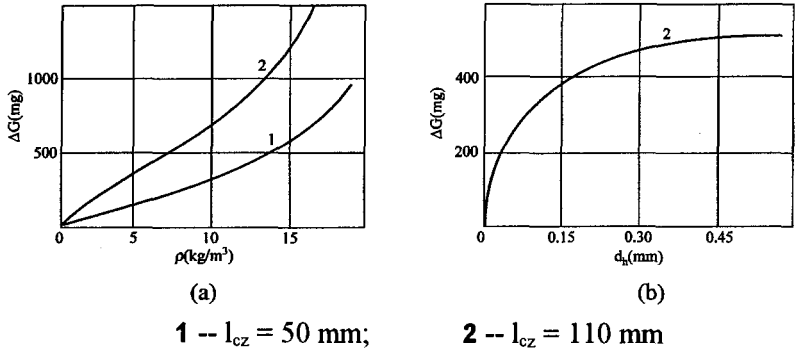

Figure 6.6 Cavitation-abrasive erosion as a function of (a) sediment concentration ρ and (b) grain size of particles d_h

Experiments were run, in this respect, with a model having the diffusion angle θ=10° (Figure 6.7 b). At higher velocities the combined erosion level exceeds the hydroabrasive one. These data are in agreement with the experimental results obtained [6.2], which confirm that the protective hydroabrasive effect of the cavitation zones in a hydroabrasive flow is only possible in case where no material is removed by cavitation.

Figure 6.8 illustrates cavitation-abrasive erosion as a function of cavitation development level, at a constant flow rate v = 30.5 m/s of a suspension-conveying mixture with solid particle content ρ = 5 g/l. The cavitational development level in these experiments was controlled by the pressure set at the inlet to the nozzle H_{in}. It is seen from the data presented that the erosion intensity rises with decrease of the cavitational number K and

remains the same, with increase of the cavitational zone length l_{cz}. The experimental results, however, make it impossible to arrive at any definite conclusions on quantitative values, since variations in the pressure H_{in} entails changes in a number of other factors, for instance, in erosion area, pressure gradients etc. It is hardly possible to isolate the individual effects exerted by these factors.

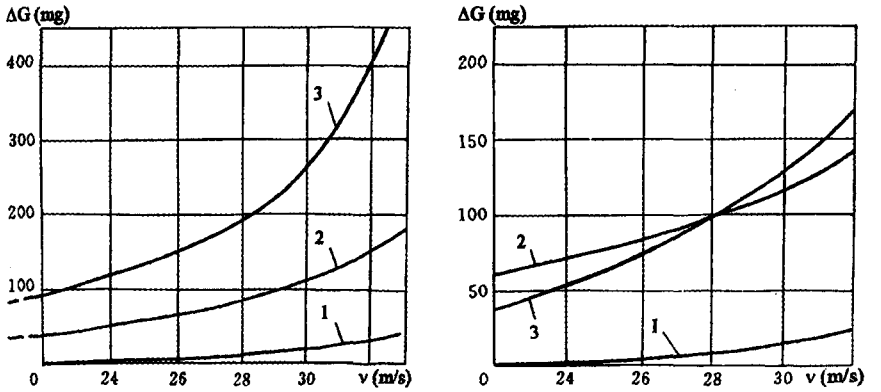

(a) for angle $\theta = 5°$ (b) for angle $\theta = 10°$;

1 - cavitation erosion; 2 - hydroabrasive erosion;
3 - cavitation-hydroabrasive erosion

Figure 6.7 Interrelation of cavitation and hydroabrasive erosion processes

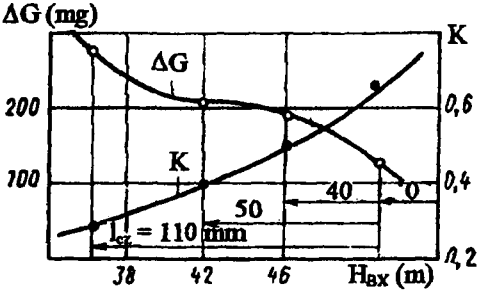

Figure 6. 8 Effect of development stage on cavitation-abrasive erosion

The research studies carried out at the V.V. Kuibyshev Moscow Civil Engineering Institute (MIEI, USSR) have shown that, in the course of the combined effect produced by both cavitation and sedimentation, there arise processes which can hardly be accepted as an algebraic sum of these two kinds of deterioration. In some cases the cavitation-abrasive erosion can be higher than the hydroabrasive erosion, whereas in other instances it may be lower. Further analyses are needed, both experimental and theoretical, to study these phenomena.

An interesting trend in development of the problems connected with the cavitation-abrasive erosion is presented in the papers written by S.P. Kozyrev. Taking into account the influence of all the factors existing in a suspension-conveying flow, namely: (H_1 - H_2), loss in the head; ($P_\infty - P_M$), vacuum value within a small space; ν_r, kinetic viscosity of the hydromixture; v_γ, rate of the suspension-conveying flow; τ_r, surface tension; Δv ,loss in the material volume caused by erosion; D , characteristic diameter of the channel; and l as the channel length, the author has established the following functional dependence which governs the erosion process being investigated:

$$\frac{\Delta V}{D^3} = F_1\left(\frac{Dv_\gamma}{\nu_\gamma}; \frac{v_\gamma^2}{gD}; \frac{P_\infty - P_M}{\rho_\gamma v_\gamma^2}; \frac{(P_\infty - P_M)D}{\tau}; \frac{H_1 - H_2}{l}\frac{d_h}{D}\frac{l}{D}\right) \qquad (6.5)$$

The solid particles, with the density greater than that of the liquid, will lag behind during the motion. The functional dependence with reference to the secondary stream participating in by-passing the solid particles will look like

$$\frac{\Delta V}{d_h^3} = F_2\left(\frac{d_\gamma v_\gamma}{\nu_\gamma}; \frac{v_\gamma^2}{gd_\gamma}; \frac{P_\infty - P'_M}{\rho_\gamma v_\gamma^2}; \frac{(P_\infty - P'_M)d_h}{\tau_\gamma}\frac{H_1 - H_2}{d_h}; \frac{D}{d_h}\frac{l}{d_h}\right) \qquad (6.6)$$

In equations (6.5) and (6.6) one can find the following criteria established to define the erosion involved:

$\frac{Dv_r}{\nu_r}$ and $\frac{d_h v_\gamma}{\nu_\gamma}$ - Reynolds numbers; $\frac{v_r^2}{gD}$ and $\frac{v_\gamma^2}{gd_h}$ - Froude numbers; $\frac{P_\infty - P_M}{\rho_\gamma \cdot v_\gamma^2}$ and $\frac{P_\infty - P'_M}{\rho_\gamma \cdot v_\gamma^2}$ - local rarefaction coefficients of cavitational

numbers, K at $P_M = P'_m = P_{ap}$ cavitation appears respectively on the component surface and behind a solid particle); $D(P_\infty - P_M)\tau_r^{-1}$ - parameter characterizing the rupture strength of the liquid; $d_\gamma (P_\infty - P_M)\tau_r^{-1}$ - parameter characterizing the liquid strength at the moment of its separation from a particle; $(H_1 - H_2)l^{-1}$ - hydraulic gradient or loss in the head within the region under review; $(H_1 - H_2)d_h^{-1}$ -resistance, while a particle is flown around; $d_h D^{-1}$ and Dd_h^{-1} - simplexes characterizing degree in lateral freedom of a particle; lD^{-1} - geometric coefficient of a unit width area being worn; ld_h^{-1} - geometric coefficient taking into account the particle-to-surface mechanism of the contact.

Although the mechanism of the influence produced by all these criteria on the erosion process is not yet known in its summarized form, the indicated criteria are most vital for a correct arrangement of researches to be promoted.

S.P.Kozyrev has succeeded in revealing the most typical versions in the development of the combined cavitation-abrasive erosion [6.2]. The line a_1a_2 in Figure 6.9 demonstrates the hydroabrasive erosion in question. The points b_1, c_1, d_1 and e_1 are correspondingly related to the erosion intensities at different cavitation development stages taking place in pure water. With the emergence of sediments and increase of their concentration the cavitation-abrasive erosion process can proceed in accordance with the patterns described below.

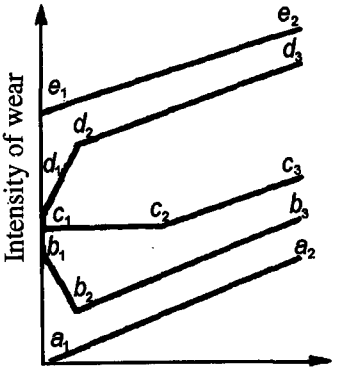

Figure 6.9 Interrelation of intensity of cavitational-abrasive erosion and sediment matter concentration

The erosion rate reduces within the region b_1b_2 as the sediment concentration is raised. This can be attributed to the fact that the cavitation erosion, provided it develops with a durable "incubation" period, starts with formation of microcracks in the surface layer of the metal, which propagates further into the metal depth, resulting in chipping out relatively large volumes of metal. During the hydroabrasive erosion one can observe, however, the formation of a thin metal "copolishing" layer, which serves to protect the surface from cavitation cracks and indentations.

A decrease in erosion may take place while cavitation erosion rate is somewhat greater than that of abrasive erosion. The moment the abrasive erosion rate starts to exceed that of cavitation erosion, due to increase in concentration of the suspended matter, there appears a rise of general failure intensity in the region b_2b_3. Here the abrasive erosion acts ahead of the cavitational erosion and thereby as though suppresses the latter.

The line c_1c_2 characterizes the erosion taking place in the events the cavitation erosion rate significantly surpasses the rate of the hydroabrasive erosion. In this rage of fluctuation, the intensity of the sediments is insufficient to alter the course of the cavitation erosion. It is only later, as the sediment content proceeds to rise, that the hydroabrasive erosion starts to be superimposed on the cavitation erosion process and, consequently, to increase the combined erosion level (region c_2c_3).

The line $d_1d_2d_3$ specifies the terms in which the cavitation erosion intensity is very great and the metals being worn out are of high plasticity (copper, aluminum, lead etc.). In this case the metal surface affected by cavitation is covered at random by material squeezed out.

The presence of sediments in the water serves to remove the metal chips, thus causing a sharp rise of the erosion process (line d_1d_2). With the further increase of the sediment concentration this effect will become weaker (line d_2d_3).

The line e_1e_2 corresponds to the highest intensity of the cavitation erosion. The presence of the suspended sediments results only in superimposing the hydroabrasive erosion over the cavitation erosion.

Within the operating components of pumps the cavitation erosion proceeds, as a rule, with a fairly long incubation period; even with the sediment content in the water equaling $0.1 \sim 0.5\%$, the hydroabrasive erosion starts to prevail over the cavitation erosion. Therefore, the pump components, which have been subjected to cavitation abrasive erosion, are identified

mainly by smooth worn-out regions, i.e. the regions with hydroabrasive erosion only. But on the operating pump components there are also other areas where cavitation erosion takes the lead over hydroabrasive erosion. Then the surface under study develops, as a result of cavitation, a sponge-like structure.

6.2. Effect of Cavitation on Hydroabrasive Erosion

The cavitation phenomena influence on the nature of hydroabrasive erosion, within the flow-passages of hydraulic machines, will further be considered with reference to a research study carried out with centrifugal pumps operating in laboratory conditions.

The analyses accomplished with the use of the simplest equipment, such as a Venturi nozzle, have demonstrated a complicated dependence of the cavitation-abrasive erosion process on the hydrodynamic features of the flow under review, the surface shape of the components as well as the quantity and composition of the sediments. Although the results available give a general idea about the basic mechanism of the material failure effected by the combined action of both the abrasive particles and cavitation, they do not provide, for the time being, definite conclusions concerning any specific qualitative recommendations.

It is most probable that things may become even more difficult in an attempt to establish feasible combinations of hydroabrasive and cavitation erosion processes taking place in such complicated hydraulic systems as in pumps. The first experiments in this direction were carried out in the V.V. Kuibyshev MIEI [6.5, 6.6]. The results obtained have revealed that the cavitation development level evaluated by, for instance, the size of cavitation margin, affects significantly the erosion of pumps operating with water which includes abrasive erosion particles.

To test centrifugal pumps, an experimental jig was used (see Figure 6.1). The pressure at the inlet to a pump (and, hence, the cavitational margin Δh) was controlled with a latch fixed in the suction pipe of the pump. The content of the sediment matter contained in the water varied for different experiments in the range of 2 to 16 g/l ($\varepsilon = 0.13 \sim 1.02\%$). The particle grain sizes were within 0.1 ~ 0.25 mm. The experiments were carried out at six different delivery modes of the pump model 4K-8, ranging from 0.54 Q_{opt} to 1.25 Q_{opt},

with various values of Δh (see Figure 6.10). At first the chipping-off cavitational pump characteristics were obtained with the pure water delivered at a constant flow Q. Then a certain amount of abrasive material was added to the jig tank and the experiments were continued with a certain number of typical values, from non-cavitation to chipping-off patterns. After each measured point a number of experimental points were "scanned" (normally from 9 to 12). The intervals between Δh values were made shorter when dealing with well-developed cavitation modes. In the normal pump operation range such intervals are of no significance since Δh values in this range do not affect energy parameters. The experiment for every Δh value lasted 4 hours. The erosion was evaluated according to the loss in mass ΔG of two test-check silumin blades of an experimental impeller.

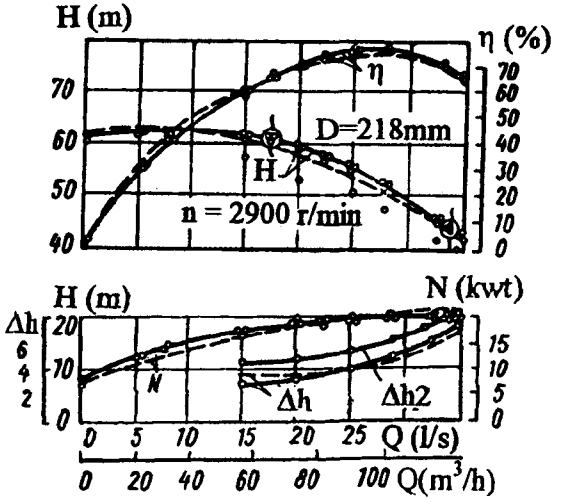

dashed line - specification provided by manufacturer
solid line - specification obtained by test

Figure 6.10 Specification of experimental centrifugal pump 4K-8

The results of these experiments, carried out at different pump discharge and with various concentrations of sediment are presented in Figures 6.11 ~ 6.13. The corresponding chipping-off cavitational characteristics of pumps

are also illustrated. With alteration of the cavitational margin Δh, the erosion rate within the blades of an impeller does not remain constant.

In centrifugal pumps it is an adopted practice to distinguish, as applied to their energy parameters, two critical values in the cavitational margin, i.e. the first and the second. The first critical of Δh_{I} corresponds to the moment of external cavitation symptom of the pump. With reference to the cavitation curves this mode is specified by reduction of the pump head or efficiency by 1 ~ 2%. The second critical value Δh_{II} refers to the moment of the pump operation failure.

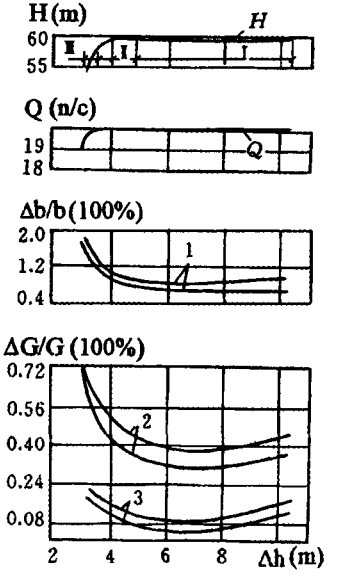

1 - $\rho = 10$ g/l; **2** - $\rho = 5$ g/l; **3** - $\rho = 2$ g/l

Figure 6.11 Erosion against cavitation margin at $Q = 0.7\ Q_{opt}$

For the pump operation points $Q = 0.7\ Q_{opt}$ (see Figure 6.11) and $Q = 0.9\ Q_{opt}$ (Figure 6.12) the pressure drop at the inlet of the pump, to the level corresponding to cavitation margin Δh_{I}, shows an appreciable decrease in the rate of cavitation-abrasive erosion in the blades, as compared to a conventional hydroabrasive erosion process. For instance, at $Q = 0.9\ Q_{opt}$,

with Δh = 6 ~ 8 m, the relative erosion of blades $\Delta G/G$ is reduced 1.5 times against the erosion level obtained without cavitation (Δh = 10.2 ~ 10.4 m).

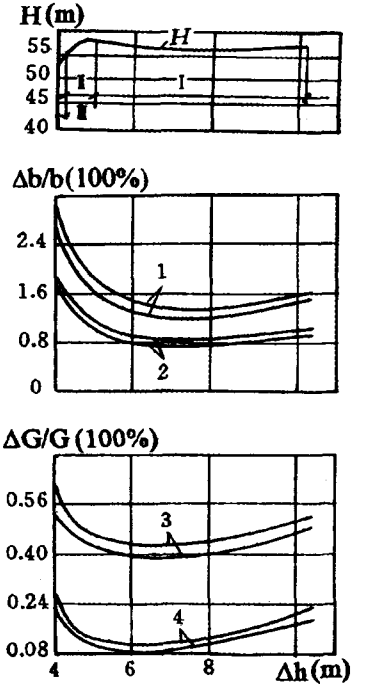

1 - ρ = 16 g/l; **2** - ρ = 10 g/l; **3** - ρ = 5 g/l; **4** - ρ = 2 g/l

Figure 6.12 Erosion versus cavitation margin at $Q = 0.9\ Q_{opt}$

At a higher delivery, such as $Q = 1.25\ Q_{opt}$ (Figure 6.13), a sharp decline of erosion rate occurs as the cavitation margin proceeds to decrease to the level up to Δh = 8.5 ~ 9.5 m. At further decrease of pressure in the suction pipe the erosion rate increases rapidly again. Consequently, the minimum intensity of the cavitation-abrasive erosion in these conditions is 1.5 ~ 2 time lower than the intensity of a pure hydroabrasive erosion occurring in the absence of cavitation.

Thus, with successive decrease of cavitation margin in a centrifugal pump operating with water containing a certain amount of solid particles,

cavitation-abrasive erosion within the blades of a pump impeller first decreases and then grows as compared with the hydroabrasive erosion process. To elucidate such an interesting phenomenon let us consider the results obtained from a generally accepted evaluation viewpoint concerning the cavitational development level in centrifugal pumps. It is a common practice to distinguish an initial cavitation, a partially developed cavitation and a fully developed cavitation [6.1].

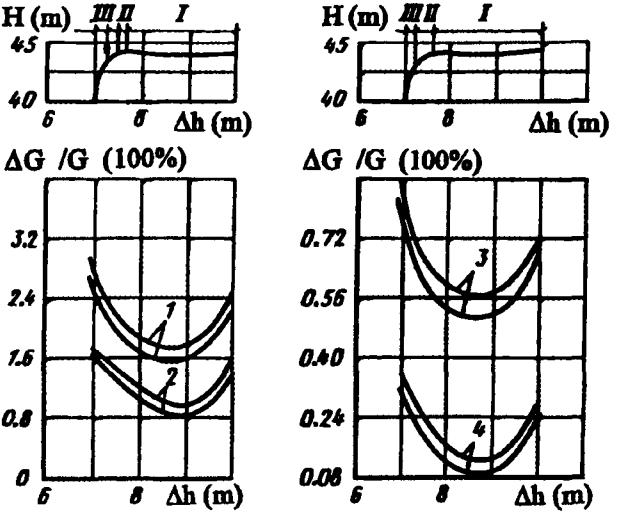

1 - ρ = 16 g/l; 2 - ρ = 10 g/l; 3 - ρ = 5 g/l; 4 - ρ = 2 g/l

Figure 6.13 Erosion vs. cavitation margin at $Q = 1.25\ Q_{opt}$

The initial cavitation stage is related to the conditions of emergence of first signs of cavitation: a weak amplification of noise and the presence of a small amount of cavitational bubbles that form an unsteady cavitational zone. As a rule, the external behaviour of a pump at this stage is practically unchanged.

The partially developed cavitation is specified by the presence of a steady cavitation zone of definite size which alters the effective shape of the guiding surface and constricts the free cross-sectional area of the flow will cause the performance of local flow velocities accompanied by emergence of secondary

flow streams. The specifications of a pump to drop due to increase of hydraulic losses.

The fully developed cavitation results in a "collapse" of the performance of a pump, the cavitational zone is already extended not so much in width as in length, i.e. along the blades of an impeller.

The theoretical analysis [6.7] and experimental results, obtained during a research study of the inter-blade channels in pumps, enable to determine the liquid flow pattern in the impeller at different operational modes of the centrifugal pumps and also to estimate the values of the appropriate pressure levels at the pump inlet in order to prevent emergence of cavitation.

At the delivery levels significantly lower than Q_{opt}, the leading edges of blades is only partly engaged with the active flow traveling from the inlet to the exit of the impeller. The greater part of it, adjacent to the front disk, is filled with the flow portion traveling in the reverse direction. This back flow, being evidently deviated in the direction of the impeller rotation, is gradually washed out by the main stream and becomes entrained in the impeller again. The vortex zone, being generated simultaneously, does not participate in the flow delivery through the impeller.

As the delivery increases (with the rotational speed being constant), the width of the active stream, at impeller inlet grows, whereas the vortex zone correspondingly decreases. At the delivery rates approaching the optimum level, the whole cross-sectional area of the inter-blade channel is practically occupied by the liquid flow, and small stagnation areas may possibly arise only nearby both sides of the blade trailing edges.

At flow rate above the optimum level, despite the fact that the active stream occupies the inter-blade channel throughout its entire height, separation still results from the pressure side of the blade and causes reduction of the flow cross-sectional area at the exit, thus increasing the average flow velocity.

With lower pressure at the inlet, the cavitation emerges within the blade channels of the impeller throughout the operational modes of the pump. The cavitation bubbles, originating in the depth of the active stream, enlarge in size and compress the vortex zone and hence the intensity of the hydroabrasive erosion at the leading edges of the blades. The further reduction of the cavitation margin results in the formation of local cavitation zones, which protect the impeller blade surfaces from the effect produced by the abrasive particles. Besides, the cavitation liquid, being of non-uniform two-

phase structure, creates within the inter-blade channel an additional resistance to the motion of solid particles, thus decreasing the margin of their kinetic energy. All this results, at the initial modes of cavitation (zone I in Figures 6.11 ~ 6.13), in a decrease of the erosion intensity, as compared with the "pure" hydroabrasive erosion process.

With the partially developed cavitation, the vortex zone disappears completely. The steady cavitation zones reduce the open area of the active flow, thereby increasing velocity of the hydromixture. Taking into account of the cavitation erosion, the intensity of the combined erosion process grows, thus reaching the intensity of the hydroabrasive erosion accomplished without cavitation process (zone II in Figures 6.11 ~ 6.13).

At further decrease of the pressure, the intensity of the cavitation-abrasive erosion of the blades starts to grow sharply (zone III in Figures 6.11 ~ 6.13). Together with the amplification of the cavitational erosion, caused by increase of the cavitational zone sizes, the situation mentioned above is derived from the fact that, due to an elevated turbulence of the flow caused by fluctuations of the velocity and pressure values, as well as by the flow stall taking place in the cavitational zones, the abrasive particles, moving within the cavitational zone and in the immediate proximity to it, obtain a considerable acceleration and thereby increase the hydroabrasive erosion.

As seen from the plots defining the relationship between the pressure fluctuation amplitudes and Δh (see Figure 6.14), for the pump delivery Q = 0.9 Q_{opt}, at the initial stage of the cavitation development (zone I in Figures 6.11 ~ 6.13), the amplitude level of the pressure fluctuation diminishes, and as the cavitation proceeds to develop (the further decrease of Δh, zones II and III in Figures 6.11 ~ 6.13), these fluctuations form a sharp rise in the flow. The region Δh = 6 ~ 9 m in Figure 6.14 can be defined as a domain in which the pressure fluctuation amplitude is maintained constant in the flow. Within the indicated region the erosion intensity in the blades is reduced as well. As indicated in the curves of the impeller blade erosion at different values of Q (see Figures 6.11~ 6.13), there exist a zone of "optimum" cavitation margin Δh, which relates to the minimum rate of cavitation-abrasive failure.

The predominance of one type of erosion over the other, in the course of the cavitation-abrasive failure, was studied by performing a specific series of experiments carried out at different delivery Q, cavitational margin Δh and growing concentration of the sediment. Similar relationships, on erosion intensity versus sediment values concentrations, have been obtained in a wide

range of Q and Δh alterations. The test results for one of operational modes taking place in a pump are given in Figure 6.15.

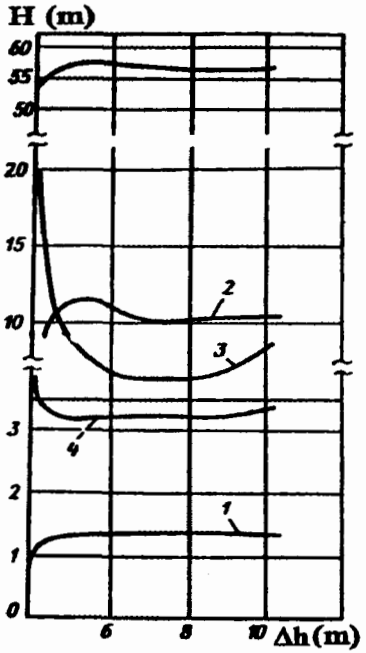

1 - fluctuation amplitude in suction piping;

2 - in spiral;

3 - in delivery branch;

4 - in discharge pipe

Figure 6.14 Pressure fluctuation in flow-passage of a centrifugal pump at different cavitation values

Every curve $I = f(\varepsilon)$ can be divide into three typical regions. The first region, characterized by a fairly fast increase of erosion intensity, confirms the joint action produced by both the cavitation and sediment erosion on the blades of the impeller (line d_1d_2 in Figure 6.9). The second region is specified by a smaller increase of the erosion intensity due to partial suppression of the cavitational erosion exerted by action of the solid particles (line d_2d_3 in Figure 6.9). Finally, the last region in which the relation between erosion intensity and sediment concentration relationship is linear (which indicates predominance of the hydroabrasive erosion over cavitation).

Hence, the results of the experimental study, obtained during the survey of the cavitation-abrasive erosion taking place in the blades of a centrifugal pump impeller, have shown that, depending on the operational conditions of a pump and the cavitation development level, the concentration of solid particles does not have equal effect on the erosion process.

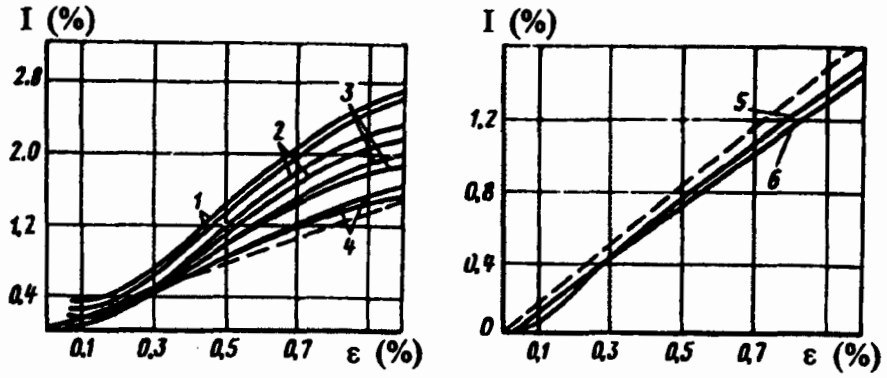

Figure 6.15 Effect of sediment concentration on cavitation abrasive erosion intensity at $\Delta h = 4.1$ m (1); 4.3 m (2); 4.7 m (3); 5.4 m (4); 6.2 m (5); 7.2 m (6); dash lined - hydroabrasive erosion, $\Delta h = 10.2$ m

6.3 Relationship between Hydroabrasive Erosion and Cavitation Erosion

The interrelation of hydroabrasive erosion and cavitation erosion, or certain mechanisms of the combined cavitation-abrasive erosion, have been studied at the V.V. Kuibyshev MIEI (under the guidance and with the participation of the authors), as applied to the operational conditions of axial-flow pumps.

With the aid of a test jig (Figure 6.16), the influence of the cavitation development level on the intensity of the hydroabrasive erosion in axial-flow pumps is studied. In the experiments carried out with use of the experimental pump ПГ 35-МА, the blades of its impeller (with 350 mm diameter) were set at angles $\varphi = +2°$, 0° and –3°, with the other parameters presented as $n = 960$ rev/min, $\rho = 10$ g/l, the particle dia. being 0.34 mm.

Four bladed impellers for this pump (two of them were experimental ones) were fabricated from silumin АЛ- 9В.

The erosion of the impeller was evaluated by loss in mass ΔG and by the position of and change in the geometric size on the silumin blades after 5 hours of operation. Cylinder-shaped specimens having 12 mm dia. and made of silumin were used to evaluate the erosion of the casing of the impeller chamber; the specimens were mounted flush with the surface of the casing. The leading parts of the blades were made to accommodate flat specimens fabricated from silumin, 100×80×3 mm in size. The working surfaces in the blades, used as the cylindrical and flat specimens imbedded in the pump parts were treated to reach the same level of surface finish.

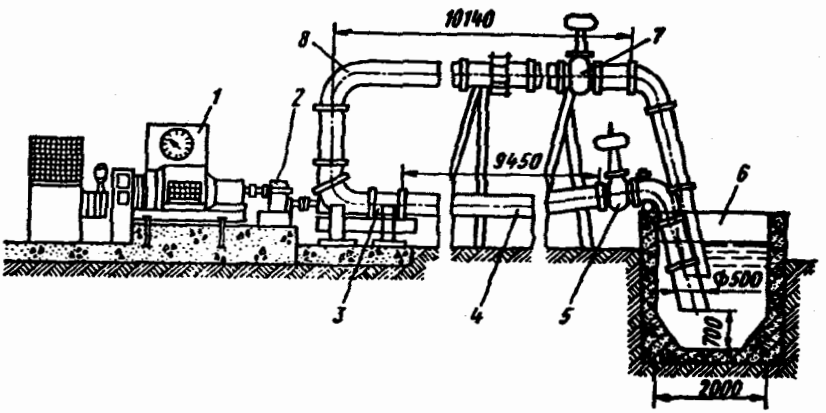

1 - electric motor; ***2*** - pressure regulator; ***3*** - axial-flow pump;
4 - suction piping; ***5*** - latch; ***6*** - reservoir;
7 - control latch; ***8*** - pressure piping

Figure 6.16 Experimental stand diagram layout for study of erosion in the flow-passage portion of an axial-flow pump

As an abrasive material chosen to be used was river sand. To maintain the concentration of the sediment constant in the system, special samples were selected during each experiment, from different points on the outlet area of the pressure piping, every 0.5, 1.5, 3 and 4.5 hours; the selected samples were checked for concentration of solid particles in all the six samples selected.

The absence of cavitation on the impeller blades was defined, in the course of the hydroabrasive erosion study, using pure water and easily removable paint coating. The research study performed at three different impeller blade angles, i.e. $\varphi = +2°$, 0° and −3°, and with various rotational speeds. The paint coating remained undamaged (not effected by cavitational) up to $\Delta h > 6.8 \sim 7.2$ m. The mechanism of the hydroabrasive erosion was analyzed at Δh being above 7.5 m.

To determine the forces acting on the walls of the impeller case, the pressure fluctuations were measured by use of oscillograms, using transducers mounted throughout the whole length of the case.

Figure 6.17 illustrates changes in the erosion in flow-passages of the pump at different values of Δh; the results are obtained for $\varphi = +2°$ and the delivery $Q = 0.356$ m^3/s $> Q_{opt}$ (Figure 6.17 a) and $Q = 0.271$ m^3/s $< Q_{opt}$ (Figure 6.17 b). As seen from the figure, the erosion intensity of the impeller and its case drops noticeably with the decrease of Δh to a certain level, which is due to the protective effect exerted by the cavitational zones. The development of this effect was ascertained by experiments carried out using a Venturi tube and by the use of a centrifugal pump. However, the same operational conditions give a gradual rise in the erosion of the leveling device, which results, most probably, from the fluctuating cavitational vortexes generated by the impeller. The chart results illustrate that the region of the minimum erosion intensity in the impeller, as presented by the characteristic curve of the pump, may be displaced to one side of the curve or the other, depending the modes of operation.

In the experiments performed with the blade angle $\varphi = 0°$, at flow rate $Q > 0.93\ Q_{opt}$, the dependencies obtained and related to Δh, are similar to those presented in Figure 6.2, 6.3 and 6.4. But at flow rate level $Q < 0.9\ Q_{opt}$ the characteristic curves change (Figure 6.18). The reduction of Δh resulted in a gradual growth of erosion intensity in the blades and the impeller case. At this stage of the study it may be explained only by the differences in motion of the suspension-conveying flow traveling through the inter-blade channels, and specifically, at low delivery levels by the formation, of cavitation zones on the blade surfaces not subjected to hydroabrasive erosion.

In the first series of experiments performed with $\varphi = -3°$ and at all flow rates of the pump, no protective effects of cavitation zones were detected at $n = 960$ rev/min, therefore additional experiments were run for $\varphi = -3°$ at $n =$

900 and 1020 rev/min, and also with a wider range of sediment concentrations.

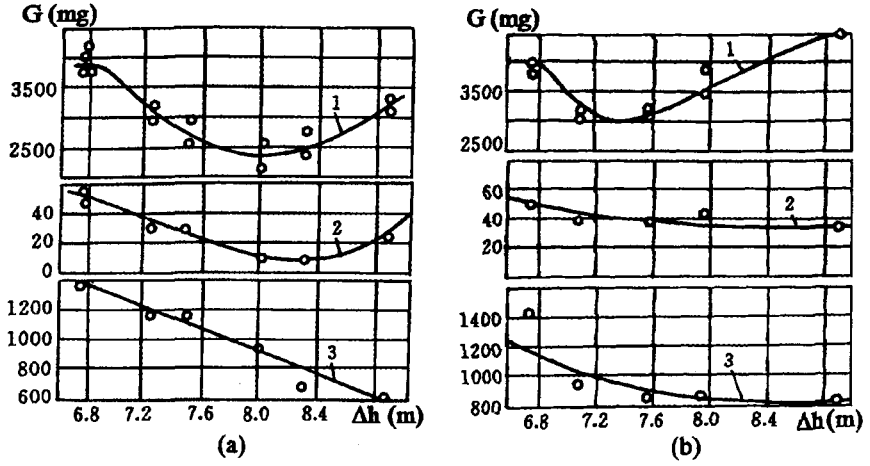

1 – impeller; **2** - impeller case; **3** - leveling device

Figure 6.17 Hydroabrasive erosion of flow-passages of an axial-flow pump versus cavitation margin

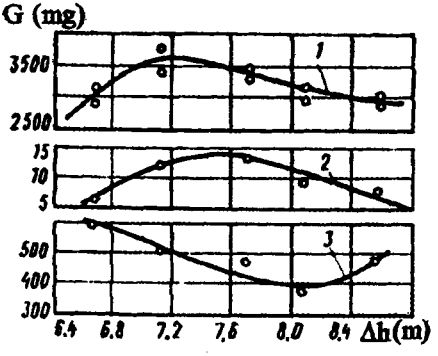

Figure 6.18 Variation of cavitation-abrasive erosion as a function of cavitation at delivery $Q < 0.9\ Q_{opt}$ and $\varphi = 0$
(**1**, **2**, **3** - the same as in Figure 6.17)

The experiments have shown have shown that for φ = -3° the cavitational zone protective effect appears at n = 1020 rev/min, only at the $Q \geq Q_{opt}$. One of such relation $\Delta G = f(\Delta h)_{opt}$ at Q = 0.297 m^3/s is presented in Figure 6.19 (curve 1). At different solid particle contents p, reducing the Δh to a certain value, a fall of the erosion intensity was seen. But at further reduction of the former, a fast rise developed in the cavitation-abrasive erosion of blades (curves 1), of the case (curves 2), of the impeller and of the leveling device (curves 3). The experimental results obtained have shown that, with increase in the content of the sediment p, the minimum erosion zone is displaced to the left, i.e. the higher the concentration of the sediment in the flow is, the later the cavitational zone effect will appear.

The similar case was noticed earlier, during the research studies carried out on hydroabrasive erosion mechanisms. It was found that, within a wide range of changes in sediment concentration and grain size, the erosion rate at Δh = 7.67 m is less intensive than at Δh = 8.42 m.

As can be seen from Figure 6.19, the curves related to the pattern of cavitation-abrasive erosion, as appeared on the experimental blades and on the reference blades (additionally prepared for this experiment from СЧ12 - 28 gray cast iron) remains unchanged at ρ = 10 g/l. In relation to this, the silumin-to-gray cast iron erosion resistance ratio is equal to 0.81.

In accordance with the relationship presented in Figures 6.11 ~ 6.13, 6.17 and 6.19, it is possible to carry out a qualitative comparison specifying the development of the cavitational-abrasive erosion processes related to the impellers of centrifugal and axial-flow pumps.

The experiments [6.5, 6.6, 6.7] have show that for centrifugal pumps with n_s = 80~100 using enclosed impellers, the erosion intensity I alters gradually for a wide range of alterations Δh values (see Figures 6.11 ~ 6.13).

In axial-flow pumps, the blade channels are connected to each other via a gap at the impeller tip. The cavitation zones being formed at the peripheral areas of blades, especially at the initial stages of cavitation development, serves the purpose of protecting the blade surfaces against the action of the solid particle, as in the case of centrifugal pumps, and also reducing the consumption of the hydroabrasive mixture flowing through the end face gap. Therefore, the erosion weight loss ΔG alteration in the impeller of an axial-flow pump, depending on Δh, is more intensive way than it does in a centrifugal pump.

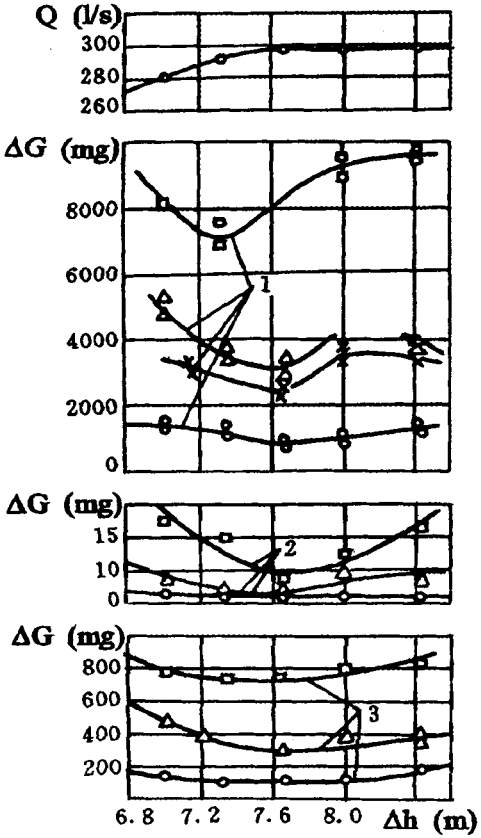

Figure 6.19 Effect of cavitational zones on cavitational-abrasive erosion in flow-passage portion of an axial-flow pump (**1**, **2**, **3** see Figure 6.17)

The experiments have shown that, as cavitation-abrasive erosion took place in an axial-flow pump, one significant factor affecting this process was the incidence angle φ, as determined by the angle of the impeller blades. Figure 6.20 illustrates the influence of Δh upon the mentioned erosion $\Delta hG/Q$ for three angles determining the position of the blades at n = 960 rev/min at delivery $Q > Q_{opt}$. The smaller the position angle φ, the later the cavitational protective effect takes place (sections I, II and III). The greatest protective effect of the cavitation zones at the given rotational speed develops at φ =

+2°. It became weaker at $\varphi = 0°$, whereas at $\varphi = -3°$ is totally absent. At $\varphi =$ +2°, when Δh is reduced from 8.84 to 8.05 m, the decrease of hydroabrasive erosion in the impeller is 24%. For $\varphi = 0°$ the hydroabrasive erosion intensity decreased by 17% when Δh was reduced form 8.5 to 7.74 m, whereas at $\varphi = -3°$ the reduction of Δh caused a continuous growth of erosion as observed in the impeller of a pump.

Therefore, for large φ values, when the difference in the angle formed between the blade axis and the axis of the suction piping is the least, the reduction of Δh is accompanied with formation of cavitation zones both on the suction and on the pressure sides of the blade, which results in decrease of the hydroabrasive erosion area within the pressure surface F_H. At small φ values the suction surface of a blade faces the suction tube to a greater extent than the pressure surface. Therefore, the increase of vacuum at the inlet to the impeller causes drop in pressure and development of cavitation on the rear surface only. This together with the hydroabrasive erosion of the pressure surface, constitute a continuous growth of the cavitation-abrasive erosion within the impeller blades.

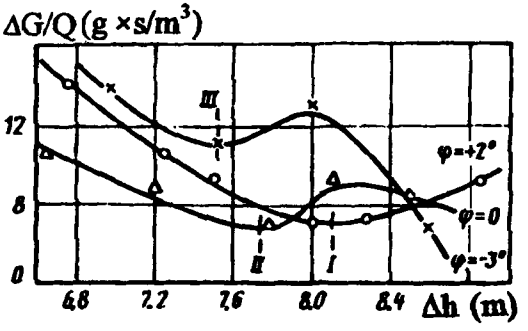

Figure 6.20 Effect of cavitation level on erosio
at different impeller blade angles

Figure 6.21 illustrates changes in fluctuation of pressure 2A' acting on the case walls and the erosion in the impeller ΔG, depending when $\varphi = 0$, n = 960 rev/min and $Q = 0.328$ m³/s. The fluctuation changes in pressure 2A', correspond to the pattern of changes of cavitation-abrasive erosion ΔG taking

place in the pump impeller. These results demonstrate again that the reduction of the pressure fluctuations in the passages of a pump, leads to a decline of the erosion rate within the pump impeller, with the decrease of Δh.

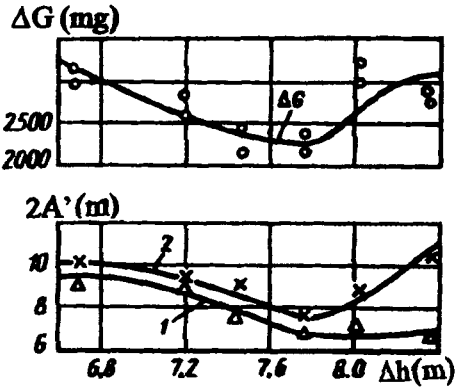

1 - in blade leading edge region; **2** - in middle of blade

Figure 6.21 Pressure fluctuation and cavitation-abrasive erosion as a function of cavitation margin

Figure 6.22 illustrates the mechanism of erosion at different regions of the impeller blades, at $\varphi = 0$, $n = 960$ rev/min, $Q = 0.336$ m^3/s, $\rho = 10$ g/l and $d = 0.34$ mm. With reduction of Δh to approximately 7.8 m, the intensity of the total loss ΔG decreases due to reduction of the erosion area F_H, caused by the protective effect of the cavitation zones being formed on the blade pressure surface. Further decrease of Δh is accompanied by enlargement of erosion areas, including the pressure and suction sides (F_H and F_B respectively) of the blade surface. With decrease of Δh, the radius of curvature R at the blade inlet region adjacent to the end face edge, is reduced as well; the angle of attack α, defining the incidence of solid particles, is changed insignificantly in this case as determined by the erosion angle formed at the inlet edge of the blade. Based on the above description, it is necessary to note that the greater the angle φ is, the faster the intensity of hydroabrasive erosion declines will be, with the decrease of Δh.

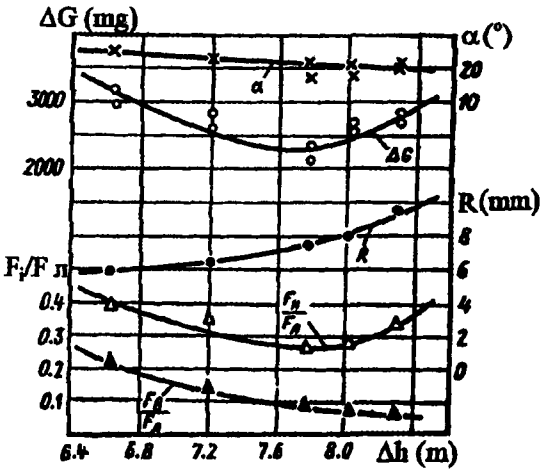

Figure 6.22 Change of erosion geometric parameters in pump impeller blades against cavitation margin

The results of the laboratory research study, aimed at the analysis of the cavitational-abrasive erosion process taking place in axial-flow pumps, are in good agreement with the data obtained during the full-scale observations carried out in a number of pump-houses. The results obtained confirm that the impeller blades, in the unified pumps 30 ПрВ-60 installed in one of the pump houses, had different erosion patterns and zone shapes, depending on the operational conditions in which the blades were used. The first pump had the greatest erosion at the blade inlet region adjacent to the end face edge, which was not the case with the second pump. Moreover, in the second pump, at the blade-trailing surface, the cavitation deterioration was predominant, and the worn-out surfaces, as a result, had a typical sponge-like structure.

When comparing operational modes of these units, it was found that the first pump station was used mostly in the spring and summer, when the level and silt content of the river water was the highest; the second station operated at lowered levels and silt content of the river water. This means that the first pump was more subjected to hydroabrasive erosion, whereas cavitation deterioration was predominant for the second unit. The worn surfaces in the impeller blades of the axial-flow pumps fabricated alloy steel, IX18H9TП

resembles a uniform wavy and scaly structure, incorporating grooves. There can be found, on the surface of the blades small local depressions. Also large craters were formed after longer duration of operation, resulting from the combined action exerted by cavitation and solid particles.

References

6. 1 Karelin V.Ya., (1975) 'Cavitation phenomenon in centrifugal and propeller type pumps, Second edit., Machinery Engineering Press, Moscow, pp.336, (in Russian).

6. 2 Kozyrev S.P., (1971). 'Hydro-abrasion of metals from cavitatio', Machinery Engineering Press, Moscow, pp. 240, (in Russian).

6. 3 Karelin V.Ya., (1978) 'Mamazhonov M., Abrasion of propeller type pumps in silt-laden flows', *Hydro-technical Production*, No. 1 (in Russian)

6. 4 Yufin A.P., (1974). 'Hydraulic mechanism', *Journal of Construction*, pp.222, (in Russian).

6. 5 Karelin V.Ya., Novoderezhkin R.A., (1976). 'Proper operating condition and suction head of centrifugal pumps for cavitation abrasion', *Vodosnabzheniye sanitarnaya teknika*, No. 6, pp. 10 ~ 12, (in Russian).

6. 6 Karelin V.Ya., Novoderezhkin R.A., Tsoy V.A., (1977). 'Variation of the pump characteristics caused by hydro-abrasion', *Hydraulic Technology and Mechanics*, No. 1, pp. 52 ~ 54, (in Russian).

6. 7 Lomakin A.A., (1966). 'Centrifugal and propeller type pumps', Second edit., Machinery Engineering Press, Moscow, pp.364 (in Russian).

6. 8 Du-tong. (1981). 'Cavitation and erosion on hydraulic machines', *Water Power and Dam Construction*, April.

Chapter 7

Corrosion on Hydraulic Machinery

M. Matsumura

7.1 Fundamentals of Corrosion

7.1.1 Corrosion Cell

Corrosion is an electrochemical process which takes place on metal subjected to a certain environment. This process is due to both current flow and chemical reactions. Electric current flows in a metal through the migration of free electrons which are characterized by metallic bonding and their free movement within the metal. In the environments (usually electrolyte) the migration of ions causes the currents. Ions are atoms which have acquired negative of positive electric charge by obtaining or losing one or more electron. Electrolyte is water-containing ions. But the current crossing the boundary between a metal and its environment cannot be explained in either of the ways mentioned above. A more reasonable explanation is that the charged states of ion and metal vary according to the electron exchange between them. For example, a positive ion (action) becomes a deposit in the form of gas or metal by obtaining electrons from metal. Or conversely, a metal atom changes into ion form by losing electrons and dissolving into electrolyte. In this dissolving process, any particular atom can be called oxidized because it has lost electrons. This process is corrosion. An important feature of the corrosion process is that the oxidation is accompanied by the equal amount of reduction.

The model figure of a corroding metal (iron, in this case) illustrates this (Figure 7.1). The area where metal atoms dissolve into environments as ions by losing two electrons (i.e. are oxidized) is called "anode". Here some quantity of metal is lost. On the other hand, the area where the oxygen in the electrolyte is reduced into hydroxide ions by acquiring electrons is called and allows reactions between oxygen and water so that no change in the metal itself takes place. In natural corrosion, the number of electrons generated at anode must be equal to that of the electrons consumed at cathode. In other words, electrons (negative charge) are moving from anode through the metal to cathode, and from cathode though electrolyte to anode. This means that positive current is flowing between the two electrodes (anode and cathode) in the direction opposite to the negative charge flow as shown by the solid line. This is called "corrosion cell".

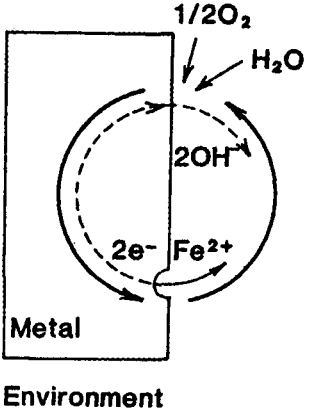

Cathode

$$2OH^- \leftarrow 1/2O_2 + H_2O + 2e^- \qquad (7.1)$$

Anode

$$Fe \rightarrow Fe^{2+} + 2e^- \qquad (7.2)$$

Figure 7.1 Electrochemical reactions occurring during the corrosion of iron in an aerated electrolyte

According to Faraday's law, a relation exists between the quantity of dissolved metal m [mol] and the amount of electricity migration through the circuit Q [coulomb]:

$$Q = nFm \qquad (7.3)$$

where, n = the number of electrons which participate in the reaction [chemical equivalent/mol] (in the case of iron in Figure 7.1, n = 2), F = Faraday constant (96,500 coulomb/chemical equivalent).

Also a relation exists between the corrosion rate and the corrosion current i_{corr} [ampere]:

$$i_{corr} = \frac{dQ}{dt} = nF\frac{dm}{dt} \tag{7.4}$$

where, t = time [sec].

7.1.2 Electrode Potentials

Environments contain usually both dissolved oxygen gas and hydrogen ions. Oxygen gas is reduced in cathode in the manner expressed in equation (7.1) of Figure 7.1. Hydrogen ions are reduced as shown in the following equation:

$$H_2 \leftarrow 2H^+ + 2e^- \tag{7.5}$$

Then, questions arise; which of the reduction reactions occurs to a metal in a certain environment and which part of the metal becomes cathode or anode? The answer depends on potential. Potential is the driving force works; we place a piece of homogeneous metal (like iron) into an electrolyte (Figure 7.2). Because the metal piece is completely homogeneous, only the anode reaction takes place across the whole surface of the iron. In other words, the iron atoms turn into ions according to equation (7.2) and dissolve into the electrolyte. At the same time, the equivalent number of electrons (an equal quantity of electricity) is stored inside the metal. With the increase in stored electrons, the dissolving rate of equation (7.2) gradually slows down according to Le Chatelier's law until it finally reaches zero. At this point, the dissolving appears to be occurring at a rate of zero, but in reality, this is a dynamic equilibrium such that oxidation (action toward right in the equation (7.6)) slows down and reduction (acting toward left) speeds up until both processed are acting at the same speed.

$$Fe \leftrightarrow Fe^{2+} + 2e^- \tag{7.6}$$

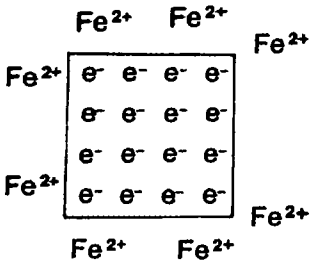

Figure 7.2 An iron in the equilibrium state in an electrolyte

The quantity of electrons stored in the metal when the reversible reaction of equation (7.6) has achieved equilibrium depends on the degree of the tendency with which the metal is ionized of oxidized. That is to say, the larger the tendency towards ionization (oxidization), the more electrons have to be stored. And, with the increase of electrons in the metal, there arises a tendency for them to escape. Actually, as is explained in the beginning of this paragraph, electrons cannot go directly out into the environment (electrolyte), but there still exists the tendency toward certain ways of decreasing their number. The tendency of electrons to escape into surroundings implies as well the tendency of positive electricity to enter the metal. This means that the potential of the metal is lower than its surroundings. The electrical position of the metal in equilibrium with its surrounding is called "equilibrium potential" or "electrode potential". The stronger the tendency of the reaction toward the right in equation (7.6), the lower the equilibrium potential. Therefore, this equilibrium potential may be calculated theoretically from the tendency of the reaction to act toward the right in the equation.

The degree of reaction tendency in the natural system can be expressed in the terms of a change in Gibb's free energy ΔG [joul]. The greater the difference in the amount of free energy before versus after the reaction, the more likely it is that the reaction will take place. So according to this principle, the equilibrium potential E_0 [volt] can be determined by the formula below.

$$nFE_0 = -\Delta G \tag{7.7}$$

where n and F is the same as in equation (7.3)

The left side of this equation represents the electrical energy. The change in free energy in a chemical reaction can be replaced by chemical potential, $\Delta\mu$. Chemical potential of a compound has long been accurately calculated from the heat of formation or of combustion of the compound. By using those data, we can calculate the equilibrium potential as follows:

$$E_0 = -\Delta\mu / nF \tag{7.8}$$

The equilibrium potential also depends on the concentration, or more accurately, the activity of metal ions in the electrolyte. Standard equilibrium potential is defined as the equilibrium potential at metal ion activity in environments = 1 at the temperature of 25°C. The equilibrium potential of metal exposed to an electrolyte of some other concentration at some other temperature can be determined by the Nernst equation below.

$$E_0 = E_0^0 + \frac{RT}{nF}\ln[M^+] \tag{7.9}$$

where, $[M^+]$ is concentration of metal ions in moles per 1000 g of water, E_0^0 is standard equilibrium potential [volt].

The potential generated between a metal and an electrolyte cannot be measured experimentally because though we can connect a leading wire from a potentiometer to metal, we cannot connect the other leading wire to the electrolyte. Thus, for practical purposes, we measure it by utilizing a standard electrode which always indicates a constant potential. Figure 7.3 shows how to measure the equilibrium potential of an electrode with the use of a hydrogen electrode as the standard. Hydrogen equilibrium potential refers to that of the electrode at equilibrium in the following reaction.

$$H_2 \leftrightarrow 2H^+ + 2e^- \tag{7.10}$$

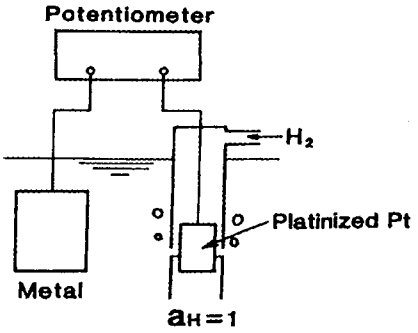

Figure 7.3 Arrangement for measuring the electrode potential of a metal

This equilibrium potential itself, however, cannot be measured experimentally, so we assume the standard equilibrium potential of this electrode to be zero, and based on this standard, we define the equilibrium potential of other electrodes. In Table 7.1 some examples are shown. The equilibrium potential experimentally measured is fairly in accordance with the calculated value. The lower the equilibrium potential, the more likely the metal is to be ionized. We call such metals "base". The higher the potential, the less likely it is to be ionized, and we call those metals "noble". What is important here is to recognize that the driving force of corrosion is not the equilibrium potential itself (base or noble), but the potential difference between the anode and the cathode of the corrosion cell. For example, with the combination of iron and hydrogen electrodes. The following corrosion cell is formed. And if both are in the standard state, the driving force is equal to 0.44V.

cathode reaction	H_2	$2H^+ + 2e^-$	0.00
anode reaction	F_e	$Fe^{2+} + 2e^-$	-0.44
driving force		(electromotive force)	0.44V

In another example, where iron and zinc are combined, the following corrosion cell is formed, and the driving force is 0.32V.

cathode reaction	F_e	$Fe^{2+} + 2e^-$	-0.44
anode reaction	Z_n	$Zn^{2+} + 2e^-$	-0.76
driving force			-0.32V

Table 7.1 Standard equilibrium potentials.

Electrode reaction	Standard equilibrium potential $E_0^0(v), 25°C$
$Au \leftrightarrow Au^{3+} + 3e^-$	+ 1.50
$Pt \leftrightarrow Pt^{2+} + 2e^-$	+ 1.19
$Ag \leftrightarrow Ag^+ + e^-$	+ 0.80
$4OH^- \leftrightarrow O_2 + 2H_2O + 4e^-$	+ 0.40
$Cu \leftrightarrow Cu^{2+} + 2e^-$	+ 0.34
$H_2 \leftrightarrow 2H^+ + 2e^-$	0.00
$Pb \leftrightarrow Pb^{2+} + 2e^-$	− 0.13
$Ni \leftrightarrow Ni^{2+} + 2e^-$	− 0.25
$Co \leftrightarrow Co^{2+} + 2e^-$	− 0.28
$Fe \leftrightarrow Fe^{2+} + 2e^-$	− 0.44
$Cr \leftrightarrow Cr^{3+} + 3e^-$	− 0.74
$Zn \leftrightarrow Zn^{2+} + 2e^-$	− 0.76
$Al \leftrightarrow Al^{3+} + 3e^-$	− 1.66
$Mg \leftrightarrow Mg^{2+} + 2e^-$	− 2.73
$K \leftrightarrow K^+ + e^-$	− 2.93

In this case, the dissolved substance is zinc. Such phenomena (the baser metal being corroded through contact with another metal with different potentials) we call "galvanic corrosion".

Let's now examine the question we asked earlier, which reduction reaction occurs on the cathode area among a variety of possible reactions in an environment? And, where is the cathode area on a metal surface subjected to the environment? The answer to the first question is: A corrosion cell is so formed that a maximum driving force is generated. For example, in a system where iron in contact with zinc, water, oxygen and hydrogen ions exists the following corrosion cell will be formed:

cathodic reaction $4OH^- \leftarrow O_2 + 2H_2O + 4e^-$

anodic reaction $Zn \rightarrow Zn^{2+} + 2e^-$

The cathodic reaction occurs on the iron surface. The possibility of hydrogen reduction reaction occurrence depends on the polarization which will be described in the next section.

The answer to the second question is that real metals are heterogeneous. For example, in the case of cast iron, the graphite carbon acts as cathode, the ferrite acts as anode, and thus a corrosion cell is formed. As corrosion proceeds, the ferrite dissolves out and a skeleton of graphite is left (This process is called "graphite corrosion"). Mild steel consists of pearlite and ferrite. Even in single component metals, the dissolubility is greatly influenced by which plane of the crystal is exposed as surface. When there is either strain of residual stress on the crystals, a difference of free energy is generated. This results in a potential difference between the stressed area and other areas.

7.1.3 Polarization

Now let's turn to the process that takes place when a piece of homogeneous metal (here it is iron) is placed in an electrolyte and current is passed through a leading wire (Figure 7.4). Current means that there are electrons flowing out through the leading wire, so the electrons in the metal decrease. Thus, the potential of the metal rises and the reaction below proceeds to the right in order to supplement electrons.

$$Fe \rightarrow Fe^{2+} + 2e^- \tag{7.11}$$

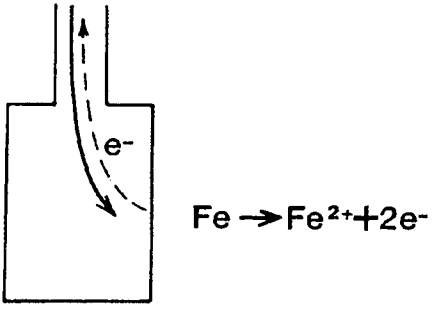

Figure 7.4 Dissolution of iron with the current allowed to flow through a lead wire.

In other words, when current flows into the metal, the potential of that metal rises higher and anodic current flows from the metal to the electrolyte. On the other hand, when current flows out from the metal through the leading wire, electrons are flowing into the metal and the potential of the metal goes down. The reaction above then proceeds to the left. In other words, a cathodic current flows from the electrolyte to the metal. These processes when expressed in terms of potential versus current are shown in Figure 7.5. i_0 is the exchange current which flows in both directions and cancel each other out giving the appearance of no current at equilibrium potential. The actual current, as indicated by the solid line, is a cathodic current when the potential is lower than the equilibrium potential and an anodic current when the potential is higher.

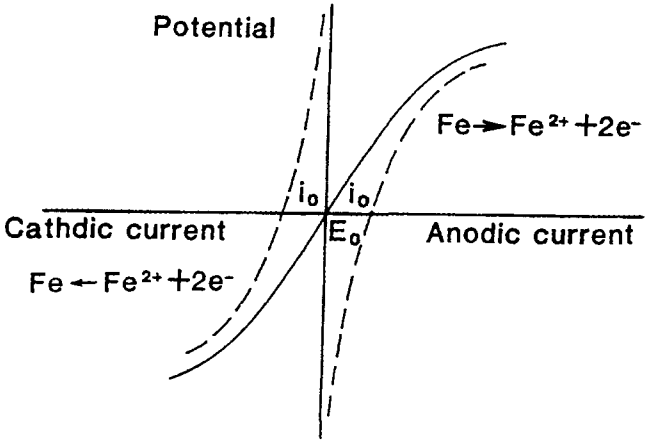

Figure 7.5 Potential versus current at equilibrium potential.
E_0 = equilibrium potential, i_0 exchange current

With the potential axis (vertical) in Figure 7.5 centered, the left half of the figure superimposed on the right, the result will be as shown in Figure 7.6(a). Further, when the current axis (horizontal) is scaled in logarithms, the result will be as shown in Figure 7.6 (b). The curves in Figure 7.6 (b) are generally called "polarization curve". In these figures, when the deviation of the electrode potential from equilibrium potential (= polarization) is assumed to

be η_a, η_c, we can find the following equation in the area where the current is larger than i_0 and is changing linearly:

$$\eta_a = b \log \frac{i_a}{i_0} = a + b \log i_a \tag{7.12}$$

$$\eta_c = -b' \log \frac{i_c}{i_0} = a' - b' \log i_c \tag{7.13}$$

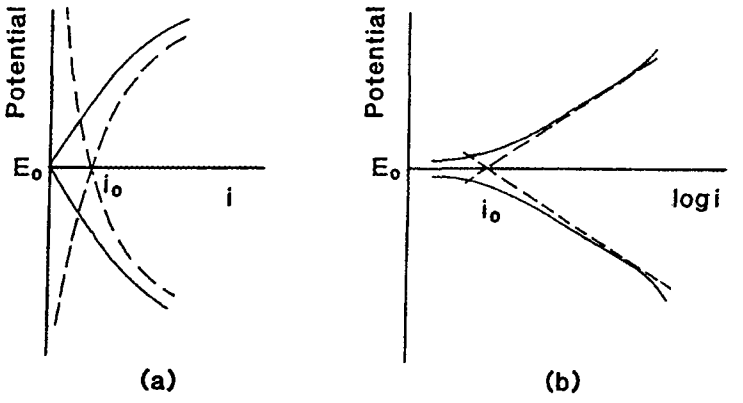

Figure 7.6 Linear relationship between electrode potential and logarithm of current

These equations are called Tafel equations and both b and b' are called "Tafel slope". The larger the slope, the smaller the change in current taking place with the change of potential. That is to say, the reaction meets a larger resistance which hinders its proceeding. As to the linear part of polarization curves, this is called "activation polarization". The slope is proportional to the activation energy which is necessary to get over the reaction barrier. The deviation of polarization curves from the straight line in the larger current zone is due to other resistances than the reaction barrier. These are known as "concentration polarization" and "resistance polarization".

When the rate of transformation of metal into ion exceeds the ion's migration rate from anode surface to the electrolyte, ions (Fe^{2+} for example) are stored on the anode surface. The increase in ion concentration limits the rate of rightward reaction of equation (7.11), making the slope of polarization curve greater. On the other hand, a lack of oxygen of cations (ions charged positive) occurs on the cathode surface when the reduction rate of cations increases. Even when the electrolyte is flowing, in very close proximity to the surface of a body there is a boundary layer where the flow velocity is quite low and oxygen and cations are migration by diffusion. Thus, due to the reduction of oxygen or of cations, cathodic current cannot exceed the current determined by the diffusion rate. In such a case, the polarization curve may by expressed in the following equation:

$$\eta_c = -b' \log(1 - \frac{i_c}{I_c}) \tag{7.14}$$

where I_c is called "limiting current".

Resistance polarization is due to the resistance, which develops when ions move through the oxide layer on the electrode surface or through the electrolyte (current flowing). In ordinary and uniform corrosion, where corrosion cells, and consequently the distance between anode and cathode are small, this kind of polarization is negligible provided that the electrolyte is highly conductive. But in a liquid such as ion-exchanged water (de-ionized water) with extremely few ions in it, the electrical resistance of the liquid is remarkably large (more than 5×10^6 Ω cm). In such a case the resistance polarization is so large that corrosion cannot take place.

7.1.4 Polarization Diagram

We can summarize the above-discussed rules of corrosion with the following statements:

i) In natural corrosion, the amount of anodic current is equal to that of cathodic current.
ii) The difference in equilibrium potential between the two electrodes is the motive force that drives the corrosion.
iii) When current flows against various resistances, a loss occurs in potential: This is polarization.

When we put these principles together into a single diagram, we will come up with the polarization diagram. An example is shown in Figure 7.7 which is composed of two polarization curves; one is the anodic polarization curves of *Fe* in Figure 7.6 (b) and the other the cathodic polarization curve of the reaction of shown in equation (7.1). Corrosion takes place at the intersection of the two polarization curves. In other words, the potential of corroding metal is equal to E_{corr} and the corrosion rate is equal to i_{corr}. This rate is equal not only to the rate at which the metal dissolves but also to the rate of oxygen consumption at the cathode.

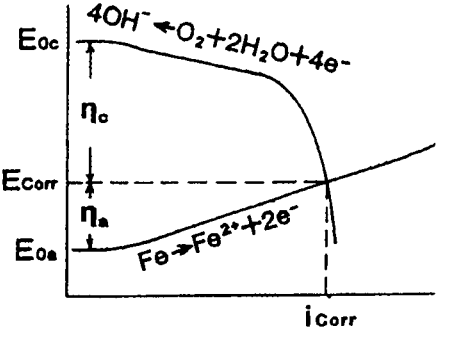

Figure 7.7 Polarization diagram showing the cathodic control situation in oxygen-consuming corrosion

The total polarization at the anode and cathode is equal to the equilibrium potential difference which is the motive force of this corrosion cell. When the extents of these two polarizations are compared with each other, the extent at the cathode is greater than that at the anode. This is because the Tafel slope of the cathode is larger than that of the anode. In this state, even if the slope of the anodic only slightly, but the corrosion current varies a great deal with the change of the slope of the cathodic polarization curve (resistance to the cathodic reaction). We call this state "cathodic control".

The discussions so far have been as to an ideal and simple corrosion cell such as shown in Figure 7.1. In corrosion of real metals there are innumerable corrosion cells of very small dimensions (e.g.,<0.1 mm) all over the surface. Furthermore the anodes and cathodes are exchanging their locations with each other from time to time to result in a uniform loss of material all over the

surface (general corrosion). Such corrosion cells are called "micro-cell" or "local-action cell". In contrast with this, in some special cases, a whole part of a machine or equipment becomes anode and the other parts cathode. As they do not exchange location, the anode part keeps dissolving resulting in severe damage on the anode part but the cathode not at all. We call such a state "macro-cell corrosion". In the macro-cell corrosion, we can measure the current flow between the anode area and cathode area by electrically isolating the parts and then connecting them through a leading wire with an ammeter in between. In micro-cell corrosion, however, we can not measure the current because the areas of anode and cathode are so small and they change their locations. A polarization curve may be impossible to measure in micro-cell corrosion. Nevertheless, we can measure E_{corr} by connecting a standard electrode and the corroding metal to a potentiometer. The value obtained here is the average potential of a large number of micro-cells. We can also measure the corrosion current i_{corr} through the weight loss of corroding metal after a giver period of time. This value is also an averaged value.Thus, at least the point (i_{corr}, E_{corr}) in Figure 7.7 can be obtained for the micro-cell corrosion. The slopes of the polarization curves will be obtained by an approximating method which will be explained in 7.2.3.

7.2 Application of Corrosion Theories

7.2.1 Pourbaix Diagram

The rate of corrosion of a metal depends, as has been explained, on the deference in equilibrium potential of electrodes as well as on the polarization of each electrode reaction. There are many causes of polarization, and thus, many factors influencing it. Therefore, it is quite difficult to predict the rate at which a given metal will corrode in a given electrolyte. However, we can calculate the equilibrium potential of electrodes by utilizing thermodynamic data and assuming two of three propositions (ion concentration, temperature, etc.). Once we know the equilibrium potential, we can predict whether the corrosion of a metal is possible or not by comparing the potential with the measured potential of the metal. As is known from Figure 7.5, there is no possibility of dissolution when the potential of metal is lower than the

equilibrium potential E_0. The Pourbaix diagram (potential vs. pH), shown in Figure 7.8, predicts the possibility of corrosion (not the rate of corrosion) based on equilibrium potential using the method just described. Figure 7.8 assumes iron as the test metal, an iron ion density of 10^{-6} mol/l in the electrolyte as the environmental condition, and 25°C as the temperature (see Pourbaix, 1966). Under these conditions, the equilibrium potential of the following reaction

$$Fe \leftrightarrow Fe^{2+} + 2e^{-}$$

can be found by the Nernst equation to be –0.62V. There is no possibility of corrosion when the potential is lower than this value, so this condition is called "immunity". The reason why pH is a factor for corrosion besides the potential lies in the following reaction.

$$3Fe + 4H_2O \leftrightarrow Fe_3O_4 + 8H^{+} + 8e^{-} \tag{7.15}$$

The concentration of H^{+} (in the right side of the above equation) is related to the equilibrium potential of this reaction. This equilibrium potential can be also defined as the threshold of immunity, a line oblique to the lateral line. Lines parallel to the vertical line have nothing to do with potential because they participate in equilibrium irrespective of electron exchange as in the following reaction.

$$3Fe^{3+} + 3H_2O \leftrightarrow Fe_2O_3 + 6H^{+} \tag{7.16}$$

In the areas described as "passivity", oxidized substances like Fe_2O_3 is stable, These oxidized substances cover the metal surface forming a protective film that reduces the rate of corrosion to nearly zero. Metal in this condition we call passivity. In the Pourbaix diagram, the following equilibrium potential ari also shown by the broken line.

$$H_2 \leftrightarrow 2H^{+} + 2e^{-} \tag{7.17}$$

$$4OH^{-} \leftrightarrow O_2 + 2H_2O + 4e^{-} \tag{7.18}$$

When the potential of iron in the electrolyte of pH2 is lower than –0.1V, both the reduction of O_2 and the evolution of H_2 are possible as cathodic reactions, but above that potential there is no possibility for H_2 gas evolution to occur as the cathodic reaction.

7.2.2 Influences of pH and Fluid Velocity upon Corrosion Rate

Figure 7.8 shows the theoretical influence of electrolyte pH on the possibility of iron corrosion. What influence does the pH of an actual electrolyte have on corrosion rate? During actual experiments, it is not possible to use 100% pure iron, and we cannot control pH freely without the use of acids and alkalis.

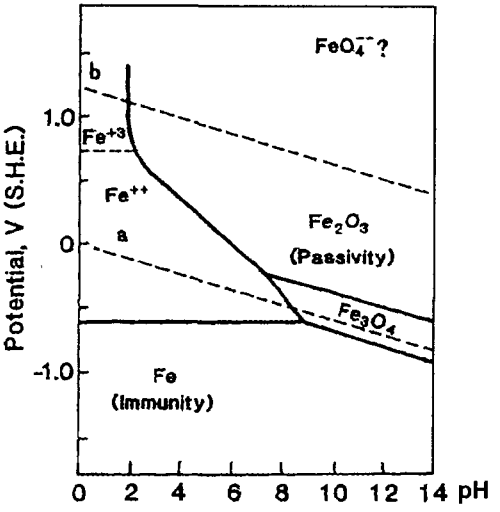

Figure 7.8 Pourbaix diagram for iron. Iron concentration, 10^{-6} mol/l; 25°C

The relationship between pH and the corrosion rate of mild steel obtained by Whitman and his collaborators in 1924 using the solutions of hydrochloric acid and sodium hydroxide may have been the result of an experiment which was conducted under the conditions closest to those of the Pourbaix diagram. This experiment utilized aerated electrolyte at room temperature and an iron ion concentration that varied from point to point but was always greater than at least 10^{-6} mol/l.

The result is shown in Figure 7.7. The corrosion activity can be classified into three categories according to pH. In a range of pH5 to pH10, the corroded surface is covered with by a film of ferrous oxide through which oxygen migrates to the surface of the mild steel and corrosion continues. On the surface of the steel, the pH is always 7.5 regardless of the pH of the electrolyte. Thus the rate of corrosion becomes constant independent of the pH out side the film. In acidic environments where the pH is less than 4, the ferrous oxide film on the surface is dissolved away and the steel is directly exposed to the electrolyte. In addition to oxygen reduction, hydrogen gas is generated and facilitates the cathode reaction, hydrogen gas is generated and facilitates the cathode reaction. Thus, the corrosion rate is greatly increased. In alkaline environments where the pH is greater than 10, a more stable and fine protective layer is formed than in the neutral environments and corrosion rate is slowed significantly.

Let us compare the experimental results of Figure 7.9 with the theory of Pourbaix diagram (Figure 7.8). Firstly, as to the effect of pH on hydrogen gas evolution the experimental result may be judged consistent with the theory because the corrosion potential of a mild steel in neutral and acidic environments is usually -0.4V to -0.5V, which is lower than the potential of a hydrogen electrode in an acidic region. In such conditions, the theory predicts hydrogen gas evolution as was already pointed out in the preceding paragraph.

Secondly, the experimental result that the corrosion rate in an alkaline environment declines due to the stable oxide film on the metal surface is well illustrated in the Pourbaix diagram.

Thirdly, as to the effect of fluid flow velocity on corrosion rate, Whitman's experiment described above was conducted in a flowing electrolyte. Generally speaking, corrosion increases with an increase in the velocity of the electrolyte flowing over the metal surface. Theoretically, the velocity of flow does not influence equilibrium potential, so we cannot explain with the Pourbaix diagram why a higher flow velocity causes larger corrosion. The reason for that phenomenon is explained as follows in the polarization diagram. The cathode polarization curve in Figure 7.10 represents the polarization of oxygen reducing reactions; the polarization curve has two parts, one with a gentle slope due to the activation polarization and the other with a steep one due to the effect of concentration polarization. As explained in equation (7.14) presented earlier, the current cannot increase

beyond the limiting current because the migrating rate of oxygen though the boundary layer gets thinner and the rate of migrating oxygen increases. Thus the limiting current moves to a higher value. With that, the current at the intersection of anodic and cathodic polarization curves (i.e., the corrosion rate) increases.

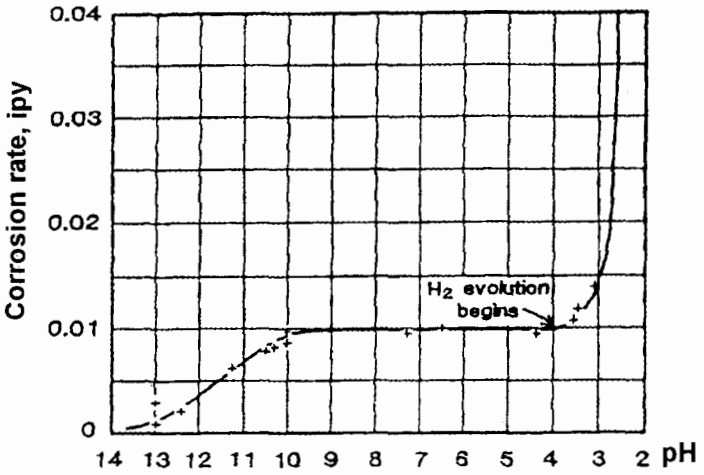

Figure 7.9 Effect of pH on corrosion rate of iron in aerated soft water, room temperature

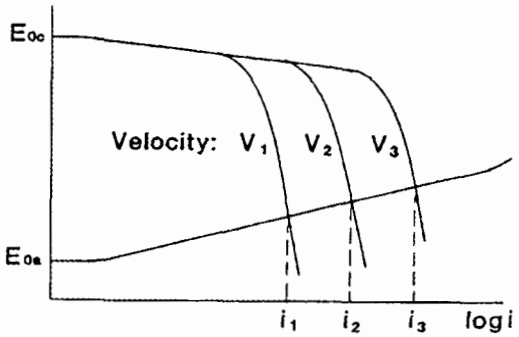

Figure 7.10 Polarization diagram showing the effect of flow velocity on corrosion rate

7.2.3 Cathodic Protection

The Pourbaix diagram in Figure 7.8 presents the possibility that iron at a potential of −0.5V in an electrolyte of pH4 with an iron ion concentration of 10^{-6} mol/l at a temperature of 25°C is likely to be corroded, but it does not tell us its corrosion rate. On the other hand, it does tell us that we can stop the iron corrosion by lowering the potential below −0.62V. Then, the iron becomes immunity and corrosion will cease. Figure 7.11 shows an arrangement for lowering the potential of the test specimen while measuring it, and Figure 7.12 shows the relationship between the current and potential during the operation. In Figure 7.11, for measuring the potential of the test specimen, a saturated colonel reference electrode is used rather than hydrogen one because it is easier to handle. This electrode shows +0.24V at 25°C (assuming the hydrogen electrode as the zero standard). In order to lower the potential of the test specimen, an external current is applied to the test specimen from the counter electrode made of inert material such as platinum or graphite carbon. Before being supplied with current, the test specimen is undergoing natural corrosion at a potential of E_{coor} and with the corrosion current of i_{corr}. On supplying the current to the test specimen, it flows in the opposite direction of the anodic current which is due to the dissolving of iron, and in the same direction as the cathodic current which is due to the reduction of oxygen. Therefore, the external current supplied from the counter electrode (through the electrolyte) to the test specimen decreases the anodic current and increases the cathodic current. These changes in the currents at the cathode and anode both lower the electrode potentials. Figure 7.12 indicates the followings: when external current i_x is applied, the cathodic current increases from i_{corr} to i_{cl}, anodic current decreases from i_{corr} to i_{al}. The potential lowers itself from E_{corr} to E_l. If the external current is increased further the potential of the test specimen is lowered further to reach E_{oa} which is the equilibrium potential of anode. At this point the anodic current drops to zero and corrosion stops. This is the principle of cathodic protection.

When we express the external current using the same axis as is used for the cathodic or anodic currents, we obtain Figure 7.13. In this figure, an external anodic current is also shown. The thick lines are external polarization curves. As the horizontal axis is scaled in logarithms, the external polarization curve almost coincides with the inner polarization curve (represented by the thin line) when the current exceeds the i_{corr}. The slopes of these curves are

particularly similar. As has been stated previously, we cannot measure inner polarization curves in real metal because of the many micro-cells that are generated on the surface. Therefore, we usually regard the inner polarization curves to be the same as the external polarization curves. This approximate method is accurate enough in comparing with the Tafel slopes in cathodic and anodic polarization.

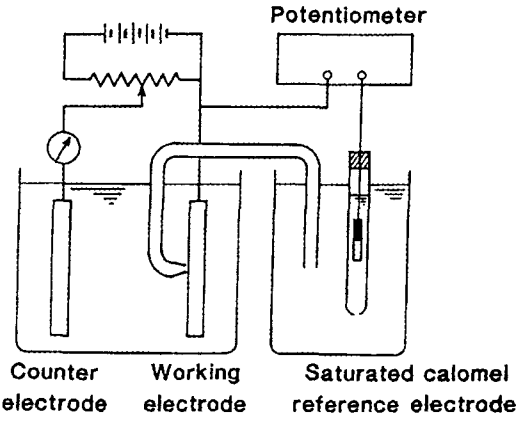

Figure 7.11 Arrangement for lowering the potential of a test specimen while measuring it

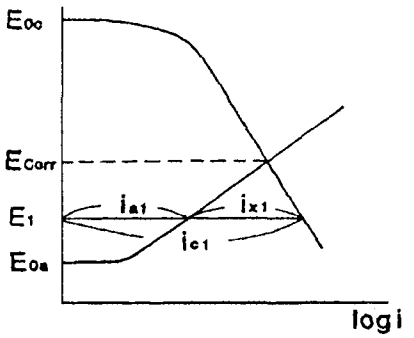

Figure 7.12 Relationships between i_x, i_c and i_a during cathodic protection

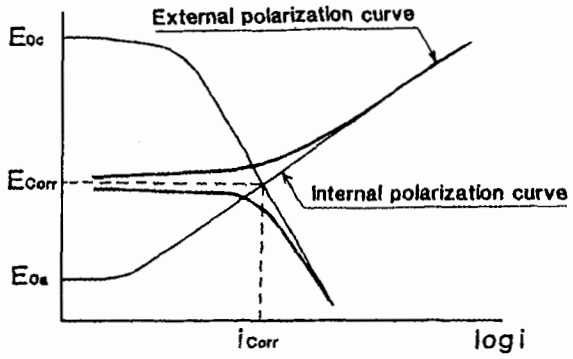

Figure 7.13 Relationships between internal and external polarization curves

7.2.4 Passivity

Another way to prevent the corrosion of an iron test specimen (in an electrolyte of 10^{-6} mol/l iron concentration, 25°C and pH4) is to put the specimen into a state of passivity by raising the potential to about +0.5V (see Figure 7.8). This method is diametrically opposite to the cathodic protection. As has already been mentioned, ferrous oxide is stable in the state of passivity. When this oxide uniformly covers the surface of the iron, the movement of oxygen and Fe^{2+} on the iron surface is inhibited and corrosion does not occur. The behavior of the external polarization curves on entering the passivity is shown in Figure 7.14. When no external current is applied, the potential of the iron test specimen is apparently at its natural corrosion potential. But if a current is supplied by using the same arrangement but in the opposite direction as in Figure 7.11, the potential of the test specimen is raised. At the same time, the corrosion current is increased. With the increase of current, when the potential reaches a certain level (passivation potential), the current is suddenly and dramatically decreased. This is because a stable and multi-ionic oxide is formed and a non-porous film of oxide covers the surface. In this condition (passivity), ions are inhibited from passing through the film and the corrosion current is extremely low. With the further raising of potential, the current remains constant for a while, but at a certain potential the current suddenly increases, this state is "transpassivity". Here the current is consumed mainly for the evolution of oxygen gas from water.

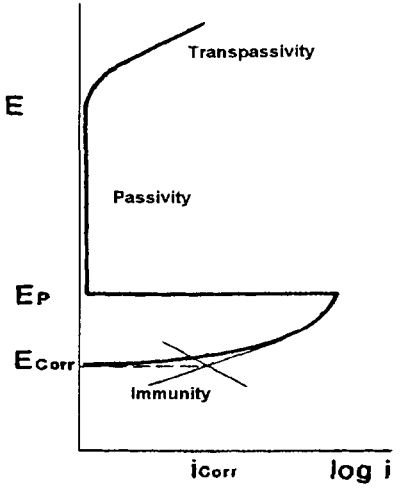

Figure 7.14 Schematic diagram of anodic polarization curve on entering passivity.

There are some ways, other than supplying an external current, to keep a test specimen in the passive state. For example, a cathode reaction of a sufficiently high equilibrium potential can be combined with the test specimen. Oxide inhibitors, like chrome-oxide of nitric acid, prevent corrosion by promoting the cathode reaction and pushing the metal potential into passivity.

Materials with low passivation potential are more likely to become passive. For example, the passivation potential of chromium is considerably lower than that of iron, and the passivity current is also small. Therefore, chromium is far more likely to become passive than iron is. The passivation potential of chromium is lower than hydrogen, so even the hydrogen gas evolution can be used to promote chromium passivity. We can get passivity characteristics similar to chromium by adding 12 ~ 18% chromium to iron. This is stainless steel.

7.2.5 Stainless Steel

There are three main classes of stainless steels: ferric, martensitic and austenitic. The austenitic stainless steels are named after the austenite phase

which is of face-centered cubic lattice and exists stable for pure iron between 910 and 1400°C only. By adding more than 8% of nickel to it, this phase can exist stable or metastable at room temperature. The typical austenitic stainless steel is the AISI (and JIS) type SUS 304 which is sometimes called 18-8 as it contains 18% *Cr*, 8% *Ni* and the *Fe*. The stainless steels of this class are the most reliable materials because they have the highest general corrosion resistance, excellent heat resistance and free from cold shortness. They have, however, some weak points in regard to pitting corrosion, crevice corrosion, intergranular corrosion and stress corrosion cracking.

Pitting corrosion is initiated by the adsorption of anions (negative charged ions), particularly chloride ions, on the defect sites in the oxide film such as at slag inclusions. The chloride ions can break the oxide film under a certain condition and cause local dissolution. Once a pit has been formed, a "passive-active cell" is set up; the inside surface for the pit is anode and the whole oxide film surface outside the pit is cathode, which results in a high current density at the very localized anodic area, and consequently a high corrosion rate. Chloride ions migrate into the pit to form their concentrated solutions of Fe^{2+}, Ni^{2+}, and Cr^{3+} chlorides with a high conductivity. A crest of hydrate is formed at the pit mouth which limits O_2 supply into the pit. Thus a differential aeration cell is also developed. Crevice corrosion proceeds in nearly the same procedure as pitting corrosion. In order to prevent pitting corrosion and crevice corrosion from occurring, the nickel content of the material needs to be increased. The austenitic stainless steel containing molybdenum (types 316, 317) is more resistant to this kind of corrosion.

Heating austenitic or ferritic stainless steels to certain temperature ranges induces in them the susceptibility to intergranular corrosion. This is called "sensitizing" and is due to the formation of chromium carbide ($Cr_{23}C_6$) at grain boundaries, which brings about the reduction of *Cr* content there. When the sensitized steel is exposed to corrosive environment corrosion proceeds along the chromium depleted grain boundaries and in extreme cases it may undermine the grains so that the metal is transformed to a powder. "Weld decay" which occurs in sensitized zones along but some distance apart from weld lines is certainly caused by the same process. Prevention of chromium carbide formation is the principle behind any practical and effective protection methods, some of which are noted below:

i) Dissolution of the chromium carbide by heating above the sensitizing temperature range, and subsequent rapid cooling (It

should be noted that the temperature range for the heat treatment is different for the different classes of stainless steels).

ii) Lowering carbon content. Stainless steels of low carbon content are designated by letter L, such as types 304L, 316L.

iii) Addition of carbide forming alloy elements such as titanium or niobium. stainless steels of this type are called stabilized grades; types 321 and 347 are of this case.

Stainless steels may crack under a tensile stress in certain environments. This is called "stress corrosion cracking (SCC)". The stress may be an applied or residual tensile stress, but compressional stresses do not cause the damage. The cracks propagate leading to a perforation or to a brittle fracture where the surface is virtually unattached and no contraction on the fracture region occurs. It is characteristic of SCC that any metal or alloy is damaged when it is exposed to a certain special corrosive environment. For austenitic stainless steels there are two major damaging ions, hydroxyl and chloride. High-pressure high-temperature water and polythionic acid are also harmful to them. In order to prevent SCC of austenitic stainless steels, cathodic protection may be effective, but this protection accelerates the failure of martensitic and ferritic stainless steels. Atomic hydrogen formed by cathodic reaction increases the tendency of those steels to crack. This is called "hydrogen cracking". For details see the books of Wranglen, 1972; Fontana and Greene, 1978; Uhlig, 1971.

7.2.6 Polarization-Resistance Method

The polarization-resistance method which was developed by Stern and Geary in 1957 is used to monitor corrosion rate by means of the polarization curve. The state of a test specimen in corrosion is expressed with E_{corr}, and i_{corr} in Figure 7.15, which is the intersection of two inner polarization curves. If a very weak external current Δi_x is supplied along with an arrangement similar to that shown in Figure 7.11, the potential of the test specimen changes slightly by the amount ΔE. Because these polarization curves can be expressed as in equations (7.12) and (7.13), and because the external current, the increments in anodic current as well as that in cathodic current can all be related in the following equation,

$$\Delta i_x = \Delta i_c + \Delta i_a \tag{7.19}$$

we can obtain the next equation,

$$\frac{\Delta E}{\Delta i_x} = i_{corr} \frac{b'b}{b'+b} \tag{7.20}$$

provided that the amount of the external current is small enough to satisfy the following equation,

$$\log(1 \pm \frac{\Delta i}{i_{corr}}) = \pm \frac{\Delta i}{i_{corr}} \tag{7.21}$$

by using the constant K for the term $b'b/(b'+b)$, we obtain.

$$i_{corr} = K \frac{1}{\frac{\Delta E}{\Delta i_x}} = \frac{K}{R} \tag{7.22}$$

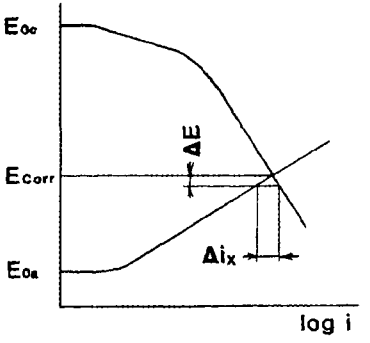

Figure 7.15 Change in potential ΔE caused by small amount of external current Δi_x

In other words, through the measurement of a slight potential change ΔE caused by the application of external current Δi_x, we can get the polarization resistance R ($\Delta E / \Delta i_x$), and from this we can calculate the corrosion current

i_{coor}. This method enables us to measure the corrosion rate electrically in a short time. This is now an indispensable procedure for monitoring corrosion. Many factors influence the polarization curves, so that a considerable error remains in this method. But many recent improvements have increased the accuracy to the point where we are now quite confident of this method (See Katoh et. al., 1985, Haruyama et. al., 1978).

7.3 Corrosion of Pump Parts

Among the various different types of pumps in use for different purposes, seawater pumps are mostly of conventional type and are apt to suffer corrosion damage. The quality of the material used for seawater pumps has been improved over the years. Recently the large-sized pumps, of which the total weight can attain 10 tons, have been made of austenitic ductile cast iron consisting of 20% *Ni* and 2% *Cr* (ASTM A 439 Type D2) or of cast stainless steel consisting of 20% *Cr*, 29% *Ni*, 2.5% *Cu* (JIS SCS 23) and so on. Adoption of such materials is considerably effective in reducing corrosion damage, but corrosion problems cannot be completely overcome even though higher-grade materials may be used. It is, therefore, desirable from an economic point of view to use common materials such as plain cast iron, carbon steel or type 316 stainless steel in skillful combination in order to deal with the problem of corrosion. Dr. Kitashima and his collaborators reported in 1986 the following examples of corrosion damage in seawater pumps and suggested methods to prevent it, in accordance with the above-mentioned concept. They are expert corrosion engineers who have engaged themselves in manufacturing of various kinds of pumps for a long time in one of the largest factories in Japan.

7.3.1 Corrosion Caused by Velocity Difference

In almost every pump, the velocity of fluid flow is different from place to place on the surface of the pump parts, which often brings about macroscopic corrosion cells which promote corrosion. Figure 7.16 shows the damage from this type of corrosion on the casing surface of a seawater pump made of cast iron. The corrosion rate of cast iron in seawater at rest is usually about 0.2 mm/year and is increased with the increase in flow velocity. On the casing

surface, however, corrosion damage was mild at the periphery of the spiral part where the fluid velocity is high, and was severe near the shaft hole where the velocity is low, and the maximum depth of graphitization have exceeded 2 mm after a 4600-h operation. This may well be attributed to the construction of a macroscopic corrosion cell where the high velocity zone near the periphery is cathode and the low velocity zone near the shaft hole is anode.

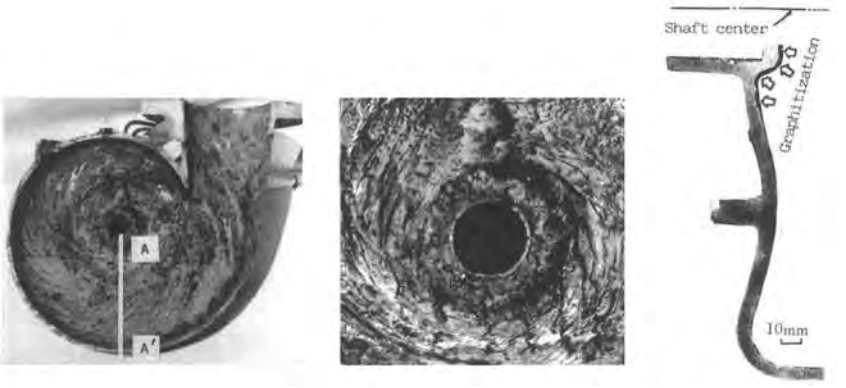

(a) (b) (c)

(a) Inner view of casing
(b) Magnification of the same as the right
(c) Cross-sectional view of casing

Figure 7.16 Corrosion of seawater pump made of cast iron (after 4600 hour neat the shaft hole)

Figure 7.17 shows the corrosion current distribution on the inner surface of a casing (cast iron) which pumped a 3% *NaCl* solution saturated with oxygen. Corrosion current was measured by using a zero-shunt ammeter between a certain piece of fraction (shown by dotted lines) and the rest of the fractions which were electrically isolated by epoxy resin but connected by leading wire. The result of this current measurement clearly substantiates the fact that the low velocity zone near the shaft hole is retained anodic.

The corrosion damage due to the velocity difference can be altered by changing the material. Figure 7.18 shows the corroded surface of a seawater

pump casing made of cast iron containing 1% *Cr*. Compared with Figure 7.16, the degree of the corrosion damage is extremely slight.

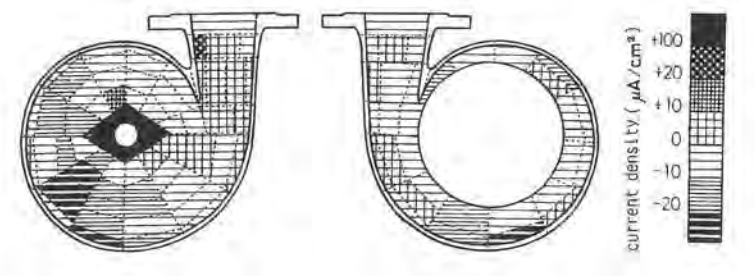

(Caused by velocity difference)
(Pump casing made of cast iron, 3% *NaCl* sol., 25°C)

Figure 7.17 Distribution of current density of macro-cell corrosion

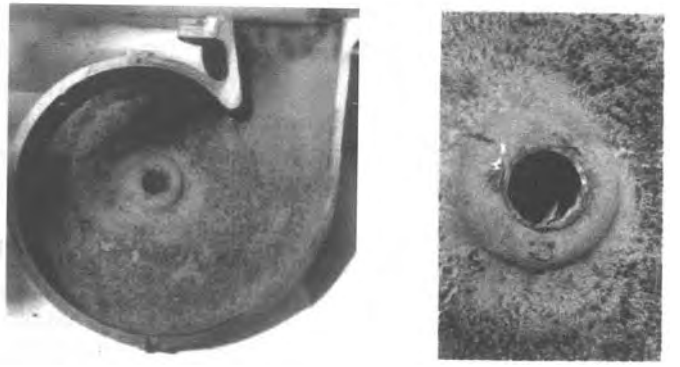

(a) (b)

(a) Inner view of casing
(b) Magnification of the same as the right

Figure 7.18 Corrosion of seawater pump casing made of 1% *Cr* cast iron; Good resistivity compared with the case shown in Figure 7.16

The corrosion current near the shaft hole of pump casings was measured using several materials. Results are shown in Figure 7.19. In the case of plain cast iron (JIS FC 20), the corrosion current increased rapidly just after the start up to reach a considerably high value indicating the occurrence of severe corrosion. The gradual decrease thereafter is apparently due to the formation of a graphitization layer on the surface which increases its thickness with the progress of the corrosion. In the case of 1% *Cr* cast iron (ES 51F, Ebara Corp. Standard, low chromium cast iron for seawater pump) and austenitic cast iron (ASTM A436 type 2), the corrosion current was extremely low compared with the plain cast iron (JIS FC 20). It is worth noting that the corrosion resistance of ES 51 F is remarkably improved by adding only 1% *Cr*.

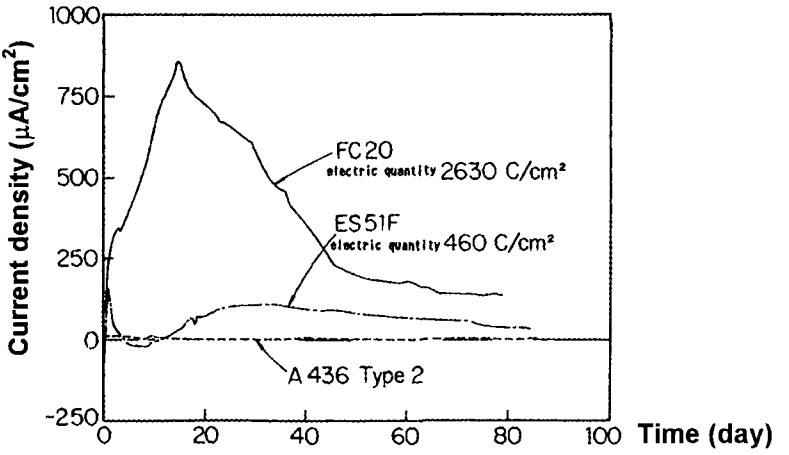

Figure 7.19 Comparison of macro-cell corrosion caused by velocity difference of several materials (corrosion current density near the shaft hole)

In contrast to cast iron, the high velocity zone of a tin bronze (FIS BC6) casing became anodic. This may be attributed to the fact that the corrosion product layer on the tin bronze surface is easily removed by a fluid flow of high velocity and dissolution of substrate is enhanced there. This difference in the influence of flow velocity between iron based alloy and copper based alloy is in accordance with the experimental results obtained by Laque in 1972 using the rotating disk test apparatus.

7.3.2 Corrosion Promoted by Mixed Use of Different Materials (Galvanic Corrosion)

Initially, use of stainless steel in large-sized seawater pumps was confined to some limited parts only. The remaining parts of the pump were of plain cast iron which acted as a sacrificial anode to protect the stainless steel parts from corrosion. This led people to the unfortunate misunderstanding that stainless steel was a perfect material for use in seawater, which further accelerated the use of stainless steel in seawater pumps. The increase of the surface area of stainless steel (cathode) and the decrease of the surface area of cast iron (anode) increased the rate of corrosion on the cast iron parts, which made cast iron lose its reputation as a construction material. Pump designers and users made another mistake in introducing tar-epoxy coating in order to reduce the corrosion damage. If they had had right knowledge of corrosion theory, they would have coated the stainless steel parts in order to reduce the cathode area. They chose, however, to do the opposite; the cast iron was coated and the stainless steel remained uncoated. What was worse, those portions of the cast iron parts which were in direct contact with stainless steel, e.g., fringe surface or faucet joint surfaces, remained uncoated in order to maintain precise measurements. As a result, corrosion currents concentrated on the uncoated surface causing decisive damage there in quite a short period (Figure 7.20). Pinholes on the coating layer also brought about severe damage (Figure 7.21).

Recently, people have gradually obtained a correct understanding of the problem and have begun to devise adequate means for its prevention. Figure 7.22 shows an example of such countermeasures; an isolating phenol resin plate as well as isolating bolts and nuts used between the stainless steel parts and plain cast iron parts.

The possibility of galvanic corrosion caused by the coupling of materials other than stainless steel and cast iron has of course to be examined before any combination is put into use. Various kinds of seawater corrosion tests were conducted from 1977 for five years at several power plants located along the coast Japan. Figure 7.23 shows the assembly and test piece for one of the above mentioned galvanic corrosion tests; in test piece A, the anode/cathode ratio was 1/1, and was variable in test piece B through the regulating of angle θ.

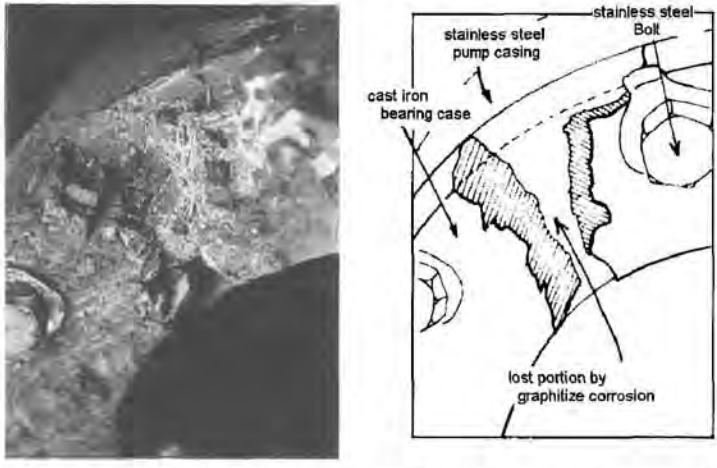

Figure 7.20 Galvanic corrosion of case iron part conducted to stainless steel part in seawater. Flange of the part (25 mm thickness) was perfectly graphitized only 2-year operation

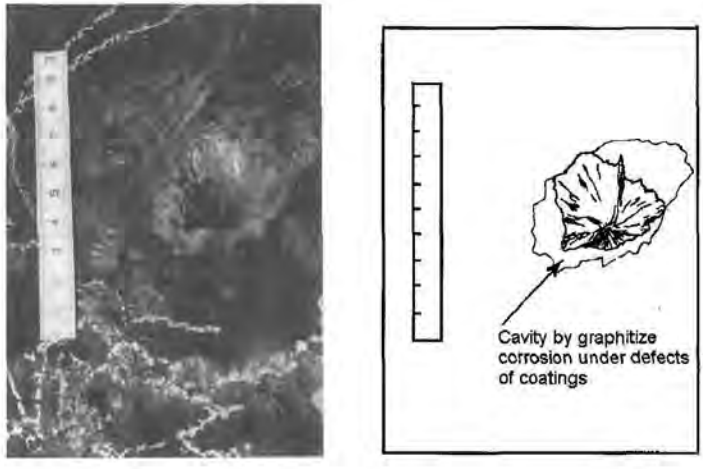

Figure 7.21 Localized galvanic corrosion at the pinhole of coating on cast iron part conducted to stainless steel part in seawater Graphitization occurred concentrically to 20 mm depth at this point only 2-year operation

Figure 7.22 Application of an isolating plate and isolating volts to a seawater pump

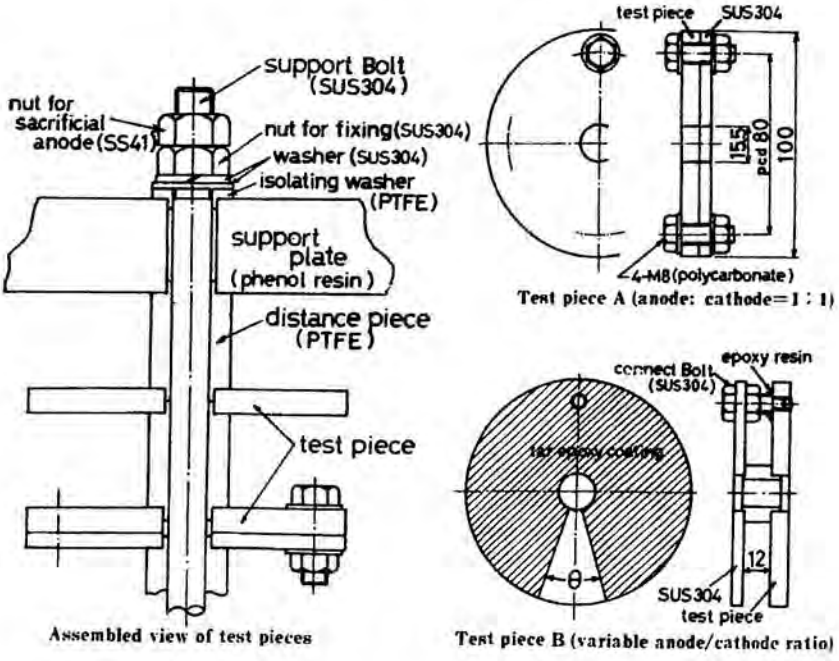

Figure 7.23 Assembly and test piece for galvanic corrosion test

In the case of 1/1 ratio coupling of tin bronze (JIS BC 6) and stainless steel (JIS SUS 304), the former was anodic and its corrosion rate was increased to 1-6 times that of it's isolated condition. The corrosion rate ranged from 0.07 to 0.45 mm/year. In the coupling of aluminum bronze (JIS AlBC 2 or AlBC3) and stainless steel (JIS SUS 304), the bronze was anodic and its corrosion rate was increased to 1 ~ 3.7 times that of it's isolated condition. The corrosion rate was 0.02 ~ 0.2 mm/year. A decrease in anode/cathode ratio brought about some crevice corrosion on the stainless at contact surface.

By the coupling of austenitic cast iron and plain cast iron, the austenitic cast iron acted as cathode to promote corrosion in the plain cast iron (see the first column of Table 7.2). On the other hand, the austenitic cast iron was seriously damaged when it was coupled with stainless steel as shown in the last column of Table 7.2.

Table 7.2 Galvanic corrosion in natural seawater at several points throughout Japan (Anode/Cathode = 1)

Geographical location	Galvanic couples		
	FC20/A436 type2	FC20/SUS304	A436 type2/SUS304
Tomakomai	0.87 mm/Y	1.12 mm/Y	0.95 mm/Y
Sendai	0.65	0.76	0.50
Fukushima	0.38	0.49	0.35
Kashima	0.45	0.56	0.35
Chiba-1	0.83	0.79	0.48
Chiba-2	0.83	0.80	0.49
Naooya	0.29	0.29	0.17
Hlmeji	0.38	0.38	0.19
Fukuyama	0.44	0.41	0.18
Tokuyama	1.37	1.43	0.63
Kokura	0.42	0.41	0.21
ō ita-1	0.46	0.43	0.14
ō ita-2	1.15	1.18	0.39
Naoasaki	0.74	0.99	0.27

Polarization curves for these materials in a 3% *NaCl* solution are given in Figure 7.24 which indicates that the austenitic cast iron acts as cathode to

promote corrosion of the plain cast iron, but it dissolves itself as anode when it is coupled with the stainless steel. Thus the polarization curves substantiate the results of Table 7.2.

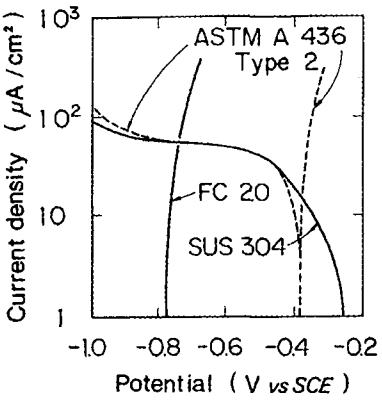

Figure 7.24 Polarization behavior of gray cast iron, austenitic cast iron and stain-less steel (3% *NaCl*, 25°C)

7.3.3 Crevice Corrosion and Other Localized Corrosion

(1) Crevice corrosion

Large-sized and yet full stainless steel pumps come into general use in accordance with the rapid economic development in Japan. They have, however, a weak point as regards crevice corrosion. Countermeasures to this type of corrosion are:

i) To use sealing material to prevent the permeation of seawater into the crevice;

ii) To use crevice corrosion resistant materials.

The first measure is not satisfactory for long term use and can not be applied to the crevices on moving parts. As for the second measure, the new types of stainless steels of higher *Cr* and *Mo* contents have been utilized and proved considerably effective in preventing crevice corrosion. Even these materials, however, are not totally immune from crevice corrosion.

Table 7.3 is a result obtained from crevice corrosion tests which were conducted parallel with the galvanic corrosion tests described in the

proceeding paragraph, using the assembly shown in Figure 7.25. High graded materials such as Alloy C, Alloy 625 or Tiganium are certainly reliable, but it is economically impossible to use such materials for large-sized pumps. Kitashima et. al. found the way out of the problem by developing an alloy for welding use which has superior resistance to crevice corrosion and by limiting its application to crevice portion only. Figure 7.26 shows an example of successful application to the overlay welding.

Table 7.3 Crevice corrosion in natural seawater at several points throughout Japan.

Geographical location	SUS 304	Alloy 825	Alloy 20	S.	Alloy S.	Alloy C	Ti Duplex 625
Tomakomai	×	×	××	○	○	○	○
Chiba-1	××	×	×	Δ	○	○	○
Nagoya	××	×	×	○	○	○	○
Tokuyama	××	×	×	○	○	○	○
Oita-1	×	×	×	○	○	○	○

○: generally free from crevice attack
Δ: occasionally subject to crevice attack
×: generally subject to crevice attack
××: generally subject to severe crevice attack

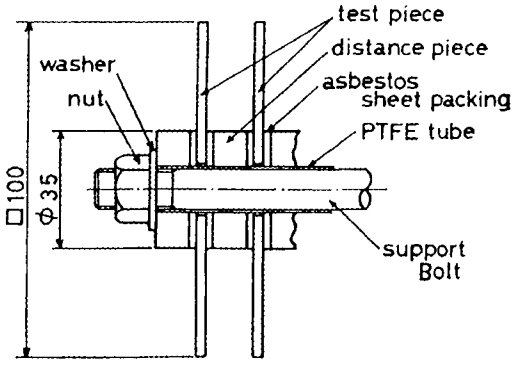

Figure 7.25 Schematic of test assembly for crevice corrosion test

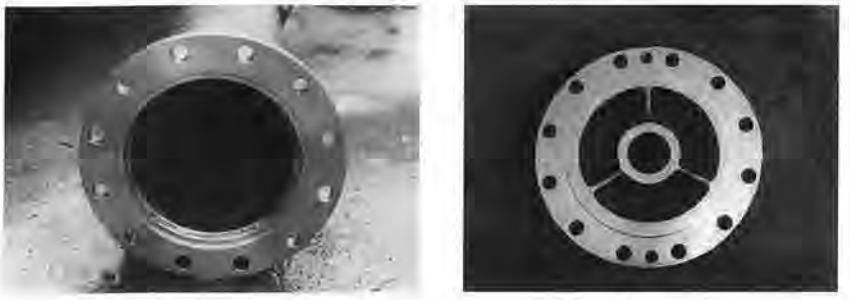

(a) (b)

(a) Flange surface of column pipe (base material; SUS316L)
(b) Flange surface of intermediate bearing support (base material; SCS 14 solution heat treatment after overlay).

Figure 7.26 Parts of seawater pump weld overlaid with corrosion resistant alloy (*Ni* 30% *Cr*-10% *Mo* alloy) after 1 year operation.

(2) Corrosion of weld metal:

A similar material to the base metal is usually used for plugging welding of the vent hole or for repairing welding of the defects in castings. Unexpected damage can occur even in these weldings. Figure 7.27 (a) shows an example of severe corrosion damage to the deposit metal at the plugging welding. The base metal was type 304-cast stainless steel (JIS SCS 13) and the environment was a dense saline solution of 70 ~ 90°Ccontaining solid particles. Investigations revealed that the microstructure of the deposit metal was normal and there was no sign of sensitization as shown in Figure 7.27 (b). A little difference, however, was found in chemical composition between the base metal and the deposit metal; deference in *Mo* content should be noted in Table 7.4 which shows the chemical composition of the metals, i.e., the *Mo* content of the deposit metal (0.006%) is lower than that of the base metal (0.67%). The contents of other elements were quite normal for type 304 stainless steel, specifically; levels of *Ni* and *Cr* were rather higher than in the base metal.

Test specimens with an exposure surface of 2 cm^2 were prepared from each metal and dipped into a pseudo-environmental liquid (without solid particles) in order to measure the potential as well as the galvanic current

between the two metals. The results are given in Table 7.5. The potential of the deposit metal was shifted basic with the lapse of time, markedly for the case of immersion after the emery paper polishing, and considerable current flow was also noted. Considering the exposure area ratio of the base metal and the deposit metal in the real pump, the corrosion rate predicted from the experiment was in relatively close accordance with the damage in the field.

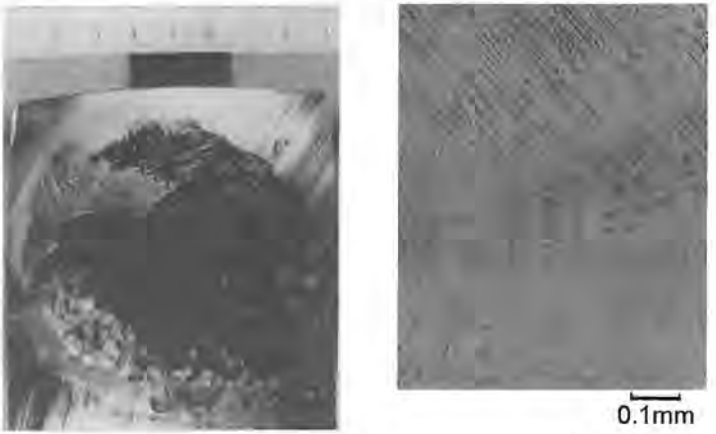

Figure 7.27 (a) Corrosion at weld repaired portion of impeller made of SCS 13 (1 year operation); (b) Cross-sectional micro-structure of the repaired weld metal.

Table 7.4 Chemical compositions of base metal and deposited metal (wt.%)

	C	*Si*	*Mn*	*P*	*S*	*Ni*	*Cr*	*Mo*
Base metal	0.064	1.32	1.14	0.025	0.019	8.93	19.57	0.67
Deposit metal	0.064	0.34	1.06	0.019	0.100	10.57	20.23	0.06

Stainless steel castings which contain up to 0.5% *Mo* are not rare among so-called 304 type stainless steels. Such excess in alloy element content is usually disregarded because it dose not reduce but improve corrosion resistance. However, when Mo containing stainless steel were brought into

contact with a *Mo* free stainless steel under some critical conditions such as high temperature, concentrated solution or erosive slurry, considerable corrosion may occur to the Mo-free material.

Table 7.5 Potential of base metal and deposited metal and short circuit current density between them

Tempera-ture of solution (°C)	Immersion time before measurement (h)	Potential (mV vs SCE)		Short circuit current density (μA/cm)	Note
		basic metal	deposited metal		
79	1	-270	-257	-	immerse after 2 4h from polishing by emery paper
	63	-280	-351	2	
90 (at start) ↓slow cool	just after immersion	-310	-210	-	immerse just after polishing by emery paper
70 (after 2h)	2	-263	-710	20	

Chemical composition of test solution (%) $CaSO_4$: 0.17; $CaCl_2$: 2.95; $MgCl_2$: 13.33 *KCl*: 8.06; *NaCl*: 12.45; *S.S:* 24;

Figure 7.28 is another example of corrosion which occurred at a weld repair section of a seawater pump made of aluminum bronze (JIS AIBC 3). It had been strictly specified that a similar or higher grade welding metal had to be used for the repair welding of AIBC 3 castings. But small defects were carelessly repaired with a lower grade welding metal by an inattentive worker. If the specification had been completely controlled, such corrosion would have been avoided.

(3) Corrosion of hard facing

Ni-or Co-baxed high carbon alloys are often used for overlay welding on the shaft sleeve surface where a high resistance against abrasion is required. These alloys were applied to seawater pump shafts made of stainless steel and brought into contact with seawater. A result is shown in Figure 7.29: the hard facing layer fell off due to the inter-granular corrosion in the sensitized area beneath the overlay. The sensitization was caused by the diffusion of carbon

from the hard facing alloy to the base stainless steel. Dr. Kitashima and his collaborators succeeded in avoiding such corrosion by using a Co-based low-carbon type hard facing alloy as shown in Figure 7.29 (c).

Figure 7.28 Corrosion occurred at weld repair portion of aluminum bronze casing

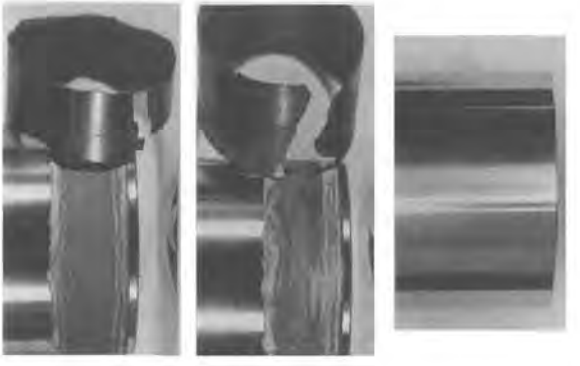

(a) (b) (c)

(a), (b) Hard facing layer fell off by corrosion in the boundary (after immersed for 3.5 month in seawater);
(c) Original state

Figure 7.29 Corrosion of the hard facing sleeve.(base metal; SUS 316L)

7.4 Interaction of Corrosion with Erosion

The combined attack of erosion and corrosion to metals has recently become serious in various engineering applications. The slurry erosion-corrosion occurring on the materials containing coal slurry in its liquefaction process is a well known example. Another example is the pump impellers in the lime slush-lime stone process for exhaust gas desulfurization which circulate the process liquid of high acidity containing solid particles of gypsum and fly ash. In such cases, both the corrosion and erosion processes probably assist each other to bring about a larger amount of damage than the simple sum of the damage caused by each process separately. Any general law, however, cannot be expected to exist for estimating the total amount of erosion-corrosion damage to a metal, because the mechanism of mutual interaction between erosion and corrosion is quite liable to variation depending on the conditions of the situation. You can easily understand this when you remind yourself of how strongly the extent and nature of the damage caused by the solid particles impact on a surface depend on the conditions such as impact angle, the shape of the particle, the impact velocity and so on, as repeatedly discussed in Chapter 2. In addition to those physical or mechanical conditions, electrochemical factors inevitably have a great influence on the mutual interaction to result a different mechanism and a different damage estimating equation for each case.

The following is the result of an investigation conducted by Prof. Matsumura and Oka (1987) which shows an example of the mutual interaction of erosion and corrosion and discusses a simple fundamental equation relating the total damage with each component.

7.4.1 Experiment on Slurry Erosion-Corrosion

(1) Testing apparatus

A schematic diagram of the fountain-jet apparatus is shown in Figure 7.30. The main tank was made of transparent polyvinyl chloride resin and consisted of two sections placed one above the other. In the lower section, of smaller diameter, a fluidized-bed was formed in which solid particles were suspended uniformly in an upward flow of liquid. In the upper section of the tank, the slurry which flowed from the test section was separated into solid particles and clear liquid. The solid particles were allowed to fall into the fluidized-bed

below. The bulk of the clear liquid was circulated by a pump into the test section and the rest into the distributor below the fluidized-bed.

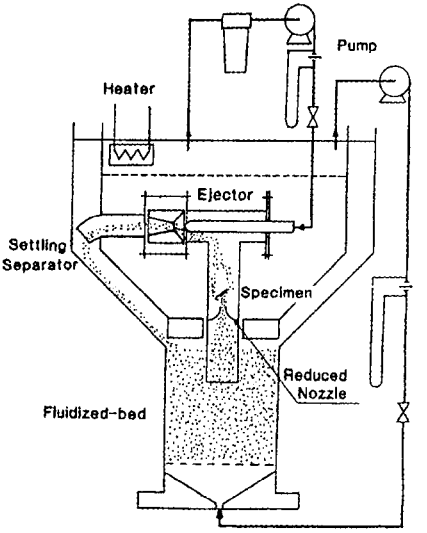

Figure 7.30 Schematic diagram of the fountain-jet testing apparatus.

By means of an ejector located at the top of the test section a stream of slurry (particle concentration of 60%) is accelerated by the reducer nozzle and allowed to impinge on the test specimen at a velocity of 3 m/sec, Figure 7.31. The test specimen, a cylinder 5 mm in diameter and 5 mm in length was held between two matching sections of silicon rubber which were held together on a bolt. Only the top flat surface was exposed to the impinging slurry since the bottom as well as the side-wall of the specimen was entirely covered by vinyl tape. The impact angle of the slurry stream on the specimen surface was regulated by turning and then clamping the support bolt. The impact angle of the slurry stream on the specimen surface was regulated by turning and then clamping the support bolt. The particle impact angle was uniform all over the test surface; it was equivalent to the angle between the slurry stream and the surface of the specimen. To ensure that direction of impingement was uniform it was necessary to restrict the test surface to a small area where the impact conditions were uniform.

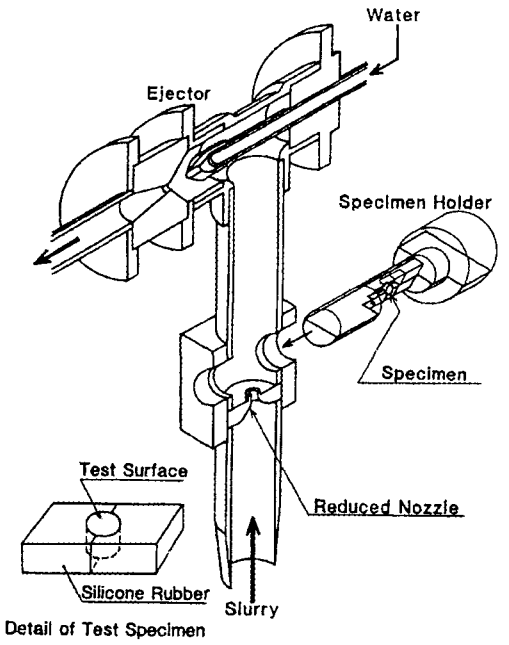

Figure 7.31 Schematic diagram of the test section of the fountain apparatus

The details of the measurement of the particle impact conditions for those apparatus have been reported elsewhere (see Oka et. al. 1984), and only the results of the measurements are listed in Table 7.6.

Table 7.6 Impact conditions of solid particle in the fountain-jet facility

Impact Velocity (m/s)	Impact Angle (deg)	Impact Frequency ($1/cm^2 \cdot s$)
3.0	10 ~ 80	$ca \cdot 10^5$

(2) Test results

Pure erosion tests on commercially pure iron were conducted in a slurry of silica sand and deionized water. The results obtained are shown in Figure 7.32 which shows the relationship between erosion rate and particle impact angle

α. The erosion rate in mg/cm^2•min (solid line in the graph) was divided by the flow rate of impacting particles to obtain an alternative erosion rate expressed in mg/kg (dashed line). The shift of the peak of the curve results from the fact that the flow rate of impacting particles depends on the angle, α between the specimen surface and the slurry stream. In this paper the erosion rate expressed in mg/cm^2•min is adopted since corrosion rates are also expressed using the same units.

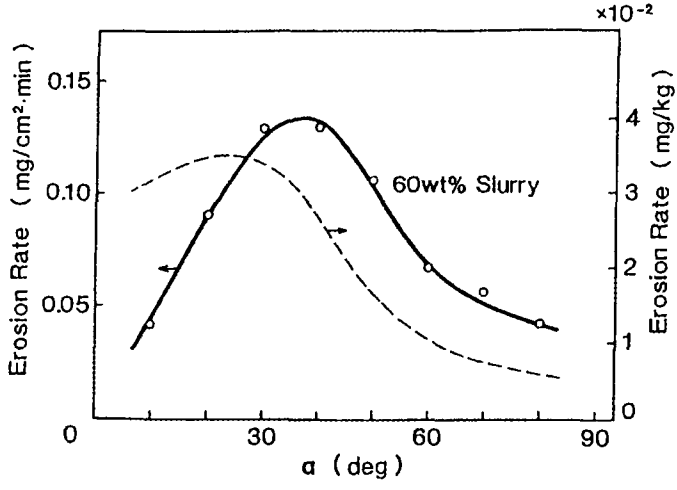

Figure 7.32 Effect of impact angle on erosion rate for iron specimens in the fountain-jet facility; jet velocity, 3.0 m/s; slurry, deionized water and silica sand of 60 wt%, 40°C

Pure corrosion tests were conducted by circulating aqueous solutions without solid particles. As shown in Table 7.7 the average corrosion rate for an hour period was found to depend on the pH of the test liquid but to be independent of the angle the specimen was set at. A comparison between Table 7.7 and Figure 7.32 makes it clear that corrosion rates and erosion rates were of the same order of magnitude except for the corrosion rate at pH12.

Combined erosion-corrosion tests were carried out in slurries of silica sand and corrosive liquids. The results are shown in Figures 7.33 through 7.35. The solid line in each graph represents the erosion-corrosion rate, $\dot{W}_t$,

as a function of particle impact angle. The broken line represents the pure erosion rate $\dot{W}$, the dotted line the pure corrosion rate $\dot{F}$, and the dashed line the sum of the pure erosion and pure corrosion rates, that is $\dot{W}+\dot{F}$.

Table 7.7 Corrosion rate of iron specimens in the fountain-jet facility

Corrosiveness	Corrosion rate (mg/ cm^2•min)
pH2	0.07
pH4	0.025
pH12	0

In the slurry of pH12 (Figure 7.35), the sum of the erosion and corrosion rates ($\dot{W}+\dot{F}$) is essentially identical with the erosion rate ($\dot{W}$); this results from the fact that the pure corrosion rate ($\dot{F}$) is essentially zero for all impact angles. Nevertheless, the erosion-corrosion rate ($\dot{W}_t$) is higher than the sun of the erosion and corrosion rates. Thus some mutual acceleration of the rates of erosion and corrosion must be occurring. In other words, the sign of the mutual interaction is positive.

In the slurry of pH4 (Figure 7.34), $\dot{W}_t$ is still higher than $\dot{W}+\dot{F}$ at large impact angles. At low impact angles, however, a change impact angles. At low impact angles, however, a change in behavior occurs and thereafter $\dot{W}_t$ is consistently lower than $\dot{W}+\dot{F}$. This is interpreted to mean that the erosion and corrosion rates are inhibited when they occur together, or that their mutual interaction is inhibitory. The same situation is observed in slurry of pH2 (Figure. 7.33), but the change in behavior occurs at a larger angle.

In order to illustrate the synergistic effect more clearly ($\dot{W}+\dot{F}$) was subtracted from $\dot{W}_t$. The relationship between this parameter and the impact angle is given in Figure 7.36. The synergistic effect tends to become negative as the particle impact angle decreases and the corrosion intensity increases.

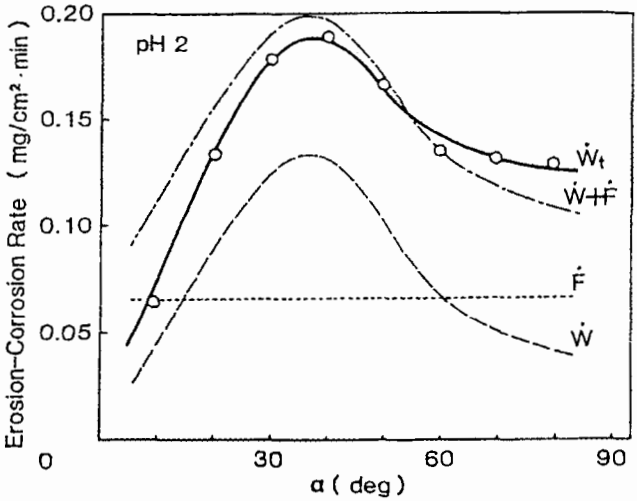

Figure 7.33 Effect of impact angle on erosion-corrosion rate for iron specimens; Jet velocity, 3.0 m/s; slurry, *Hcl* acid solution of pH2 and silica sand of 60 wt%, 40°C

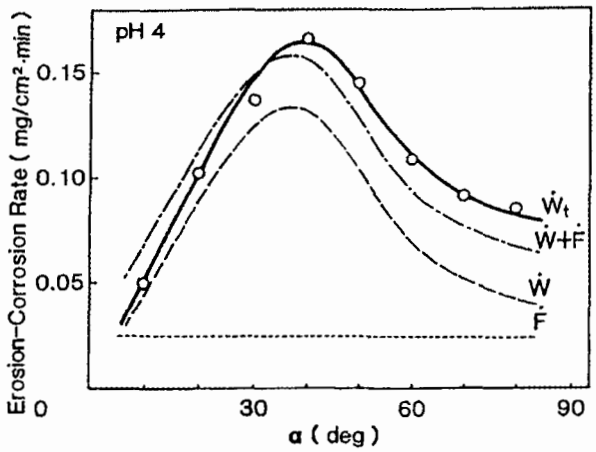

Figure 7.34 Effect of impact angle on erosion-corrosion rate for iron specimens; Jet velocity, 3.0 m/s; slurry, *Hcl* acid solution of pH4 and silica sand of 60 wt%, 40°C

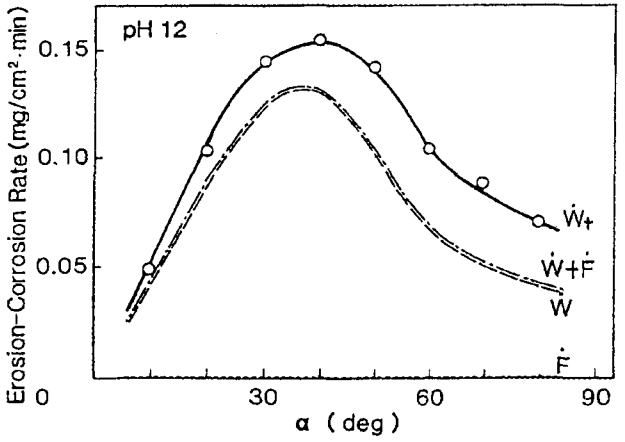

Figure 7.35 Effect of impact angle on erosion-corrosion rate for iron specimens; jet velocity, 3.0 m/s; slurry, *NaOH* solution of pH12 and silica sand of 60 wt%, 40°C

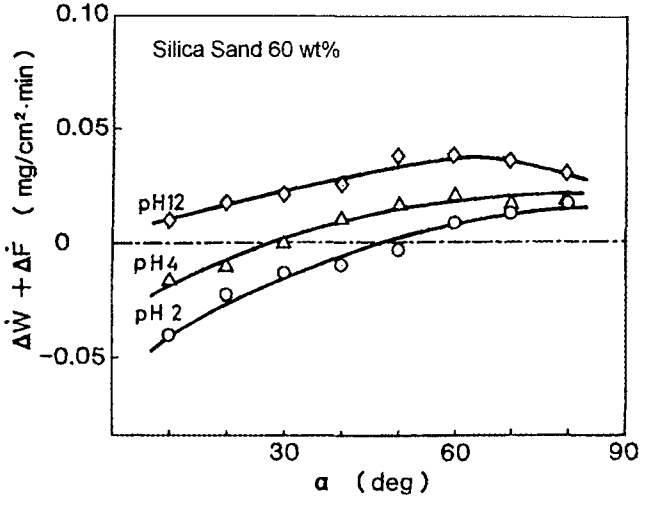

Figure 7.36 Effect of impact angle on the amount of synergistic effect of erosion and corrosion for iron specimens; jet velocity, 3.0 m/s; slurry, corrosive liquids and silica sand of 60 wt%, 40°C

7.4.2 Basic Equations Describing the Combined Effect of Erosion and Corrosion

For the interpretation of the observed results, the application of the basic equations previously developed for erosion-corrosion processes with cavitation will be attempted.

$$W_t = W' + F' \tag{7.23}$$

This equation postulates that the total damage to a metal in erosion-corrosion, W_t, consists of W' and F', where W' is the amount of erosion, that is, the amount of material which separates itself from the surface as small metallic particles, and F' is the amount of corrosion or the amount of material which dissolves from the surface as metallic ions. Differentiation of Equation (7.23) givers:

$$\dot{W}_t = \dot{W}' + \dot{F}' \tag{7.24}$$

Each term of the equation has dimensions of rate, namely, mg/cm^2•min. Further, $\dot{W}'$ and $\dot{F}'$ may each be separated into two components because it is considered that the rates in slurry erosion-corrosion are independent of the testing time:

$$\begin{aligned} \dot{W}' &= \dot{W} + \Delta\dot{W} \\ \dot{F}' &= \dot{F} + \Delta\dot{F} \end{aligned} \tag{7.25}$$

In Equation (7.25) $\Delta\dot{W}$ is the increment in erosion rate caused by corrosion and $\Delta\dot{F}$ is the increment in corrosion rate caused by erosion. By combining Equation (7.23) and (7.24), the extent of the mutual interaction, namely, of the synergistic effect of erosion and corrosion is obtained as follows:

$$\dot{W}_t - (\dot{W} + \dot{F}) = \Delta\dot{W} + \Delta\dot{F} \tag{7.26}$$

Of considerable interest is determination of the magnitude and sign of $\Delta\dot{W}$ and $\Delta\dot{F}$. In order to answer this question, $\dot{W}'$ and $\dot{F}'$ were independently and quantitatively determined by using the method shown in Figures 7.37 and 7.38. Erosion-corrosion tests conducted with a corrosive slurry of pH 2 were suddenly switched our to pure erosion tests (at a testing time of 60 min) by exchanging the corrosive slurry with a noncorrosive one (slurry of silica sand and deionized water). The change in damage rates at particle impact angles of 10° and 80° which were brought about by the exchange of the slurries is shown in Figure 7.37. The damage rates decreased gradually to eventually reach the individual pure erosion rates (compare with Figure 7.32). The extrapolation of these curves back to the time of the slurry exchange is considered to give the erosion rates under the erosion-corrosion condition, namely $\dot{W}'$. The same procedure was adopted to obtain $\dot{F}'$, but in this case the erosion-corrosion tests were followed by pure corrosion tests. The values $\dot{W}'$ and $\dot{F}'$ thus obtained for impact angle of 10° and 80° are listed in table 7.8. Excellent agreement is obtained between the observed value of $\dot{W}_t$ and the sum of $\dot{W}'$ and $\dot{F}'$.

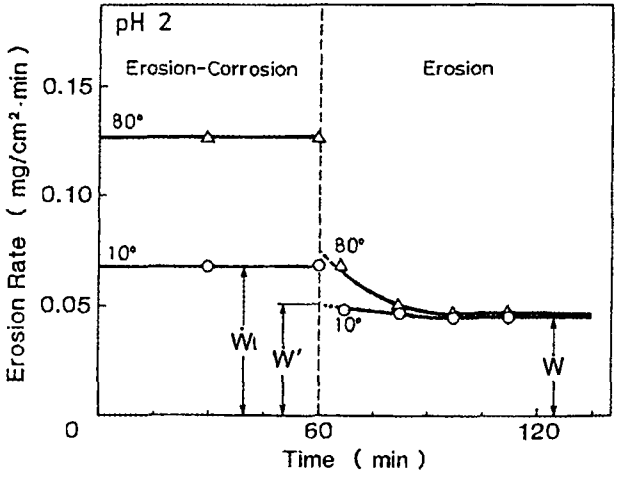

Figure 7.37 Erosion-corrosion test followed by erosion test on iron specimens; jet velocity, 3.0 m/s; slurry *Hcl* acid solution of pH2 and silica sand of 60 wt%, 40°C

Table 7.8 Comparison of erosion-corrosion rates.

Impact angle (deg)	$\dot{W}_t$	$\dot{W}'+\dot{F}'$	$\dot{W}'$	$\dot{F}'$
	(mg/cm^2•min)			
10	0.067	0.078	0.047	0.031
80	0.125	0.128	0.075	0.053

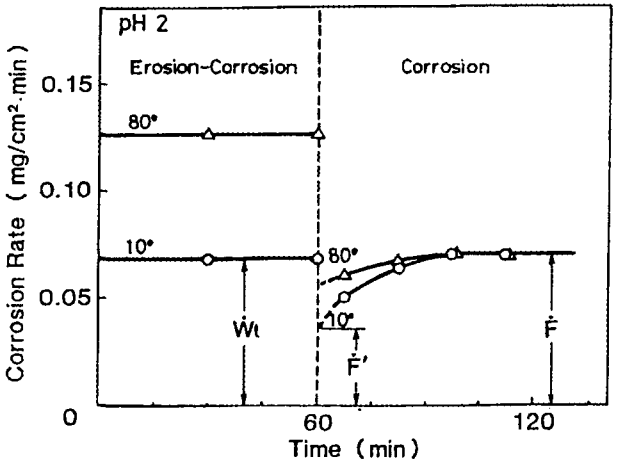

Figure 7.38 Erosion-corrosion test followed by erosion test on iron specimens in environmental liquid of pH 2; jet velocity, 3.0 m/s; temperature of liquid, 40°C

The results shown in Figures 7.37 and 7.38, and including Table 7.8 indicate the following:

i) The extrapolation method described above is useful for determining each component for combined erosion and corrosion conditions.

ii) Equation (7.23) is considered to be valid for slurry erosion-corrosion of commercially pure iron in the slurry of silica sand and hydrochloric acid solutions.

iii) The negative mutual interaction in Figure 7.36 is to be attributed to the effects of $\Delta\dot{F}$, because in Figure 7.38 $\dot{F}'$ is lower than $\dot{F}$, thus $\Delta\dot{F}$ is negative. This means that corrosion is inhibited by erosion even though

this appears to be contrary to common sense. This unexpected result is supported by the experimental results, however. It appears that $\Delta\dot{F}$ takes on a larger negative value at the impact angle of 10° than at 80° (Figure 7.38), in agreement with observed interaction as shown in Figure 7.36. On the other hand, $\Delta\dot{W}$ is positive for all impact angles as may be observed in Figure 7.37.

7.4.3 Analysis on a Single Crater

(1) Crater formation by free-falling projectile:

The detailed mechanism of the observed interaction including the inhibiting effect of erosion on corrosion, and even of the accelerating effect of corrosion on erosion must be found. In order to do this, the process of crater surfaces needs to be explained. The dimension of a crater formed by a single impact of a silica sand particle is too small to be fully observed even though a SEM is used. Therefore craters of larger dimension have been formed by allowing a projectile to fall freely onto specimens of relatively large surface area (12×30 mm^2) as shown in Figure 7.39. The head of the projectile was a cylindrical rod 4 mm in diameter. Its impact on the specimen surface formed a crater of approximately 3 mm in width at an impact velocity of 8 m/sec, and the length depended on the impact angle.

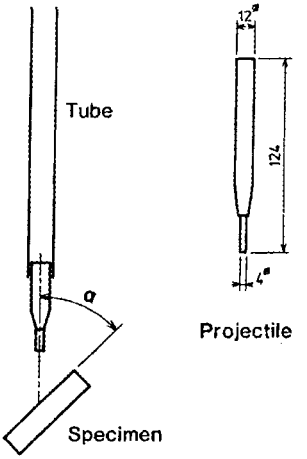

Figure 7.39 Schematic diagram of free-falling indenter unit

(2) Effect of dissolution on crater formation:

The acceleration effect of corrosion on erosion may be attributed to the dissolution of the strain-hardened layer and the increase in surface roughness accompanying the dissolution. Repeated impacts of particles are expected to cause strain hardening of the surface and further impacts on this surface of higher hardness will result in shallower and smaller craters. Dissolution of this hardened surface layer by corrosion will accelerate erosion by causing the formation of larger craters. The dissolution of the surface layer will also result in the formation of hills and valleys on the surface, which, in turn, will catch the particles or projectile and result in yet larger craters.

Two specimens were finished by milling in order to obtain hardened surfaces, one of which was then annealed to get rid of the hardened layer. Thus, two specimens were prepared, one with, and the other without a strain-hardened layer on the surface but with the same surface roughness (see Figure 7.40). The profiles of craters which were formed on each specimen by impacting the projectile at impact angles of 30° and 70° are shown in Figure 7.41. At an impact angle of 30°, little difference is observed between the craters. On the other hand, at an angle of 70° a deeper crater was formed on the annealed surface.

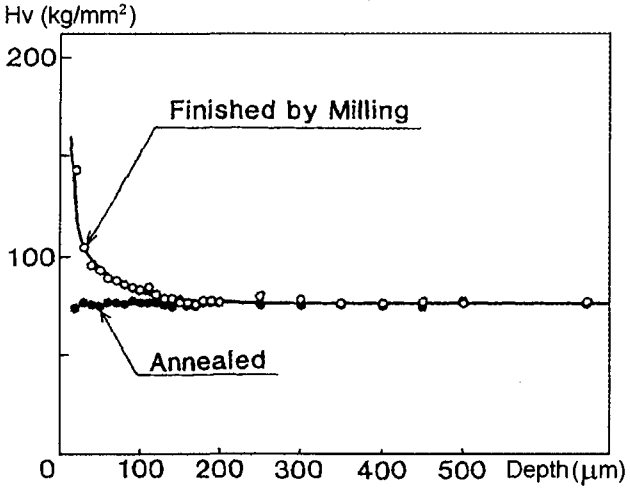

Figure 7.40 Hardness distribution on iron specimen annealed or finished by milling

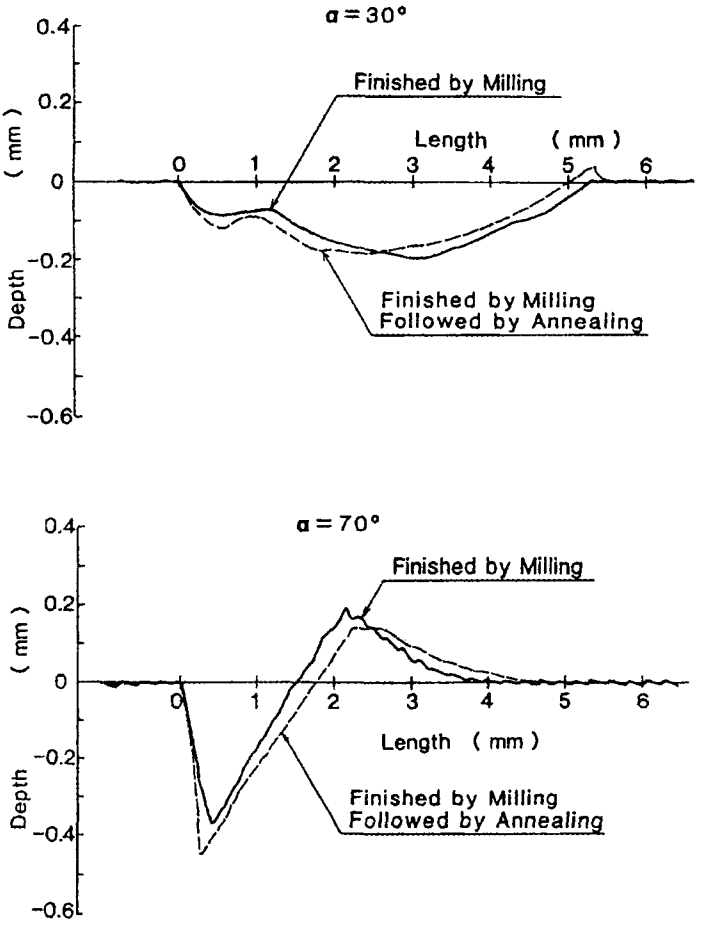

Figure 7.41 Profile of craters formed by free-falling projectile impacted on iron specimen surfaces annealed or finished by milling; impact velocity, 8 m/s

The effects of surface roughness are shown in Figure 7.42. The profiles of craters which were formed on one surface smoothed by polishing are compared with another surface roughened by dissolution in a corrosive liquid producing an average roughness of 20 μm. In this case, an effect is distinctly

observed at an angle of 30°; a deeper crater was formed on the surface roughened by corrosion.

Thus, the dissolution of the hardened surface and the increase in surface roughness are possible causes for acceleration of erosion by corrosion.

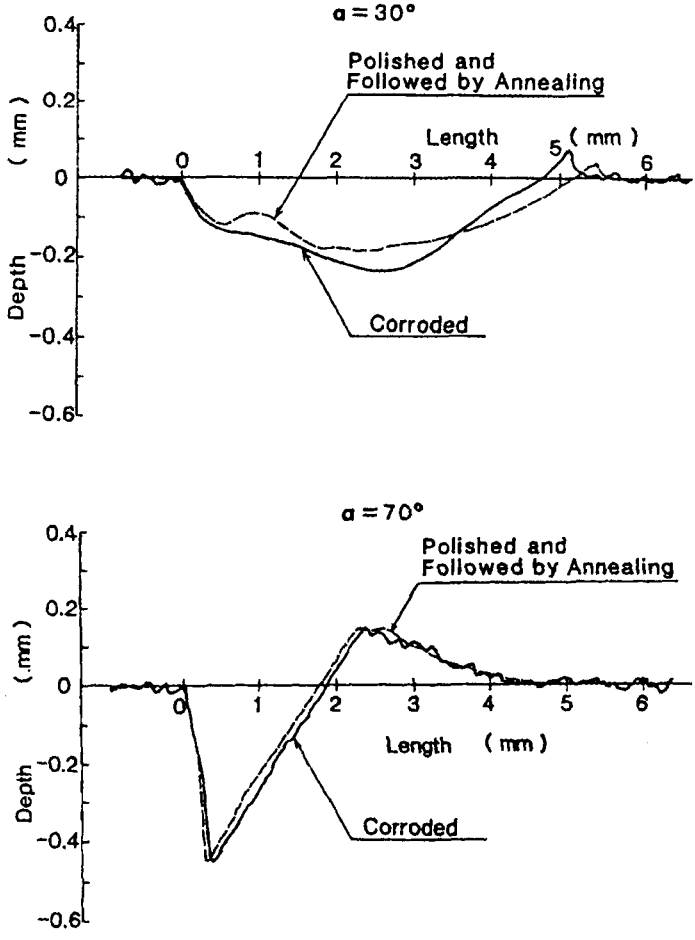

Figure 7.42 Profile of craters formed by free-falling projectile impacted on iron specimen surfaces in *Hcl* acid solution of pH2; impact velocity, 8 m/s

(3) Characteristic cross-sectional shapes of craters:

Careful observation was performed of shapes of cross-section of craters to permit some general characterization of the surfaces. Possible types of surfaces are the displaced surface ① the lip surface ② the surface produced by sliding ③ as obtained for the crater with an impact angle of 50°, and a cut surface ④ as obtained for the crater at an impact angle of 30° as shown in Figure 7.43. The displaced surface ① is considered to be the portion of original surface which has been pushed down and inward by the flat head of the projectile. The original surface as well as the subsurface grain boundaries remained undisturbed. By contrast with this, the lip surface ② consisted of material which was extruded from the crater. A considerable amount of plastic deformation and some twins were observed in the inspection of the crater cross-section. A lot of microscopic as well as macroscopic defects such as cracks were expected on this surface. Both the surface ③ and the cut surface ④ were formed by the projectile sliding on the specimen surface. A great amount of deformation by shear stress was brought about just under the surface, which was similar to the "fibrous structure" usually observed as a result of wire-drawing. The difference between surface ③ and surface ④ is that some amount of material was actually cut out of surface ④ but no material was removed from surface ③.

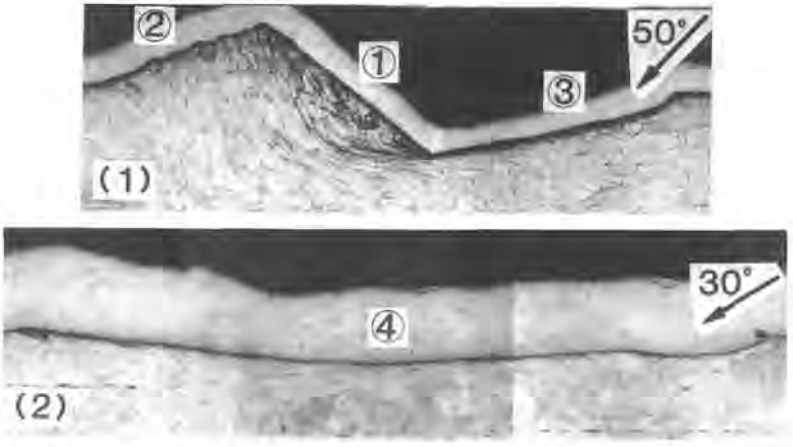

(1) impact angle of 50°; **(2)** impact angle of 30°

Figure 7.43 Cross-sections of craters formed on iron specimens

(4) Dissolution rates of polished and indented-surfaces:

Dissolution rates of characteristic surfaces were obtained by measuring the weight loss of a specimen dipped into an acid solution of pH2. Each specimen had a few craters formed at the same impact angle on its surface and was masked completely by an anticorrosion paint except for one of the characteristic crater surfaces. The results are shown in Figure 7.44 as a function of duration of exposure to the acid solution. The dissolution rate of the original polished surface without craters is also given by a broken line. All of the dissolution rates change with time to converge upon a certain common value. This may result from that the dissolution process removes surface material until a depth is reached where on further influence of the particle impact of polishing is observed. The initial dissolution rate of a characteristic surface may be obtained by extrapolating each curve back to the initial time. The dissolution rates so-determined of a displaced surface ① and a polished surface are nearly the same at about 0.10 mg/cm^2•min. The rate for a lip surface ② is approximately 0.30 mg/cm^2•min, which is three times higher than that for a polished surface. In contrast, the rates for a sliding surface ③ and a cut surface ④ are both 0.02 mg/cm^2•min, which is only one fifth of that for a polished surface.

The question then arises as to why a lip surface ② dissolves at a rate fifteen times higher than that for a sliding ③ or a cut ④ surface. This may be attributed not only to the corrosion acceleration agents of the microscopic as well as macroscopic defects on the surface ②, but also to another important cause which reduces the dissolution rates of other surfaces (③ and ④) to one fifth of a polished surface. The cause might involve the arrangement of certain crystal planes on crater surfaces. Figure 7.45 shows SEM micrographs of etch pits formed on the different characteristic surfaces. On a polished surface, each pit took a different form depending on the crystal grain on which it was located, Figure 7.45 (a). This suggests that the polished surface consists of various crystal planes. A similar situation was observed on the displaced surface ① (Figure 7.45 (b)), as well as on the lip surface ② (Figure 7.45 (c)). In addition to this, a larger number of pits were formed on the lip surface ②, indicating the presence of many microscopic defects. Macroscopic defects such as swelling and cracking are also observed. In contrast with these, all of the pits on a cut surface ④ assumed regular square shapes arranged in a common direction independent of the crystal grains, Figure 7.45 (d). The same was observed on the sliding surface ③. Moreover, the inner

facet of each pit assumed a common shape. This appears to prove that the crystal plane {110} corresponded to that surfaces and those the projectile sliding direction was <111>. These are characteristic slip planes and slip direction of a bcc metal. Also, it has been well established that among crystal planes of a bcc metal the dissolution rate of {110} planes is second lowest, the lowest being {100} planes. Accordingly, this particular crystal structure is considered to cause a sliding surface ③ or cut surface ④ to dissolve at a lower rate than that for a polished surface.

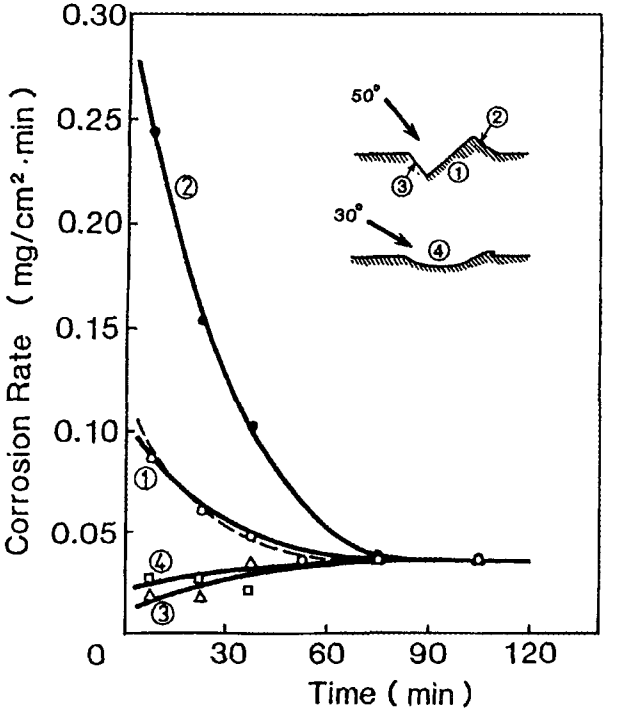

① displaced surface, ② lip surface, ③ sliding surface, ④ cut surface.

Figure 7.44 Dissolution rate of characteristic surfaces

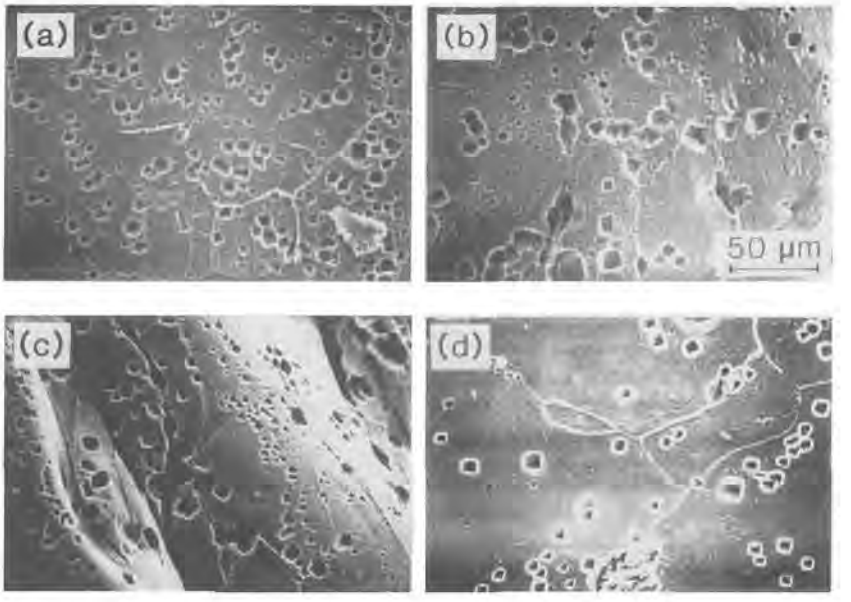

Figure 7.45 SEM micrographs of etch pits in characteristic surfaces of (a) polished surface, (b) displaced surface, (c) lip surface, (d) cut surface. impact direction, left to right

7.4.4 Parameters Affecting the Mutual Interaction Mechanism

(1) Effect of impact angle on dissolution rate:

The above discussion regarding the mechanism of the mutual interaction of erosion and corrosion are totally based upon the behavior of relatively large craters formed under special conditions. Accordingly the details of the mechanism as obtained of real situations. However, the different mechanisms described so far are able to satisfactorily explain the experimental results of Figure 7.36.

Let us first consider the effect of impact angle on the amount of mutual interaction, that is, the relationship between $\dot{W}_t - (\dot{W} + \dot{F})$ and α in Figure 7.36. The mutual interaction becomes more inhibitory with a decrease in impact angle. It has been made clear that the lower the impact angle, the more likely are the crater surfaces to be of the characteristic surface types ③ and

④. For these surface types the dissolution rate is decreased, while it has been shown that $\Delta\dot{W}$ is smaller at lower impact angle (see Figure 7.37). Thus the tendency in Figure 7.36 is reasonably understood.

Secondly, we consider the effect of the pH of slurry. In Figure 7.36 the mutual interaction becomes more inhibitory with a decrease in pH. A decrease in pH results in an increase in the corrosion intensity, and consequently increases $\Delta\dot{F}$, while $\Delta\dot{W}$ possibly remains within a certain value. Thus $\Delta\dot{F}$ dominates the mutual interaction term $\Delta\dot{W}+\Delta\dot{F}$. Since $\Delta\dot{F}$ is negative for all impact angles as shown in Figure 7.36, the values for $\dot{W}_t-(\dot{W}+\dot{F})$ in Figure 7.36 are reduced as the corrosion intensity increase.

(2) Effect of the relative magnitude of the erosion and corrosion rate:
It has been made clear that the impact angle, actual rates of erosion and corrosion as well as the relative intensities of erosion and corrosion are important parameters which determine the extent of the synergistic interaction. These results may be compared with the previous investigation (see Oka and Matsumura, 1987) for conditions where erosion is predominant. It is noteworthy that the synergistic-controlling component was erosion, and the mechanism of the acceleration was quite different; it involved hydrogen embrittlement. The effect of hydrogen was also examined in this investigation, but no influence on the erosion rate was observed. A conclusion which can be drawn from this comparison is that the relative magnitude of the erosion and corrosion rates determined not only the amount of synergistic interaction but also its mechanism.

The influence of relative magnitude of erosion and corrosion rates may explain the cause of the often-encountered annoying problem in evaluation of material for practical use; results of laboratory tests are not always in agreement with experience in the field. A laboratory test conducted in conditions of, for example, accelerated erosion naturally brings about an order of merit of materials totally different from that in the field. This is simply because the relative magnitude of erosion and corrosion rates in the test was different from that in the field and the mechanism of damage was also different.

References

7. 1 Fontana, M. G. and Green, N. D., (1978). 'Corrosion Engineering', McGraw-Hill, New York.

7. 2 Haruyama, S., Tsuru, T. and Anan, M., (1978). 'Impedance of Corroding Electrode', *Boshoku Gijutsu*, vol.27, No.9, September, pp. 49 ~ 456.

7. 3 Katoh, M. and Kayama, M., (1985). 'Improvement of the Polarization Reistance Method-Measurement of the polarization from the initial transient curve under a constant current --', *Boshoku Gijutsu*, Vol. 34, No. 4, April, pp. 215 ~ 221.

7. 4 Kitashima, N., Ichikawa, K., Kinoshita, K. and Miyasaka, M., (1986). 'Corrosion in Seawater Pumps and Its Prevention', *Boshoku Gijutsu*, Vol.35, No. 11, November pp. 663 ~ 641.

7. 5 Laque, F. L, (1972). 'Effects of Specimen size on Results of Corrosion Tests', Proceedings of Fifth International Congress on Metallic Corrosion, Tokyo, pp. 1 ~ 7.

7. 6 Matsumura, M. and Oka, Y., (1987). 'Slurry Erosion-Corrosion of Commercially Pure Iron in Fountain-Jet Testing Facility', Proceeding of Seventh International Conference on Erosion by Liquid and Solid Impact, Cambridge, pp. 401 ~ 408.

7. 7 Oka, Y., Matsumura, M., Ohsako, Y. and Yamawaki, M, (1984). 'Particle Impact Conditions in Vibratory Sand-Erosion Facilities', *Boshoku Gijutsu,* Vol. 33, No. 5, May, pp. 378 ~ 283.

7. 8 Oka, Y. and Matsumura, M., (1987). 'Slurry Erosion-Corrosion on Commercially Pure Iron in a Vibratory Testing Facility', Proceedings of Seventh International Conference on Erosion by Liquid and Solid Impact, Cambridge, pp. 391 ~ 398.

7. 9 Pourbaix, M., (1966). 'Atlas of Electrochemical Equilibrium in Aqueous Solutions', Pergamon Press, New York.

7. 10 Stern, M. and Geary, A. L., (1957). 'Electrochemical Polarization', *Journal of Electrochemical Society*, Vol. 104, No. 1, January, pp. 56 ~ 63.

7. 11 Uhlig, H. H., (1971). 'Corrosion and Corrosion Control', John Wiley & Sons Inc., New York.

7. 12 Whitman, G. W., Russel, R. P. and Altier, V. J., (1924). 'Effect of Ion Hydrogen-Concentration on the Submerged Corrosion of Steel', *Industrial and Engineering Chemistry*, Vol. 16, No. 7, July, pp. 665 ~ 670.

7. 13 Wrangle, G., (1972). 'An Introduction to Corrosion and Protection of Metals', Halsted Press, New York.

SERIES ON HYDRAULIC MACHINERY – VOL. 2

Abrasive Erosion & Corrosion of Hydraulic Machinery

This book gives a systematic exposition of abrasive erosion and corrosion of hydraulic machinery in both theory and engineering practice, and is the first comprehensive volume to cover this area in depth.

All the important subjects are discussed including fundamentals, calculation, analysis and numerical simulation of liquid–solid flow design, erosion-resistant materials, interaction between cavitation and abrasive erosion, and corrosion of hydraulic machinery.

P272 hc

ISBN 1-86094-335-7

9 781860 943355

Imperial College Press

www.icpress.co.uk